

Raindrop Erosion of Wind Turbine Blades in Various
Environments.

PhD Thesis

Kieran J Pugh

TriboS Research Group

Department of Mechanical and Aerospace Engineering
University of Strathclyde, Glasgow, Scotland

February 20, 2023

This thesis is the result of the author's original research. It has been composed by the author and has not been previously submitted for examination which has led to the award of a degree.

The copyright of this thesis belongs to the author under the terms of the United Kingdom Copyright Acts as qualified by University of Strathclyde Regulation 3.50. Due acknowledgement must always be made of the use of any material contained in, or derived from, this thesis.

Signed:

Date:

Abstract

Renewable energy is the solution to a greener, more sustainable future and wind energy is a massive contributor, especially in Scotland. One of the limiting factors to wind turbines is the leading-edge erosion of the blades. This is a developing and growing issue in large multi mega-watt wind turbines within the wind industry as it affects blade performance and thus generating efficiency. The research presented aims to contribute to the scientific community investigating this topic by developing a fuller picture of the problem encountered in laboratory testing, analysing data and utilising the results in predictive models. This research work builds upon previous investigations into the erosion of wind turbine blades by determining the effect that stress has on the erosion rate and therefore the efficiency of the turbine this is particularly applicable with the new larger turbine blades. To achieve this objective a custom rain erosion test facility and stressed sample holder were designed, manufactured and commissioned as part of this research to fully understand the problem. The results demonstrated that the applied bending stress increases the erosion rate and the trend does not follow the general accepted trends seen within the literature. This research therefore investigates the development of an alternative erosion-based model centred around the theta projection method which followed the trends observed in the experimental results more closely. Theta projection model and geographical rain data were utilised to develop site specific erosion predictions for the individual blade size and geometry which determines the impact velocity of the droplet and the stress within the material. Future developments are aimed at further expanding the research and providing knowledge to optimise turbine blade maintenance and thus efficiency.

Contents

Abstract	ii
Contents	iii
Preface/Acknowledgements	viii
Scientific Contributions	ix
List of Abbreviations	xi
1 Introduction	1
1.1 Growth of Wind Energy and Technology Development	1
1.2 Environmental Resistance of Wind Turbine Blades	4
1.3 Purpose of Current Research	6
2 Wind Turbine Background	7
2.1 Wind Turbine History	7
2.2 Wind Turbine Design	10
2.3 Further development on wind turbine technology	13
2.4 Aerodynamics	14
2.4.1 Control of Blades	14
2.5 Loads on Wind Turbine Blades	15
2.5.1 Aerodynamic Load	15
2.5.2 Gravitational and Centrifugal Loads	17
2.5.3 Flapwise Bending	18

Contents

2.5.4	Edgewise Bending	20
2.5.5	Fatigue Loads	21
2.6	Blade Materials	22
2.6.1	Material Selection	22
2.6.2	Fibre Reinforced Composites	24
2.6.3	Composite Material Designs	25
2.6.4	Reinforcement Fibre Materials	25
2.6.5	Matrix Materials	28
3	Rain Erosion	29
3.1	History of Rain Erosion and Industrial Applications	29
3.2	Erosive Parameters for Wind Turbine Blades	34
3.2.1	Impact Velocity	34
3.2.2	Droplet Size	35
3.2.3	Droplet Shape	36
3.3	Droplet Impact Physics	38
3.3.1	Impact Event	38
3.3.2	Water-Hammer Pressure	38
3.3.3	Stress Waves	40
3.3.4	Lateral Jetting	42
3.4	Erosion Damage Mechanisms	45
3.4.1	Effects of Erosion Parameters	48
4	Leading Edge Erosion Testing	54
4.1	Techniques for Simulating Leading Edge Erosion	54
4.1.1	Purpose of an Erosion Testing Facility	55
4.1.2	Jet Erosion	56
4.1.3	Ballistics/ Rocket Testing	58
4.1.4	Wind Tunnel Testing	60
4.1.5	WARER (Whirling Arm Erosion Rig)	61

Contents

5	Construction of Custom Rain Erosion Testing Facility	64
5.1	Basis of Design	64
5.2	Material Selection	68
5.3	Sample Holder	72
5.4	Stress Analysis	73
5.5	Commissioning and Calibration	75
5.6	Safe Operation	80
6	Leading Edge Erosion Analysis	82
6.1	Materials Characterisation	82
6.1.1	Coating Adhesion Strength	86
6.1.2	Coating Layer Thickness	86
6.1.3	Stiffness, Storage Modulus and Loss Modulus	86
6.1.4	Hardness	87
6.1.5	Tensile Properties	88
6.1.6	Damage Resistance	89
6.2	Surface Analysis	90
6.2.1	Optical	91
6.2.2	Scanning Electron Microscope (SEM)	93
6.2.3	Profilometer Analysis	95
6.3	Subsurface analysis	97
6.3.1	Ultrasound	98
6.3.2	Radiology	100
6.3.3	Microwave Imaging	100
6.4	Standardised Methods for Assessing Damage	102
6.4.1	Mass and Volume loss Analysis	102
6.4.2	Surface Roughness	103
6.5	Discussion and Conclusions	105
7	Computational Blade Stress Analysis	107
7.1	Wind Turbine Shape and Performance Analysis	107

Contents

7.1.1	Aerofoil characteristics and Element Theory	109
7.1.2	Finalised Blade Geometry	110
7.1.3	Material Properties	116
7.2	Turbine Blade Loading Conditions	116
7.3	CFD Loading Setup	118
7.4	Boundary Conditions for CFD	120
7.5	Results	122
7.5.1	CFD Loading	122
7.5.2	CFD FEA	123
7.6	Discussion	123
7.6.1	CFD Loading Configuration	123
7.6.2	FEA Discussion	125
7.7	Conclusions	126
8	Experimental Work	128
8.1	Rain Erosion in On-Shore Conditions	128
8.1.1	Methods and Materials	128
8.1.2	Testing Apparatus	129
8.1.3	Design of Experiment	131
8.1.4	Experimental Run Time	132
8.1.5	Mass Measurement	132
8.1.6	Materials	133
8.1.7	Results and Discussion	134
8.1.8	Conclusions	142
8.2	Effect of Bending Stress on Rain Erosion in On-Shore and Off-Shore Conditions	143
8.2.1	Aims and Objectives	143
8.2.2	Experimental Apparatus	143
8.2.3	Test Conditions	144
8.2.4	Post Processing	145

Contents

8.2.5	Results	145
8.2.6	Discussion of Unstressed Fresh Water Erosion	148
8.2.7	Discussion of Unstressed Salt-Water Erosion	150
8.2.8	Discussion of Applied Bending Stress in Fresh Water and Salt Water Erosion	152
8.2.9	Conclusions	157
8.3	High Speed Rain Erosion in Large Scale Experiment	158
8.3.1	Aims and Objectives	158
8.3.2	Experimental Constants	160
8.3.3	Experimental Variables	161
8.3.4	Bending Stress Calculations	162
8.3.5	Experimental Procedure	166
8.3.6	Results and Discussion	167
8.3.7	Conclusions	176
9	Construction of a Predictive Model	180
9.1	History of Rain Erosion Prediction Models	181
9.2	Development of Rain Erosion Predictive Models	182
9.3	Geographical Data	185
9.4	Data Projection Method	193
9.5	Prediction Model and Application	196
10	Overall Discussion	201
11	Conclusions	207
12	Recommended Future Work	210
	Bibliography	213
	List of Figures	228
	List of Tables	235

Preface/Acknowledgements

I would firstly like to give thanks to my academic advisor Professor Margaret M. Stack for her guidance, support and encouragement throughout my PhD studies. Professor Stack has contributed a significant amount of support and input into my research, shaping my efforts in publishing the findings of my work and encouraging my development throughout my PhD studies. Her drive and scrutiny has helped to get the best out of me and my research.

This work was facilitated by funding from the SPIRE2 project. Their aim to further develop the energy storage model for renewable energy sources was the catalyst for this research.

My fellow PhD students; Georgie, Alessio, Philipp and James have maintained my motivation and drive throughout the project. In addition, all the Technical staff in the MAE laboratories have been generous with their help.

I would like to thank my closest friends Emily McNicol and Madeline Watson for their belief in me and continual support.

Last, but by no means least, I would like to thank my loving family, Gail, John and Rachel for their constant support and encouragement throughout.

Scientific Contributions

Peer Reviewed and Published Journal Articles

1. “Some thoughts on mapping tribological issues of wind turbine blades due to effects of onshore and offshore raindrop erosion” K Pugh, G Rasool, MM Stack, Journal of Bio-and Tribo-Corrosion 4 (3), 1-8 (2018)
2. “Raindrop erosion of composite materials: some views on the effect of bending stress on erosion mechanisms” K Pugh, G Rasool, MM Stack, Journal of Bio-and Tribo-Corrosion 5 (2) (2019)
3. “On analytical tools for assessing the raindrop erosion of wind turbine blades” K Pugh, JW Nash, G Reaburn, MM Stack, Renewable and Sustainable Energy Reviews 137, 110611, (2021)
4. “A study of raindrop impacts on a wind turbine material: velocity and impact angle effects on erosion MAPS at various exposure times” S Groucott, K Pugh, I Zekos, M M Stack, Lubricants 9 (6), 60 (2021)
5. “Rain erosion maps for wind turbines based on geographical locations: A case study in Ireland and Britain” K Pugh, MM Stack, Journal of Bio-and Tribo-Corrosion 7 (1), 1-7 (2021)

Peer Reviewed Conference Papers

1. “Review of analytical techniques for assessing rain drop erosion resistance of materials” K Pugh, JWK Nash, MM Stack, G Reaburn, 14th Conference on Sustainable Development of Energy, Water and Environment Systems (2019)

Conference Presentations

1. K Pugh, JW Nash, G Reaburn, MM Stack, Presentation given at the SDEWES Conference held in Dubrovnik in 2019 entitled “Review of analytical techniques for assessing rain drop erosion resistance of materials”
2. K Pugh, Presentation given at the All Energy Conference in Glasgow in 2018 entitled “The effect of rain erosion on multi-megawatt wind turbine blades in Off-shore conditions”
3. K Pugh, Presentation given at the SPIRE2 Conference in Belfast in 2022 entitled “Wind Turbines in Erosive Environments – Testing, Understanding and Evolving”

Journal articles in writing

1. K Pugh “The Accumulation of Rain Erosion with Applied Bending Stress for Large Multi-Megawatt Wind Turbine Blade Materials.”
2. K Pugh “The Development of a Predictive model to Determine Wind Turbine Blade Erosion Using Meteorological Data”

Journal paper statistics

- Total citations: *54*
- h-index: *4*
- i10-index: *2*
- Total downloads: *10,811*

List of Abbreviations

ABS	Acrylonitrile butadiene styrene
CAD	Computer aided design
CFD	Computational fluid dynamics
CFRP	Carbon fibre reinforced polymer
CLSM	Con-focal laser scanning microscope
CMM	Co-ordinate measuring machine
ETS	Engineering technical supervisor
FES	Finite element analysis
GFRP	Glass fibre reinforced polymer
HAWT	Horizontal axis wind turbine
HDPE	High density polyethylene
HSE	Health and safety executive
IOS	iPhone operating system
LEE	Leading edge erosion
LIE	Liquid droplet erosion
NACA	National advisory committee for aeronautics

List of Abbreviations

NDT Non destructive testing

PJET Pulsating jet erosion testing

SEM Scanning electron microscope

SENT Single edge notch tensile test

SICD Surface impact circular deformation

UDL Universally distributed load

VAWT Vertical axis wind turbine

WARER Whirling arm rain erosion rig

WDE Water droplet erosion

Chapter 1

Introduction

In recent times the drive to implement renewable energy resources from political, social, and economic movements has been at an all-time high. This movement has arisen for the need to suppress carbon emitting sources of energy and replace the power demand with renewable sources such as wind, tidal and solar. In Scotland wind energy is currently at the forefront of renewable generation with 9.655GW capacity (as of Q4 2021). Scotland is also home to Europe's largest onshore wind farm at Whitelee 19 miles from the University of Strathclyde. This wind farm along with other renewable sources have been pivotal in the effort to accomplish the Scottish Government target of 100% electricity generation originating from renewable energy and in 2020 it reached 97.4% from renewable sources [1].

1.1 Growth of Wind Energy and Technology Development

With the ever-growing popularity and reputation of wind energy, the installation of wind turbines has experienced a substantial escalation in recent times. Europe (including UK) has installed 15.4GW of new power capacity in 2019 which results in a total of 205GW of wind energy capacity. This an increase of 27% new capacity from 2018 and an increased focus has been put onto offshore capacity especially in the UK with 1764

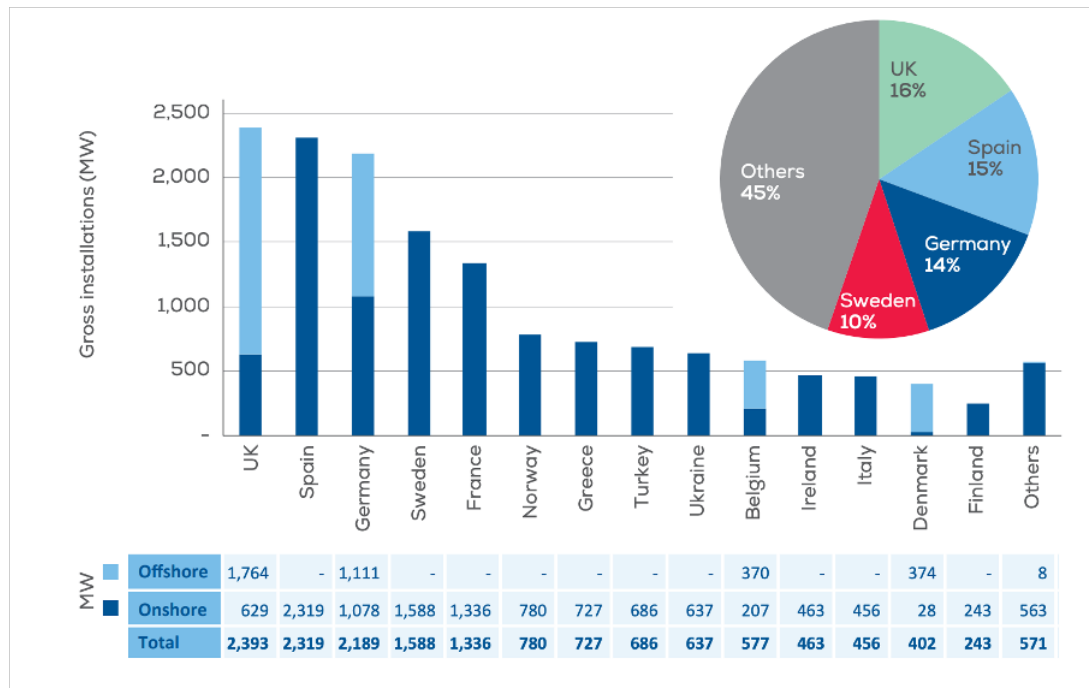


Figure 1.1: 2019 New onshore and offshore wind installation in Europe [2]

new installations in 2019 as shown in Figure 1.1 [2]. The US are investing large sums of money into renewable energy, including wind shown in Figure 1.2 [3] and have installed 13.4GW of wind energy in 2021 bringing their total wind capacity to 136GW [4]. Also, in Australia wind is becoming more prevalent with it being the largest contributor to the renewable energy generation at 35.9% and all renewable energy making up 27.7% of Australia's total electricity generation. It is also part of an Australian state pledge to become completely emission free by 2045 which involves many new wind farms [5].

Wind energy has not only become a focal point for world governments but it is also very prevalent within changing industries including oil and gas refinery companies such as BP. To date BP have implemented 1.66GW of wind energy capacity to the US [6] and have just recently purchased land offshore of Scotland to install some larger wind turbines [7].

With this pivot in energy production to wind turbines, it is in the interest of all

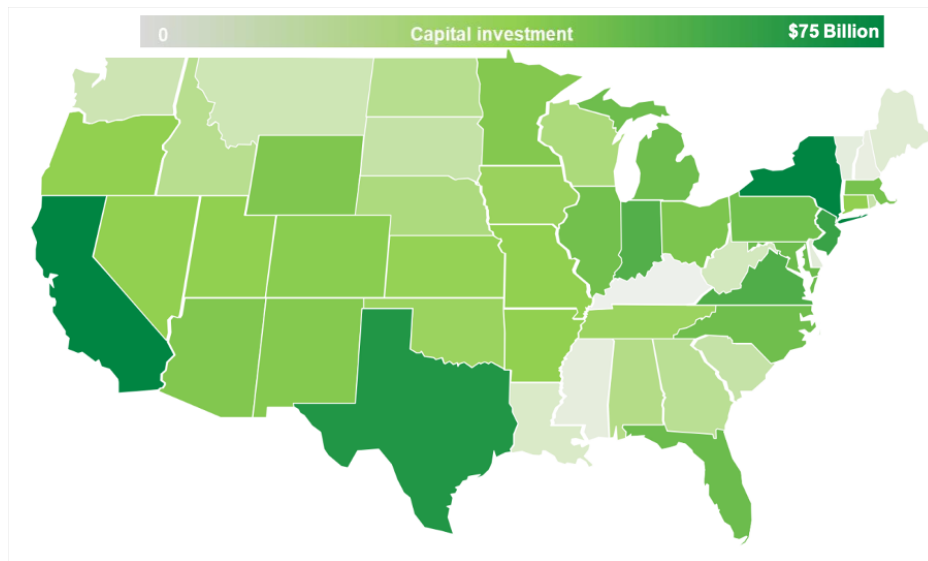


Figure 1.2: Total US investment wind and solar - cumulative capital investment, 2020-2030 [3]

parties involved to progress the technology and harness as much electricity from the wind as physically possible. This trend of higher wind capacity has generated a demand for an increase in energy production per wind turbine which has translated to a rapid increase in the turbine blade length [8]. The average length of installed turbine blades is gradually increasing as the popularity of offshore wind farms climbs and thus more research is required to fully understand the erosion of these new larger blades. An added factor to this trend is also the marketing of wind turbine manufactures and suppliers as a larger blade length represents a greater engineering feat, in a similar fashion as the largest buildings in the world are admired.

The large wind turbine diameters as observed in Figure 1.3 have resulted in much greater tangential tip velocities. Due to their scale it can be deceiving how quickly some turbine blades are travelling as some existing turbine blade tips are experiencing in excess of $100ms^{-1}$ as shown in Figure 1.4 [10]. The combined effect of the increased turbine size and the tangential tip velocity have brought about their own challenges involving operation and maintenance. Within these challenges lies the issue of leading-edge erosion. As the turbines are purposefully placed in exposed locations due to the high availability of constant wind, the consequent weather conditions are detrimental

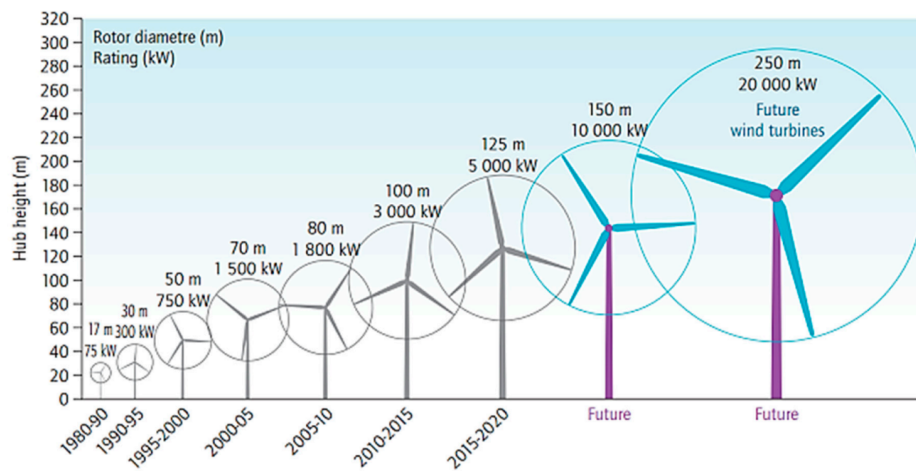


Figure 1.3: Growth in size of wind turbines since 1980 and future prospects [9]

to the turbine blades.

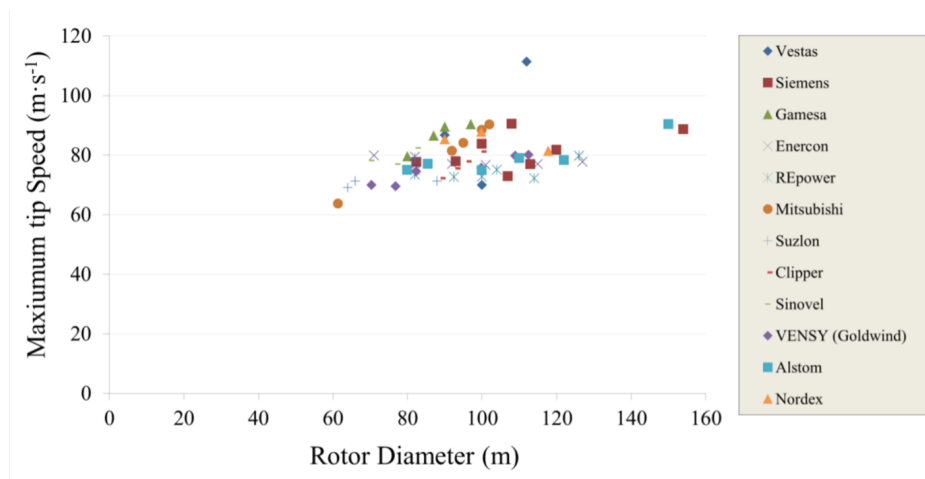


Figure 1.4: Maximum tip velocity and rotor diameter for various wind turbine suppliers [10]

1.2 Environmental Resistance of Wind Turbine Blades

As wind turbines are generally located in harsh environments with consistent wind to ensure greater generating capacity for the turbine this can create problems as the environment starts to attack the turbine. These attacks differ depending on the country and the associated climate, this results in the location of the wind farm being crucial,

not only for efficient power production but also for the structural integrity of the turbine.

Some of the ways in which turbines can be affected by the environment are as follows:

- **Rainfall:** This is by far the most common environmental factor and is the main issue which will be investigated. The small droplets create high impact collisions when struck by an operational wind turbine, especially when the collision occurs at the tip of the blade and in this case the impact velocity can surpass $150\text{m}\cdot\text{s}^{-1}$
- **Hail:** Although hail strikes onto turbine blades are drastically less common, the damage they create is exponentially more destructive. The impact site of a hail strike can also lead to further erosion by rainfall as the more vulnerable layers as the turbine composite will be exposed.
- **Lightning Strikes:** Within the environment the turbines are placed in they are most likely the tallest structures within for a considerable distance making them prone to lightning strikes.
- **UV Exposure:** All wind turbines will experience some level of UV degradation from exposure to the sun, however, this will vary with the country the wind turbine is located.
- **Acid Rain:** This environment erodes the blade with two mechanisms, namely mechanically and chemically which can cause increased damage.
- **Sea water spray for offshore turbines:** The general trend for offshore wind turbines is that they have larger blades and hence the tips are traveling considerably faster, this coupled with sea water spray is not only more erosive regarding the wind turbine blades but also creates a corrosive atmosphere for the ferritic components.
- **Suspended dust particles:** Depending on the location of the wind turbine, particles in the air can be a prevalent problem and disturb the airflow over the

aerofoil. Some wind farms placed near quarries have reported faster eroding blades and increased fouling [11].

1.3 Purpose of Current Research

This research is required to enable the optimisation of the life of wind turbine blades in order to produce reliable energy. Wind energy has grown in importance due to geopolitical pressures impacting dramatically the cost and the acceptance of high carbon emissions of energy produced via oil and gas. This growth in power output has been facilitated by the dramatic increased diameter in industrial wind turbine blades particularly offshore wind turbine blades, combined with the severity of climate conditions the turbines are operating in is creating complex challenges with the materials and the structure. These challenges are inducing problems such as blade performance and the maintenance of the blades.

Due to the rapid advancements in wind turbine design the research to understand the modes and rate of degradation are currently lagging behind due to the time scales required to conduct appropriate tests and analyse the data. A particular gap is the evaluation of whether the application of stress has synergistic effect with the droplet to influence the erosion rate. A key aim of the research work is to understand the effect of stress and to develop an application that utilises the data generated in this research work and coupled with detailed geographical weather information estimate maintenance requirements on specific wind turbine blades.

To achieve this required the design and construction of a high speed test rig that would accommodate stress samples under different environmental conditions. It also required the development and assessment of test sample analysis, predictive model development and application programming.

Chapter 2

Wind Turbine Background

2.1 Wind Turbine History

Wind turbine design technology and design has progressed immensely from the very first wind turbine to produce electricity. This notable invention was by James Blyth from Anderson's College which is now The University of Strathclyde. He constructed a "small windmill for supplying electric light by means of storage cells" in the garden of his holiday cottage at Marykirk.



Figure 2.1: Wind turbine constructed by James Blyth at his Marykirk home circa 1887 [12]

Chapter 2. Wind Turbine Background

As can be observed in Figure 2.1 this was a tripod design, with a 33 foot windshaft, four arms of 13 feet with originally canvas sails, and a Burgin dynamo driven from the flywheel using a rope. This windmill which Blyth created is the first known example of the wind being harnessed to produce electricity [12]. Despite this early pioneering accomplishment of harnessing electricity from the wind in the late 1800s, the technology was not developed and proliferated fully taken on by industry. This was due to many factors including plentiful fossil fuel resources, no realisation of the damage these fuels do the environment and no economic gain from transitioning to green energy.

The next leap in development came about at a time when it was uneconomical. In 1941, a pioneer, Palmer Cosslett Putnam designed the very first multi-megawatt sized wind turbine, the construction is shown in Figure 2.2. It was manufactured by the S. Morgan Smith Company at Grandpa's Knob in Castleton, Vermont as shown in Figure 2.3. The Smith-Putnam wind turbine was a feat of engineering with steel blades spanning 53m in diameter producing 1250kW with full span pitch control and flapping blades to reduce loads.



Figure 2.2: Construction of the Smith-Putnam Wind Turbine [13]

Chapter 2. Wind Turbine Background

Unfortunately, the turbine had a catastrophic failure where one of the blade spars failed due to fatigue in 1945. This project, although scrapped after the loss of mechanical integrity was a great success and remained the largest wind turbine installation for approximately 40 years. It demonstrated the capability of wind turbine technology and the energy it can produce. The failure highlights the importance of understanding degradation mechanisms, material performance and design in constructing and operating such massive structures.



Figure 2.3: Smith-Putnam Wind Turbine on Grandpa's Knob, [13]

In the 1970s the renewable industry became much more prevalent and economical as war influenced political pressure adversely influenced oil and gas abundance and consequently cost. The Danish Government were a pioneer in the widespread adoption of wind energy, this was driven by desire to make Denmark less dependant on imported energy supply following the 1973 oil driven energy crisis [14]. The environmental factor of renewable energy also became a defining factor as many Western governments mandated a certain percentage of their country's power production to be generated renewably. Many wind turbine projects arose from this sudden influx in funding of renewable energy. In the USA there were a series of prototype turbines developed which

started with the 38m diameter 100kW Mod-0 in 1975 and climbed to a 97.5m diameter 2.5MW Mod-5B in 1987. Similar projects also were commissioned in the UK, Germany and Sweden and the initial design innovations were made during this period including the three rotor HAWT (Horizontal Axis Wind Turbine) we recognise today.

In the UK an alternative approach was undertaken to optimise the power output with a VAWT (vertical axis wind turbine) which was proposed by Dr Peter Musgrove and constructed a 500kW prototype. The benefits would be that the turbine did not need to be readjusted to access the wind as the turbine would operate with any wind direction, however, for large scale wind turbines this method is not as efficient as a HAWT as it cannot access the higher "cleaner air", it cannot vary the blades angle of attack and it is also not self starting and requires a motor.

2.2 Wind Turbine Design

In operation, rotor designs accumulate minor losses resulting from; tip losses, wake effects and drive train efficiency losses. Due to these fundamental operations the maximum theoretical efficiency of 59% (Betz limit) will not be achieved [15] [16]. Centuries of development has produced many different designs as shown in Figure 2.4 and Table 2.1.

The earliest designs of harnessing the power of the wind, before the generation of electricity, dates to the Persians who utilised wood and cloth as means of drag to spin a shaft (Figure 2.4a). Similar to the design of the Parisians is the cup type differential drag rotor (Figure 2.4b) used in modern times for anemometers to calculate airspeed, this design is utilised for this function due to its multi-directional operation and due to its simplicity hence ease of operation and calibration.

The quintessential American farm windmill (Figure 2.4c) was one of the very first designs centred around a high torque lift driven motor with a high degree of solidity.

Chapter 2. Wind Turbine Background

This design is still in operation today and its main purpose is normally pumping water. The Dutch windmill (Figure 2.4d) is very similar to the American farm windmill, they

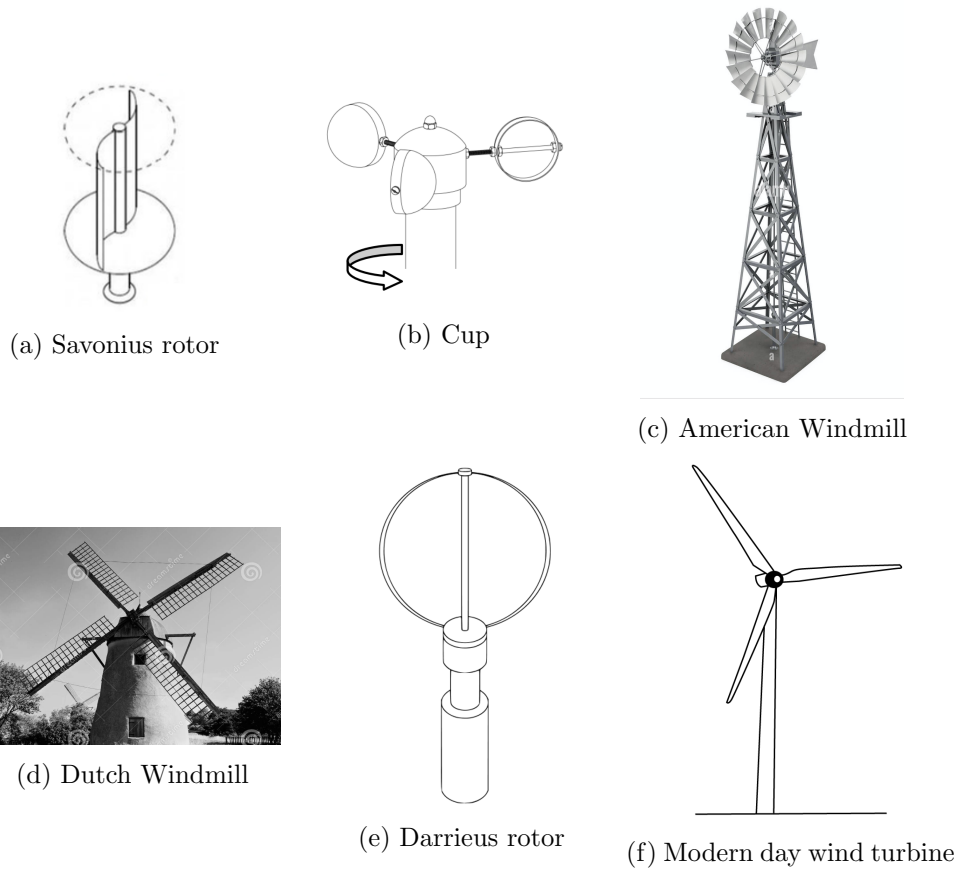


Figure 2.4: Modern and historical rotor designs, linking to Table2.1. Source [17]

both share a similar design and are both early examples of lift orientated functionality, its main purpose when built was for pumping water to aid with reclaiming land, however, nowadays they are predominantly tourist attractions. The first of the modern turbines on the table is the Darrieus VAWT (Figure 2.4e) which is an aerodynamic aerofoil blade design on a vertical axis with great potential [18], however, despite the extensive research and development it is unable to provide a peak efficiency high enough to be in competition with the modern HAWT [19]. Lastly on the table is the modern day HAWT (No.6) and due to its high peak efficiency and ease of control it has become the industry standard. Note: these are maximum values and very few modern wind turbines reach this peak efficiency number.

Ref No.	Design	Orientation	Use	Propulsion	Peak Efficiency
a)	Savonius rotor	VAWT	Historic Persian Windmill to modern day ventilation.	Drag	16%
b)	Cup	VAWT	Modern day cup anemometer.	Drag	8%
c)	American Farm Windmill	HAWT	18 th century to present day, farm use for pumping water, grinding wheat, generating electricity.	Lift	31%
d)	Dutch Windmill	HAWT	16 th century, used for grinding wheat.	Lift	27%
e)	Darrieus Rotor (egg beater)	VAWT	20 th century, electricity generation	Lift	40%
f)	Modern Wind Turbine	HAWT	20 th century, electricity generation	Lift	1 blade: 43% 2 blades: 47% 3 blades: 50%

Table 2.1: Modern and historical rotor designs, table adapted from [17]. Peak efficiency is dependant on design, values displayed are maximum values [20]

Along with the overall architecture of the wind turbine evolving, the blades themselves have also progressed through the years to become very efficient. The engineering obstacles which are presented when designing a large multi-megawatt wind turbine are immense. There are many factors which need to be considered including length and subsequent weight of components, the structural strength of the material, the materials resistance to fatigue, the materials ability to form complex curves and importantly for this research work resistance to environmental erosion.

2.3 Further development on wind turbine technology

Due to its dominance within the wind industry, the three rotor HAWT has been extensively researched and investigated in order to maximise its efficiency and tailor its operation to the desired application, whether that be onshore, offshore, local or industrial wind farm.

The three blade design shown in Figure 2.4f has been adopted as the most efficient design to coincide with environmental, commercial, and economic constraints and hence is the most prominent design in the wind industry. Commercially available modern wind turbines are at the cutting edge of technology and are packed with complex control systems, safety systems and remote monitoring devices and a typical modern day wind turbine specifications is shown in Table 2.2.

Rotor		
Diameter	90 m	
Swept Area	6362 m^2	
Rotational Speed	9 - 19 rpm	
Direction of rotation	Clockwise from the front	
Weight including hub	36T	
Top Head Weight	106T	
Blades		
Quantity	3	
Length	44 m	
Aerofoils	Delft University and FFA - W3	
Material	Pre impregnated epoxy glass fibre and carbon fibre	
Mass	5800kg	
Tower		
Tubular modular design	Height	Weight
3 Section	67 m	153 T
4 Section	78 m	203 T
5 Section	100 m	255 T
Gearbox		
Type	1 Planetary stage, 2 helical stages	
Ratio	1:100	
Cooling	Oil pump with oil cooler	
Oil heater	2.2 kW	

Table 2.2: A typical modern day 2MW wind turbine adapted from [17]

2.4 Aerodynamics

The aerodynamic lift each rotor provides is fundamental to the operation of the wind turbine and its efficiency. The lift force produced by the blades is responsible for the output power of the turbine, therefore, it is essential to maximise the aerodynamic lift to gain optimal efficiency. The opposing force to the aerodynamic lift is the drag force which also induces friction into the system which is undesirable. To gain more efficiency it is advantageous to design a rotor blade with a high lift to drag ratio (equation (2.1)).

$$\text{Lift to drag ratio} = \left(\frac{\text{Coefficient of lift}}{\text{Coefficient of drag}} \right) = \left(\frac{C_l}{C_d} \right) \quad (2.1)$$

A rotor blade is normally chosen if it has a lift to drag ratio greater than 30 [21]. The coefficients are more easily calculated experimentally with tables correlating lift and drag at various angles of attack and Reynolds number [22].

2.4.1 Control of Blades

The lift generated by the rotor blades is determined by the incoming air stream and the angle of attack of the blades. Each individual wind turbine will have an optimum rotational speed to produce the maximum output power, to be able to maintain this optimum rotational speed the angle of attack from the rotors must be adjusted. This is achieved by altering the angle of pitch therefore altering the angle of attack in real time with the incoming wind speed to maintain the same the same lift force and hence rotational speed. Every large-scale modern wind turbine with this feature has a control centre within the mast of the turbine and is measuring the wind speed and making second-by-second adjustments to the angle of twist to optimise the efficiency of the turbine.

Having this control over the blades also is beneficial when protecting the internals of the turbine. When the weather is too harsh, and the winds are too extreme to the point where the rotors would spin the turbine to dangerous rotational velocities, the blades are feathered. This prevents any lift force to be generated from the blades and

keeps the turbine at a standstill to prevent any damage to the turbine.

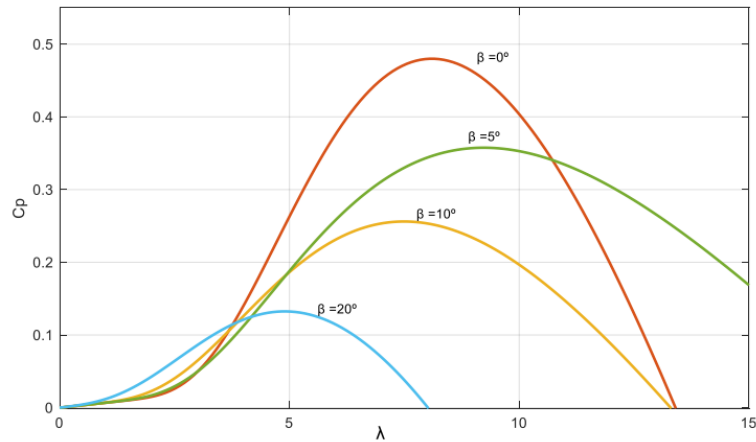


Figure 2.5: Variation of the $\lambda-C_p$ curve depending on the pitch angle of the blades (β)

The aerodynamic characteristic of a wind turbine can be altered by adjusting the pitch angle (β) of the blades. This technique is known as pitch control and it is usually applied in large wind turbines. Figure 2.5 illustrates a set of $\lambda-C_p$ curves displaying various pitch angles where each angle has a different maximum co-efficient of power at different λ value.

2.5 Loads on Wind Turbine Blades

2.5.1 Aerodynamic Load

Aerodynamic loading on the blades is a direct result from the lift and drag components in operation. The magnitude of aerodynamic loading is dependent on the wind velocity, blade velocity, angle of attack of the blades (α) (dependant on the twist and pitch), yaw of the blades and the surface finish on the blades.

The aerodynamic lift and drag produced is visualised in Figure 2.6. These loads are influenced by the thrust the blades produce (C_t) and the thrust varies with λ as shown in Figure 2.7.

Chapter 2. Wind Turbine Background

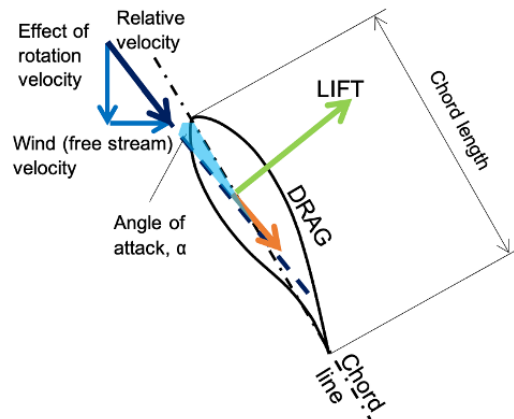


Figure 2.6: Aerodynamic forces acting on a turbine blade. Source [17]

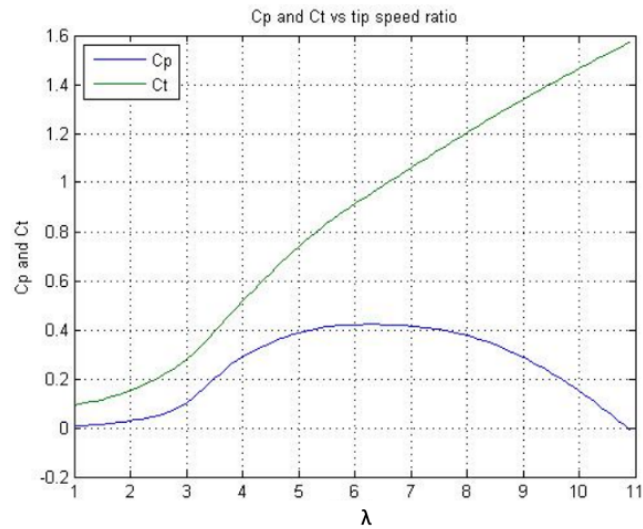


Figure 2.7: C_p and C_t plot against λ . [23]

The wind speed is a critical factor in the amount of electricity generated by a turbine. Below the rated speed the power output will increase cubically with wind speed as shown in Figure 2.8 Note the cut out speed in this graph is the shut down point for the turbine to avoid damage.

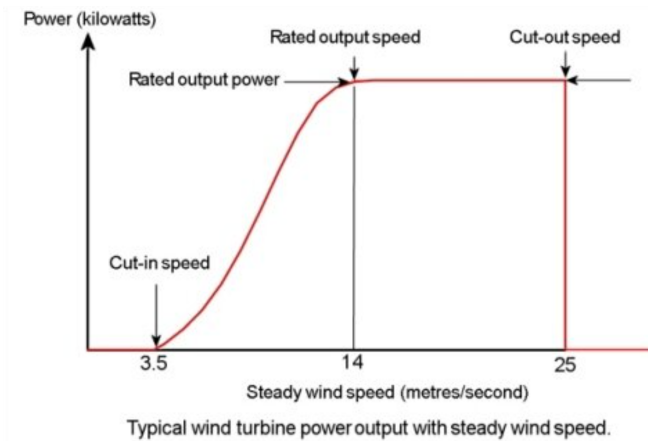


Figure 2.8: Typical wind turbine power with wind velocity. [24]

2.5.2 Gravitational and Centrifugal Loads

Gravitational and centrifugal forces on wind turbine blades are mass dependant and the general rule is that the forces cubically increase with mass [25]. With smaller independent wind turbines this is a minimal issue, however, with the increasing propensity of very large multi mega-watt wind turbines more than 100m, this involves complex engineering challenges and encountering material limitations to withstand the significant loads primarily from the weight of the blades.

The gravitational force is simply defined as the mass multiplied by the gravitational constant and this force always acts towards the ground. The centrifugal force is an outcome of the blades rotational velocity squared and its mass. This force always acts outwards from the centre from the turbine through its rotation. Centrifugal and gravitational loads are superimposed to give a positively displaced alternating condition with a wavelength equal to one blade revolution.

2.5.3 Flapwise Bending

Flapwise bending is the moment force produced by the aerodynamic load on the blades where they attach to the hub. The load case can be modelled as a cantilever beam with the root of the blade at the centre of the turbine being the fixed support and the rest of the blade is the cantilever in bending with a uniformly distributed load from the aerodynamic lift produced by the aerofoil shape of the blade as shown in Figure 2.9. From this diagram it shows how bending occurs about the chord axis which in turn creates tensile stresses on the leading edge and compressive stresses on the trailing edge. In order to quantify these stresses classical beam bending can be applied (Equation 8.3 via calculating the second moment of area of the load bearing material.

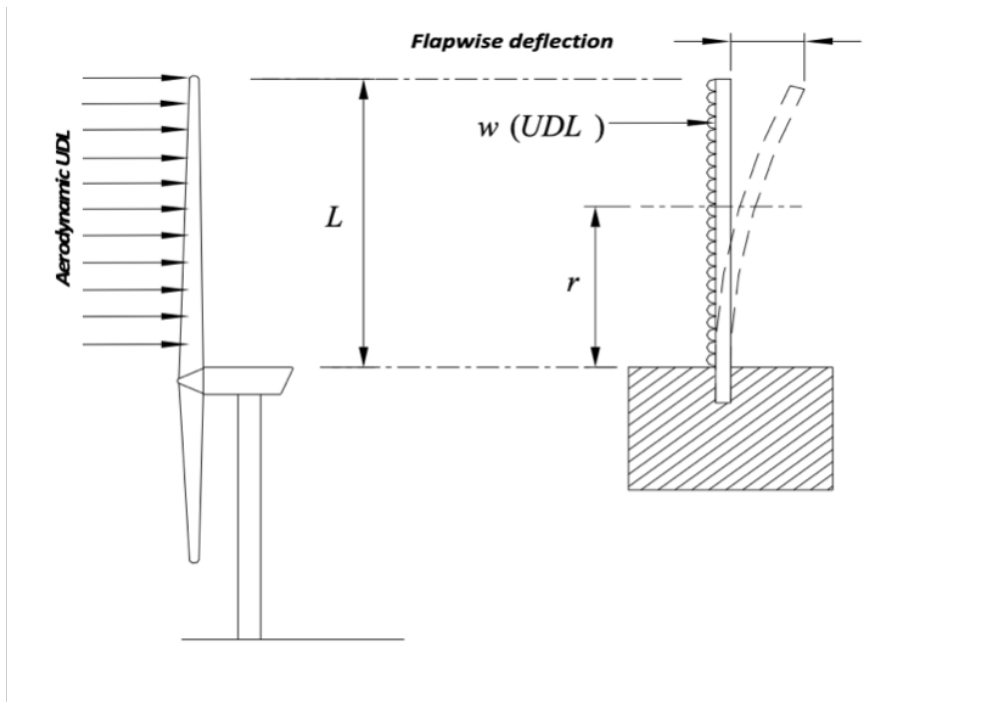


Figure 2.9: Wind turbine blade displayed as a cantilever beam under a uniformly distributed load from an aerodynamic lift force [17]

$$I_{xx} = \int \int (y - y_1)^2 dx dy \quad (2.2)$$

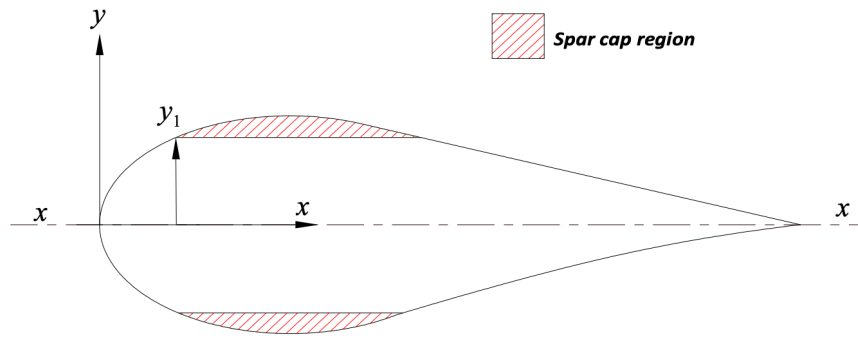


Figure 2.10: Flapwise bending along the axis xx [17]

$$M = -\frac{1}{2}w(L - r)^2 \quad (2.3)$$

$$\frac{\sigma}{y} = \frac{M}{I} = \frac{E}{R} \quad (2.4)$$

Where:

- | | |
|------------------------------|------------------------------------|
| L = Total length of blade | y = Distance from the neutral axis |
| M = Bending moment | I = Second moment of area |
| w = UDL | E = Modulus of elasticity |
| r = Radial distance from hub | R = radius of curvature |
| σ = Stress | |

Once the second moment of area has been determined localised material stresses and deflections at various points along the turbine blade can then be calculated using the fundamental beam bending Equation 2.4.

When calculating the second moment of area using equation 5 and increasing the length of the turbine blade which translates to increasing the distance from the central axis of bending results in a cubic increase of stress. Another result from the beam bending equation 2.4 that can be observed is that when load bearing material is moved away from the central plane of bending x the material stress is decreased by a factor of

two. Therefore the most ideal location to have load bearing material is on the spar cap region to reduce stress as shown in Figure 2.10. This fundamental design has dictated large multi-megawatt wind turbines to have thicker blades rather than slender, more aerodynamic blades. The balance between slender aerofoils for greater aerodynamic efficiency and thicker blades for larger more structurally sound geometries is a balance between efficiency and reliability.

2.5.4 Edgewise Bending

The result of the mass of the blade and the effects of gravity lead to the turbine blade experiencing edgewise bending. As mentioned previously an increase in the turbine blades length results in a cubic increase of the mass of the blade, therefore the internal stresses increase with the length of the blade [26].

Similarly to Flapwise bending the blade can be thought of as a cantilever beam but with a distributed load concentrated towards the support and this configuration is only when it is completely horizontal during its spin as shown in Figure 2.11. The edgewise bending condition is considered when the plane of central bending is normal to the chord line. As mentioned previously, in the case of flapwise bending it is common to strengthen the blade centrally in the spar cap region, at the extremities of the aerofoil profile, which results in moving load bearing material away from the flapwise plane of bending. This, however, is not ideal for edgewise bending due to the centre of the spar cap being exceedingly close to the central plane of bending (yy). This derives the balancing act of giving structural material for both edgewise bending and flapwise bending resistance [27].

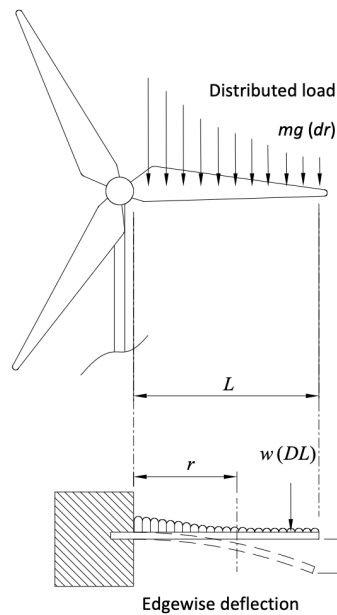


Figure 2.11: Wind turbine blade modelled as a cantilever beam under gravitational load [17]

2.5.5 Fatigue Loads

Fatigue loading occurs on a turbine blade when there is a repetitive, non-continuous load of the material applied over time. The balance therefore is to design an efficient turbine which has sufficient design life. To increase the design life the slender, light aerofoil design would need to be reinforced. Such a design would result in an increase in the thickness of the blade decreasing its output power and the cost would increase. Therefore blades are designed with a finite number of fatigue loads to optimise cost and maximise efficiency.

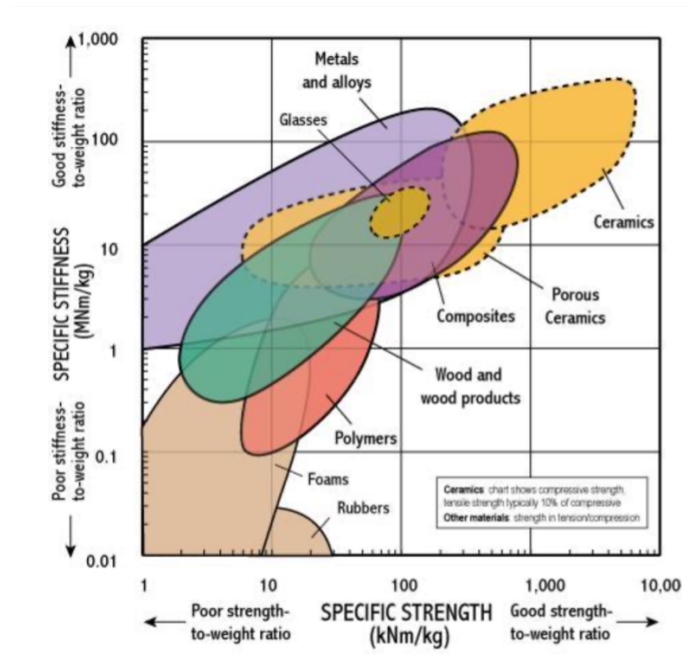
Similarly to many of the loading issues on turbine blades, fatigue loading is a result of gravitation forces, in this case however it is cyclic gravitational loads, this can be quantified as the number of full rotations a turbine makes in its lifetime. The manufactures quoted lifetime is normally 20 years and in addition to external stochastic forces, this total to approximately 10^9 cyclic loading in its entirety [28]. The design of turbine blades must then be designed to exceed this number of cycles to prevent a major failure.

2.6 Blade Materials

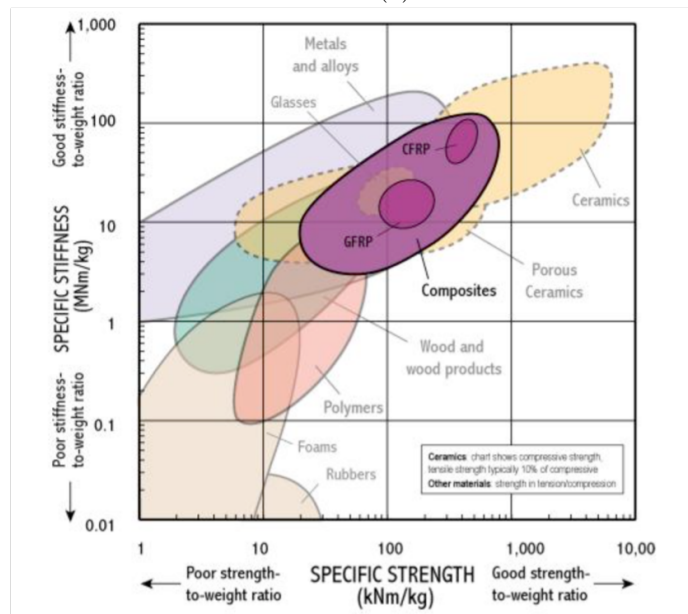
2.6.1 Material Selection

Wind turbine blade manufacturers recognise the engineering challenges with the requirements of a turbine blade and acknowledge the need for blades to require specific material properties such as high strength and stiffness while allowing some flexibility and remaining lightweight. From the start of large blade manufacturing in the 1980's some blade materials and technologies have been discontinued. Steel rotor blades were replaced due to their weight, aluminium was also found to be impractical due to concerns regarding fatigue and wood rotor blades had problems with moisture absorption. The problems with wood blades was resolved by a wood-epoxy system developed by the Geougeon brothers in the US and then further developed in the UK, however, this technology soon became obsolete with the increasing use and popularity of composite materials containing fibers made from glass or carbon. The use of glass and carbon fibres in a composite material quickly evolved to a more sophisticated material that possessed reliable high strength to weight performance necessary for the application of a wind turbine blade rotor. The specific strength and stiffness for a selection of materials is shown in Figure 2.12a and Glass Fibre Reinforced Polymer (GFRP) and Carbon Fibre Reinforced Polymer (CFRP) are highlighted in the graph in Figure 2.12b.

It is evident from Figures 2.12a and 2.12b that composite materials offer material properties which are very desirable for the application of wind turbine blades. The only material group which is deemed superior in the graph is ceramics, however, for large structures a ceramic material would be unsuitable as they have inadequate ductility. As a result, the industry standard material for turbine blades has become composite based and the popular choice is GFRP rather than CFRP as it is much more economically viable.



(a)



(b)

Figure 2.12: (a) Specific stiffness and strength of various material groups (b) Specific stiffness and strength of various material groups, highlighting CFRP and GFRP [10]

2.6.2 Fibre Reinforced Composites

The theory behind a composite material is to combine different constituent materials that enhance the positive properties and minimise the negative in order to create a new material with overall superior engineering qualities. In the case of GFRP the two materials that have been combined is glass and epoxy resin. The glass is in the form of fibres, normally in a weave configuration, has extremely stiff and strong material properties, however, it is very brittle and thus alone would not be suitable for wind turbine blade applications. Epoxy resin has opposing material qualities where it is very weak under tensile load, however, is extremely ductile and resistant to cracking. When glass fibres are combined with epoxy resin to create GFRP the mechanical properties are inherently changed in relation to the individual components, resulting in a new material which offers both strong tensile strength as well as resistance to cracking and flexibility. This is demonstrated in Figure 2.13.

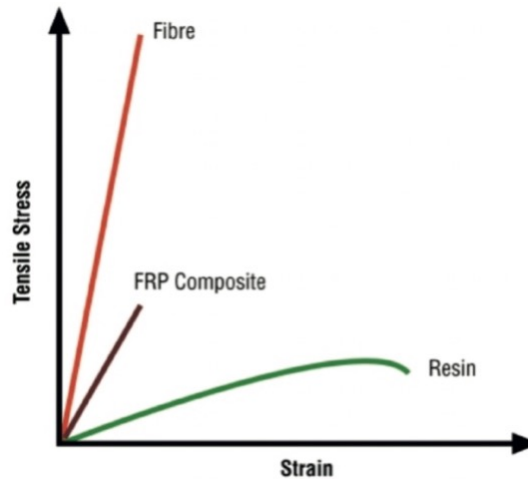


Figure 2.13: Stress strain curve of composite material and its components [10]

The generalised rule of composite materials can be a useful tool into predicting the mechanical properties of the product of two materials based on their given properties, fibre orientation and ratio of mixture. This is shown in equation (2.5).

$$E_{\text{comp}} = \eta_L \eta_o E_f V_f + E_m V_m \quad (2.5)$$

Chapter 2. Wind Turbine Background

The subscripts f and m are fibre and matrix respectfully, E is the material property of interest, η_L and η_o are constants in order to include the impact of fibre length and fibre orientation respectfully and V is the volume fraction.

The combination of materials to create a new composite is currently an active development field within material science and is leading the way in many engineering challenges including Formula 1 car design. The careful consideration of constituents in each composite and the ratio can be used to tailor make a bespoke material for a specific application and in this case allows wind turbine blades to be manufactured to enormous lengths while withstanding the load of the wind and the weight of the blade from a fixed point on the root. Evolution of materials will continue and allow for further advancements and hence greater efficiencies of wind turbines.

2.6.3 Composite Material Designs

As well as the variety of different materials to be combined for optimising mechanical properties, the way in which the materials are composed can also have an effect. The greatest difference can be found with the layup of the reinforcement fibres, whether that be in a unidirectional layup, 90-degree layup, 45-degree layup or a variety of all and more. The matrix component of the composite, which is epoxy in the case of GFRP, can have a determining factor depending on how it is applied, whether that be already pre-impregnated into the fibres or painted on during layup. Different combinations of these factors can change the product of the composite.

2.6.4 Reinforcement Fibre Materials

The fibres within the composite are responsible for the strength and stiffness of the material and when selecting the fibres careful consideration is required to choose the material which will best suit the application and be compatible in a composite material. The main factors to consider when selecting fibres are; the mechanical properties of the

fibre, the nature of the interface between the fibre and the matrix, the fibre volume fraction (the ratio of fibre to matrix within the composite) the orientation of the fibres and the cost [29].

Material Type	Tensile Strength (MPa)	Tensile Modulus (GPa)	Typical density (g/cc)	Specific Modulus
Carbon HS	3500	160 - 270	1.8	90 - 150
Carbon IM	5300	270 - 325	1.8	150 - 180
Carbon HM	3500	325 - 440	1.8	180 - 240
Carbon UHM	2000	440+	2.0	200+
Armid LM	3600	60	1.45	40
Armid HM	3100	120	1.45	80
Armid UHM	3400	180	1.47	120
Glass - E glass	2400	69	2.5	27
Glass - S2 Glass	3450	86	2.5	34
Glass - Quartz	3700	69	2.2	31
Aluminum Alloy(7020)	400	1069	2.7	26
Titanium	950	110	4.5	24
Mild Steel (55 Grade)	450	205	7.8	26
Stainless Steel (A5 - 80)	800	196	7.8	25
HS Steel (17/4 H900)	1241	197	7.8	25

Table 2.3: Material properties for fibres used in composites [29]

Table 2.3 displays common fibre materials within composites and their mechanical properties as well as some other engineering materials for comparison. From this table carbon, armid and glass display very high tensile strengths compared to conventional metals and alloys. Figure 2.14 displays the stress strain lines for both tensile and compressive situations of carbon, armid and glass fibres in a unidirectional pre-impregnated laminate. The graph shows these materials stressed until failure. The gradient of each line is representative of the stiffness (modulus) of the material, the steeper the line the greater the stiffness [29].

From these graphs it is apparent that the high strength in both tensile and compression situations are qualities which reside in making a strong and stiff composite material. It is interesting from these two graphs to compare how some materials, such

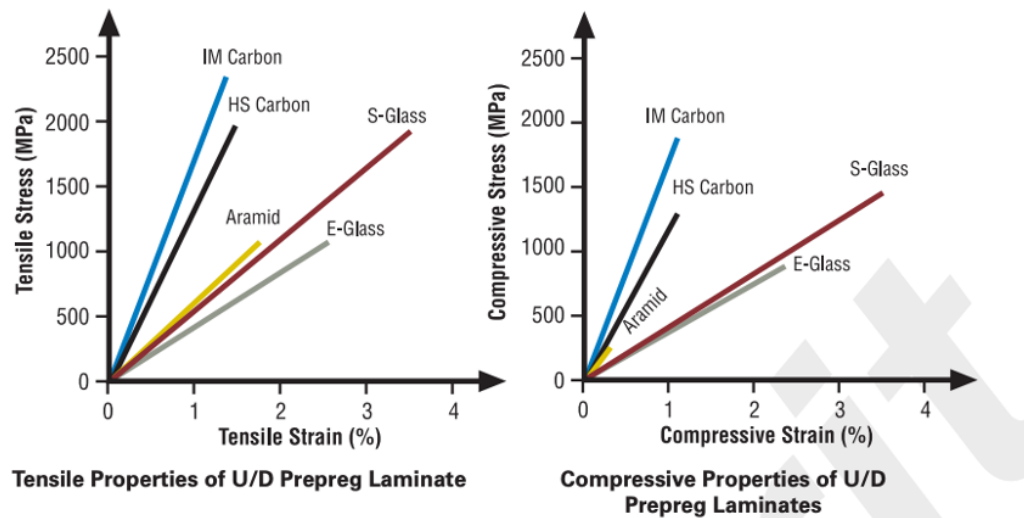


Figure 2.14: Tensile and Compressive stress strain line graphs for various fibres used within composites [29]

as aramid react differently when loaded in compression and tension. The stiffness characteristics are not however the single determining factor when deciding the material selection for a wind turbine blade as it requires some flexibility. E-glass, for example, is slightly weaker in strength and stiffness but provides increased laminate impact performance due to its lower stiffness and hence more elastic. There is a compromise between selecting a reinforcement material which is the strongest and one which obtains some ductile properties when in a laminate.

When selecting the composite and its combined constituents for a desired application, it is important to design the material for the specific loads. Although the loads for a wind turbine blade can be generalised there will be specific loads and moments on various types of blade, depending on the manufacturer and therefore different manufacturers will select materials which meet their individual requirements for their own unique design. Siemens and Enercon both utilise their own combinations of composites in their large multi-megawatt turbine blades. Vestas have developed an economically viable method of creating a wood/carbon weave as the reinforcement fibres in an epoxy

to create a semi natural composite and Gamsea have woven together both carbon fibres and glass fibres in an epoxy composite to further extend the material properties to comply with their requirements in their massive offshore blades. Not only will material choice vary between manufacturers but also between different model designs of turbine blade.

2.6.5 Matrix Materials

When referring to composites within the wind turbine blade application for either glass or carbon reinforcement fibres, the most common type of bonding employs a thermosetting polymer matrix mix usually either an epoxy or polyester resin. All polymers inherit an important property which is that they are composed of simple, single units of atoms which are repeated to produce long chain molecules. There are two groups of polymers, thermosetting and thermoplastic, the difference between the two is often defined as their properties when being reheated, thermoplastics when heated will soften and can be reshaped, thermosetting do not re-soften. Thermoplastics include nylon, polypropylene, and ABS and these are normally bonded with short, chopped fibres such as glass. Thermosetting materials include polyester and epoxy. For wind turbine blade applications thermosetting matrix materials are utilised to avoid resoftening and epoxy variants are the most prevalent.

Chapter 3

Rain Erosion

3.1 History of Rain Erosion and Industrial Applications

Water droplet erosion (WDE), formally known as liquid impingement erosion (LIE), is a mode of wear which is produced by water droplets impacting a material at a high enough velocity to cause damage to the material [30]. The main difference between WDE and jet erosion is that WDE has discrete water droplets, meaning that the stagnation pressure of liquid jet is considerably lower as it does not consider individual droplets. Cavitation is different to WDE as it is usually encountered amongst a gaseous or vaporous phase which contains discrete water droplets whereas cavitation is normally experienced in an unbroken liquid phase or fully submerged which carries discrete gaseous bubbles or cavities [31].

WDE has been an ongoing concern for materials in machinery travelling at very high velocities, in particular blades within machinery. The problem was first recognised within steam engines in the early 1920s [32] [33] where WDE was observed on the blades of the steam engines after the engine was run on a low-pressure cycle. To increase the efficiency of a steam engine under low pressure it is advantageous to increase the length of the blades to overall increase the output power [34]. The increase in blade length hence increases the tip speed of the blade and within some steam engines this could be up to $900\text{m}\cdot\text{s}^{-1}$, this extreme speed coupled with a wet steam environment of

operation resulted in erosion of the blades [35]. This is demonstrated in Figure 3.1.

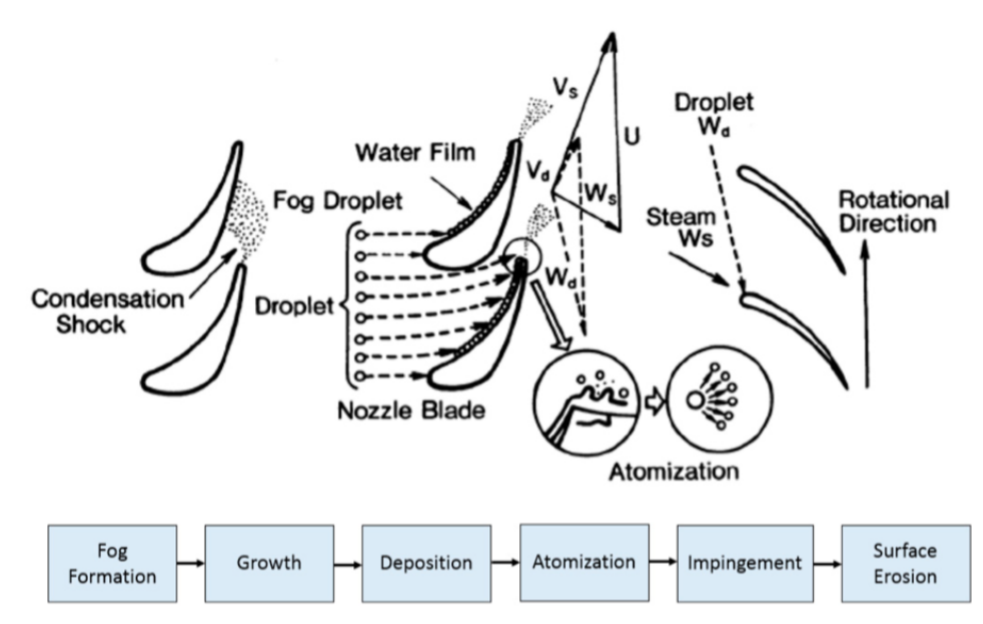


Figure 3.1: Blades in a low pressure stage in a steam turbine [36]

WDE is also experienced on compressor blades of gas turbines as when the air intake of the compressor contacts the compressor blades the air is cooled which increases the air density to allow for maximum of intake air mass [37]. This method proved to be very effective at increasing the efficiency of the compressor, however, it creates water droplets through condensation and hence severe erosion of the compressor blades [38]. This causes imbalance within the finely balanced system and the small irregularity creates vibrations and hence severe fatigue damage [39]. A compressor of a gas turbine is illustrated in Figure 3.2.

Another common occurrence of WDE is on helicopter blades as the blades are long, travelling at close to supersonic speeds and in wet conditions it can cause damage to the leading edge of the rotors [40]. Even compressors of turbochargers fitted to everyday cars are starting to experience WDE on the compressor wheel [41].

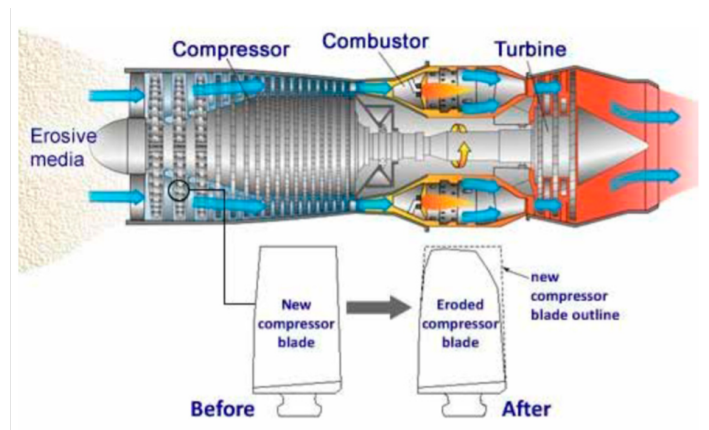


Figure 3.2: Compressor of a gas turbine [39]

Although WDE is primarily a problem with rotating blades such as steam engines, compressors in a gas turbine, helicopter blades and compressor wheels of a turbo charger there are some blades which travel linearly which experience WDE, such as rockets and aeroplanes. The erosion caused by rain droplet impacts on the surface of aircrafts such as the leading edge of an aerofoil has been an ongoing issue in aviation [42–44]. Aircrafts are composed of multiple materials with various properties and the impact from water droplets occurs at different intensities around the aircraft. This results in the WDE having different effects on the various components of the aircraft. The erosion appears normally at the leading edge of the aerofoils in the form of pitting, paint stripping and failure of rivets [43]. Figure 3.3 shows a diagram of a commercial plane and all the locations WDE is most likely to occur [45].

WDE is also observed within a nuclear energy powerplant. The steel pipelines which are carrying hot steam are vulnerable to WDE and can cause wall thinning [46–48]. This occurs when the suspended water droplets in the hot steam which is flowing through the pipeline interferes with the wall of the pipe, normally when the pipe is changing direction. These interferences over time erode the pipe and create vulnerable areas for failure. This was the ultimate failure of the Onagawa power plant in 2007 [48] and the cause of the fire and explosion at the ConocoPhillips Humber refinery in 2001 [49] (Figure 3.4). The interaction is illustrated in Figure 3.5.

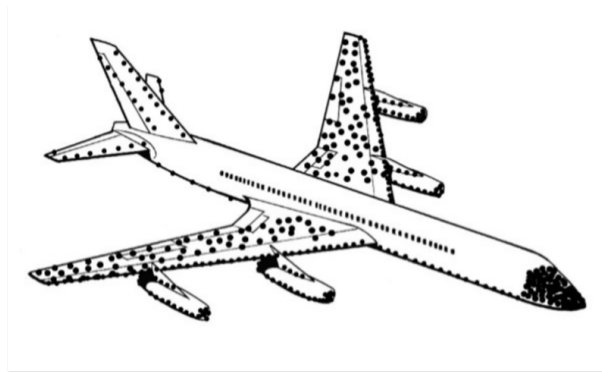


Figure 3.3: A commercial aircraft showing the density of wear from WDE by black dots [45]

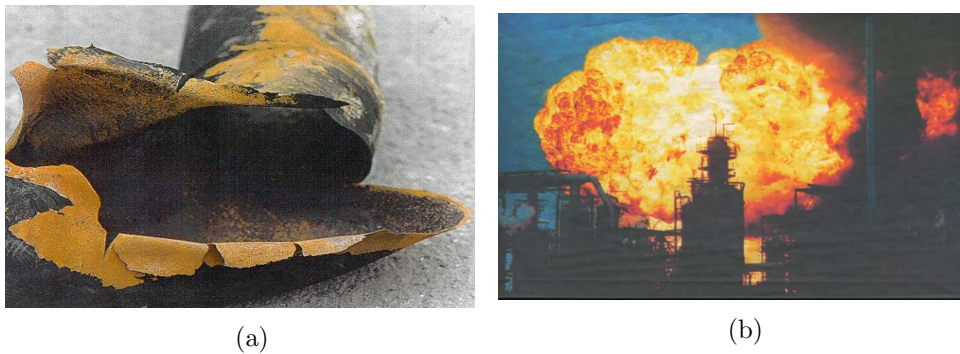


Figure 3.4: Fire and explosion at the ConocoPhillips Humber refinery in 2001 showing (a) The failed elbow causing the explosion (b) Fire and secondary fireball [49]

Table 3.1 is a summary which includes a variety of instances which WDE occurs and characterises the conditions within each piece of equipment for the most influential variables which cause the most damage including impact velocity and droplet size. The impact velocity and droplet size are given as rough estimates as the actual size and speed of the droplet is difficult to determine and within each application will have a range.

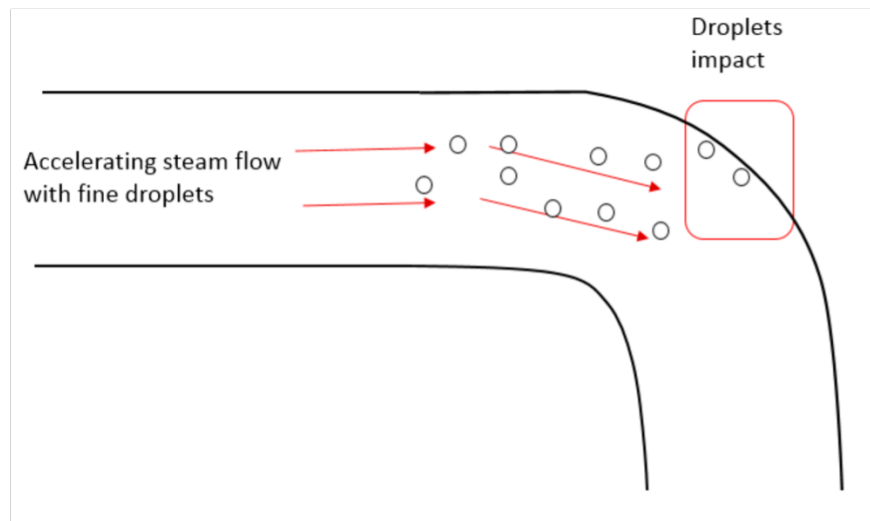


Figure 3.5: Steam pipes of a nuclear power plant experiencing WDE [50]

Application	Parts Affected	Impact Speed	Droplet Diameter
Steam Turbine	Blades of the low-pressure stage	$400 - 900m.s^{-1}$	$50 - 400\mu m$
Gas Turbine	Compressor blades	$100 - 600m.s^{-1}$	$200 - 600\mu m$
Wind turbine	The outer power-producing part	$70 - 150m.s^{-1}$	$0.5 - 5mm$
Nuclear Power Plant	Cooling pipes	$\approx 200m.s^{-1}$	$60 - 80\mu m$
Aero Engine	Fan blade	$200 - 400m.s^{-1}$	$1 - 5mm$
Aircrafts	Rain erosion of different parts	Civil airplanes $\approx 250m.s^{-1}$ Fighter Jets \approx up to 5 Mach	$1 - 5mm$

Table 3.1: Summary of the erosion conditions in some applications [50]

3.2 Erosive Parameters for Wind Turbine Blades

3.2.1 Impact Velocity

The magnitude of the impact velocity between the turbine blade and a rain droplet is determined on the relative speed between how fast the rain droplet is falling and the tangential velocity of the turbine blade. The terminal velocity of the tip of the blade is a simple calculation and depends on the rotational speed of the rotors and the radii to the tip. The velocity of the falling droplet is dictated by the mass of the droplet that is falling which is dependent on the size and density, the velocity is also dependant on the climate conditions including temperature, humidity and wind.

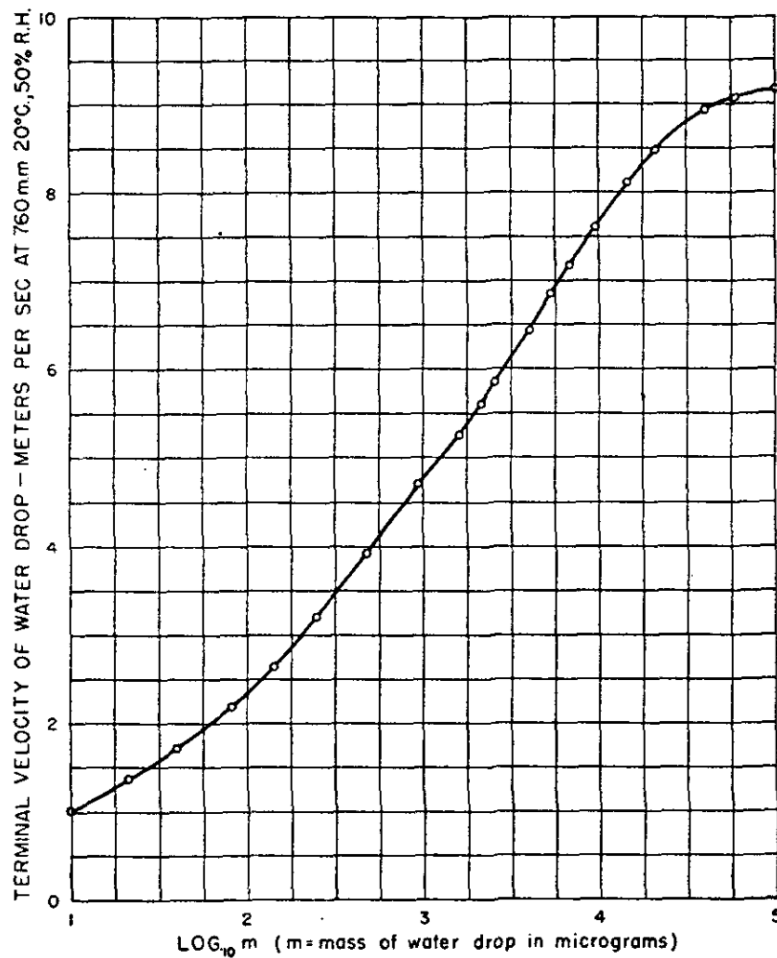


Figure 3.6: Terminal velocity of water droplets of various diameters [51]

A study was conducted by Gunn and Kinzer [51] where they determined the terminal velocity of falling droplets of various diameters in stagnant air using different sized hypodermic needles to produce different sizes and the results are shown in Figure 3.6. In another investigation by Wood [31] to determine the terminal velocity of a falling water droplet the following equation was proposed:

$$v_t \cong \sqrt{\frac{\rho}{\rho_a} g D_0} \quad (3.1)$$

From equation (3.1) Where v_t is the terminal velocity, D_o is the droplet diameter, g is the gravitational constant, ρ is the density of the droplet and ρ_a is the density of air and the terminal velocity can be graphed as seen in Figure 3.6.

3.2.2 Droplet Size

The diameter of a rain droplet is dependent primarily on the climate conditions it is created in. The common rain droplet diameter is recorded from 0.5mm to 5mm [52]. If the droplet becomes any larger than 5mm in diameter the droplet reaches an unsteady state and it is energetically favourable to split into smaller droplets.

In most cases the falling rain droplet has a non-homogeneous size, and it is therefore difficult to characterise a single droplet. Instead, a continuous distribution is normally used to characterise the number of droplets in a known volume of air. Kubilay et al [53] produced a plot containing the probability of raindrop size against rain droplet diameter as seen in Figure 3.7.

From this probability plot in Figure 3.7 it is evident that the larger diameter droplets (4mm and above) are only present in extreme weather conditions where the rain rate is exceedingly high. The most common droplet size is between 0.5-3mm. Within the experimental environment a droplet of diameter 2mm is often chosen as a standardised diameter for erosion tests [54] Another reason for selecting a droplet diameter of 2mm

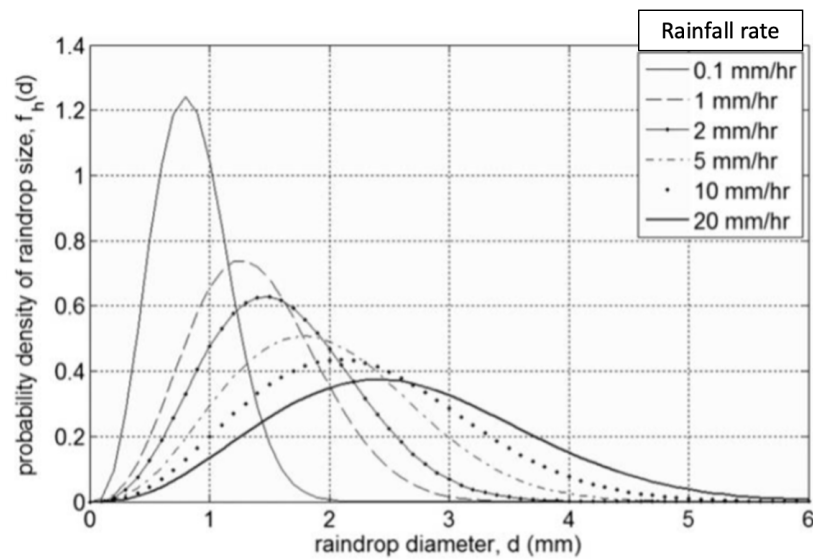


Figure 3.7: The probabilistic density of raindrop size due to the rain fall rate [53]

is that it is thought to best correlate with conditions that cause the most damage to a turbine blade as a 2mm diameter droplet would correspond to a rain intensity of approximately 20-25mm/h which is classified as heavy rain [55].

3.2.3 Droplet Shape

In most cases the shape of a droplet is considered perfectly spherical when its diameter is less than 2mm. This encompasses most of rain that falls and almost all experimental cases of induced rain erosion. When a droplet is larger in diameter, (approximately 2-5mm in size) then the droplet is misshapen due to the resultant air resistance and becomes flat bottomed, this is observed in Figure 3.8 where the droplet starts to become very flat in frames 4 to 7. If the droplet is any larger than 5mm in diameter then the structure becomes unstable and tends to create a parachute shape from a larger unbalance of air resistant forces which can be seen in frame 9 and 10 within Figure 3.8 [32] which ultimately leads to the droplets surface tension not being strong enough to hold the water together and it breaks into smaller droplets.

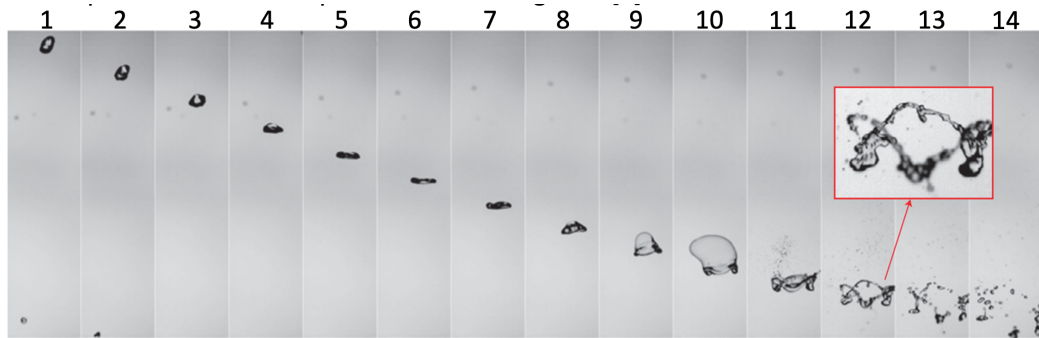


Figure 3.8: The fragmentation of an oversized droplet [32]

In real world conditions it is very difficult to reliably determine the intensity and frequency of rain droplets impacting onto wind turbine blades in operation. B. Amirzadeh et al [56] conducted a study into the developing a stochastic rain texture model to generate three-dimensional fields of raindrops consistent with the rainfall history at the turbine location. This was conducted by integrating the raindrops size and spatial distribution with its integral properties such as the relationship between the average volume fraction of raindrops and rain intensity. The proposed model established a relationship between the rain intensity and the number of raindrops per unit volume of air and allowed reproduction of three-dimensional fields of raindrops through a compound stochastic point process. These studies are critical to the laboratory investigations as they are the starting point to the initial parameters for experimental findings. They create an environment which will more realistically simulate the conditions which are found in the field. It also helps to verify results within simulations and practical experimental findings. Input wind speed to a turbine can have the effect of breaking and combining rain droplets creating a wide range of droplet diameters impacting the leading edge, however for this study the droplet diameter was kept constant.

3.3 Droplet Impact Physics

3.3.1 Impact Event

When a droplet impacts a solid surface pressure waves are generated both within the droplet and transferred into the solid surface [57]. These pressure waves or pulses can be responsible for erosive wear within the surface. It initiates by creating a shocked envelope, which is the disturbed region of contact between the droplet and the surface. This occurs only for a very brief moment, normally only lasting a few microseconds. The moment of impact is often referred to as the stagnation moment and within this instance two important phenomena occur which include the water hammer pressure and the propagation of stress waves.

3.3.2 Water-Hammer Pressure

From a study by Cook [58] in the 1920s, the impact of droplets on steam turbine blades was becoming a major concern and an investigation into the mechanical behaviour of the droplet impact was conducted. It was first believed that the damage on the steam turbine blades was from a corrosive nature, however, Cook [58] succeeded in applying methods similar to those adopted previously [58] to the calculations of the impact pressures and was able to demonstrate that pressure pulses account for the observed erosion. Cook [58] named this pressure “water hammer pressure” and proposed the following equation to describe such pressure:

$$P = \rho_o C_o V \quad (3.2)$$

Where ρ_o is the liquid density, C_o is the speed of sound and V is the relative impact velocity of the droplet and the solid surface. At the moment of impact, the water droplet compresses and creates a large pressure named the ‘water-hammer pressure’ and in that moment the outer boundary of the fluid propagates supersonically with the sonic speed in the fluid. This equation and discovery appropriately generated a

lot of attention as it represented the primary loading condition of the droplet impact. Where the conditions are a compressible liquid meets a rigid body and a shock of velocity C_o propagates through the liquid. It is more likely, however, that the solid surface which is being impacted by a water droplet is not a rigid body and experiences compression thus a variation of this equation must be applied. Dear and Field [59], continued Cooks [58] studies and they attempted to compensate for an impact of a non-rigid body and constructed the following equation:

$$P = \frac{\rho_o C_o C_s V}{\rho_o C_o + \rho_s C_s} \quad (3.3)$$

Where the subscripts o and s are the liquid and solid respectfully. Bowden and field also showed that the compressible behaviour was also exhibited in a larger droplet, which is not spherical and its geometry is curved within its impact area. This is due to the contact initially expanding supersonically in relation to the shock wave within the liquid. This high-pressure stage lasts until the release of the compressed liquid as a jetting motion, which will be discussed later in section 3.3.4. The duration of this high pressure moment is given by the following equation, where R is the radius of the contact area:

$$r = \frac{3RV}{2C^2} \quad (3.4)$$

The pressures then decrease to those typically found in incompressible flow with a stagnation pressure given by the following equation:

$$P = \frac{\rho V^2}{2} \quad (3.5)$$

There have been many studies which have investigated the impact pressure of a droplet onto a solid surface [60–63] and the effect this pressure on the spatial and temporal distribution in the impact zone as well as the maximum pressure the droplet applies to the solid surface. It is believed that the moment of maximum pressure is when the most damage occurs on the solid surface, this peak pressure occurs at the critical contact radius r_c . Hyemann's approximation [61] of this pressure is as follows:

$$P = 3\rho_o C_o V \quad (3.6)$$

Heymann's approximation [61] was later confirmed by Rosenblatt et al [63]. Once the impact pressure is obtained, it is usually used as a boundary loading condition acting on the solid target.

These stages are displayed in Dear and Fields [59] investigation as they use high speed photography coupled with the schlieren effect to visualise the shock propagation's within the droplet as it impacts the solid surface. This is displayed in Figure 3.9.

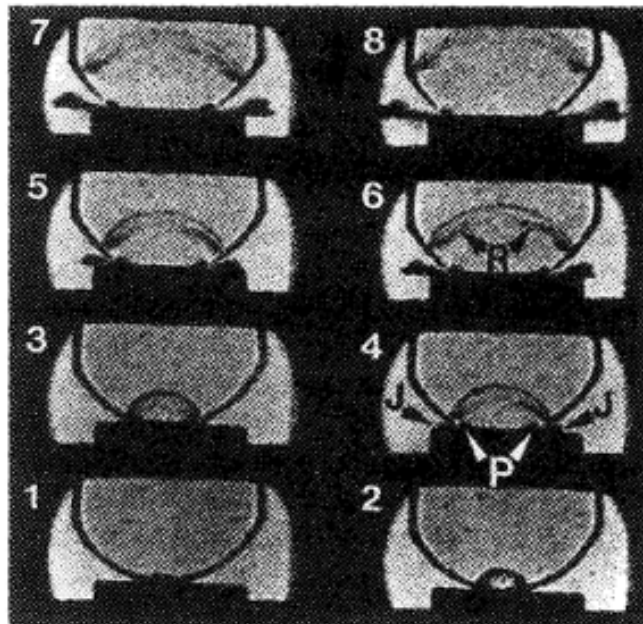


Figure 3.9: Impact at $150ms^{-1}$ between a water droplet and a metal disc. Source [59]

3.3.3 Stress Waves

As well as the pressure waves occurring within the droplet, they also propagate through the material which the droplet is impacting. Three stress waves emerge from the impact zone between the droplet and the solid surface and spread to the rest of the material, these include; a dilatational wave travelling which travels in the longitudinal direction,

a shear wave which travels in the transverse direction and a Rayleigh wave which travels along the surface of the material [57] [64]. These waves are illustrated on Figure 3.10.

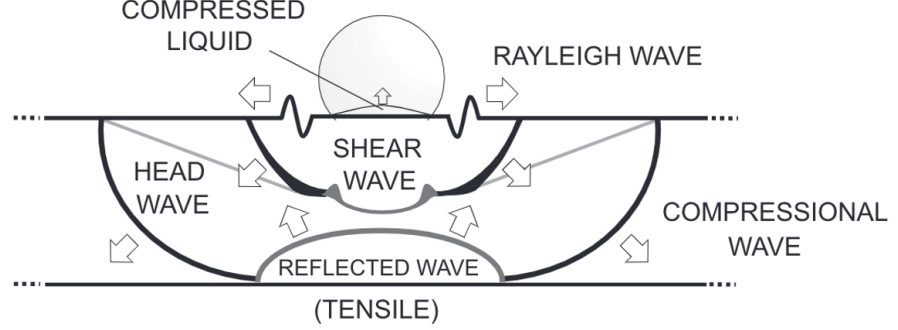


Figure 3.10: Schematic view of a shock wave propagation occurring during the impact between a material and a falling droplet illustrating the three stress waves propagating the material. Source [45]

The velocity of these stress waves are dependent on; the elastic modulus of the target material, poisons ratio and its density. And the formulas of them are as follows.

Longitudinal wave.

$$C_L = \left\{ \frac{E}{\rho(1+v)} \left(\frac{v}{1-2v} + 1 \right) \right\}^{\frac{1}{2}} \quad (3.7)$$

Transverse wave.

$$C_T = \left(\frac{E}{\rho(2+2v)} \right)^{\frac{1}{2}} \quad (3.8)$$

Rayleigh wave.

$$C_R = \left(\frac{0.862 + 1.14v}{1+v} \right) \left(\frac{E}{2(1+v)\rho} \right)^{\frac{1}{2}} \quad (3.9)$$

Where v denotes poisons ratio, p is the density of the target material and E is the Youngs modulus. These stress waves can induce a fracture within the material by having a sufficient amplitude and duration above the target materials dynamic fracture

strength. The stress waves can also interact with the microstructure of the target material and in the case of a composite material it can interact with imperfections of the layup, this the defects acting as stress concentrators, attracting stress waves. Therefore the propagation of these stress waves is considered one of the main mechanisms which can cause failure within the dynamic interaction of a high-speed liquid droplet impact.

3.3.4 Lateral Jetting

After the compression of the liquid upon impact creating the water-hammer pressure the liquid depressurises and this occurs by the droplet jetting laterally from the contact zone after the impact. The jetting action of the water is expected to begin when the shock front of the compressed liquid region which is propagating inside the liquid droplet creates a free surface, this is illustrated in Figure 3.11. This free surface is theorised to begin when the contact line velocity between the droplet and the surface becomes equal to the propagating shock front.

It has been concluded from multiple studies [57,65,66] that the velocity of the jetting water can be multiple magnitudes greater than the impact velocity, one study in particular by Jenkins and Booker [67,68] where the velocity of the lateral jetting was measured for a 2mm droplet over a wide range of impact velocities from 100ms^{-1} to 1140ms^{-1} . The results are displayed in Figure 3.12 and show the relationship between the lateral jetting velocity and the impact velocity over the range tested.

From Figure 3.12 it can be observed there is a higher velocity ratio at impact velocities less than 400ms^{-1} . This means that in the scenario of raindrop erosion on turbine blades which is in the range of $60\text{-}150\text{ms}^{-1}$ the relative effect of lateral jetting is greater to the surface of the material. It can also be seen that a higher the impact velocity results in a higher lateral jetting velocity. From a tribological viewpoint the high impact velocity and subsequent high lateral jetting velocity is important in the initiation of erosion on the surface of the material due to its high magnitude force which can easily attack any irregularities on the material surface. A study conducted by Najafabadi [69]

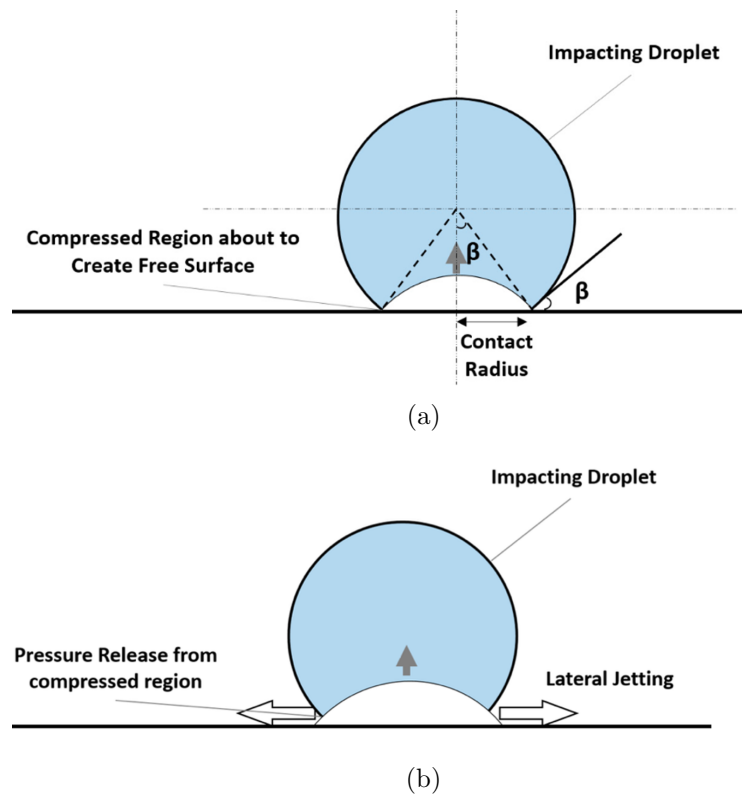


Figure 3.11: Schematic of the beginning of lateral jetting formation [50]

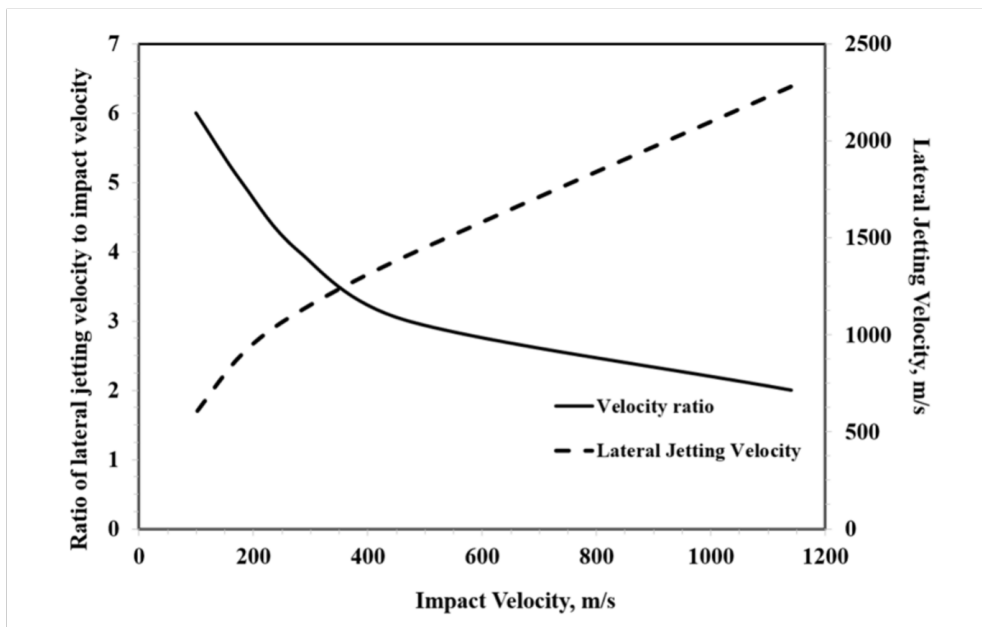


Figure 3.12: Ratio of lateral jetting to impact velocity, redrawn by [50]

concluded that surface irregularities larger than $100nm$ have a high propensity of being eroded by lateral jetting. As well as the surface of an aerofoil needing to be smooth for efficient airflow and optimal lift this will also aid erosion resistance by minimising the initiation points of erosion.

It is important to note that the lateral jetting velocity is time dependant of the impact and the velocities graphed in Figure 3.12 is the initial jetting velocity immediately after the droplet impact. The velocity of the jetting water decreases rapidly after impact as demonstrated by the work of Engel [70] who measured the velocity of the jetting water using high speed photography and confirmed the large lateral jetting velocity to impact velocity ratio and the rapid decrease immediately after impact. The experiment conducted by Engel [70] was using a relatively low impact velocity at $8.2ms^{-1}$ and the results are shown in Figure 3.13.

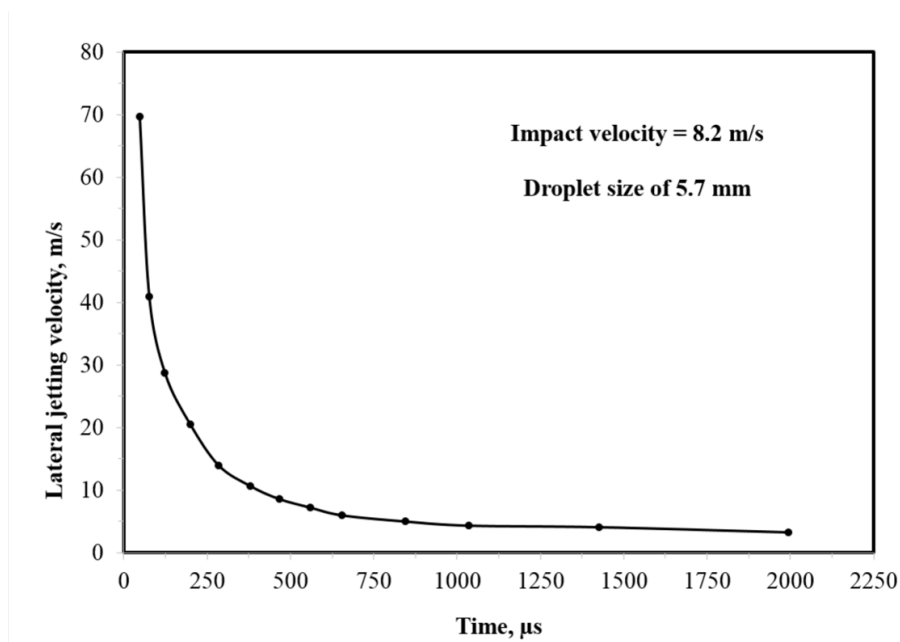


Figure 3.13: Time dependency of lateral jetting immediately after droplet impact on a surface [70]

It is demonstrated from Figure 3.13 that the highest lateral jetting velocity occurs

immediately after impact and then quickly dissipates to a much slower velocity, smaller than the impact velocity. Engel [70] also provided an equation which calculates the lateral jetting velocity immediately after the droplet impacts a surface and it is as follows in equation (3.10):

$$v_1 = \sqrt{\alpha c V} \quad (3.10)$$

Where v_1 is the lateral jetting velocity, c is the speed of sound, V is the droplet impact velocity and α is a coefficient which defines the fraction of the impact velocity imparted to the liquid molecules. α is mainly determined by the fraction of the liquid which is engaged with the compressional wave which moves through the droplet creating the free surface for the lateral jetting to occur [70].

This equation does not, however, entirely agree with the study by Jenkins and Brooker [67]. The value of alpha tends towards one as the impact velocity increases which would suggest that the lateral jetting velocity would be smaller than the impact velocity as it approaches the speed of sound in the liquid which contradicts the data in Figure 3.12.

The complexity of the physics and the damage mechanisms associated with the event of a droplet impacting a material or in this investigation the leading edge of a turbine blade increases as the impact frequency increase. Although there have been some models developed which characterise water droplet erosion including Springers model [71], there is no convincing current erosion model to explain all aspects including especially in advanced materials such as composites.

3.4 Erosion Damage Mechanisms

Within prior research there has been extensive investigation of the initiation and progression of erosion damage from either a single droplet impact, this can be either from an experimental investigation [72] or a computation exploration [73] and multiple im-

pact fatigue erosion which is predominantly investigated by an experimental route.

What has been concluded from the investigations that have been conducted thus far is that erosion can be categorised into erosion regimes. This means that the type of erosion that occurs has dependencies which are mainly the impact velocity, impact angle and the response of the target material.

The initiation of erosion has taken precedence within the research in hopes to mitigate the issue completely, therefore there is a range of explanations covering the initial mass loss of the target material [64, 74, 75] and the conditions that leads to this event.

For this investigation, which is focusing on the erosion of wind turbine blades by water impact the target material will be polymeric and consisting of a composite material. Due to these materials being predominantly used within this application there are some assumptions that can be made on the types of erosion mechanisms occurring during droplet impact [68, 76], these include:

- From high-speed droplet impacts deformations can occur on the surface of the material
- There will be stress waves propagating through the material upon impact
- The surface of the material will fatigue due to the repeated nature of rainfall and sea spray always being present in the climates
- Initial surface defects, including pits and dents from high-speed impacts create initiation points which are vulnerable to lateral jetting and hydraulic penetration eroding the material further
- In the event of a heavy rainfall the turbine blade material does not have time to recover from each individual impact and there is an accumulation effect.

The effect of surface fatigue was highlighted as a main concern as it was thought it was the principle erosion mechanism responsible for the initiation of erosion on wind turbine blades [77, 78]. This was postulated to be due the nature of the initiation period of WDE as erosion does not immediately start with one droplet impact and takes multiple impacts to show any signs of damage which fits the model of surface fatigue. The impact is assumed to be below the fracture threshold velocity as the accumulation of the impacts leads to an accumulation of stress within the material which ultimately results in the formation of pits, gauges, and cracks. This accumulation of stress is interesting as a dictator in the length of the incubation period. While a wind turbine blade is in operation there are multiple structural stresses already applied to the material 2.5, whether these stresses in the material are cumulative and effect the length of the incubation period making the blade more vulnerable to erosion has never been studied before and could be a determining factor. Another indicator that fatigue might have a predominant role is the existence of a lower threshold speed or erosive conditions below which erosion is unlikely to occur. This has been experimentally investigated previously [79–82] and concluded that there are materials that can suffer fatigue failure. Other studies [83–85] have also observed microscopic fatigue marks on sample material which has been subject to WDE and secured the idea of surface fatigue to be the primary erosion mechanism for erosion initiation on wind turbine blades subject to WDE.

Before the main concern of WDE was on wind turbine blades the focus was on steam turbines and aircraft discussed in section 3.1 where the target material was metallic and not polymetric, the main erosion mechanism was already established to be fatigue. However, Adler [86, 87] set out to investigate this established idea’s validity, and after a thorough investigation into the materials microstructure after WDE exposure and analysing the damage Adler [86, 87] concluded that fatigue was only a secondary erosion mechanism for WDE damage. Adler [86] conjectured that the damage was mainly from the high-speed lateral jetting and hydraulic penetration. Another method he used to investigate the surface defects from WDE was to examine the cross section of

erosion craters, to which he found that the crack fronts which were assumed to originate from the erosion damage were very blunt which would suggest that the formation of the cracks are from a tunnelling process rather than a standard crack propagation which would display a very sharp geometry. This discovery about surface fatigue from WDE by Adler [86] was later confirmed when surface treatments which are known to improve a materials fatigue life including deep rolling, laser shock, peening and ultrasonic nanocrystalline modification showed almost no improvement to erosion resistance.

Despite the fact that this was the conclusion for metallic surfaces and not applicable to leading edge erosion (LEE) as the materials are dominated by polymeric composites it demonstrates the importance of rigorously assessing all erosion mechanisms. It could be the case that some materials are more heavily influenced by a specific combination of surface fatigue and lateral jetting which could lead to failure prematurely. Some materials which are being introduced more commonly onto wind turbines recently for coating protection are very soft and are able to elastically recover from water droplet impact far quicker than materials which are harder and obtain historically higher erosion resistance properties. As a result the softer material has potential to outlast the harder material due to its elastic properties. This demonstrates the need for further investigation into the damping effect of materials to recover from an impact in parallel with its surface erosion from lateral jetting and hydraulic penetration. This can be achieved by investigating further into the moment of impact between the droplet and the target material and the dynamic response of the material including the changing topography of the surface.

3.4.1 Effects of Erosion Parameters

As discussed previously WDE is heavily determined by the impact velocity, droplet size, droplet shape, the geometry of the target material, the target materials mechanical and surface properties. This is because these parameters dictate the magnitude of the water hammer pressure, amplitudes of stress waves, lateral jetting speeds and the response

of the material.

Several studies [60, 88, 89] have theorised that the impact velocity is the most destructive parameter creating the largest effect on the material erosion. Note although impact velocity is a combined vector of falling droplet velocity and blade tip velocity the ratio between the two is small and thus dominated by the tip velocity. According to Heymann [31] from his experimental data the erosion rate is exponentially proportional to the impact velocity given by the following equations (3.11), (3.12) and (3.13):

$$ER = aV^n \quad (3.11)$$

$$ER = a(V - V_c)^n \quad (3.12)$$

$$ER = ae^{nV} \quad (3.13)$$

Where ER is the erosion rate, a is a constant, V is the impact velocity, n is the speed exponent, V_c is the threshold velocity. V_c is the velocity, below which no erosion takes place. The value of the exponent value, n , can reach up to a value of 10 however Eisenberg et al [83] has determined a value of $n = 6.7$ for the application of LEE on wind turbine blades.

Another parameter, not yet discussed, which is of great importance is the angle of impact the water droplet creates on the target material. Although it can be argued that when it is a liquid as the erodent abrasion does not take place, however, there are studies which have demonstrated experimentally results showing defects on the material surface reminiscent of abrasive wear. It is therefore important to investigate the effect of abrasive erosion mechanisms. The available literature is predominantly for solid particle erosion for various impact angles, however there are mechanisms which are transferable.

Erosive wear refers to wear mechanisms which occur when relatively small particles impact against mechanical components or materials. The known mechanisms are shown in Figure 3.14.

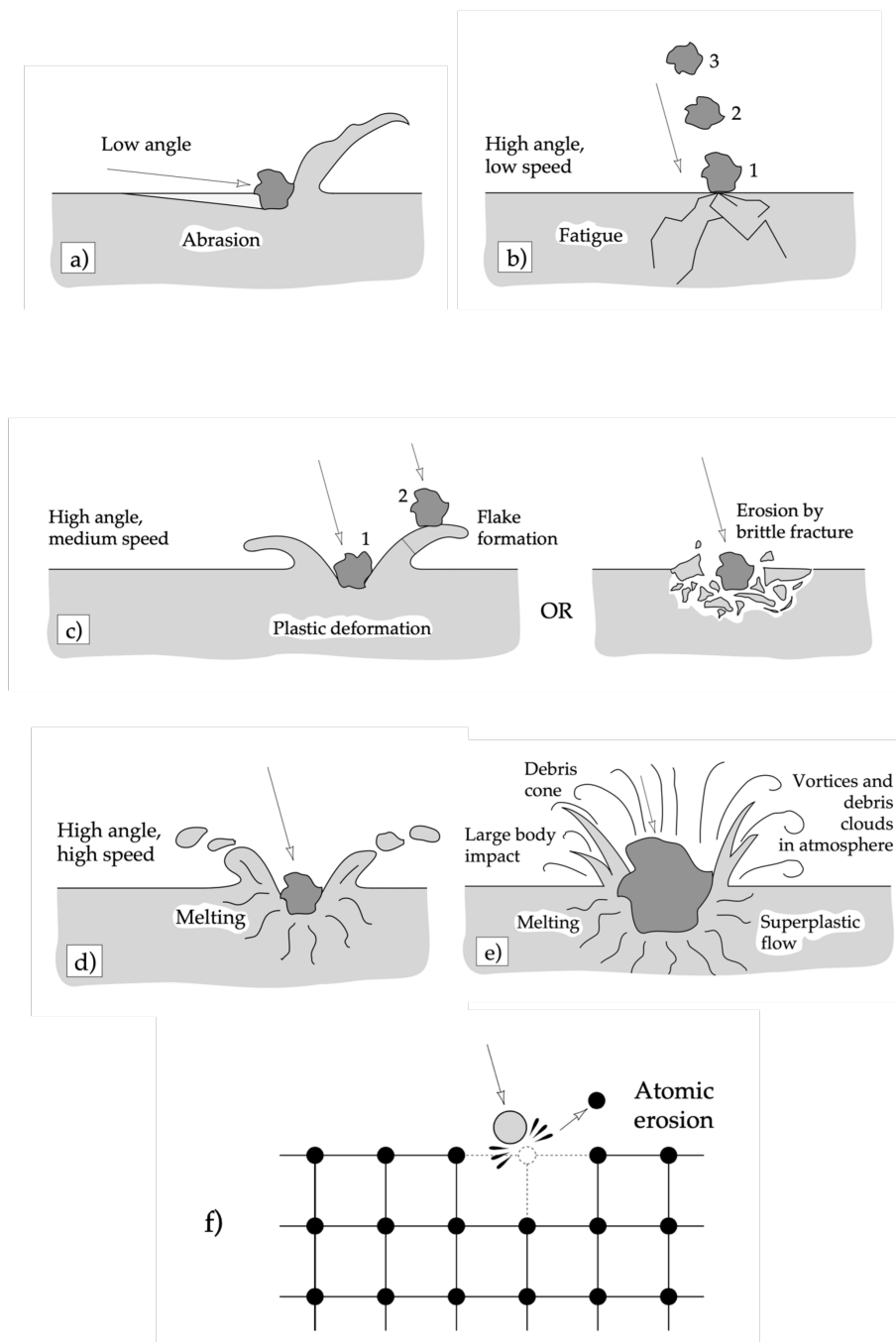


Figure 3.14: Possible mechanisms of erosion including a) A low impact angle producing abrasion b) a high impact angle at a relatively low impact velocity inducing surface fatigue c) a high impact angle from a relatively high impact velocity producing brittle fracture or multiple deformation d) at extreme high impact velocities which result in surface melting e) macroscopic erosion with secondary effects f) crystal lattice degradation from impacts by atoms. [90]

The impact angle or impingement angle is the angle of incidence between the target surface and the trajectory of the particle the instant before contact as shown in Figure 3.15.

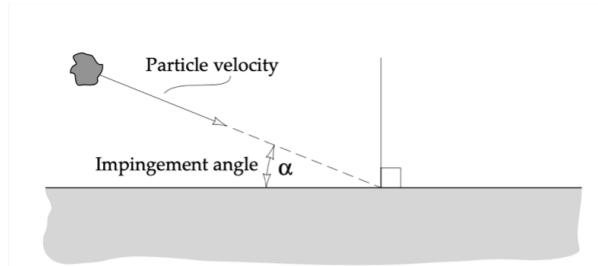


Figure 3.15: Impingement angle of a particle causing erosion of a surface [90]

A low angle of impingement is more likely to cause damage in the regimes of abrasion as the particle tends to slide over the surface after impact creating wear damage. A high angle of impingement is much more common and is the typical erosion mechanisms such as surface fatigue, deformation and brittle fracture or cracking. When the material is very brittle the most common action of erosion is via subsurface cracking or in the case of LEE of wind turbine blades this can also lead to delamination of composite layers.

The impact velocity also plays an important variable on the wear process and which mechanisms are more likely to occur. As seen previously with a water-droplet, if the impact speed is insufficient to exceed the fracture limit, the particle does not create any deformation as the stresses on impact are very low. Alternatively, the particle erodes the surface via a surface fatigue mechanism, the same way in which a water droplet acts. As the impact velocity of the particle increases the likeness of deformation upon impact increases and when the impact speed is at extreme velocities the impacted surface may even melt.

Some of these qualities can be seen in WDE when at a high enough impact velocity, after initial compression of the droplet upon impact the water droplet acts as an incompressible fluid acting as a solid and causing gauging of the material [90].

The angle in which the particle or droplet impacts the material not only dictates the mechanism in which erosion occurs but also its magnitude. The range of impact angles is $0^\circ \leq \theta \leq 90^\circ$, at zero impingement there is negligible wear as the projectile does not impact the target. Even at relatively low impact velocities, if the target material is soft then a shallow angle of $\theta_{im} = 20^\circ$ can be enough to inflict serious damage. At these shallow impact angles wear similar to abrasive wear is most common. If the target material is harder and more brittle then wear by fragmentation of the surface may occur and the maximum wear rate will increase to 90° . The relationship between impingement angle and wear rate for ductile and brittle materials is shown in Figure 3.16.

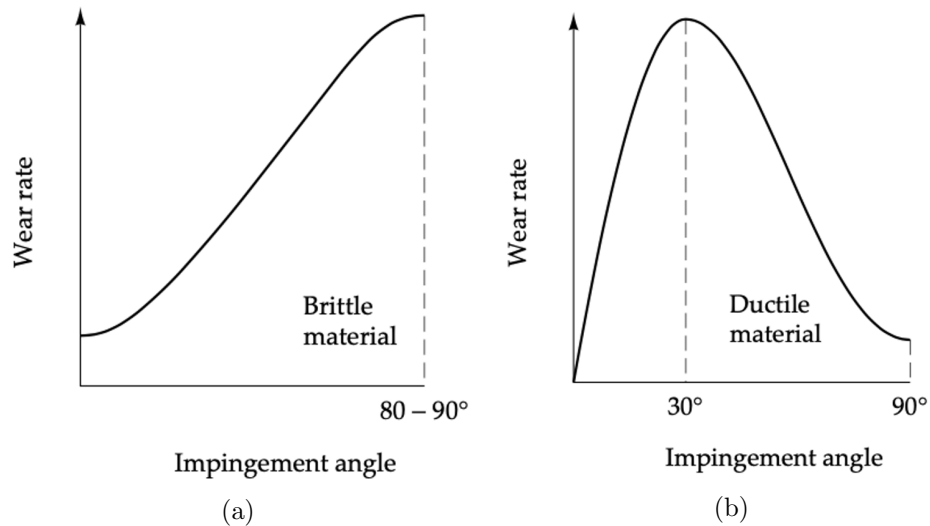


Figure 3.16: Graphs depicting the trend in wear rate over impingement angle of a (a)Brittle material (b)Ductile material [90]

In the scenario where the greatest magnitude of erosion occurs at a low impingement angle between the projectile and the target material it can be concluded that the ductile mode of wear is most prevalent. Conversely in the scenario where the greatest magnitude of erosion occurs at a high impingement angle between the projectile and the target material it can be concluded that the brittle mode of wear is most prevalent.

Chapter 3. Rain Erosion

The problem becomes much more complicated in the case of LEE on wind turbine blades as the material is a composite, composed of hard and soft materials. This means that in the event of WDE the erosion mechanism changes depending on the impingement angle. In low impingement angles the dominant mechanism will be abrasion and gouging will occur as the droplet is mainly damaging the softer epoxy resin. During the high impingement angles the dominant mechanism will be brittle wear as the harder glass fibres are being susceptible.

The impingement angle between a water droplet and the leading edge of a turbine blade can vary depending on where it impacts as the leading edge of the blade is a curved profile. This results in varying erosion mechanisms acting on the glass fibre composite shown in Figure 3.17.

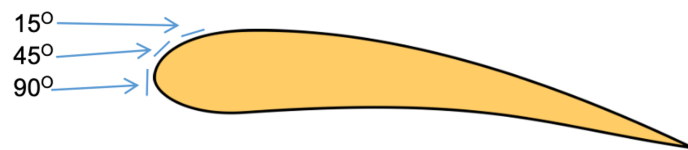


Figure 3.17: Impingement angles onto the leading edge of a wind turbine blade

In summary, rain erosion has been a problem in aviation where the wings of aircrafts were eroding from repeated impacts with rain droplets and therefore not functioning as efficiently as intended. The problem was also found in other industrial machinery with adverse effects and in some cases creating fatal situations. The factors which influence the erosion rate include the impact velocity between the droplet and the target material (influenced by the upstroke or down-stroke of the turbine blade), the impact angle, the composition of the target material and the droplet shape and size. The physics of the impact has been studied in great detail and shown to be a high pressure event with erosive qualities including lateral jetting. It has shown itself to be a tangible problem relating to the erosion of wind turbine blades and demonstrated the need for further research to be concluded in order to extend the lifetime of the blades.

Chapter 4

Leading Edge Erosion Testing

4.1 Techniques for Simulating Leading Edge Erosion

Erosion predominantly occurs on the leading edge of wind turbine blades. This region is located at the front spar of the blade as shown in Figure 4.1 and is the area that will be in first contact with air and rain. The following section will discuss the need for an erosion testing facility and why it is a useful tool within the industry, it will also discuss the various forms an erosion rig can take and the different methodologies the rigs have.

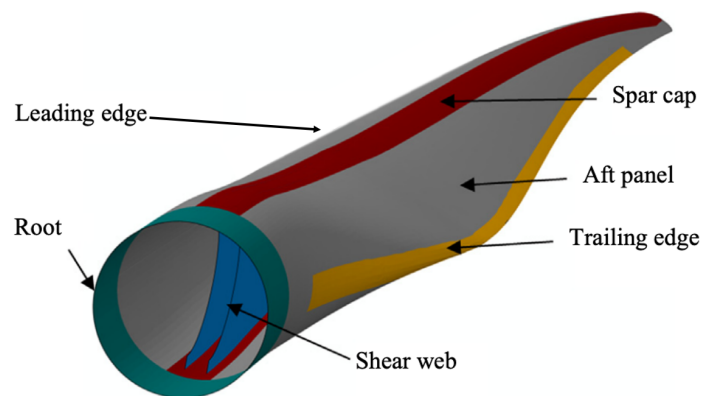


Figure 4.1: Regions of a wind turbine blade. Source [91]

4.1.1 Purpose of an Erosion Testing Facility

The purpose of an erosion testing facility is to artificially recreate the environmental conditions which are recorded at the site of erosion, which in this case would be the climate conditions at the wind turbine. The experiments which the testing facility conducts are accelerated conditions to condense years of erosive wear which would be witnessed in the field down to weeks and days of testing. It should be noted that there is not currently a direct correlation between the testing environment and service life. This is due to the limited data crossover between erosion of old turbine blades in the industry and test samples. This lack in cross-over is mainly due to wind turbine owners not wishing to share data about their eroding turbine blades as it may have a negative effect on the perceived performance of the components and thus a detrimental effect on the sales of the company. Testing does, however, allow for qualitative assessment of erosion, where various erosive parameters can be tested to determine what yields the most erosion and how it affects the surface of the material. These include, the impact velocity, impact angle, bending stress on the material, salt content of the water droplets, and the material. All these parameters can be related to the erosion that is encountered within operation of a wind turbine and the severity can be determined from the relation to different samples.

There have been many testing facilities utilised throughout the literature [52,92–94]. Rain erosion testing facilities can be characterised under two criteria [95], the first being whether the target material is moving or stationary and the second criteria is whether it is a single impact setup or multiple impact. The ways in which these four variations can be setup is to the scientist's discretion and has generated innovative solutions for testing methodologies.

Figure 4.2 describes the different types of erosion facilities and which category they fall under. The single and multiple water droplet erosion rigs are usually used to investigate slightly different phenomena. A single drop erosion facility is used to investigate the fundamentals of the droplet impact as discussed in section 3.3 whereas multiple

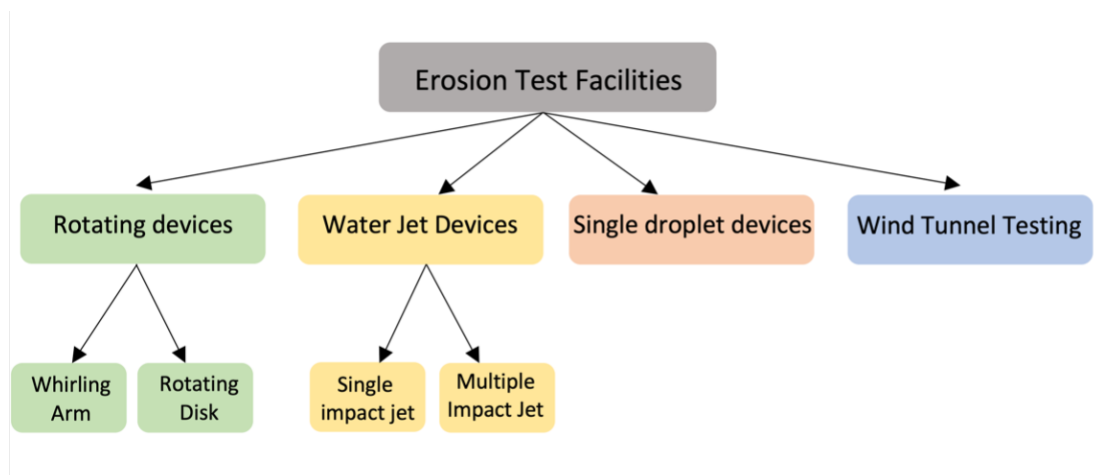


Figure 4.2: Classification of erosion test facility, adapted from [50]

droplet erosion testing facilities are used to gather information on the erosion effects of the cumulative impacts on selected materials.

4.1.2 Jet Erosion

One way to simulate the material effect of high velocity water impacts is through a high pressure jet erosion facility. The main characterisation of this type of facility is that the target material is stationary or has relatively low velocity compared to the water velocity. There are many advantages to this type of facility including the level of control which is available as the impact of the water onto the target material can be finely tuned to meet the desired input parameters. This type of facility also produces results extremely quickly, in the event that the experiment is a single impact test then the period of the experiment is the time it takes for the water to hit the material which is almost instantaneous when testing high velocities. The pressure system which controls the impact velocity of the water can be charged to set the velocity to extreme speeds which is advantageous when simulating leading edge erosion of a wing on a plane travelling close to Mach 1.0.

An example of a single impact jet erosion rig is shown in Figure 4.3 [96]

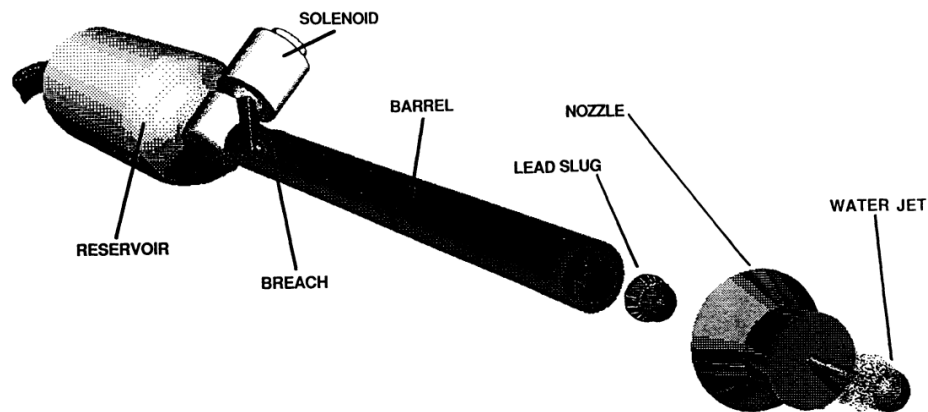


Figure 4.3: Jet erosion testing facility [96]

There are, however, some disadvantages of this type of testing rig, this includes the inability to control the droplet size of the water. When using high pressure systems the water droplets which are impacting the target material are not similar to the droplets which would impact the leading edge of a wind turbine blade. This makes this testing unrealistic to the environmental conditions which are present at the site of impact between a rain droplet and the leading edge of a wind turbine.

Other jet erosion facilities have attempted to bridge the gap to become more related to a wind turbine blade investigation. This was completed by implementing a multiple impact setup named a PJET (Pulsating Jet Erosion Test rig) as shown in Figure 4.4. This test rig was developed at EADS IW [97] and the idea was developed by the Cavendish Laboratory in the University of Cambridge where the basic concept is that the water jet can cause similar damage as water droplets if the front of the water jet has a ball shaped geometry similar to water droplets [98] [99].

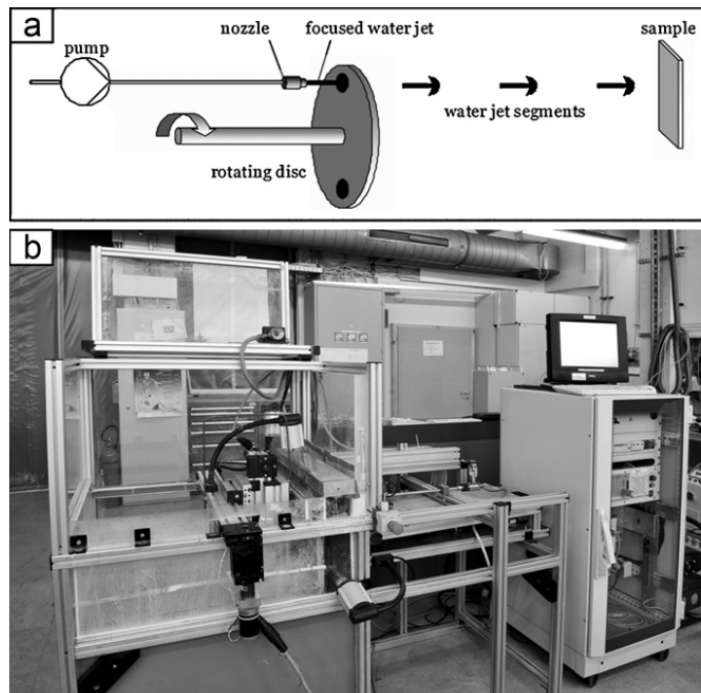


Figure 4.4: (a)The principle of how the PJET test rig operates. (b)A laboratory photograph of PJET

4.1.3 Ballistics/ Rocket Testing

A unique, rare and expensive way of testing the effects of droplet impacts on a leading edge is by ballistic impact along a rocket sled. This method was used when investigating the effects of supersonic leading edge impacts commonly only encountered when operating missiles or high speed planes. These test were almost exclusively conducted by the military. A test from 1985 by the US military is outlined in Figure 4.5

This method is not optimised for testing the conditions for rain erosion on wind turbine blades, however, it does demonstrate the need for research on the interaction of particles on leading edges at very high speeds. The scale and expense of the rocket sled facility shows the importance of testing for erosion of leading edge and how it can effect the performance of the aerofoil of either the wing of a jet plane or the 100m+ blade of an off-shore wind turbine.

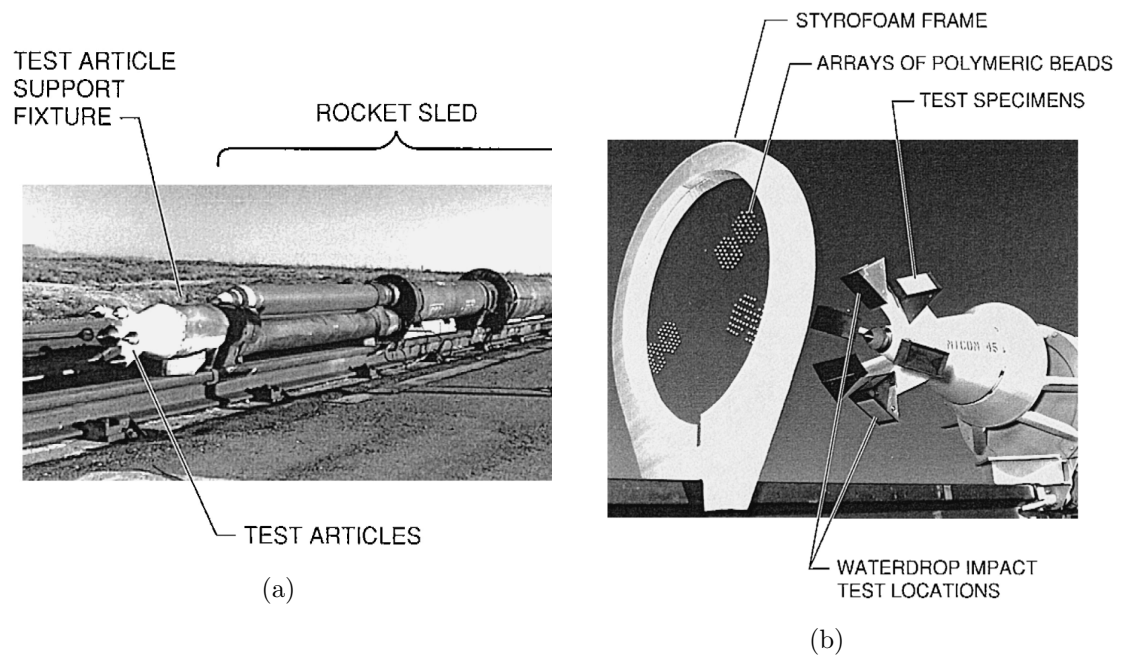


Figure 4.5: Ballistic/ rocket sled facility showing (a) An Overview of the rocket sled at Holloman Air Base in New Mexico. (b) The polymeric bead arrays supported on fine threads in a styrofoam frame placed on the test track for impact with specimens mounted in wedged-shaped holders on the front end of the rocket sled. The specimen arrangement is seen in the background. [100]

4.1.4 Wind Tunnel Testing

Wind tunnel testing is different from the other methods described in Sections 4.1.5, 4.1.3 and 4.1.2 in that it is not normally used as a method for simulating and accelerating erosion and is more used as a tool to understand the effects of erosion. In a study conducted by Sareen et al [101] leading edge profiles were tested within the wind tunnel as shown in Figure 4.6 to measure their lift and drag co-efficients. The leading edges which were tested included damaged blades of different magnitudes. Three levels of erosion were tested, type A: small pits present, type B: pits with gouges and type C: pits with gouges and leading edge delamination. These three types were created with reference to photographic evidence supplied by 3M and thus the aerodynamic effect of the leading edge erosion was evaluated.

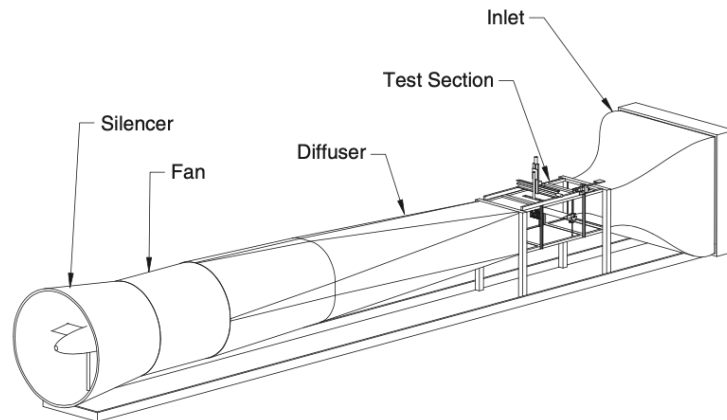


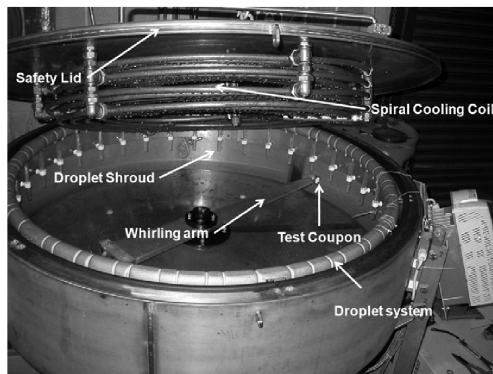
Figure 4.6: Schematic of the University of Illinois at Urbana-Champaign low-turbulence subsonic wind tunnel. [101]

This type of leading edge erosion testing is an extremely useful tool to create a relationship between the erosion which has occurred due to the rain droplet impacts and the aerodynamic effects of the aerofoil. This is important as it can give an insight into the effect of the decline in efficiency of wind turbine blades. It can also demonstrate the rate and magnitude of decline in efficiency for the increasing levels of erosion as the study by Sareen et al [101] goes on to investigate.

4.1.5 WAREER (Whirling Arm Erosion Rig)

One of the most common types of simulating and accelerating rain erosion is through the use of a WAREER (Whirling Arm Rain Erosion Rig) some examples are shown in Figure 4.7. The function of such a facility is centered around a main spinning arm or disc at high rotational velocities. At the edge of the arm or disc is the target material which is being tested. Above this spinning apparatus will be a form of rainfall dispenser which is usually via hypodermic needles connected to a water source. This type of facility is primarily used for a multiple impact studies and the tests are usually relatively long (hours, days or weeks). There have been many studies which have used this type of facility to study leading edge erosion either within a aerospace application or specifically for investigating the effect of rain erosion on wind turbine blades [102–108]. The main difference between this type of facility and a jet erosion rig is that the target material is moving through the simulated rain field rather than the rain being projected at the target material. Having a configuration like this creates more control within the impact velocity and the size of the droplet. It is considered more realistic to wind turbine blade conditions [109] as the droplet retains its shape until impact as it would with rain droplet impacting on the leading edge of a turbine blade. The droplet diameter can be easily adjusted for each experiment by changing the needles appropriately and the impact velocity can be adjusted by adjusting the rotational velocity. One factor which is unique to WAREER's over other facilities is the ability to adjust the rain rate subject to the material which allows for a correlation to the locations of wind turbines. This correlation is further discussed in Section 9.3.

Chapter 4. Leading Edge Erosion Testing



(a)



(b)



(c)

Figure 4.7: WARE facilities (a)University of limerick [108] (b)R&D Commercial rig (c) WARER utilised by Busch et al in dornier system gmbh friedrichshafen, germany [110]

There are some disadvantages of this type of test rig including the expense to construct such a facility and also the difficulties to create high impact velocities (v_{im}). The average impact velocity of a large scale WARER is around $v_{im}150 - 200 \text{ ms}^{-1}$ [108]whereas a jet erosion rigs are able to greatly exceed this. The range of impact velocities achievable by a WARER, however, is within the range of even the largest wind turbine blades, therefore it is deemed the optimal tool for simulating and accelerating erosion for these components.

Chapter 4. Leading Edge Erosion Testing

In conclusion there are pros and cons detailed for the various test facilities within this section. To most accurately simulate the erosion on large scale wind turbines it is determined that the WAREER dynamic sample testing best represents real world conditions as it simulates the movement of the blade through the droplet field, thus the droplet geometry is not changed and realistic impact velocities can be achieved. As a result it was selected for this investigation. Critical importance is the velocity factor. The previous WAREER available in the University is not able to achieve adequate velocity to simulate the new larger wind turbines, thus as part of this work a custom built, dynamic erosion test facility was constructed to allow real world velocities to be achieved.

Chapter 5

Construction of Custom Rain Erosion Testing Facility

From the literature it was evident that for testing wind turbine blade materials most realistically to their conditions met in the field a WARER was the best suited facility for the task. At the beginning of this research test were conducted on the existing WARER within the University. As this research is focused on the newer larger multi mega-watt turbine blade, a new test rig was required to achieve the higher impact velocities. The existing test rig was restricted to $v_{im}60ms^{-1}$ for the new test rig speeds in the range of $v_{im} = 100 - 150ms^{-1}$ were required. In order to achieve these speeds, the new experimental rig was created with a much larger profile and the radius of the whirling arm was increased from 0.3m to 0.8m. This in turn brought about many design and engineering challenges which required careful consideration and evaluation. In order To fully meet the requirements of the experiments it was decided to design, construct and operate a custom rain erosion testing facility within the University.

5.1 Basis of Design

The design process was a multi-step iterative process. It included producing CAD models implementing the ideas from the list of capabilities, making sure it was compli-

ant with the DNVGL guidelines [111] and then consulting the Engineering Technical Supervisor (ETS). Ideas and designs were challenged for ease of manufacture and construction. As a result, initial complex design concepts were simplified as much as possible, this included the outer surround which was initially going to be a large cylinder to replicate the small rig, however basing the entire rig in a circle proved extremely difficult for manufacturing. Instead, an octagon geometry was used, this allowed for the rig to be modular and eight identical sections which bolted together to form the octagon.

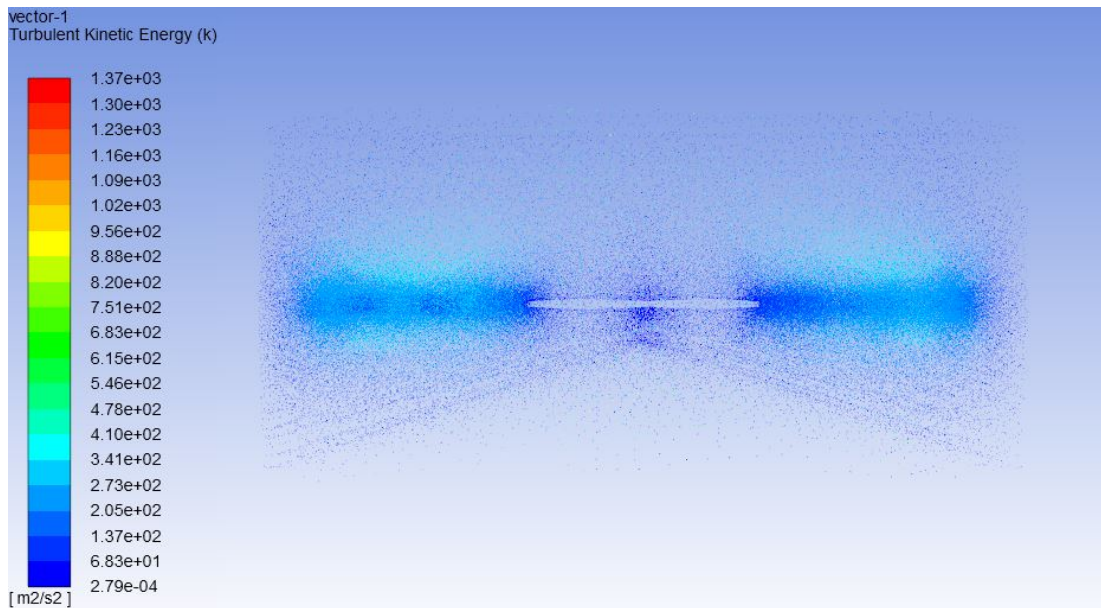


Figure 5.1: ANSYS computational analysis to calculate the turbulence within the WARER running at 1000rpm

Eight sides was the optimal balance between the aerodynamics inside the rig and the number of panels for practical manufacturing. A circle would be the optimal geometry as there would be no fluctuation in distance between the spinning sample and the outer enclosure, whereas in an octagon there would be instances where that distance would increase then decrease indefinitely. With a geometry with more sides the fluctuation would be less but induce a more complex geometry. To reduce the wall effect, the outer enclosure was increased in size and to check there was no turbulence effect fluent calculations were completed, seen in Figure 5.1 this was also used to de-

Chapter 5. Construction of Custom Rain Erosion Testing Facility

termine if there would be any aerodynamic effect with having two sample holders and whether the trailing edge turbulence of one of the sample holders would affect the other.

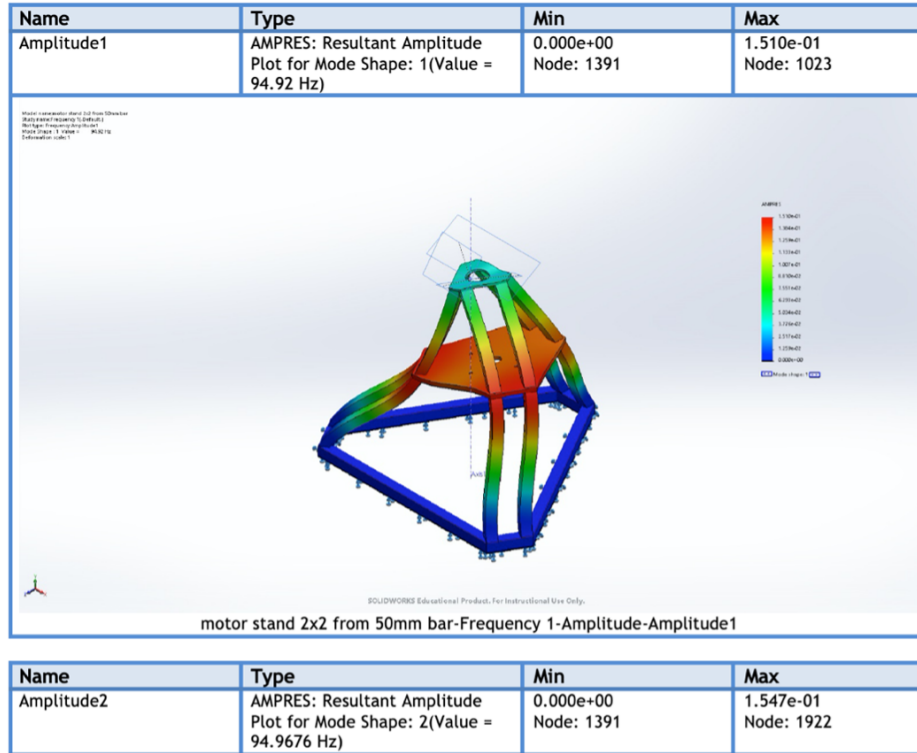


Figure 5.2: Structural analysis computed with Solwidworks to determine natural frequencies of the motor stand.

To aid the design of this experimental rig, other test rigs were researched and visited. The motor stand design was primarily influenced by other designs and consists of a three sided pyramid with a plate positioned in the middle to hang the motor from and space at the top to mount the bearing. This design was also the strongest structure that was designed and tested and showed no resonant frequencies within operational ranges. The analysis was conducted using Solidworks own integrated design analysis and the results are shown in Figure 5.2 and an image of the final assembly is shown in Figure 5.3.

Another way in which the rig design and construction was aided was to utilise parts and assemblies from other industries which were already analysed and specified for



Figure 5.3: Motor stand frame under the main octagon of the WARER.

specific functions. The two main examples of this being implemented within this rig are the drive train and the water system.

The drive train of the rig is housed within the motor frame which is a separate assembly from the octagon outer enclosure. A motor was selected to achieve the required rotational speed and torque to rotate the large mass and was hung from the bottom plate on the three-sided pyramid and on the top there is a Mercedes Sprinter van rear wheel hub which can spin freely when bolted into the frame. There is a splined half shaft from the van which inserts into the wheel hub and then adapted to connect to the Siemens motor. Also between this connection there is a rubber joint used which is also utilised when testing the power of a an engine on a dyno and its use is to dampen any small vibrations which could be transferred along the drive shaft. The schematic of the WARER setup is shown in Figure 5.4 and an image of the WARER in the blast proof enclosure is shown in 5.5

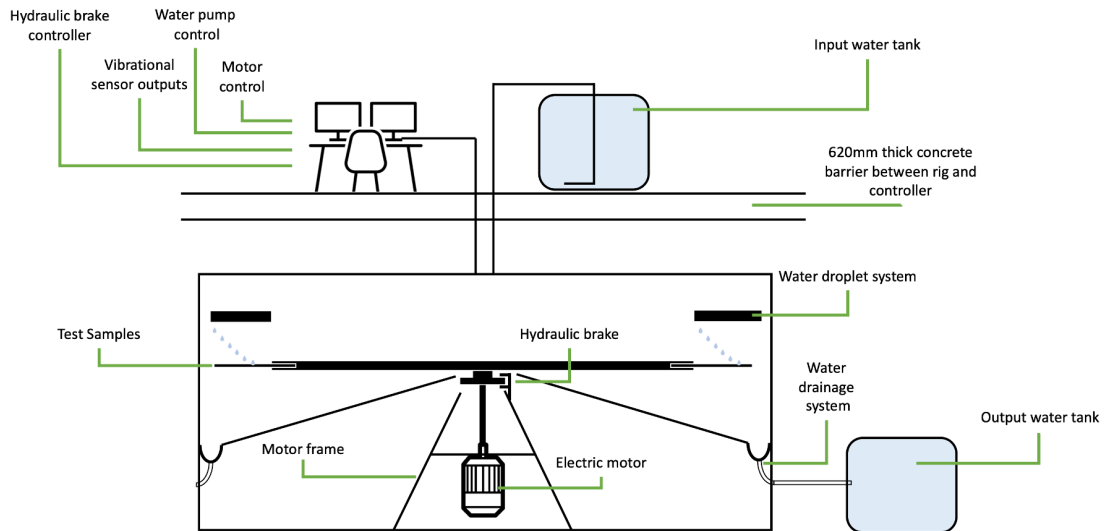


Figure 5.4: Schematic of the WARER at the University of Strathclyde.

The water system was heavily influenced by the use of medical equipment. The dispersion of droplets is created using a layout of hypodermic needles and the connections between all the pumps and needles are lure locks for easy removal and an easy transfer to a different gauge of needle in the case of running an experiment that requires a different droplet size as shown in Figure 5.6.

Using these already established parts and assemblies increased confidence in the overall operation of the rig and also confirmed their operational lifespan and had been tested by an independent company.

5.2 Material Selection

Another consideration which was paramount to the overall design process was the material selection for all components. The previous, smaller, experimental rig tested specimens with salt water to simulate sea spray for offshore wind turbines and the new, larger rig was designed to continue these experiments, therefore extra consideration was

Chapter 5. Construction of Custom Rain Erosion Testing Facility



Figure 5.5: WAREER at the University of Strathclyde (Picture taken January 2022).

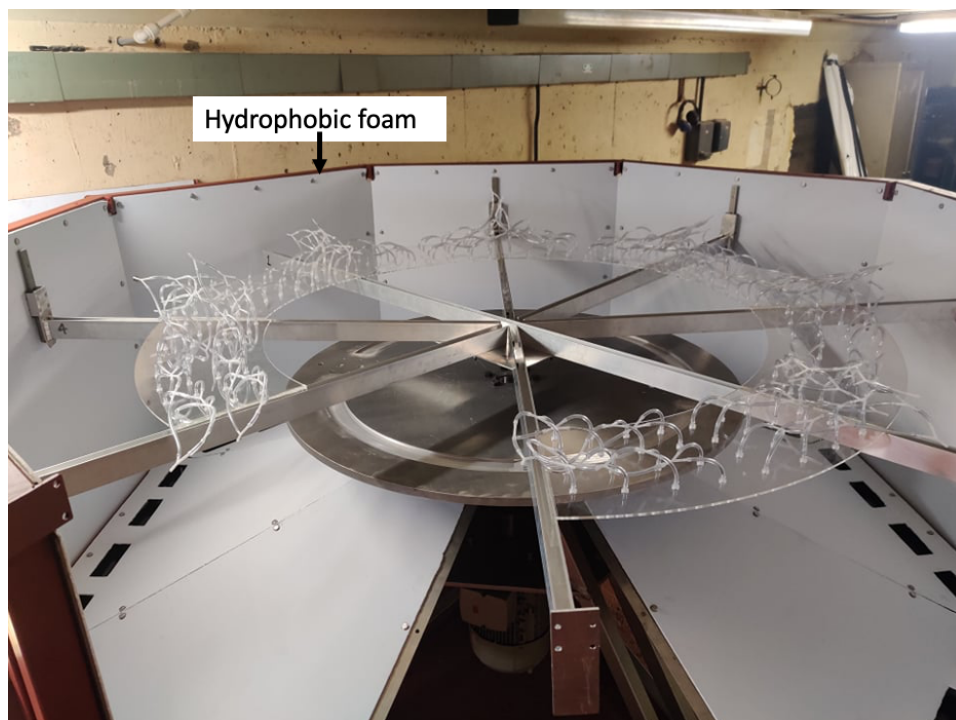


Figure 5.6: WAREER with the lid removed (Picture taken January 2022).

taken for the prevention of corrosion. As well as corrosion prevention considerations were also made for the strength, impact resistance, luminosity and sound deadening of certain components. The eight outer walls are 3mm 316 stainless steel as that was proven to be the highest performing material in terms of strength, impact resistance and corrosion resistance. It is, however, relatively expensive, but the decision was made to prioritise the outer container with higher quality materials to increase its safety and longevity. The main frame which holds the stainless panels together in the octagon shape is made from 50mm box section carbon steel as this is on the outside and will not be in contact with any of the water. It is coated in a rust preventative paint to prevent galvanic corrosion. The stainless panels are also lined with a self-backed adhesive hydrophobic foam, this is the white lining seen in Figure 5.6. This was to add another layer of corrosion prevention and more importantly to scatter light more evenly within the rig and create a much brighter environment. The reasoning behind this was to allow for higher frame rates to be achieved when using the high-speed camera as it required more light when recording video for slower playback rates. The powerful LED floodlights which are installed inside the rain chamber with the added white interior allows the camera to be stopped down in aperture and still provide the same frame rate producing higher quality images. The white hydrophobic foam was a suitable material for the task as it carried out three separate tasks which included corrosion prevention, providing more luminosity and it also dampened the sound inside the rig by reducing vibrations, ultimately increasing the performance of the rig.

The one other major expense was the main spinning disc which the sample holders attach to. The design of the disc is to spin the samples in a balanced motion with the least aerodynamic drag possible. Some WARER's utilise an arm with the sample on one end and a counterbalance weight on the other end. This design is much lighter and puts less load on the motor, however, these can be difficult to balance correctly and has tendencies to create unwanted turbulence within the erosion chamber. A spinning disc has little to no aerodynamic drag when spinning and is much simpler to balance, the only downside is that is much larger and heavier than a spinning arm and requires

more torque from the motor to initiate motion, however when running at speed it can require less power. When selecting the material for the disc the main considerations were, mass, corrosion resistance, strength and machinability. The material which was chosen was an aerospace grade aluminium (Al 7075-T7351) . The materials under consideration were evaluated for their corrosion rates and are shown below for 20°C in spray conditions taken from “Design Guidelines for the selection and use of stainless steel” [112]

Material	Potable Water	Sea Water
304	<1mpy	5mpy
316	<1mpy	<5mpy
Aluminum (Al 7075-T7351)	1mpy	<5mpy

Table 5.1: Corrosion rates of materials used on WAREER. 1mpy = 0.025mm/year 5mpy = 0.127mm/year (The maximum allowable stainless steel metal temperature is 50° to mitigate the potential for Cl-SCC)

5.3 Sample Holder

The new, larger experimental rig was designed to accommodate currently two separate PhD investigations and future investigations, therefore, the rig had to be adaptable for multiple types of experiments. In order to achieve this many of the implemented features were easily replaceable and adjustable including the rain system and sample holders. For this investigation the stress on the blade was of interest, therefore sample holders were designed to hold flat samples which can be put under a bending stress, as shown in Figure 5.7.

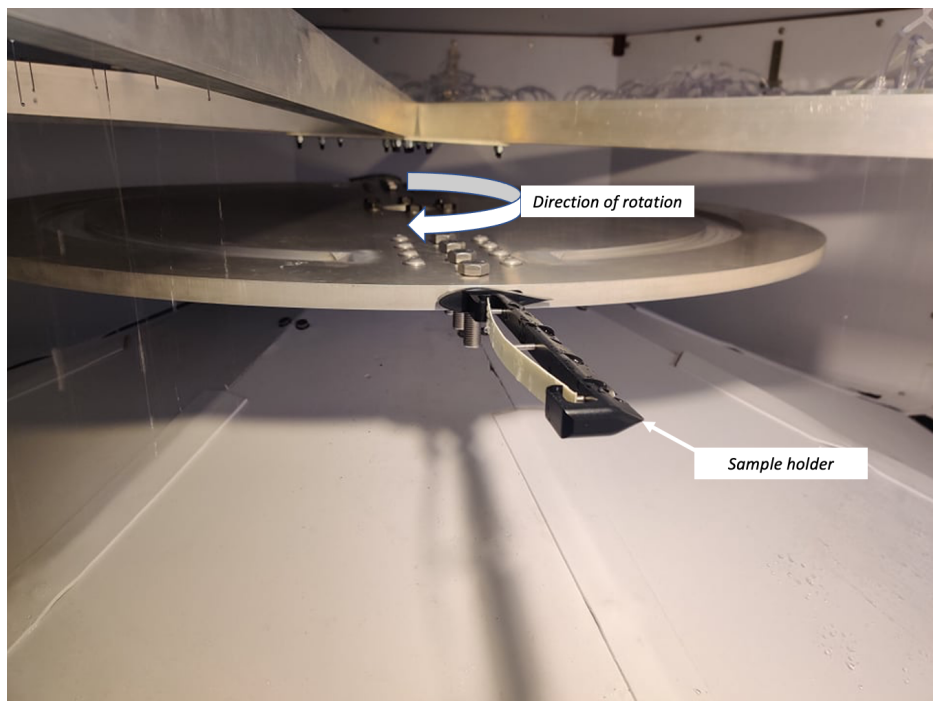


Figure 5.7: Sample holder mounted in position within the WARER.(Picture taken February 2022)

The way in which these sample holders (annotated in Figure 5.7) attach onto the main spinning disc is via a slot in the side and then held in place by four M12 bolts. As there is no insulator between the disc and the sample holder to minimise galvanic corrosion it has been manufactured from the same material and grade of aluminium and the sample holder has also been anodized black for extra protection from corrosion.

5.4 Stress Analysis

Before these sample holders were tested a computational analysis was completed in order to confirm the design would be able to withstand the centrifugal forces when running at maximum rotational speed. The analysis setup is shown below, showing the mesh generated by Solidworks and the point of rotation.

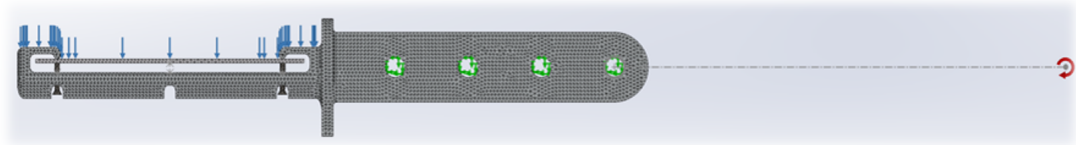


Figure 5.8: Analysis set up for the sample holder using the in built Solidworks software

The analysis took into consideration the mounting points of the sample holder, the compressive clamping force by the bolts and the aerodynamic drag induced to the frontal edge of the holder. The results from this computational analysis is shown in Figure 5.8.

Stress	Value (MPa)
Average	2.496
Maximum	1.203e+02
Minimum	2.260e-03

Table 5.2: Sample holder stresses when operating at 1000rpm

Type of failure	Safety Factor
Yield / failure	4.5
Fatigue	1.3*

Table 5.3: Safety factors of Sample holder operating at 1000rpm

The same analysis was repeated but this time with the main spinning disc as the subject, the results are shown in Figure 5.9, Table 5.4 and 5.5

*This safety factor is relatively low however it was calculated for 500 million cycles which far exceeds the expected lifetime of the sample holder. Consequently the results

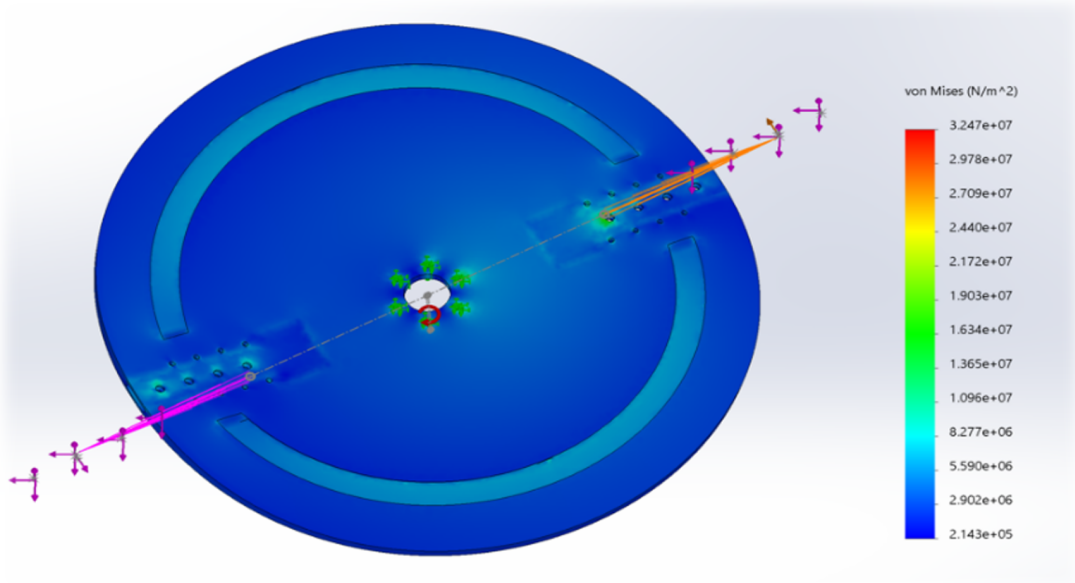


Figure 5.9: Stress map of the main spinning disc and the sample holder

Node	X (mm)	Y (mm)	Z (mm)	von Mises (N/m ²)
63632	69.9216	6.07485	232.404	3.24661e+07

Table 5.4: Peak stress found within analysis of spinning main disc with sample holders in position

Type of failure	Safety Factor
Yield / Failure	13.4

Table 5.5: Safety factor of disc spinning at 1000rpm

are acceptable.

5.5 Commissioning and Calibration

During the testing period, all the variable inputs were calibrated which included the input speed of the motor, the rainfall rate of the pumps and the droplet size produced by each gauge of needle.

For the output speed of the motor, it was calibrated with two separate measurement devices. An implemented encoder was installed onto the bottom of the motor drive and the information was fed back to the inverter to be viewed on the remote control panel. The input speed from the software was compared to the encoder output speed to ensure the correct rotational velocity was achieved. This was further verified by using the Chronos 1.4 high frame rate camera which was set up looking into the rig via the polycarbonate window to capture the rotation of the rig at high frame rates. The time for each revolution can accurately be determined by the camera and therefore the rotational speed. All measurements were coherent with each other and within 1rpm of tolerance.

The water pumps which supply water to the needles were all individually calibrated along with their respective motor controller. The motor controller has a percentage output and an adjustable wheel to vary the power sent to the pump. As the experiments schedules will be using different rain rates each of the different levels supplied to the pump by the motor controller was evaluated for its volume flow rate. The flow rates were calculated by pumping water by the pump for a set length of time and then measuring the volume of water displaced. This was then repeated for all levels of input for the controller and then again for each of the four pumps to account for any discrepancies between pumps. The volume flow rate results of this calibration were then converted to rainfall rate by using the distributed area the droplets fall, these rates are used on each individual motor controller to finely control the rain rate inside the rig.

As mentioned previously, the needles which generate droplets within the rig can be replaced in order to provide different sized droplets. To calibrate the size of each droplet from its respective needle the high-speed camera was again used. In a controlled environment, each of the needles was fed water and the high-speed camera was used to capture an image of the droplet as it fell adjacent to a ruler. The image was then post processed in ImageJ in order to determine the diameter of the droplet. The set up and results are shown in Figures 5.10 and 5.11 and Table 5.6.

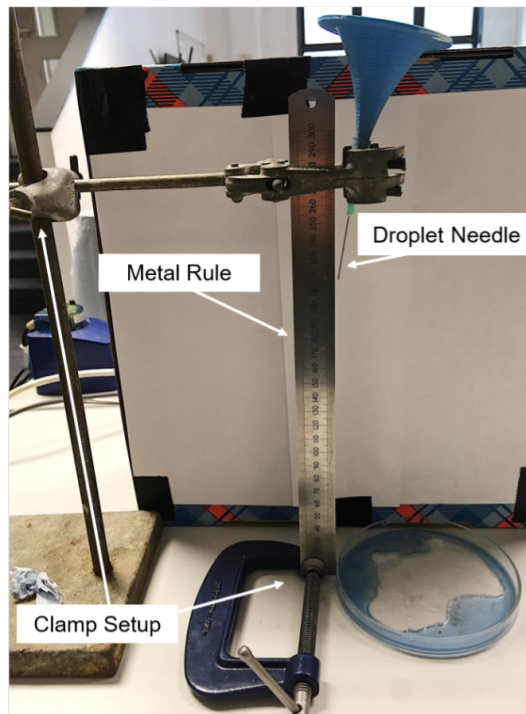


Figure 5.10: Setup for measuring the droplet diameter

Needle Gauge	21G	23G	24G	25G
Average Diameter	2.40mm	2.25mm	2.03mm	1.96mm

Table 5.6: results from measuring various gauges of needles

The water which is supplied to the needles is configured in such a way to allow for control of the flow remotely and also the extraction of the used water to be drained remotely. The start of this system is a 1000l water tank which sits up above the rig

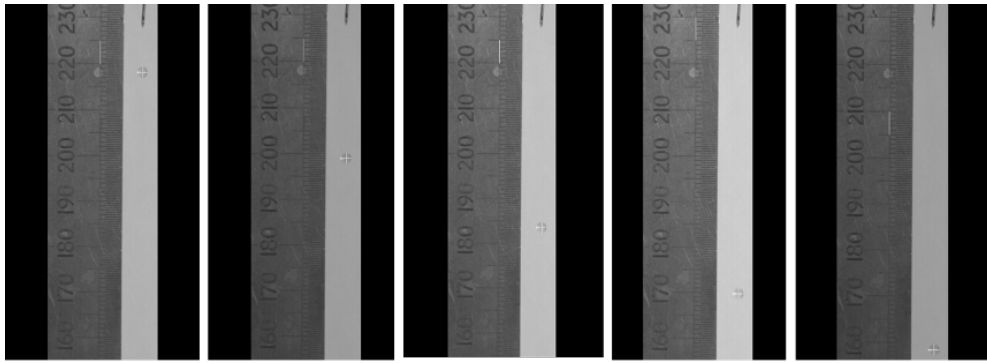


Figure 5.11: Falling droplet captured in high speed in order to evaluate its diameter

beside the control panel and has a tap connected to mains water in order to fill it up. There are four peristaltic pumps placed on the exterior of the rig, on the same elevation as the needles to negate head pressure, which pump water from this input tank and disperses the water through the needles via the plumbing. The pumps are controlled by four motor controllers, located on the control panel, to finely tune the rain rate to the desired level. Once the water had been ejected from the needles and used within the experimental rig, it is collected via a guttering system on the perimeter of the octagon, and it is funnelled to the guttering as the inside of the rig is effectively one large cone with the top peak in the middle to focus water away from the motor underneath. The water collected by the guttering system is then stored in an output 1000 litre tank which is connected to a drainage pump. This pump will turn on intermittently as necessary to drain the water in this tank when the water reaches a predetermined level and the feedback to control the pump is supplied by a float switch which is inserted into the drainage tank.

During the start-up tests where all the calibrations were made the rig itself was tested to ensure all systems were running smoothly. This was completed in a progressive manor, starting off at low rotational speeds and increasing it gradually with regular checks to ensure everything was performing as intended. To allow for easier inspection, all the critical bolts were marked in order to visually see if they had turned and therefore starting to become loose. The motor drive and inverter combination proved to

be a complex configuration and it was all software controlled. There was a few weeks delay in starting commissioning as the motor drive was not communicating correctly to the drive train and the safety measures were being triggered as it assumed there was a fault. This issue was resolved by modifying the software configuration to take cognisance of the geometry and weight distribution of the spinning mass. The start-up tests were run for five days, accumulating over ten hours of run time and they were continued until maximum rotational speed for the experiments was achieved and there was complete confidence in the operation of the rig.

During these run up tests there were two sets of accelerometers attached to the rig feeding information up to the control panel allowing for a vibrational analysis to be recorded and the acceleration, velocity, and displacement of the motor stand to be calculated. The data from the accelerometers was fed into the LabView program and it was presented in a real time output, the results showed very little movement, less than $2\mu m$. When experiments started the accelerometers were still operational and the outputs were continued to be shown in order to give more insight to the health of the rig. During the run up tests the accelerometers were placed in various positions to ensure there were no vibrations coming from unlikely sources. There were also two sets of accelerometers used feeding into separate devices in order to compare readings and justify the numerical result, this was successful as both systems produced the same result, confirming the readings.

The control panel seen in Figure 5.12 is where all the information is fed to from the rig and also where all the variables are controlled. The four water pumps are controlled by calibrated motor controllers as seen in Figure 5.12 On the right most screen is where all the data from the accelerometers is displayed. The top screen is a live video feed from four CCTV cameras placed around the rig in order to view the rig in operation, the cameras are placed as follows; one in the inside of the chamber looking at the spinning disc and the samples, one looking at the entrance stairs to the bunker on which the rig is situated, one located on the motor stand pointed at the main bearing and the last is

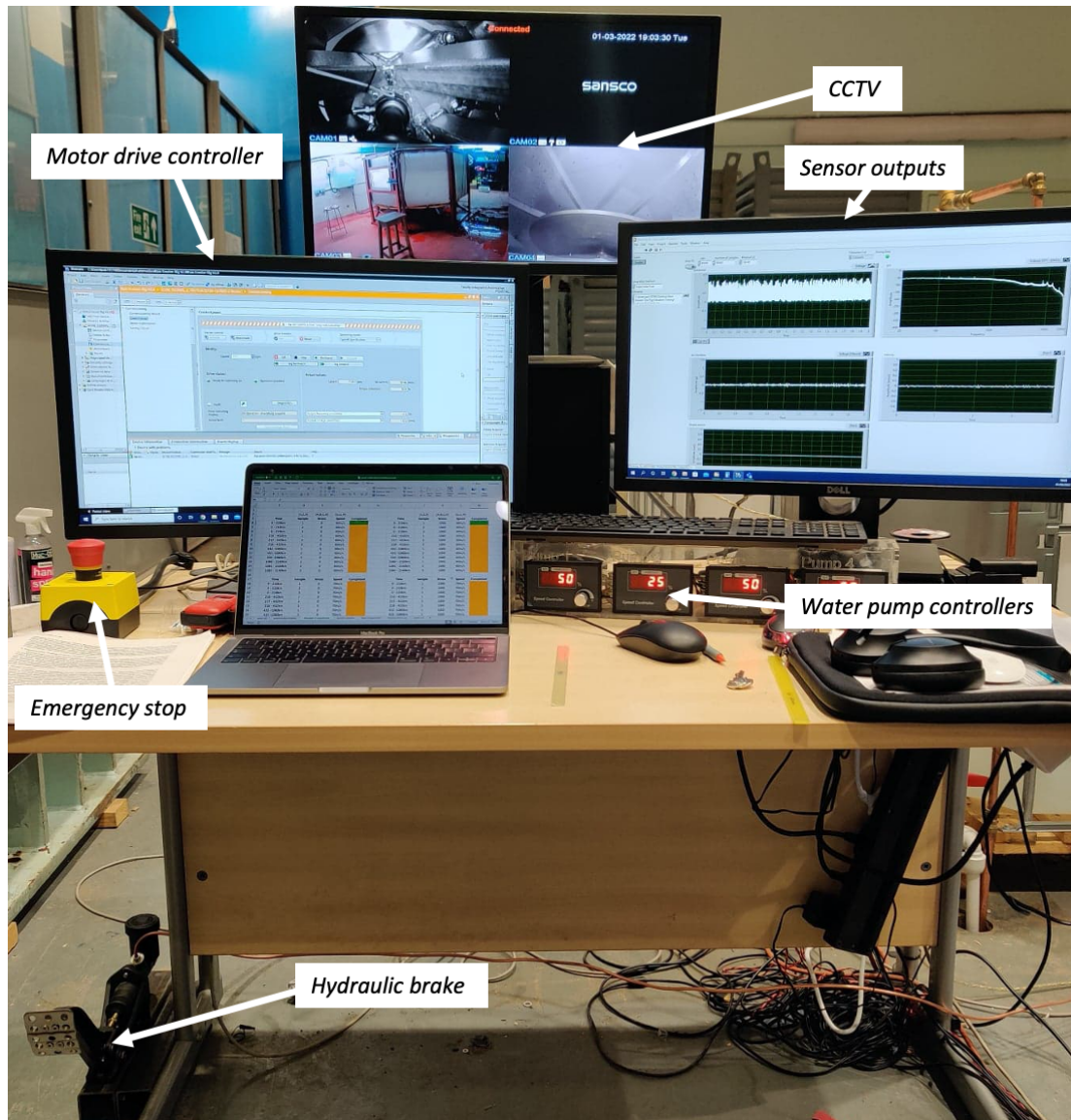


Figure 5.12: Control Panel for WAREER (Picture taken February 2022)

a general view of the outside of the rig. These perspectives are shown in Figure 5.13



Figure 5.13: Video feed from the CCTV cameras set up to monitor the WARER.(Picture taken February 2022)

5.6 Safe Operation

Prior to commissioning a detailed procedure and multiple risk assessments were produced and signed off by the relevant personnel. The risk mitigation includes the hydraulic brake and the emergency stop as annotated in Figure 5.12. As this rig has significant inertia energy due to it being a large mass spinning at high velocities there have been many measures implemented to mitigate the risk. These mitigation's include placing the rig in an underground bunker with 620mm thick concrete walls and everything being controlled remotely from outside the bunker. To make sure that no personnel enter the test bunker during operation mitigation's include two levels of interlocks, one is placed on the door of the rig and the other is on the gate at the top of the entrance stairs to the bunker if the gate is opened when the rig is on all power is cut to the inverter and the disc is brought to a stop. The second interlock on the door of the rig is a failsafe and works in the exact same way. As well as these interlocks which cut all power there is also an emergency stop on the control panel which is there to be activated if anything on-toward is observed on the CCTV or the feed from the

Chapter 5. Construction of Custom Rain Erosion Testing Facility

accelerometers becomes irregular. The hydraulic brake is actuated by a pedal on the floor, left of the control panel, and once pushed the disc comes to a stop within 3 seconds (determined by testing) which is only to be used in an emergency to stop further damage.

This project of designing, manufacturing, and commissioning this custom WAREER has been an extremely challenging and rewarding process. The end product was a successful and reliable test rig, capable of producing accurate results at parameters required for current and future wind turbine blades. Safety was a key consideration when designing the test rig, the outer shell of the WAREER was designed to contain the samples in the event of a failure and an emergency stop facility was implemented in the event of a failure. In addition the complete WAREER is located in a underground reinforced concrete test facility that effectively removes all personnel from danger when the tests are running.

Chapter 6

Leading Edge Erosion Analysis

The work in this section was peer reviewed and accepted for publication in the journal Renewable and Sustainable Energy Reviews "On analytical tools for assessing the raindrop erosion of wind turbine blades" K Pugh, JW Nash, G Reaburn, MM Stack, Renewable and Sustainable Energy Reviews 137, 110611, (2021)

6.1 Materials Characterisation

The impact event and subsequent erosion of a droplet hitting a surface is a problem which has been researched in great detail. Most of the recent studies which are based on the erosion on wind turbine blades use the model developed by Springer [71] and the calculations published in his book "Erosion by Liquid impact" [113]. The most used model is one which provides a relationship between the life estimation of a material, n , the material's strength, S , and the pressure from a droplet impact, P . The application of this model has been utilised and proven by Eisenberg et al. [114]. An alternative model has also been produced by Slot et al. [115, 116], which also provides a life estimation of a material subject to impact by droplets, however, this model was developed using a jet erosion rig where the incubation period could not be determined and allowed no time for the material to recover after a droplet impact. The area of interest within the material characterisation of rain erosion within the wind turbine blade application

is primarily coated and uncoated composites. The Springer model [71] has a broad applicability to materials that are ductile and agreement with some brittle materials. The model does, however, have limited application to materials such as elastomers due to their different material properties, therefore a separate approach would need to be utilised to study them. The Springer model [71] relates the number of impacts, material strength and pressure, these equations are outlined below for reference (see equations 6.1, 6.2, 6.3).

$$n_{ic} = 7x10^{-6} \left(\frac{S_{ec}}{\sigma_o} \right)^{5.7} \quad (6.1)$$

$$S_{ec} = \frac{4\sigma_{uc}(b_c - 1)}{(1 - 2\nu_c)(1 + k|\psi_{sc}|)} \quad (6.2)$$

$$P = \frac{\rho_L C_L V}{1 + \rho_L C_L / \rho_S C_S} \quad (6.3)$$

The equations stated here from Springer [71] apply to materials without coatings. Rain erosion is reliant on the material parameters and so the results of droplet impacts follow the same trends in material parameters. Equation (6.1) provides a value of the incubation period, the basis of the model is essentially the mass loss rate of the material over time and the main erosion rate is given when the material reaches the stage of steady state erosion, however the incubation period is also determined by the material properties such as strength and pressure parameters.

Equation (6.2) provides a value for a coating's strength in terms of rain erosion resistance. This, however, can only be used as a rough estimate as the materials used within this investigation are uncoated but within the industry this proves to be a useful tool as most turbine blades are coated in an elastomer material to reduce rain erosion.

Equation (6.3) provides a value for a coating's strength in terms of rain erosion resistance. As stated previously, the Springer model [71] was developed for ductile

materials, not elastomers and so the use of terms as the ultimate tensile strength, σ_{uc} , or endurance limit are not appropriate descriptors.

The combination of materials and coatings with different acoustic velocities and densities (usually combined into the term acoustic impedance, Z) can have synergistic effects, with the coating potentially becoming an amplifier for the stress wave in magnitude [117]. If the thickness of a coating is chosen incorrectly, it can lead to further problems in that it generates stress wave reflections, accelerating fatigue failure [118]. Note that the variable P has been exchanged for the variable σ^o in equation 6.1 to account for this and that the equation for strength includes the terms k , a variable relating to the stress wave reflections, and $\psi_s c$ which relates to acoustic impedance differences [113]. A further explanation of how exactly P and σ^o relate can be found in [113].

The impact pressure, P , is typically approximated using a modified form of the water hammer equation (see equation 6.3) [113, 115, 119]. The terms, ρ , C and V are the density, speed of sound, impact velocity, respectively, with the subscripts L for liquid and S for substrate. The acoustic velocity is dependent on the stiffness properties of a material, whose definition can be found in Springer [113]. This equation provides a reasonable approximation for most materials, but begins to diverge this equation for materials with particularly low stiffness properties upon which it underestimates the impact pressure. Elastomers such as polyurethane are an example of such materials and so the stiffness properties of a material or coating must be considered, as should their densities. It is important to note that the impact pressure cannot be accurately determined using this equation, only that it provides an estimation.

Whilst the model provides a good basis for rain erosion resistance, the influence of a number of parameters has not been mathematically deduced. These parameters include hardness, toughness, surface roughness, interfacial strength, with the addition of appropriate tensile and viscoelastic properties of elastomeric coatings. Some of these

materials also have a noted temperature sensitivity around their operational range, with thermal aging also having the potential to influence their behaviour [120–122]. The application of the Springer model [71] to a material and coating combination should either be linked to an appropriate temperature, with the respective material properties stated at that temperature or mathematical models of those material properties should be calculated and incorporated into the model.

Currently, there are standardised documentation for testing of various properties of rain erosion coatings [111, 123]. These documents describe the testing regimes that materials and coatings should undergo. Table 6.1 shows a number of test methods which are applicable.

Name of Test/ Equipment	Property Tested	ISO Test Standard	Source
Pull-off Test	Adhesive strength	ISO 4624	[111, 117, 124–126]
Peel Test	Adhesive strength and coating layer thickness	ISO 2808-2007	[111, 117]
DMA	Stiffness, storage modulus, loss modulus and glass transition temperature		[120, 122]
Nanoindentation	Hardness		[117, 127]
Tensile Test	Ultimate tensile strength, failure strain, max strain rate and Poisson's ratio	ISO 527 - 3	[111, 120, 122, 125]
Tensile Cyclic Loading	Fatigue performance		[122]
SENT	Fracture toughness	ISO 1183-1	[120]

Table 6.1: Outlining the preferred testing methods to obtain parameters that are relevant to rain erosion

6.1.1 Coating Adhesion Strength

A key indicator of coating performance is its ability to adhere to its substrate material. The 'Pull Off' test is the most widely used standardised method to test for coating adhesion [111, 117, 124–126], with its ease of use and proven applicability makes it the preferred choice of method. The peel test is another method, but is used to a lesser extent. It cannot be used for all material coatings, as the material must be flexible and so works better for tape type coatings [117]. There are reports of both the material flaking or breaking off in whole pieces during rain erosion testing and a concern of tape type coatings peeling away from the material, hence, both tests prove their validity.

6.1.2 Coating Layer Thickness

The coating layer thickness is significantly important, defects such as sagging or coating delamination can be caused due to incorrect coating thicknesses [128]. Therefore it is important to apply the correct coating layer thickness, for performance and minimise defects [113, 118].

6.1.3 Stiffness, Storage Modulus and Loss Modulus

In order to produce approximations for the impact pressure and evaluate the strength of a material (see eq. 6.3 and eq. 6.2), the acoustic impedance is necessary and can be calculated using the material's stiffness [113]. For materials with limited viscoelasticity, simple methods like tensile testing as outlined in [111] provide values for the elastic modulus. For strongly viscoelastic materials, however, stiffness properties are more complex and dependent on temperature, frequency and loading regime. Therefore, the storage modulus can be used [117]. The stiffness of viscoelastic materials can be described by three properties; the storage modulus (the amount of elastic energy stored by the material), the loss modulus (the amount of energy dissipated through heating and viscous losses) and the tan delta value (the ratio of loss modulus to storage modulus). The

importance of these parameters, with respect to their rain erosion performance has been investigated by O'Carroll et al. [127] using nanoindentation. These investigations established a negative correlation between storage modulus and rain erosion performance, but failed to do the same with loss modulus and rain erosion performance. Such approaches can only typically measure these stiffness properties at one frequency and temperature. For this reason, dynamic mechanical analysis (DMA) machines would be the most favoured method of testing LEP coatings. As mentioned above, several coatings of interest have temperature sensitivities around their operational range and so DMAs with their ability to run frequency and temperature sweeps are desired [120,122].

6.1.4 Hardness

Rain erosion testing on materials have provided information about the relationship between hardness and erosion rate. Different authors have claimed increasing hardness either improves or degrades rain erosion performance and there is conflict in the observed results. In metals, hardness appears to increase rain erosion resistance [129], but conversely the opposite appears to be true with respect to polymers as shown in Figure 6.1 [125,127]. This is likely to be related, at least in part, to the way in which a material responds to an indentation test. One possible reason is explained by Shaw and DeSalvo [130]. They state that solids should be divided into two different classes when considering hardness, one for metals and one for glasses and polymers. This is based on their stiffness to uni-axial compression flow stress ratio. Metals typically have much higher stiffness to flow stress values than glasses and polymers. So during indentation from a blunt indenter, glasses and polymers tend to distribute stresses in a more uniform manner over the indentation area, but metals typically produce Hertzian distributions.

The DIN EN 59 hardness test for coatings stated in the DNVGL standards documentation [111] for testing rain erosion protection coatings is designed for use with thicker coatings ($\geq 0.5\text{mm}$). Coatings used on wind turbine blades are known to be

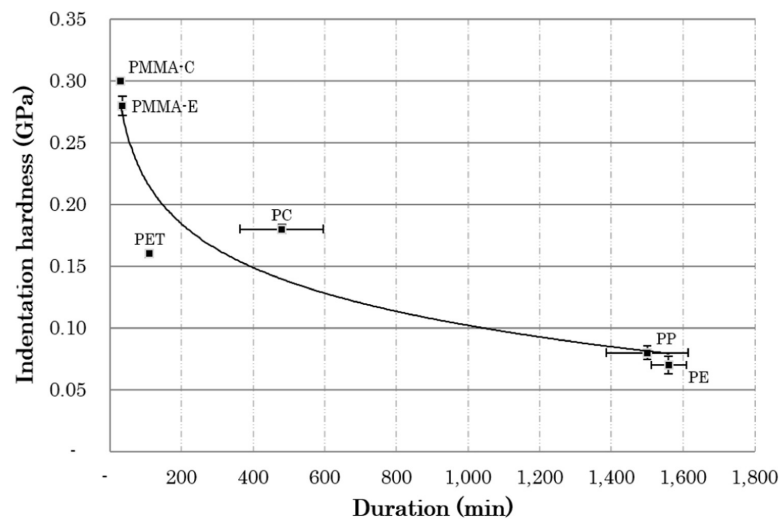


Figure 6.1: Hardness Vs. Rain Erosion Resistance of polymers. Figure from O'Carroll et al. [127].

thinner than this minimum thickness and thin films often display different properties to that of the bulk material as the close proximity to the interface can influence the result, so more appropriate testing regimes have been sought after [117]. Recent studies have shown the potential of nanoindentation testing, with its favourable applicability to thin samples ($\leq 0.5\text{mm}$), like those used in the multi-layer coating systems for wind turbine blades [117, 127, 131].

6.1.5 Tensile Properties

The tensile properties can be found using the standard tensile test outlined in ISO 527-3, using specimen type 2 for flexible materials. As the strength model outlined by Springer [113] is intended for ductile materials, it is of value to investigate other properties aside from those outlined in the model. Elastomeric materials typically fail when exceeding a strain rate higher than the material can withstand or an elongation higher than the material can accept [115, 120, 122, 125]. More appropriate parameters may therefore be used to describe the material's strength, S . Tensile-tensile cyclic loading testing should also be used to produce the Wohler curve as is necessary for the Springer model [71], as seen in [122].

6.1.6 Damage Resistance

For materials to be resistant to rain erosion, their ability to resist damage initiation and limit its propagation should be important factors. The importance of fracture toughness in the literature reviews of Keegan et al. [119] and Gouhardani [132] is the relation of fracture toughness to the damage evolution in the rain erosion phenomenon. Springer [113] speculated that fracture toughness would influence rain erosion performance, which has been supported by Busch et al. [110] with their investigation into the notch sensitivity of various polymers and rain erosion. Previous work by Evans et al., sought to relate the erosion of brittle materials from solid projectiles to their fracture toughness with good agreement (see equation 6.4) [133]. Keegan [119] used this equation to show the significant effect this could have on epoxy coatings with different fracture toughnesses as shown in Figure 6.2. Zhang et al. [125] investigated the impact resistance of various coatings and their rain erosion performance; however, the experimental work in this regard was limited and a fracture toughness value was not produced. The results showed that the coating with a poor rain erosion performance also failed during the impact test by detaching from the surface, compared with the two that performed significantly better in both. Another damage resistance characteristic investigated by Zhang et al. was the abrasion resistance, which showed a correlation in abrasion resistance and rain erosion resistance. This indicates that the abrasion and erosion process may follow similar trends, and therefore could occur through the same or similar mechanisms.

$$V_{DT} \approx 1.41 \left(\frac{K_{IC}^2 c_R}{\rho_w^2 c_w^2 d_w} \right)^{1/3} \quad (6.4)$$

V_{DT} is the damage threshold velocity, above which the material damage will occur. The definition of this damage is not stated. K_{IC} is the fracture toughness, c_R is the Rayleigh wave velocity, ρ_w is the density of water, c_w is the speed of sound in water and d_w is the droplet diameter.

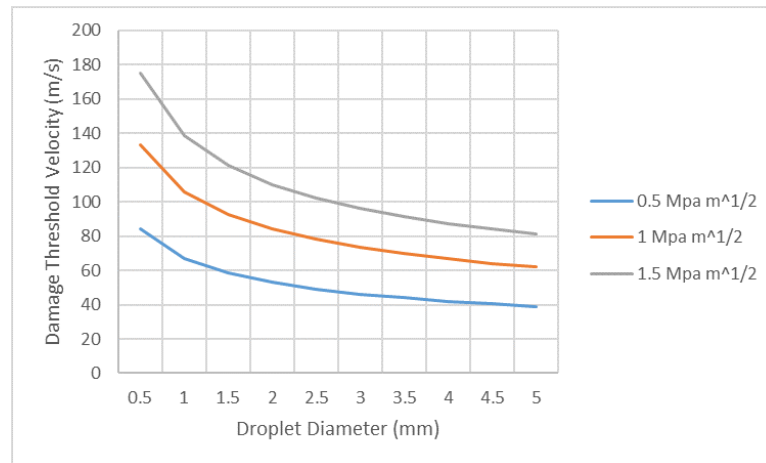


Figure 6.2: Damage Threshold Velocity (DVT) Vs. droplet diameter using 6.4 from [133] for epoxy coatings with different fracture toughnesses. Figure adapted from [119]. Rayleigh wave velocity, $c_R = 942 \text{ m s}^{-1}$, Density of water, $\rho_w = 1000 \text{ kg/m}^3$, Speed of sound in water, $c_w = 1490 \text{ m s}^{-1}$.

The link between damage resistance characteristics and rain erosion isn't clear with the limited data available, and so the selection of an appropriate toughness parameter is not currently possible. During rain erosion, a material or coating is continuously attacked from one side. Damage can be initiated through direct failure, surface fatigue or through the presence of a defect. In the majority of situations, failure develops from the exposed side of the coating or material. Fracture toughness analysis should therefore use single edge notch tensile (SENT) testing (see [120]). Currently the most appropriate methodology utilises to the use of bulk materials testing regimes. Rain erosion in itself is not a steady state or quasi static situation, it involves the repeated impulses from droplet impacts. As a result cyclic or transient testing format would be most applicable.

6.2 Surface Analysis

Surface analysis is a key subject in assessing erosion damage. There are many techniques that can be utilised in surface analysis depending on the scale of the subject. For liquid impact erosion the test samples are usually inspected on the micro scale.

During analysis the features that are of interest include pits, gouges and delamination.

Due to the various analytical techniques available in surface analysis many studies will use multiple techniques in order to confirm their results or to obtain a different perspective with a different analytical tool. This allows for direct comparison between methodologies and an insight on tools that are used conjunction with each other.

6.2.1 Optical

Generally the first step of any surface analysis is optical examination, optical analysis has a greater variance in equipment. Optical analysis can include anything from close visual examination in the field all the way to microscope images taken in the laboratory. Optical examination provides qualitative assessment of the surface of the material. It will likely detect larger scratches and groves, however, details relating to surface roughness and smaller defects may be missed. This method of analysis is limited due to the small depth of field and is reliant on the skill and ability of the operator [134].

A common method of recording erosion is conventional photography with little or no magnification [52,108,119,124,135–137] as this is a repeatable method, however, the level of detail captured is minimal. This type of recording data is useful for comparing experimental data to the pictures captured within the field as the images recorded from services teams are unable to conduct high detail scans due to availability. The images however only show large features once the blade has undergone considerable erosion, it would be impossible to detect the microscopic pitting from the initial stages of erosion using this method.

For laboratory analysis a high magnification optical microscope can be used to detect all the stages of erosion of GFRP. It can also be repeated during the experiment as the sample requires no treatment in order to be analysed, this allows for the progression of erosion to be recorded on a single sample at different stages of the experiment.

This is desirable as the rate and mechanisms of erosion are more likely observed and measured. This methodology has been used by Zhang [125] to see the progression of erosion between two coatings for wind turbine blades. The results show two different mechanisms of erosion, one being a failure of the epoxy matrix and the other by defects which caused cracks and loss of material.

Optical analysis can be used in conjunction with SEM analysis as observed in the literature [138,139]this allows for a direct comparison between the two types of surface analysis. In a recent study [138] which examined the effect of stress on the material while being subject to rain erosion, the topography analysis used both SEM and an optical microscope. The two images presented different features. The SEM images showed the fibres in high detail and the loss of material whereas the optical microscope displayed the deformation of the top epoxy layer which was missed in the SEM. This could have been user error however, it is more likely due to the lighting angle accentuating the undulations. Another study which compared SEM and optical microscope images directly is research carried out by Thomason [139]. This research investigated natural fibres and obtained images from the SEM and optical microscope both in the same magnification observing the same feature. Having such images creates an opportunity to accurately compare the detail obtained from both pieces of equipment. The results show more detail from the SEM. It could be argued, however, that some features are more clearly observed from the optical microscope as shown in Figure 6.3.

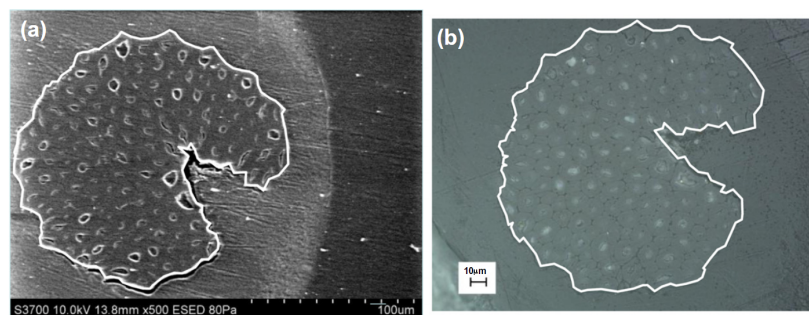


Figure 6.3: Comparison between SEM imaging and Optical imaging [139]

6.2.2 Scanning Electron Microscope (SEM)

The SEM (Figure 6.4) is a common analytical tool for assessing morphological features on a surface. To be able to analyse glass fibres, which is the most commonly used material for constructing wind turbine blades, the sample requires gold plating in order to obtain an image. This is to create a conductive surface for the flow of electrons. The images obtained from analysing GFRP can range from a low magnification in order to observe pits in the surface (Figure 6.5) [93] which could be seen by the human eye to a very high magnification in order to observe the surface texture of a single glass fibre (Figure 6.6). This large range in magnification is achieved without a loss in depth of field thus allowing many of the features obtained during rain erosion to be analysed by one machine in one operation.

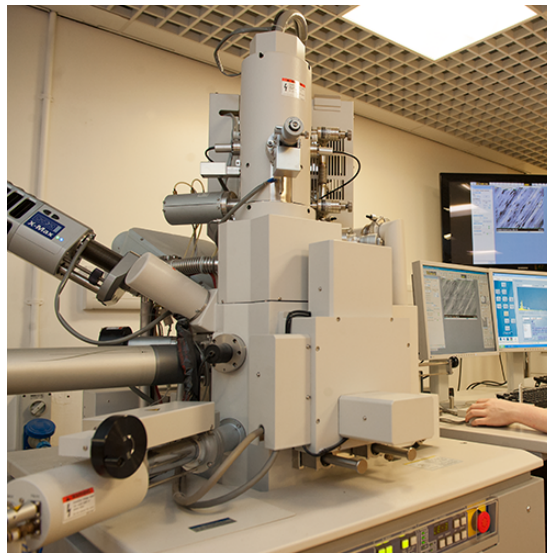


Figure 6.4: SEM at the University of Strathclyde within the Advanced Materials Research Laboratory [140]

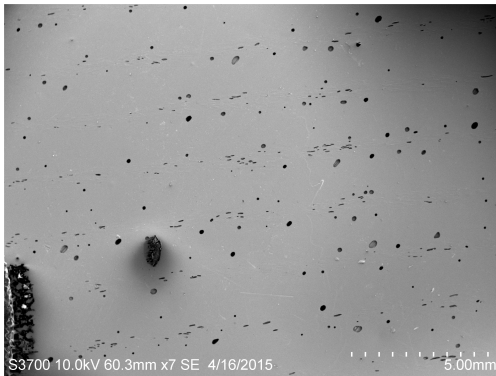


Figure 6.5: SEM image of pinholes on GFRP [93]

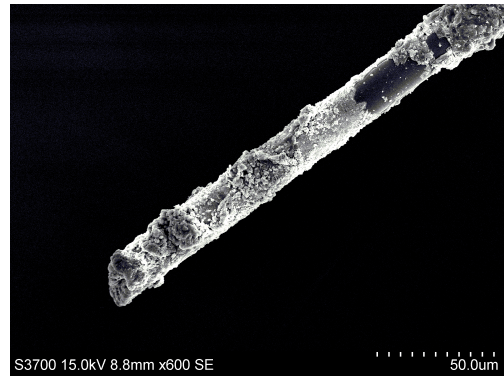


Figure 6.6: SEM image of glass fibre [138]

SEM analysis whilst a powerful tool may present some issues. Confusion can occur when the image is misleading creating an optical illusion. This can lead to the uncertainty between peaks and troughs.

When investigating the erosion of metals using a SEM the sample can be analysed without a gold coating allowing the different stages throughout testing to be analysed as the surface is already conductive. This method has been used to visualise the surface damage at different known number of impacts [141]. This is not possible when investigating the erosion of GFRP as the required gold plating would affect the subsequent exposures. This means that the analysis is only applicable at the end of the investigation, this is very common within studies [93, 134, 142–144]. Arguably this is the biggest issue with SEM analysis as the information which is gathered during the investigation is of great importance as it can help identify the process of erosion. For the specific investigation of erosion of wind turbine blades where the blades are mainly manufactured from GFRP the SEM analysis serves as a perfect tool for an end of investigation analysis however for investigating the rate of erosion there are more appropriate tools.

6.2.3 Profilometer Analysis

One form of topography analysis which is becoming more prevalent for the inspection of eroded samples is the use of a profilometer to image and also measure the material surface. This is a form of measurement device that evaluates the changes in surface height on a very small scale and outlines a profile. From these measurements an image can be created illustrating the topography. From the literature there are two variants of profilometer; stylus, that uses a tactile probe that physically moves along the surface as shown in Figure 6.7 and optical, which is a device that uses a laser to scan the surface as shown in Figure 6.8. These devices are designed to quantify the surface roughness of a material which is essential when investigating the erosion of wind turbine blades as it can help determine the aerodynamic efficiency of the blade and hence the overall efficiency of the turbine.



Figure 6.7: Stylus profilometer [138]

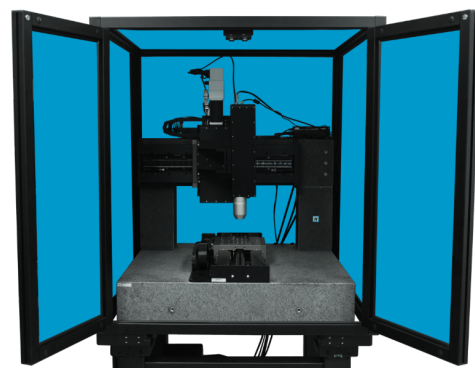


Figure 6.8: Optical profilometer [93]

The Stylus profilometer is not as commonly used for measuring rain erosion. This could be due to the reduced resolution, however, it would be useful for larger samples

including a leading edge of a blade as the Co-ordinate Measuring Machine (CMM) has a larger range of depth it can scan within one analysis. This is due to the CMM not being restricted by the field of view limit that exists in the Confocal Laser Scanning Microscope (CLSM) due to the use of lenses.

The technology behind the CLSM has developed significantly since its inception in the mid-1970s [145]. The use within tribology research has becoming more prevalent. The features of this type of analysis are ideal when investigating micro level defects on a materials surface and the effect that the surface morphology has on the roughness and hence the drag. Figure 6.9 is a CLSM scan of a sample used in [134] subject to salt water erosion, this Figure describes the surface profile in a 3D image that can be used to evaluate the distance between the highest trough to the deepest groove.

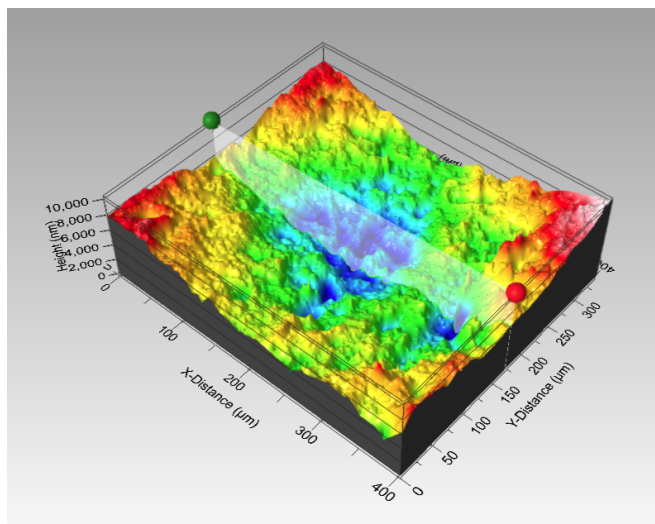


Figure 6.9: CLSM scan of sample subject to salt water erosion [139]

Recent research has used this technology to look into the topic of rain erosion on wind turbine blades [92,108,135,146]. In Tobin's recent work he studied the incubation period in rain erosion using a CLSM. In the investigation scans of the material were carried out at different time stages which allowed for various measurements to be taken during the investigation, this includes parameters describing the surface roughness and

mass loss [146].

6.3 Subsurface analysis

When considering rain erosion, little attention has been given to the presence of subsurface features or damage initiation inside the coating layers. The presence of defects in composites, such as voids or porosity has been widely documented [124, 147–149]. When single and multi layer coating systems are then introduced onto composite manufacture, this presents further possible sites for defects to exist [128]. Given the size of wind turbine blades, manufacturing defects such as these are relatively common. With the difficulty of detection and considering the cost of discarding blades with defects or coating defects, especially as coatings are non structural, subsurface defects are likely to be present on blades.

During rain erosion testing, subsurface defects are one possible reason for inconsistent results, in situations where there appears to be a smooth and otherwise good surface [125, 150]. There are two reasons as to why defects are of concern; firstly is their ability to affect material/ coating performance and secondly, their ability to cause stress wave reflections. The defect size of interest, that are likely to lead to interfacial failure are those that are of comparable size to the coating layer thickness and larger [151]. The defect size of interest with respect to stress wave reflections is dependent on the wavelength of stress waves emitted during impact. Acoustic waves only interact with defects of comparable size to their wavelength and larger. In ultrasound Non-Destructive Testing (NDT), to obtain good wave reflections to allow defect detection, the defect should be at least about half of the wave length of the frequency used [152]. Although it is currently not possible to measure the wave length of the wave emitted through the coating during droplet impacts, the time period of the waves generated will be related to the impact velocity. Higher velocity impacts should cause higher coating particle velocity during impact, which would generate higher frequency waves inside the material. This would lead to smaller wave lengths and so will therefore

interact with smaller defects. The penetration of acoustic wave reduces with increased frequency. Therefore, smaller defects will likely only influence damage propagation due to reflections close to the surface, but as distance increases only larger defects will likely be of importance.

This topic is yet to be fully investigated, so the true influence is currently limited. The ability of different methods to detect various defect types will be discussed, with comments on the considerations for designing a test setup and some other considerations will be addressed. The aim of this discussion is to provide some insight into the available methods of imaging defects within coated composites. The methods found to be applicable fall into three main categories; ultrasound, radiology and microwave methods.

6.3.1 Ultrasound

Ultrasound is one of the most common NDT methods, with its application widespread. It works on the basis of generating mechanical vibrations within a material, typically propagated in compressive or shear wave form through the material. When these waves come to interfaces between materials of differing acoustic impedances, liquids or gases, they are reflected back and the signal is received and processed. There are two possible configurations; the first is a combined transmitter and receiver probe, called transceiver and the second is a separate transmitter and receiver probe. The data is typically generated into B- and C-scan forms, which produces cross sectional views of the specimen and plan views, respectively.

With modern developments of phased array probes, robotic scanning arms or gantry systems and computers 3D scans of samples can be generated. Due to inherent limitations with the near field effect in contact probes, they cannot be used for thin samples like those used in rain erosion testing. It could be possible to use an immersion probe, which would require submerging the whole or part of uneroded and eroded components

into water. This may not be feasible to do as submerging components in water for periods of time may affect the material's properties through absorption.

An alternative method would be to use a laser ultrasound generation method. This method has been shown to work and achieve reasonable results in carbon fibre composites, but has yet to be investigated for GFRP [153,154]. This method would enable eroded specimens to be analysed without immersion inside a tank, but importantly the laser impulse on the surface could effect the material properties of any particularly temperature sensitive materials.

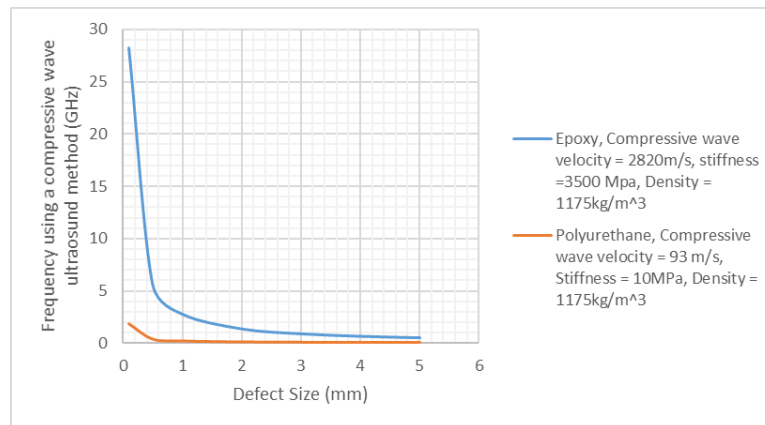


Figure 6.10: Displayed here is a graph showing defect size vs. approximate frequency required to detect it. Materials data was sourced from Slot et al. [115]. Wave speed was calculated using the equation provided by Springer [113]. Frequency was calculated using the standard wave equation $c = \lambda f$, where c is the speed of sound, f is the frequency and λ is the wavelength.

To achieve a high resolution, it will be necessary to use high frequency ultrasound as shown in Figure 6.10. It's likely that a scanning rig would need to be set up to automate the inspection of the specimens and produce a 3D model of the subsurface. The exact form of data that will be collected will still need to be determined, both pulse echo and time of flight diffraction have their individual merits and it appears possible to collect both and use them in a complimentary fashion. The exact frequency selected will be dependent on the materials tested. The main benefit of using ultrasound would

be that the price would be significantly less than X-ray [152, 155]. One of the main concerns surrounding ultrasound and its use in testing composite components is due to the high attenuation, caused by scattering from the fibres [156]. It can also be difficult distinguishing between the initial impulse and reflections caused by defects in thin samples [153].

6.3.2 Radiology

Radiology methods are desirable with their significantly higher resolving power, they can provide a much higher level of detail (individual fibres) than other techniques. There are a few different methods for radiology: gamma radiology, x-ray radiology and neutron radiology (although this is different in operational principle). Gamma radiology and x-ray radiology follow the same principles, but their difference is the source of photon energy and how it is generated. They operate on the principle of irradiating a sample, with different materials and defects having different absorption properties. The transmitted radiation is then detected electronically rather than film used previously. The result is a 2D image of the specimen and so the orientation of the component can be key in detecting defects. The absorption of a material is dependent on the density of the specimen and its thickness [155, 157]. This presents a problem for polymeric materials, due to their low density, which gives a poor contrast [156]. With the development of computers, computed tomography has become available allowing a series of 2D X-ray images to be compiled into 3D scans which can help to reduce problems with orienting the specimen properly. Although this is desirable in most cases, X-ray imaging begins to become very costly and is also a slow process. In addition health and safety precautions are necessary when utilising radiology examining techniques [148, 155–157].

6.3.3 Microwave Imaging

Microwave imaging relies on passing microwaves through a specimen using a transducer and receiving the signal either in the sample probe, or using a separate probe.

Microwaves are reflected at interfaces between materials with different dielectric properties. It therefore has significant potential in the testing for defects in polymer coated composites. It has advantages over traditional inspection techniques such as x-ray, being that it is significantly cheaper and safer. In addition it can detect stacked defects within samples. It is well suited to testing of high porosity composites (>2%) and less attenuation occurs whilst scanning GFRP composites, which typically make Ultrasound methods challenging. Currently, defects of approximately 1.5mm in diameter and a thickness of 0.5mm can be detected. The technology is relatively immature and is currently being developed at the National Physics Laboratory and other institutions. It's main application is the investigation of butt welds in high density polyethylene (HDPE) pipes and as well as some composite components [158–160]. It should be noted that microwave NDT cannot be used to image carbon fibre or graphite composites, due to the carbon fibre's high conductivity which attenuates most of the microwave signal. Air-gaps of 0.25mm are also possible to image (ideally larger at 0.4mm), which essentially constitute delaminations. Disbonds of 0.03mm can be imaged. Microwave NDT can also provide information on the state of cure as well as moisture ingress as shown in Table 6.2 [156].

Layer	Relative complex permittivity	Thickness (mm)	Estimated thickness (mm)
Rubber	4.80 - j0.17	3.175	
Teflon	2.00 - j6E-4	0.381	0.385
Rubber	5.31 - j0.22	6.350	
Teflon	2.00 - j6E-4	0.508	0.518
Rubber	4.80 - j0.17	3.175	

Table 6.2: Thin sandwich structures of Teflon and rubber have been imaged, alternating in material to mimic delamination. The layers of Teflon were estimated using microwave imaging techniques respectively. Adapted from [156].

6.4 Standardised Methods for Assessing Damage

6.4.1 Mass and Volume loss Analysis

The most common characterisation of wear and erosion, and in most cases the easiest to measure, is mass loss. This is achieved by comparing the mass of the sample before and after testing. This methodology has been used in many research papers examining the erosion of wind turbine blade materials [52,71,92–94,110,117,124,134,135,138,146,161]. The measurement of mass loss is a valuable but simplistic parameter as it does not describe the erosion mechanisms in any detail, however it does allow for a direct comparison between investigations.

The mass loss is displayed differently within different investigations ranging from a table of results [137] to wear maps [134,138]. The most common format is a cumulative mass loss line graph as shown in Figure 6.11 [52,92–94,113,146], this displays the mass loss of the sample at different periods during testing. When the information is displayed in such a way the rate of erosion becomes more apparent and the stages in which the material degrades can be observed.

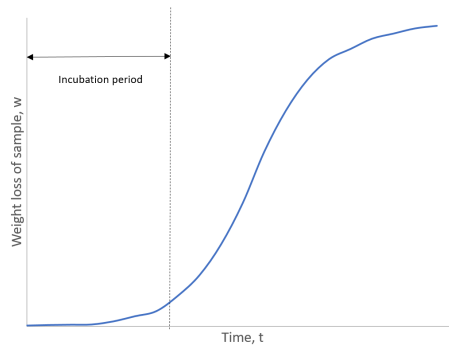


Figure 6.11: Line graph displaying weight loss against time [113]

If the investigation is testing more than one range of variables an appropriate way to display the mass loss information would be through a wear map. For example if the investigation is examining impact angle and impact velocity as previously conducted

in testing [138] the mass loss results are set in a matrix form to produce a wear map (Figure 6.12).

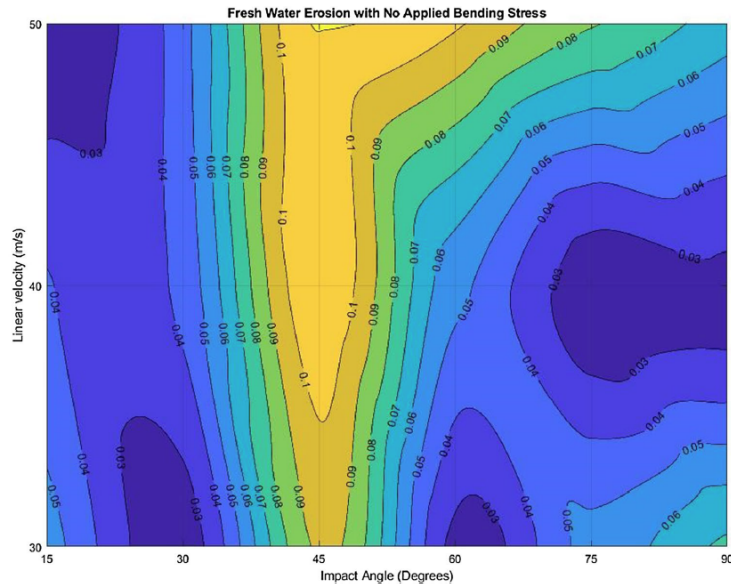


Figure 6.12: Wear-map showing mass loss with respect to impact velocity and angle [138].

Due to the relatively simplistic nature of mass loss analysis in terms of measuring erosion it is almost always accompanied by surface analysis to determine the mechanisms of erosion and also to pin point the locations of mass loss to confirm and explain the results. The accompanying analysis can also be from a profilometer, if a scan of the sample is taken before and after testing the volume loss can be measured. With this technology it is possible to locate exactly the points where material was lost and the severity. This analysis is useful when testing new materials for wind turbine blades and understanding their vulnerable aspects.

6.4.2 Surface Roughness

Surface roughness has been a parameter investigated thoroughly. An early study by Boermans and Selen [162] was carried out on sailplanes where adhesive backed polyester

film was wrapped around the wings to collect insects during flight. These insects were then removed from the sailplane and inserted onto a test aerofoil in a wind tunnel to test the changed aerodynamic properties of the compromised wing that would now have a different surface roughness.

When investigating the erosion on wind turbine blade materials a measurement of surface roughness is required in order to evaluate the change in surface parameters [163, 164]. The way in which surface roughness is classified is by measuring the variation in height on the samples surface including the depth of pits which form during erosion. This measurement can be taken by a profilometer as mentioned before in the previous section. This parameter can help define the aerodynamic properties of the material if it were to be used in a wind turbine blade. The development of surface roughness initiated by erosion can provide a good indication of the more resistant materials to rain erosion.

In recent studies [165] the effect of increased surface roughness from erosion on the leading edge was studied by examining the lift coefficient of various aerofoils at three stages of surface roughness. This provided practical data that can be transferred to the output efficiency of a turbine generator. In a study by Pechlivanoglou [166] the initial surface roughness of a newly manufactured blade was observed and it was evident that prior to the blade being commissioned it has a substantially rough surface. This can result in multiple initiation points for erosion, and within this study sand build up. Overall surface roughness provides quantified information on the surface imperfections and can be used to measure the development of pits, gauges and cracks within the material and after erosion. The measurements can be carried out at different stages of experimentation and can provide rates of evolution.

6.5 Discussion and Conclusions

During rain erosion testing it is critical that material properties are systematically documented in order to examine the rain erosion resistance of a material. The preferred methods of testing material properties have been outlined here (See table 6.1).

In this review, possible methods available for the subsurface analysis of rain erosion protection coatings and wind turbine blade materials used during rain erosion testing have been investigated. This work has revealed that X-ray scans have the ability to provide detailed information, however, the cost is relatively high and there is the health and safety considerations. It's also possible that due to the low density of polymeric materials, the contrast of any image may be limited and so the distinction of defects may prove difficult. Ultrasound may provide a possibility for imaging using immersion techniques and high frequencies, but submerging the samples may not be possible. It may also prove difficult to image samples due to the complexity of the composite structure causing attenuation and noise and imaging stacked defects may not be possible. Microwave methods have shown potential, but their application has been limited and still in the development stage. Individuals seeking to investigate the phenomenon further should test these methods in a comparative manner and critically assess the application and results of each.

The technology of surface analysis is evolving producing new and exciting techniques for describing, analysing and evaluating a materials surface. It is clear from the literature that it is beneficial to utilise multiple analytical tools in evaluating a sample. These can work in harmony to accurately define the surface parameters and monitor the changes when subjected to erosion. When investigating rain erosion on wind turbine blades, which primarily relates to the erosion of GFRP material a profilometer is a key technique to provide analytical information as it produces quantified data of the samples coupled detailed images. In a research project it would be appropriate to combine this analysis with another form of analysis such as SEM or optical to provide

Chapter 6. Leading Edge Erosion Analysis

additional information and confirm results. Coupling the profilometer and SEM/optical with the established mass loss data provides the key features for an investigation, these are the magnitude of the wear/erosion (from mass loss) the location and extent (from profilometer) and the identification of the relevant features (from SEM and optical).

Chapter 7

Computational Blade Stress Analysis

In order to investigate the physical effects on wind turbine blades an analysis of the stresses was conducted. Wind turbine blades have developed significantly over the last 15 years. In their paper Schubel and Crossely [167] state that the optimal shape for a turbine blade is complex in its nature with decreasing width, twist, and thickness from the root to tip sections along the blade's length. They also highlight the conflicting design parameters of the structural thickness and aerodynamic slenderness. From aerofoil lift and drag performance values they demonstrate it is possible to optimise the blades performance.

7.1 Wind Turbine Shape and Performance Analysis

In order to optimise blade design CFD is increasingly utilised to predict performance. This method is used to evaluate the reaction of the blade in contact with a fluid and has gained more popularity in recent years with increased computing power. It does still necessitate a high computational cost, with run times taking more than 2 days (at times) and also limited success in convergence has been reported.

In the past, general aviation aerofoil sections such as the NACA four- and six-digit light aircraft aerofoils were used in the 1980's and 1990's for wind turbine blade designs. They are also still found today in some wind turbine blades, however, this choice of aerofoil does have some limitations for this application. This is primarily thicker sections required closer to the blade root experience premature boundary layer transition from laminar to turbulent flow causing significant drops in performance [167].

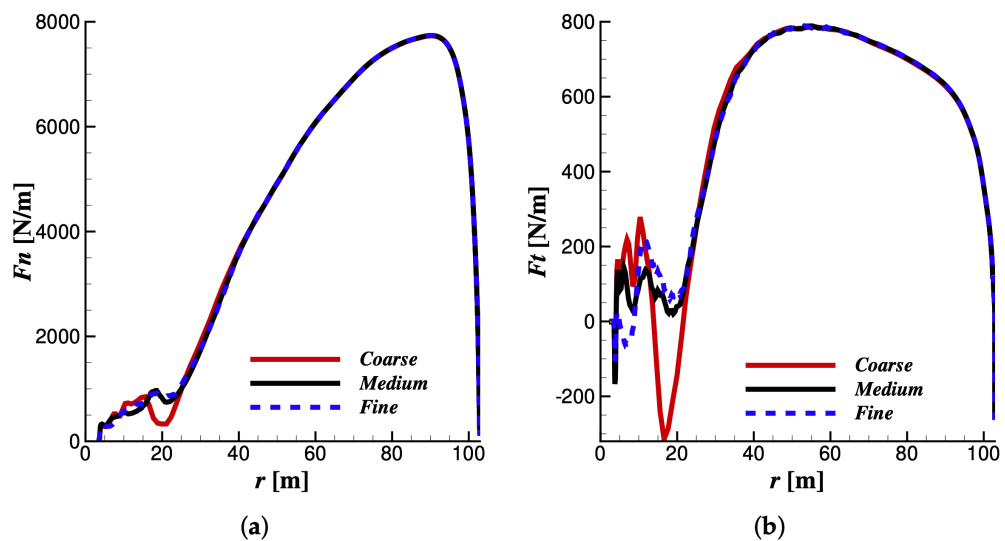


Figure 7.1: Typical wind loading on a wind turbine blade root to tip for a rotating scenario ignoring gravitational effects calculated using a CFD approach comparing different mesh refinement density in the (a) Axial and (b) Tangential directions [168]

With the wind turbine blade's shape being the main driver in its aerodynamic performance it is important it is fully optimised. Resultantly, the structure and materials used in turbine blade design are tailored to this shape. It is also important to minimise blade mass and the resulting blade loading due to the weight force whilst ensuring sufficient structural rigidity so that blades can withstand normal and extreme operational loading. Figure 7.1 shows typical wind loading on a wind turbine blade root to tip for a rotating scenario ignoring gravitational effects.

7.1.1 Aerofoil characteristics and Element Theory

An aerofoil is a complex geometric shape that has been refined through wind tunnel testing to provide optimal lift and drag coefficients. Airflow meets the aerofoil from the front and splits passing over the upper and lower surfaces. In doing so it imparts its momentum on the blade and creates a pressure difference. These two combined effects push and suck the aerofoil in the direction of a generated lift force (perpendicular to the incoming airflow).

For a wind turbine blade the angle at which the airflow meets the blades aerofoils cross section is usually very high. This high inflow angle of air is brought about from the rotational velocity and air wind flow over the blade becoming a vector velocity addition as depicted in Figure 7.2.

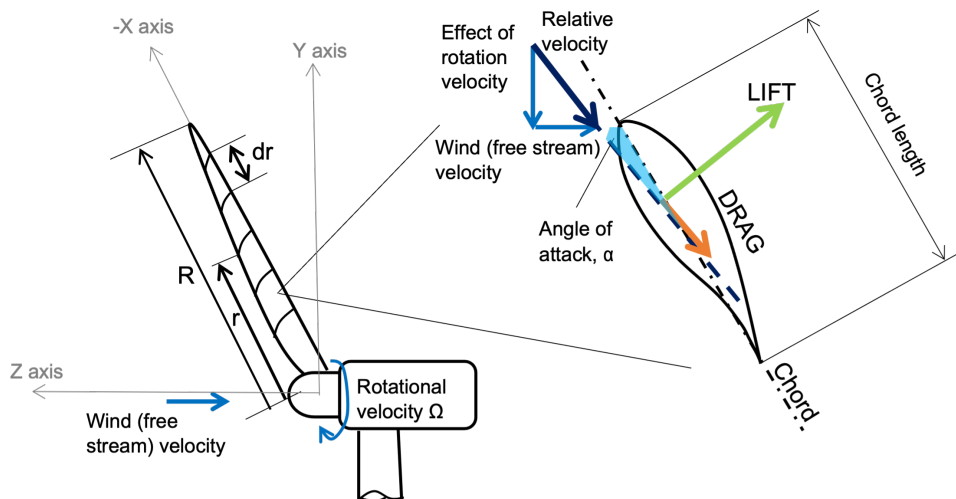


Figure 7.2: Turbine blade split up into elements dr , and details of the aerofoil basic characteristics at each element along the blade length R visually allowing the high angle of attack at which wind turbine blades are set to be observed.

As the shape and angle of impact changes along the length of the blade, in order to assess the effects the blade has been split into several sections with an aerofoil cross section at different points, r , along the length of the blade, R , with thickness dr . Relating this to the aerofoil characteristics the torque and thrust force at each section are

defined as components of the aerofoil elements lift and drag forces.

For the purposes of this evaluation it has been assumed that there is no aerodynamic interaction between elements and that the forces on the blades are solely determined through the lift and drag characteristics at that element.

Using the torque and thrust forces the forces in the y- and z-axes on the blade (dF_T and dF_N) are defined. Equations 7.1 and 7.2 show how the torque and thrust forces simplify by inclusion of the axial and tangential induction factors a and a' .

$$dT = \rho U^2 4a(1 - a)\pi dr \quad (7.1)$$

$$dQ = 4a'(1 - a)\rho U \pi r^3 \Omega dr \quad (7.2)$$

By considering Figure 7.2 the setting angle of the blade, ϕ , is defined and the twist angle of the blade θ_T calculated from this value. Initially it is assumed that the twist angle accounts for the pitch angle ($\theta_P = \theta$).

$$\Theta_T = \varphi - \Theta_P - \alpha \quad (7.3)$$

$$\varphi = \frac{2}{3} \tan^{-1} \left(\frac{1}{\lambda_r} \right) \quad (7.4)$$

$$c = \frac{8\pi r}{BC_l} (1 - \cos\varphi) \quad (7.5)$$

7.1.2 Finalised Blade Geometry

A blade geometry was created based on the aerofoil distribution developed by Tang et al [169] [170] who used the DU93-W-210 (base aerofoil with 21% thickness to chord ratio) with differing values of thickness to chord ratio along the blade length however no blade twist was implemented. To obtain the optimal shape in terms of structure and

aerodynamics a thick root cross section and thin tip cross section is desirable. Hence the aerofoils were distributed from a circular section at the root to the thinnest aerofoil (18% thickness to chord ratio) at the blade tip as shown in Figure 7.4. Figure 7.3 shows the experimental aerofoil data which combined with literature [169,170] determined the optimal angle of attack to be set at 8° with a lift coefficient of 1.35, any greater than this the lift coefficient becomes independent from the angle of attack Reynolds number is a critical factor which influences flow characteristics and hence performance of wind turbine blades. Mingwei et al has studied 1.5 to 3MW designs and the influence of the Reynolds number in optimising the design [171]. As the angle of attack increases the lift coefficient increases until stall, the stall angle increases with Reynolds number which means. This work by Mingwei et al has reported that the maximum Cl/Cd increases rapidly up to Reynolds number $2E6$ and beyond this point increases at a slower rate, indicating the point of Reynolds independence

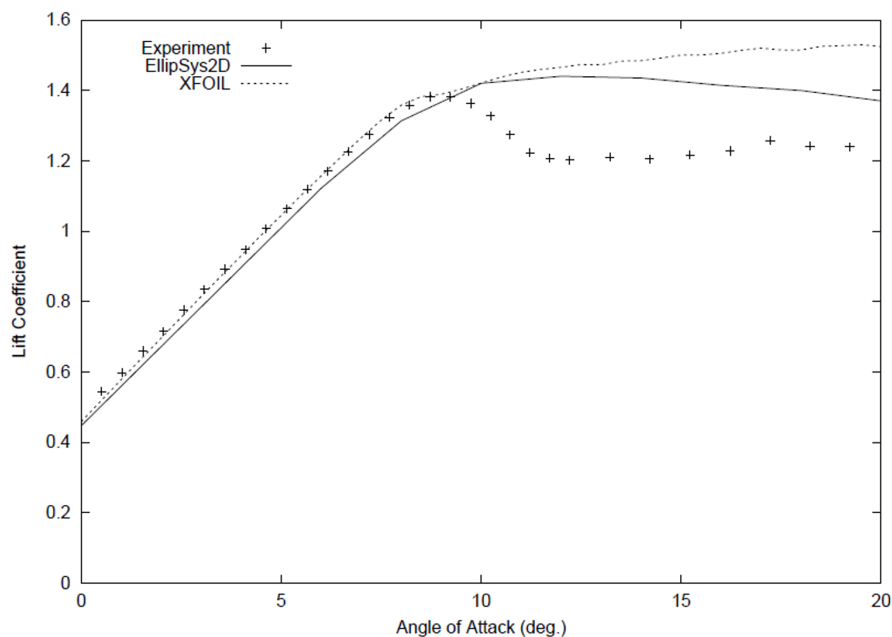


Figure 7.3: Lift coefficient against angle of attack for the Du93-W-210 aerofoil as obtained through computational and experimental data [172]

With the aerofoils set, the other design aspects were determined from previous

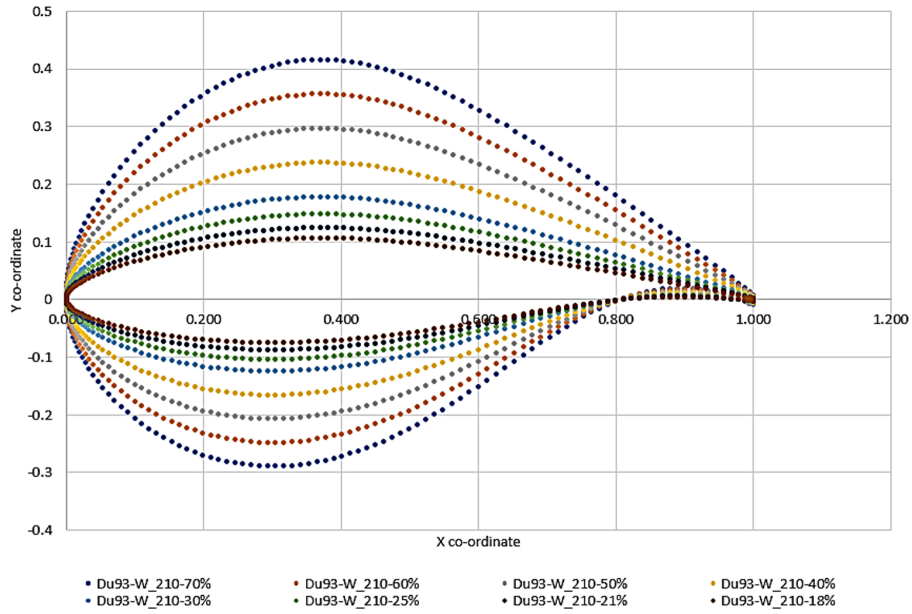


Figure 7.4: Aerofoil shapes for different thickness to chord ratios (as indicated by percentage values in the aerofoil name) used along the designed blade length

wind turbine designs. The rotor diameter and wind class specification were initially based upon the Siemens Gamesa SG14-222DD 10MW offshore turbine [173]. From this turbine design the initial C_p value was determined with the rotor diameter and rotational speed being set using equation 7.6.

$$P = C_p \eta \frac{1}{2} \rho \pi R^2 U^3 \quad (7.6)$$

The efficiency of the turbine's generator and mechanical parts, η , is assumed to be 1 (100% efficient) and hence an initial power coefficient of 0.5 was estimated. This is idealised and it should be noted that in practical terms an efficiency value of 1 is not found to be possible. Using this and by defining the turbine as class I [174] the average wind speed at the blade U was set as 10ms^{-1} and the density ρ taken as the standard international atmosphere $1.225\text{kg}/\text{m}^3$ [175].

With the rotor diameter set with no root to tip twist, the tip speed ratio was also determined from literature which indicates for a three-blade horizontal axis turbine the

optimal tip speed ratio is around 7 [176]. Given this, a rotation speed and RPM value can be determined for the wind turbines normal operation. These were set at $0.7\text{rad}s^{-1}$ and 6.68rpm.

Equations 7.4 and 7.5 were used to determine the optimum blade angle and chord at each section. From this, the approach determined by Yang [177] for blade linearisation was applied and the final blade shape was generated.

The final blade characteristics were a length of 117.3m, split into 23 elements, with a power calculated from equations 7.6 of 9.68MW. This gives a tip speed value of $96.186\text{m}s^{-1}$ which is just over the limit as described by Hoyland [178] for consideration of noise. This results in a final tip speed ratio of 8.2. The individual aerofoil sections were then imported into Solidworks where they were set at the optimum angle and chord length to build up a 3D model of the turbine blade. The final blade geometry is shown Figures 7.5, 7.6 and 7.7.

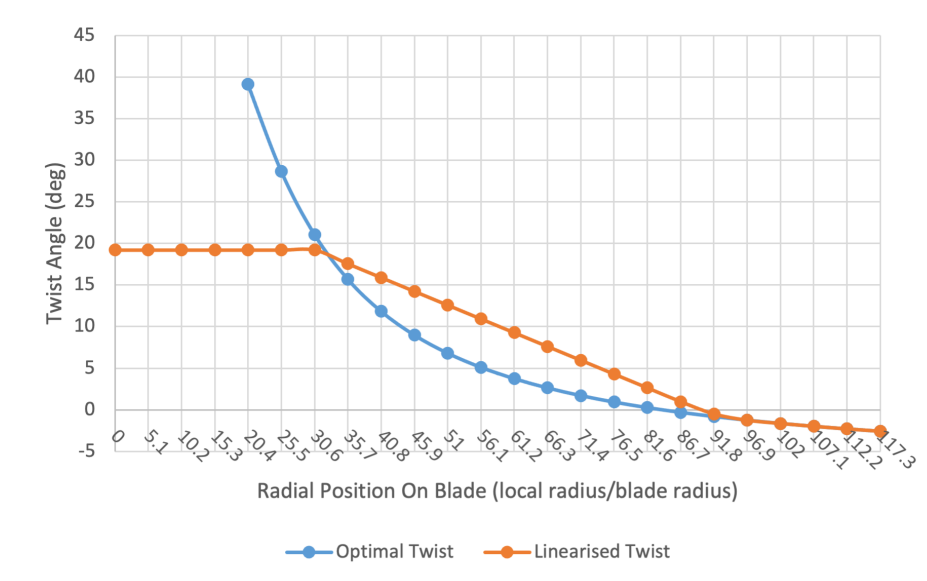


Figure 7.5: Optimal and linearised final blade twist angles for the blade geometry generated along the blade radius

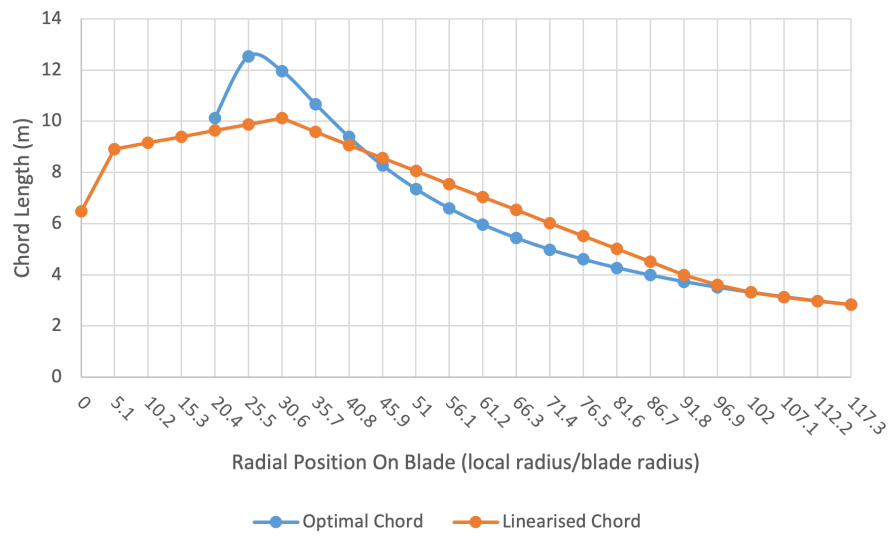


Figure 7.6: Optimal and linearised final blade chord length for the blade geometry generated along the radius

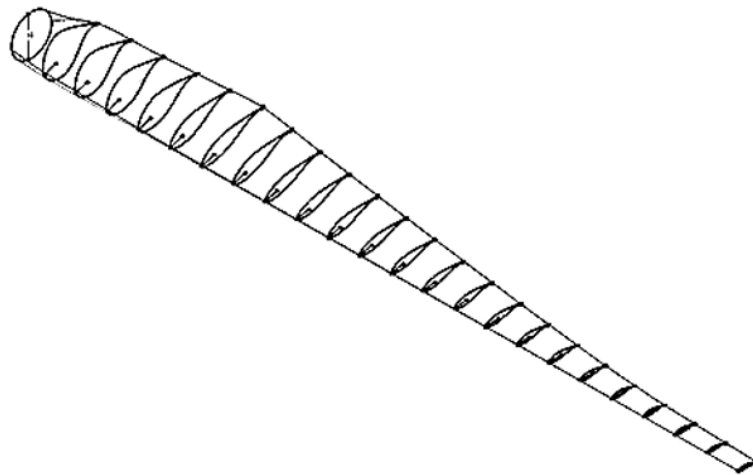


Figure 7.7: Final blade aerodynamic shell geometry as modelled in CAD showing the aerofoil shape at the different elements along its length

Inside the aerodynamic shell it was chosen to select a main spar design running from 5.1m in from the hub to the blade tip. Further consideration led to a combination of carbon and glass fibre for its material distribution. To protect against buckling loads whilst reducing the overall weight it was chosen to make the spar webs out of 3mm glass fibre either side of 80mm foam. The spar flanges were constructed from carbon fibre with a glass fibre aerodynamic shell as used in the design by Hoyland [178]. As also discussed by Hoyland [178] the thickness of the main spar was set to be 33.5% of the chord length along the blade starting from the $\frac{1}{4}$ chord point for reasons identified in the literature.

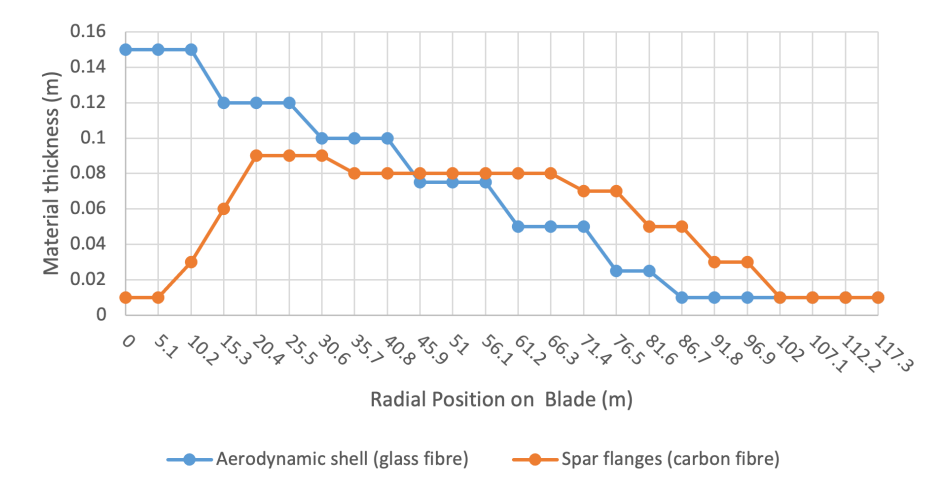


Figure 7.8: Final blade material distribution and thickness as set for the FEA analysis

The material thicknesses were set using the Sandia National Laboratories carbon blade design [179] as a starting point the derived values are shown in Figure 7.8. They were then further adapted to achieve the best compromise between stress and weight. The final blade geometry model is shown in Figure 7.9. This geometry with the associated material properties were all included in the FEA presented in subsequent sections.

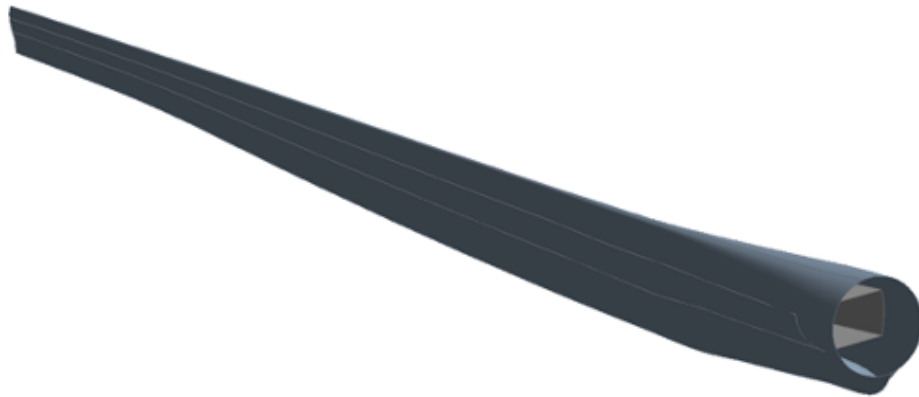


Figure 7.9: Final blade geometry computer model used for FEA analysis

7.1.3 Material Properties

The following material properties in table 7.1 was used for the analysis of the blade. The mechanical properties were obtained from literature [178] [180].

Property	Glass Fibre
Density	1890 (kg/m ³)
Youngs Modulus x-direction	41 (GPa)
Youngs Modulus y-direction	9 (GPa)
Youngs Modulus z-direction	0.009 (GPa)
Poisson's ratio x-y	0.3
Poisson's ratio y-z	0.3
Poisson's ratio x-z	0.35
Shear Modulus x-y	4.1 (GPa)
Shear Modulus y-z	4.1 (GPa)
Shear Modulus x-z	3.3 (GPa)
Max tensile strength	1.2 (GPa)
Max compressive strength	-0.84 (GPa)

Table 7.1: Material properties for G10 epoxy glass used for computational analysis

7.2 Turbine Blade Loading Conditions

The wind turbine designed was defined as a Class I turbine in line with the IEC classification of wind turbines [181] and covered by the British and International Standard BS EN IEC61400-1 [182]. From the standards, the average design wind speed is $10ms^{-1}$.

Figure 7.10 shows the wind loading case for this wind speed at an operational pitch angle.

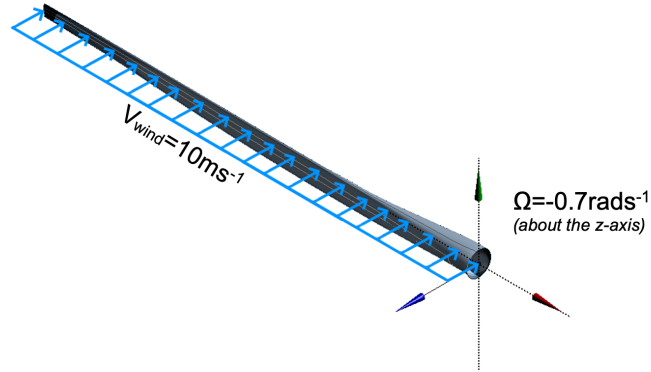


Figure 7.10: Wind loading - 10ms^{-1} wind speed loading at an operational pitch with a rotational velocity of 0.7rad/s about the z-axis

It is assumed that the wind acting on the turbine is in the negative z-axis direction only and steady in state. All turbulent effects and potential wind shear (sudden change in wind speed or direction) effects are not taken into consideration to simplify the analysis.

A point to note made by Hoyland [178] is that a blade will often reach its maximum deflection well before its material limits are reached. Therefore, another critical design parameter is to ensure that the deformed turbine blade does not contact the turbines tower. Numerous solutions to this problem have been suggested such as setting turbine rotors at an angle to the tower. This is however, not considered fully in this investigation as no tower design is proposed but this should be considered in potential future work.

7.3 CFD Loading Setup

The CFD simulation was constructed in ANSYS Fluent to perform the analysis the blade model was set up in a fluid geometry. The CFD approach taken was based upon that proposed by Wang et al [183] in their fluid structure interaction modelling of a 5MW wind turbine blade. To reflect the expanding nature of the flow around the turbine blade the fluid geometry was given a smaller inlet than outlet area. The dimensions about the origin for this set up are shown in Figure 7.11. The geometry is also based on a 120° radial stream tube segment reflecting the three-blade design. This allows for a simplification of the analysis by utilisation of the symmetrical axis of rotation at the centre of the blades. The turbine blade was modelled in this fluid geometry as a stationary nonslip wall located 3.5m in from the origin in the negative x-direction. The whole geometry is modelled in a rotational frame of motion at -0.7rads^{-1} about the Z-axis (as per the right-hand rule).

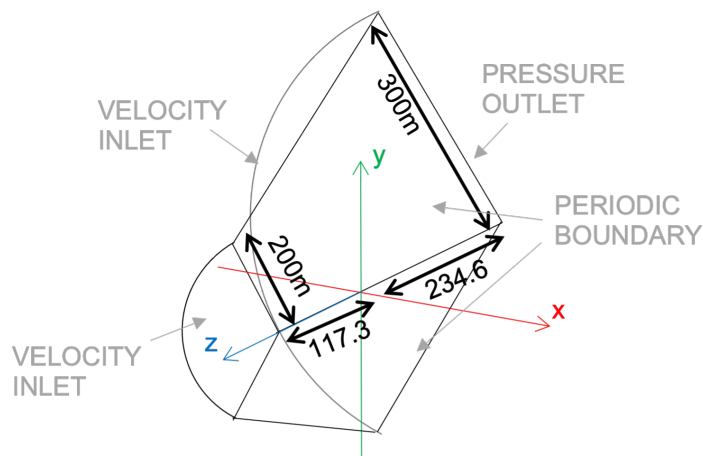


Figure 7.11: Fluid geometry for CFD analysis

Wang et al [183] chose to use such a geometry as experimental results suggest a conical expansion in the turbine blades wake. By using such a geometry it allows for full expansion of the post blade flow. The use of a rotating frame of motion allows for simplifications in the computation by avoiding a potentially unsteady flow which could arrive from the use of a rotating mesh, and so saves on computational time.

The fluid was then meshed using an unstructured 3D mesh which was deemed superior to a structured mesh due to the complex nature of the geometry and the ability to localise mesh density at regions of interest. Inflation layers were added at the blade surface to better capture the boundary layer effects as per the literature [183]. The two rotational faces were given periodic meshes which ensure the mesh matches up between the three segments in the full 360° of the turbine rotor. In addition to this, a sphere of influence (with centre at the centre of the blade) and a mesh sizing refinement was added to the blade surface. Both give better refinement of the near blade mesh and, hence, flow characteristics at these regions.

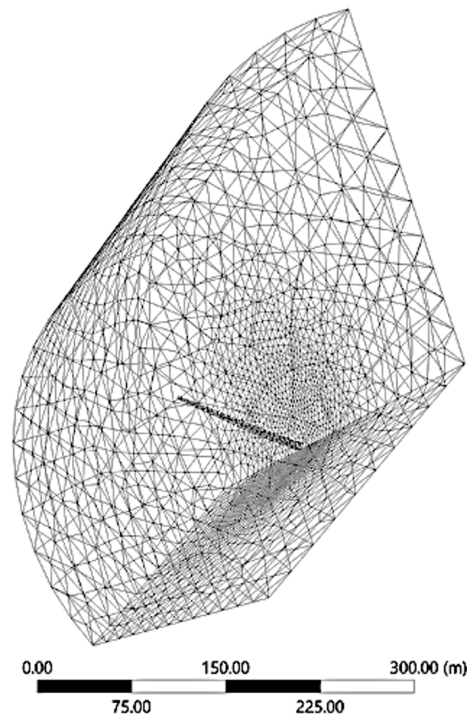


Figure 7.12: Final CFD ANSYS Fluent mesh as used for the simulation of the aerodynamic loading on the blade

The mesh, depicted in Figure 7.12 has the average quality parameters of a skewness of 0.26429 and orthogonal quality of 0.7347. Both these values have a range of between 1 and 0. A perfect mesh would have a skewness of 0 with less than 0.5 being accepted.

For orthogonal quality as high a possible value is desired with 1 being considered perfect.

The geometry was then imported to Fluent and run for the operational conditions. The mass imbalance was noted to be less than 0.1%, indicating the mass conservation assumption is appropriate, as per the work by Wang et al [183].

For the CFD simulation the RANS $k - \omega$ SST turbulence model was used. This model defines the kinetic energy, k , based upon an eddy velocity scale, hence, the turbulent kinetic energy can be determined with the frequency of the turbulence, ω , tending to infinity at the flow's boundary [184]. Menter [184] noted that the basic $k - \omega$ model was insufficient for negative pressure gradients and so the SST model was developed improving upon the numerical stability and model constants. It does so by moving from the $k - \varepsilon$ model at free stream flows to the $k - \omega$ model at the boundary layer taking advantage of both model's strong points [183,184]. This model has been used extensively in wind turbine (and aircraft) aerodynamic analysis giving good results and hence, was chosen for this simulation in line with literature sources [183,185–188].

This method made it possible to obtain reasonable results for the CFD simulation that met the convergence criteria in a computational time of just under 14 hours with 5,000 iterations.

7.4 Boundary Conditions for CFD

The forces along the blade were applied to the surface at the quarter chord point along its length at the centre of the element through which they would act. This was applied in the positive y-axis and negative z-axis as per the CFD loading results. The respective rotational velocity components were added to the entire geometry for the loading case. The gravitational force was applied in the negative y-direction. The final set up can be seen in Figure 7.13. The point loads being applied to the surface a pressure

Chapter 7. Computational Blade Stress Analysis

distribution can be applied. This was achieved by directly coupling the ANSYS Fluent results to the ANSYS static structural inputs as shown in Figure 7.14.

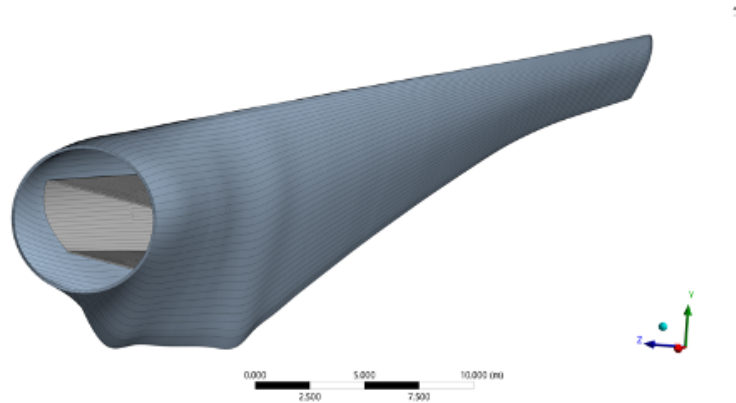


Figure 7.13: Final mesh for the generated blade

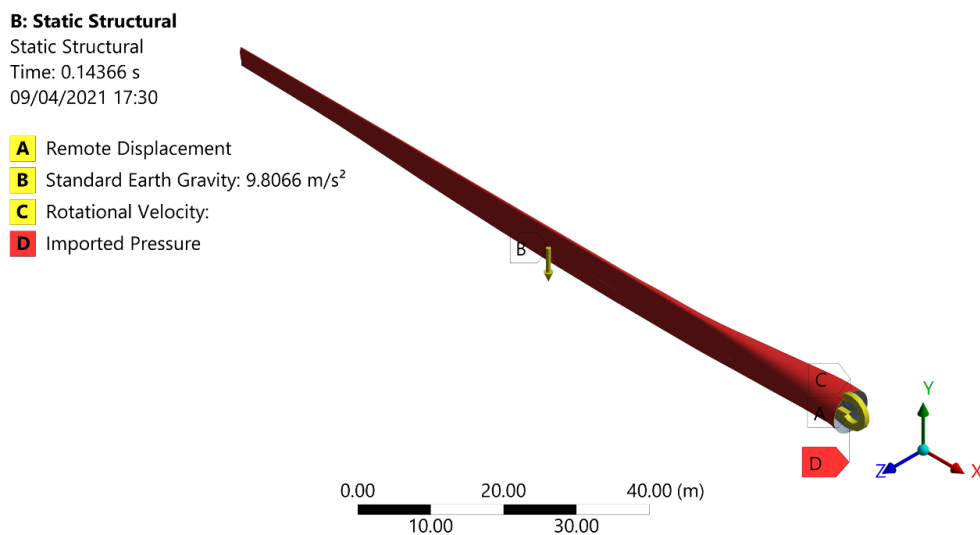


Figure 7.14: Analysis Settings as implemented in ANSYS for the CFD loading results showing the rotational velocity, gravitational loading and surface aerodynamic pressure loading

7.5 Results

7.5.1 CFD Loading

The results from the CFD loading are shown below:

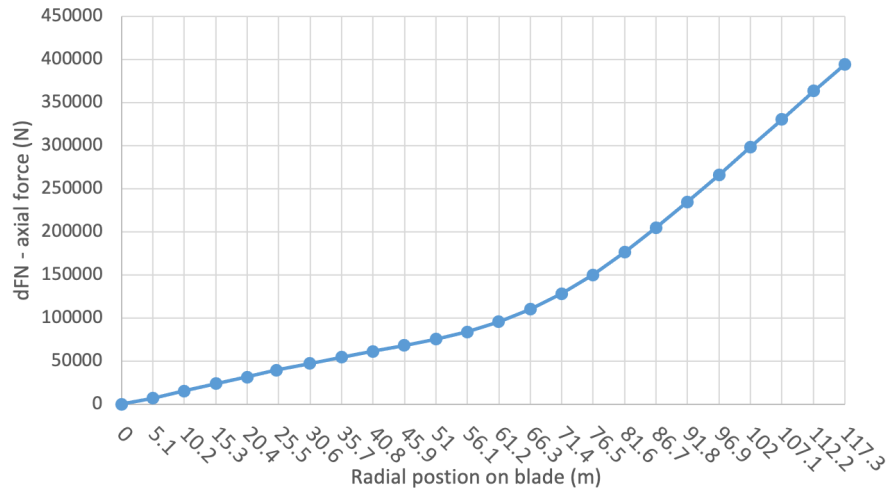


Figure 7.15: CFD loading for axial force loading. Single blade results showing cumulative axial force from root to tip.

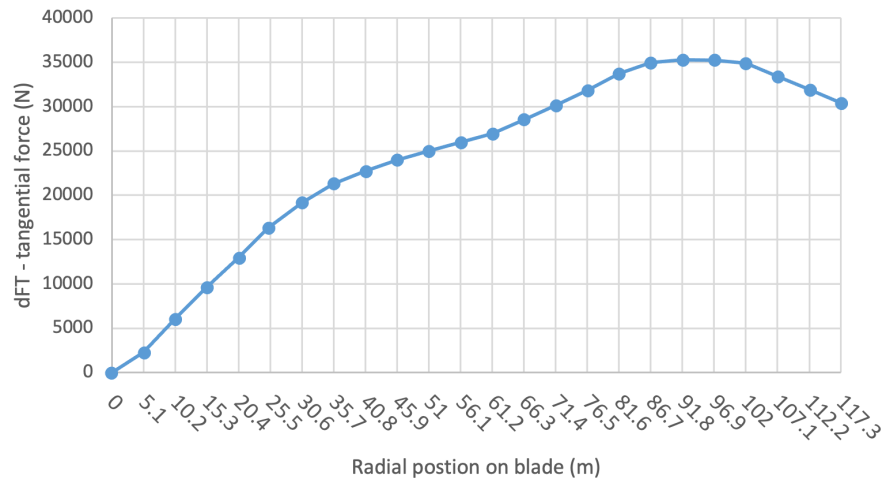


Figure 7.16: CFD loading for Tangential force loading.

7.5.2 CFD FEA

The CFD results presented were found using the method as outlined in section 7.2 and 7.3. The loading results applied are presented in Figures 7.17, 7.18 and 7.19.

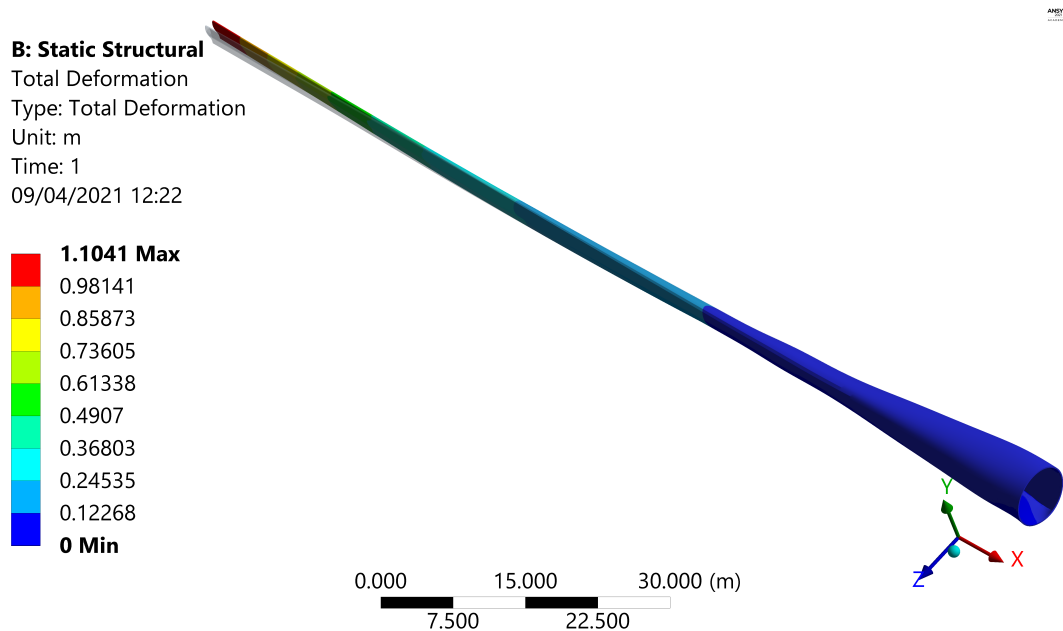


Figure 7.17: CFD Total Deflection results for operational pitch at $10\text{m}\cdot\text{s}^{-1}$ wind loading. Maximum deflection of 1.1014m at a blade radius of 117.3m.

7.6 Discussion

7.6.1 CFD Loading Configuration

Loading results on initial inspection agree with the general trend observed in the literature [185]. These results follow the curve with the forces starting at 0 and sharply falling away to 0 at the tip. The CFD loading results shown in Figure 7.1 and table 7.2, have good agreement with the attained results. A more variable loading at the inboard blade section shown by Figure 7.1, which is not found in this investigations results, would have been expected. This more variable loading pattern would show a more realistic capture of the potentially turbulent loading at the root sections. Not

Chapter 7. Computational Blade Stress Analysis

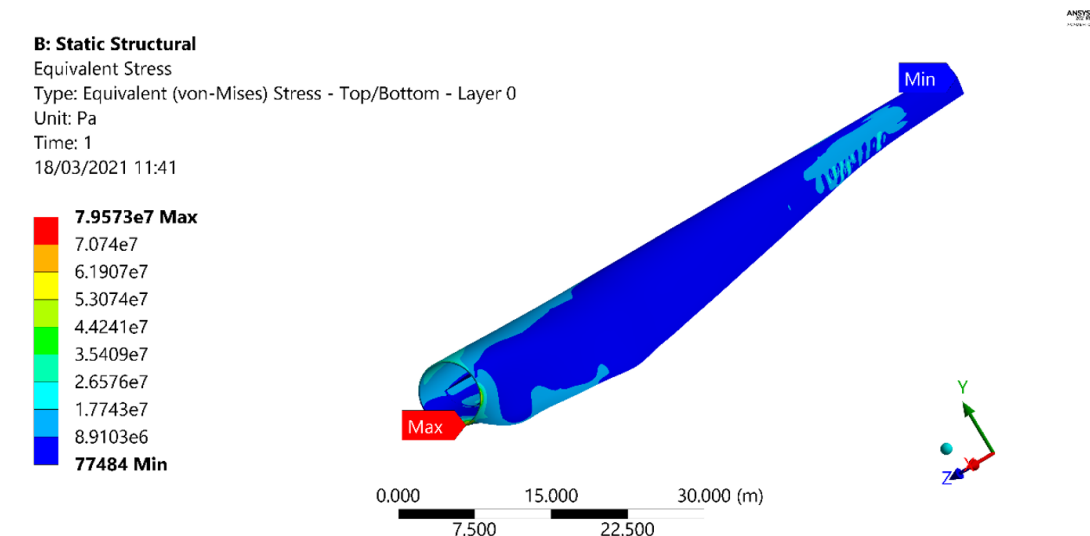


Figure 7.18: CFD Equivalent von Mises stress results for operational pitch at $10\text{m}\cdot\text{s}^{-1}$ wind loading. Maximum equivalent stress of 79.573MPa (at a blade radius of 0m on the inner surface geometry) and minimum equivalent stress of 77484Pa at a radius of 117.3m .

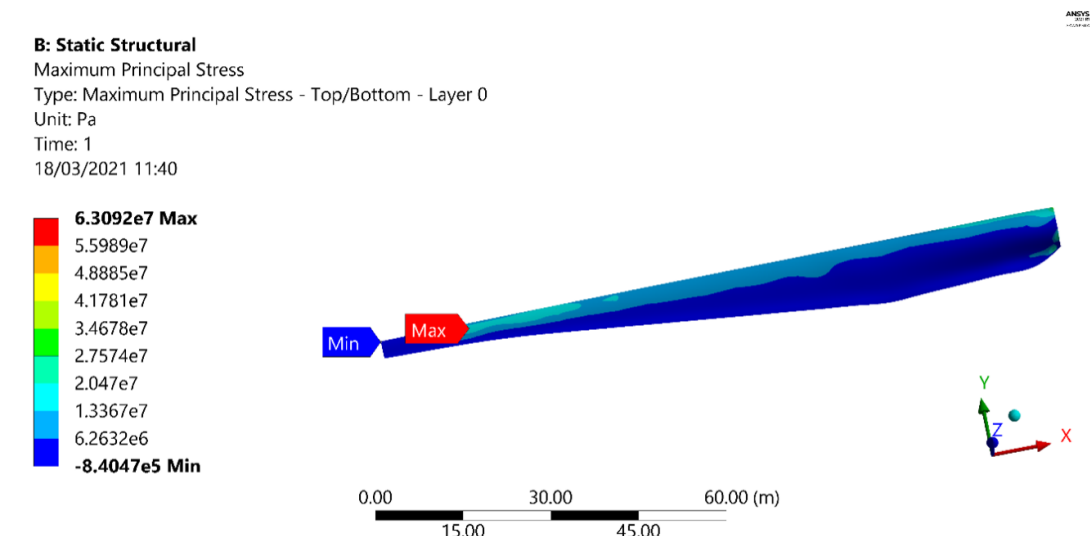


Figure 7.19: CFD Maximum Principal Stress results for operational pitch at $10\text{m}\cdot\text{s}^{-1}$ wind loading. Maximum principal stress of 63.092MPa (tension) at a blade radius of approximately 105m and minimum principal stress of -0.84047MPa at a blade radius of approximately 117.3m .

being seen in the results potentially reflects the fact that more work is required on the transition model as was identified in the literature.

Operation Case	Maximum Von Mises Stress as a percentage of the material maximum tensile strength	Minimum Von Mises Stress as a percentage of the material maximum compressive strength
CFD Loading		
1 (operational pitch at $10ms^{-1}$ wind speed)	6.631% (Glass Fibre)	0.00923% (Glass fibre)

Table 7.2: Maximum Stress in compression and tensile.

It is observed that the z-axis (axial) force starts off low and increases to a maximum of 394kN near the blade tip. Meanwhile the y-axis (tangential) force has a much larger region of higher force in the centre of the blade having started from zero.

The CFD results show a good trend in change of loading along the blade radius. Further analysis refinement would be desirable for verification of the magnitude of these results. The basic procedure is shown to be sound with the expected loading trend and verified to be correct.

7.6.2 FEA Discussion

The maximum principal stress (tension) of 63.1MPa was at approximately at 105m from the blade root and is within the operational limits of the material. It is likely that the location of the maximum and minimum stresses along the blade radius is likely to be due to changes in the root bending moment. These occur due to pitching of the blade forward for optimal operation at higher wind speeds.

The maximum compression stresses were -0.8MPa, this is reflected in the literature when it is observed that a main design point for a turbine blade should be careful

consideration of buckling failure, which is most likely to be caused by compressive forces [189]. In addition, glass fibre is more suited to the aerodynamic shell than carbon fibre which generally has a lower compressive strength [190].

Considering the blade alone, the tip deflection has little impact on the design with the materials chosen having good flexural properties. For the design of a full offshore wind turbine high tip deflections would have more impact when considering potential collision between blade tip and supporting tower structures. Such potentially high deflection values should be fully considered before any such blade designs are implemented in real world offshore wind turbine designs.

7.7 Conclusions

This investigation has analysed a 117.3m offshore wind turbine blade's flexural stresses for a range of operating conditions. This was accomplished by FEA analysis of the geometry's stress distributions. The condition were selected to meet the recognised British and international standard for the design of such blades.

The geometry and material distribution were set according to the literature sources. The blade loading for the generated geometry was then calculated using CFD.

It has also been shown that the material properties of the glass fibre and carbon fibre materials far exceed the mechanical properties required for the blade and thus isf more than adequate for normal operation. The blade geometry has the required strength for normal operational conditions as defined by the relevant standards for blade design.

By inclusion of aerodynamic optimisation, composite material properties and complex structural requirements in the FEA this investigation has enabled the normal

Chapter 7. Computational Blade Stress Analysis

loading conditions for a 9.68MW offshore turbine blade geometry to be examined.

This work fulfilled the aim to determine the stresses that a blade experiences during normal operation. This information is utilised in the experimental work to stress the GFRP sample to determine if this has an effect on the erosion mechanisms and rate of degradation.

Chapter 8

Experimental Work

The work in this section was peer reviewed and accepted for publication in the journal of lubricants titled "A study of raindrop impacts on a wind turbine material: velocity and impact angle effects on erosion MAPS at various exposure times" S Groucott, K Pugh, I Zekos, M M Stack, Lubricants 9 (6), 60 (2021)

8.1 Rain Erosion in On-Shore Conditions

This investigation explores the transitions between different wear states by running laboratory simulated conditions to a wind turbine in operation under harsh climate conditions and measures the wear periodically to identify a progression of erosion. Erosion maps were constructed showing the variation of wastage based on the conditions.

8.1.1 Methods and Materials

The primary variables chosen for this investigation were the impact angle (θ_{im}) and impact velocity (v_{im}). The first was chosen to represent the different angles at which rain impacts on the turbine blade leading edge and helps to indicate the erosion wear mechanism taking place on the sample. The impact velocity represents different rotor velocities along the turbine blade, which is maximum at the blade tip. It helps indicate the level of erosion with a change in velocity and how this affects the rate of wear and

indicates the location on the blade where the maximum erosion will occur. The impact angles of the leading edge of the blade are demonstrated in Figure 8.1. All samples had the same test repeated in four identical cycles to produce continued, gradual wear to associate the exposure time of the samples to the defects such as pin holes, gouges and cracks [93].

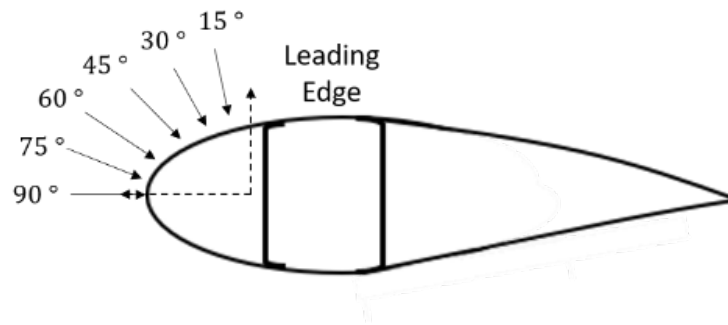


Figure 8.1: Test sample impact angle simulated to that of a point on a wind turbine leading edge

To improve accuracy during each experiment, certain parameters were kept constant and a consistent methodology was followed. Common tap water was chosen as the best replacement for rainwater available and was taken from the same laboratory source. Each experiment was performed in the same laboratory at room temperature and the temperature inside the rig was monitored and maintained at approximately 20°C .

8.1.2 Testing Apparatus

An existing WARER at the University of Strathclyde was utilised in this research which is located in tribology laboratory and its purpose is to artificially generate a rain field [93,134]. This was achieved with a water tank connected to the peristaltic pump through tubing, then connected to 16 droplet needles of the chosen gauge (23 G). The flow rate of the peristaltic pump was calculated to ensure it was consistent with the manufacture claim and the rainfall flow rate. The flow rate was calculated during the test experiments and the weight of the water in the supply water tank for

the pump was weighed before and after testing and the time the pump was running for to calculate the flow rate and hence the rainfall rate which was calculated to be 50mm/h. Note, 50mm/h is regarded as the value between heavy shower and very heavy shower simulating the upper end of rainfall rate. The water delivery system is shown in Figure 8.2, inside a stainless-steel enclosure. Two samples of different impact angles were secured in the sample holders at each end of the removable rotor arm and adjusted to their suitable angle orientation. The rotor arm was then secured in the test rig by a central hub, connecting it to the driving motor. The pump reservoir tank was then filled appropriately. Before testing, the pump was switched on and left to run for 5 minutes to ensure flow equilibrium and that all droplet needles were active.

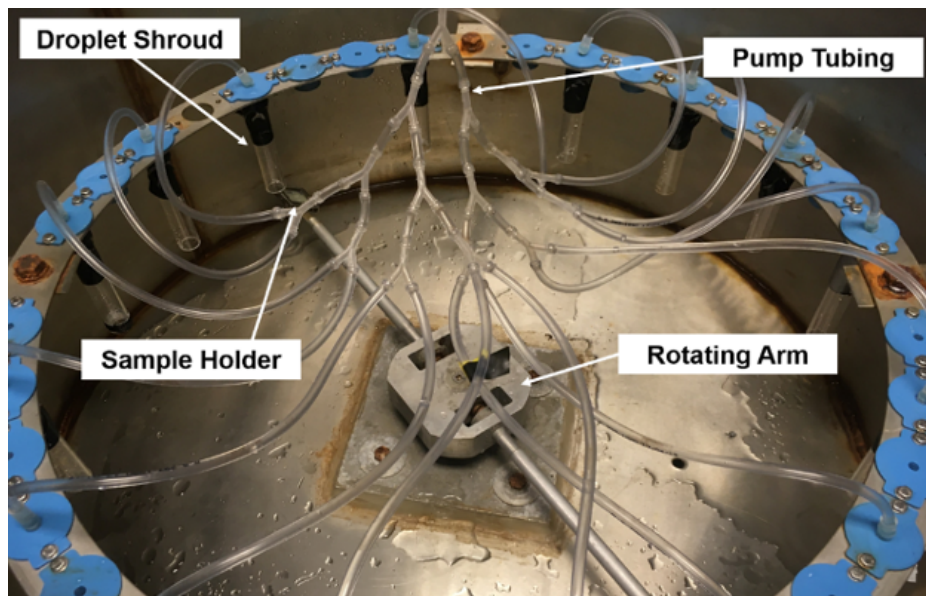


Figure 8.2: Whirling arm erosion rig in the tribology lab within The University of Strathclyde

A Perspex lid was then placed to enclose the test apparatus and the motor frequency was set for the corresponding impact velocity. A stopwatch was started once the motor reached the desired velocity, then stopped at the required experimental time. The motor and the rain-field were then stopped concurrently. The lid was removed once the arm came to a complete stop and samples were removed and left to dry in the tribology

laboratory for at least 24 hours.

The variable ranges were ($15^\circ - 90^\circ$) and ($40\text{ms}^{-1} - 60\text{ms}^{-1}$) for the impact angle and velocity respectively, at increments of 15° and 10ms^{-1} . Each experiment ran the same total distance of 216km with tests running for 90, 72 and 60 minutes for 40ms^{-1} , 50ms^{-1} and 60ms^{-1} respectively. The distance of 216km was selected to align with the previous, smaller experiments as this was the maximum distance it could achieve at its highest speed. Four repeated cycles were conducted in order to analyse the erosion periodically and hopefully produce stages of gradual erosion.

8.1.3 Design of Experiment

For this investigation to analyse the erosion of GFRP under onshore conditions the experiment was set up as follows:

Variables investigated and their application to Wind Turbines:

- Impact Angle - Area of leading edge affected
- Impact Velocity - Rotational velocity of the turbine blades and the radius from the root
- Bending Stress - Design and size of the blade
- Water Salinity - Location, Onshore or Offshore

Constants throughout the investigations:

- Droplet diameter
- Temperature
- Humidity
- Distance travelled between inspection

- Rainfall rate
- material

8.1.4 Experimental Run Time

Samples were tested for the longest possible time to maximise exposure and the amount of erosion, while maintaining safe, laboratory conditions in the WARER. The highest safe operation velocity of the rig was deemed to be 60ms^{-1} this limitation is one of the reasons for developing the larger test rig to simulate larger turbine blades. Taking this as the maximum test velocity, the distance to be travelled by each sample was then calculated by running the rig at 60ms^{-1} for maximum time before the temperature conditions within the chamber varied from initial conditions due to the heat from the motor. The distance travelled was based on the midpoint of the sample, rotation distance and number of rotations. This resulted in a run-time of 60 minutes and a corresponding distance of 216 km. Details for each tested are displayed in table 8.1, where $r=0.3$ m and is the radius to the sample centre.

Impact velocity, v_{im}	Run time, t	Distance travelled, S
40ms^{-1}	5400s (90 min)	216km
50ms^{-1}	4320s (72 min)	216km
60ms^{-1}	3600s (60 min)	216km

Table 8.1: Experimental duration

8.1.5 Mass Measurement

The primary method for recording erosion after cycles was by measuring each sample's mass loss using an AND BM-252 balance, measuring accurate to 0.01 mg. This allowed for a direct comparison between each stage of testing and provided data detailing the impact angles and speeds most vulnerable to erosion for the G10 Epoxy Glass Fibre material [191]. Before testing, each sample had its mass measured five times, resulting in an averaged initial mass. This process was then repeated for each sample after test-

ing and the drying period, giving a percentage error of 0.016%.

Four wear-wastage maps were then created using mass loss data after each consecutive cycle. They indicated the accumulated percentage mass loss after each cycle with boundaries of 0.005% difference. Each intersection between the tick marks of velocity and impact angle indicates a sample's data point on the maps, with contour lines generated by interpolation with the `contourf` function within MATLAB.

To allow for analysis of continued gradual wear after each test cycle for each individual sample and for direct comparison, mass loss data was also collated into a line graph shown in Figure 8.7. This allowed for comparison of an individual sample mass loss after each cycle, as well as compared to other samples. It also detailed the accumulated mass loss at each total distance travelled, after each respective cycle. The data is presented in these two forms as it was assessed to provide the clearest information and visualisation into the progression of erosion and an insight to mechanisms acting on the material.

8.1.6 Materials

G10 Epoxy Glass Fibre, consisting of carbon-based epoxy and silicate oxide fibers orientated in a 90-degree cross-weave, was the chosen sample material. GFRP is a common material in a turbine blade structure as it combines the structural rigidity needed to build large structures with the lightweight capabilities of complex geometries. The samples used were 18 coupons with dimensions of 30 x 30 mm and 1 mm thickness. Samples were marked with their corresponding number, impact angle and sample holder orientation on their underside. This was specified to ensure the samples were exposed at the same orientation, given the directional nature of the fibres in the material and their effect on mechanical properties. The samples required a drying period after testing due to the absorptive nature of the polymer material, as this would also significantly alter later mass measurements due to their moisture content. The properties of the material

used is shown in table 8.2.

Property	Value
Flexural Strength (<i>MPa</i>)	482
Tensile Strength (<i>MPa</i>)	320
Shear Strength (<i>MPa</i>)	131
Impact (Notched Charpy) (<i>kJm⁻²</i>)	65
Density (<i>gcm⁻³</i>)	2
Specific Gravity	1.82
Water Absorption (<i>mgm⁻²</i>)	8
Rockwell Hardness (M-Scale)	110
Standard Finish	Satin/Glossy

Table 8.2: material properties of G10 epoxy glass used in this experiment

8.1.7 Results and Discussion

The mass loss from each sample was recorded and is shown in the form of an erosion map which displays the relationship between impact velocity and impact angle in terms of mass loss [191]. The four maps, Figures 8.3, 8.4, 8.5 and 8.6 show the four cycles the samples were exposed to and the combinations of linear impact velocity and impact angle which result in the most erosion.

The wear maps are set up displaying mass loss as a percentage and each colour in the wear map represents a range of 0.005%. The wear map can be used in a similar fashion to an isobar map where the spacing between the lines represents the differential in erosion. The first wear map, Figure 8.3, displays the mass loss from the samples as they undergo their first cycle of 216km equivalent exposure time. It is within this cycle the largest increase in mass loss is observed; however, there are no specific combinations of impact velocity and angle that demonstrate more substantial erosion than others as displayed by the large spacing between the erosion lines.

In Figure 8.4 the wear map displays the mass loss for the second cycle the samples were exposed to now equivalent to 432km travelled. This wear map displays another

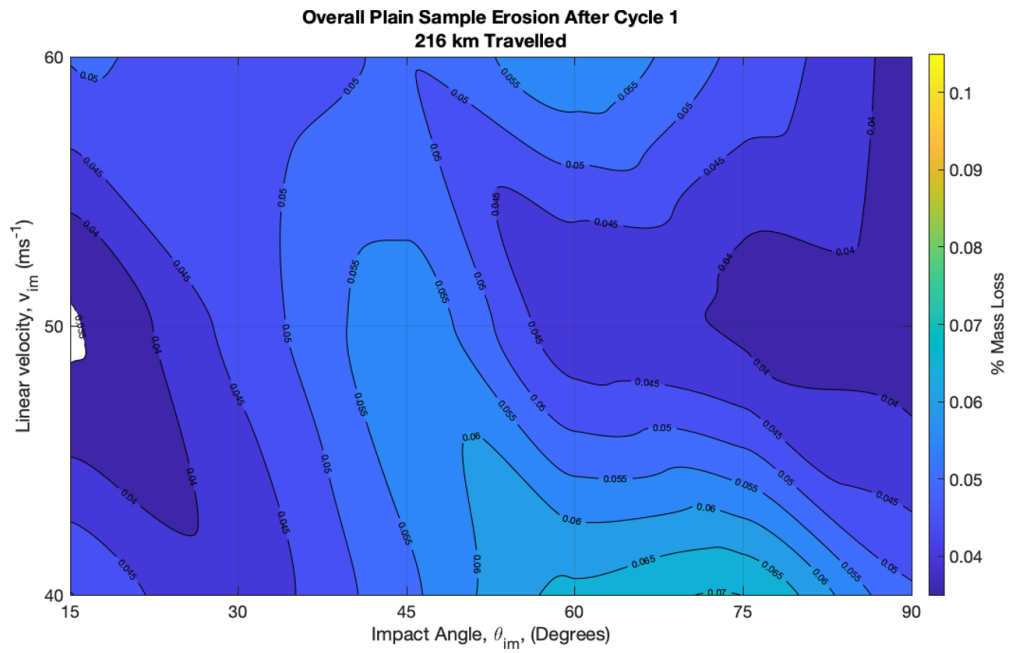


Figure 8.3: Wastage map post Cycle 1. Highest percentage mass loss occurred at $\theta_{im} = 75^\circ$, $v_{im} = 40 \text{ ms}^{-1}$ with a loss of 0.070% (1.104 mg). The lowest percentage mass loss occurred at $\theta_{im} = 90^\circ$, $v_{im} = 60 \text{ ms}^{-1}$ with a loss of 0.037% (0.548 mg)

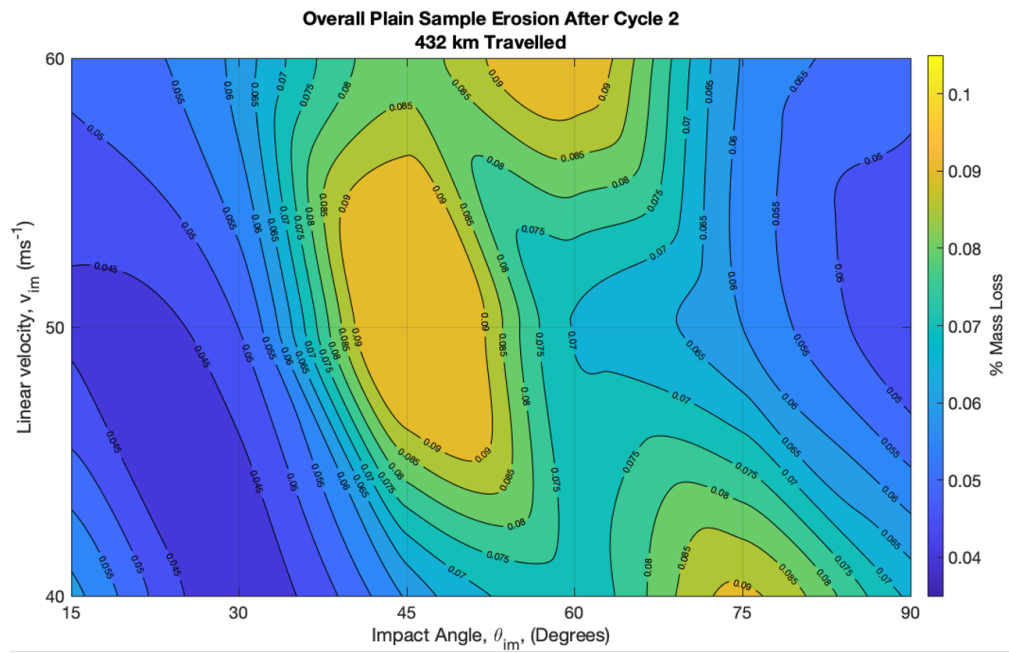


Figure 8.4: Wastage map post Cycle 2. the highest percentage mass loss occurred at $\theta_{im} = 45^\circ$, $v_{im} = 50 \text{ ms}^{-1}$ with a loss of 0.102% (1.58 mg). The lowest percentage mass loss occurred at $\theta_{im} = 30^\circ$, $v_{im} = 40 \text{ ms}^{-1}$ with a loss of 0.042% (0.68 mg)

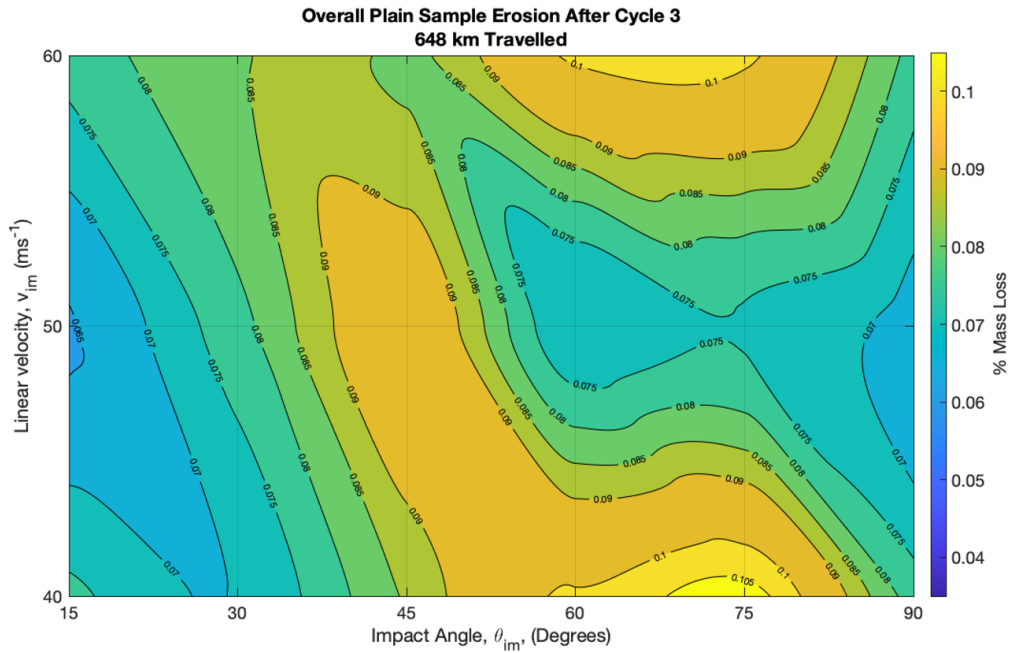


Figure 8.5: Wastage map post Cycle 3. The highest percentage mass loss occurred at $\theta_{im} = 75^\circ$, $v_{im} = 40ms^{-1}$ with a loss of 0.107% (1.692 mg). The lowest percentage mass loss occurred at $\theta_{im} = 90^\circ$, $v_{im} = 50ms^{-1}$ with a loss of 0.070% (1.06 mg)

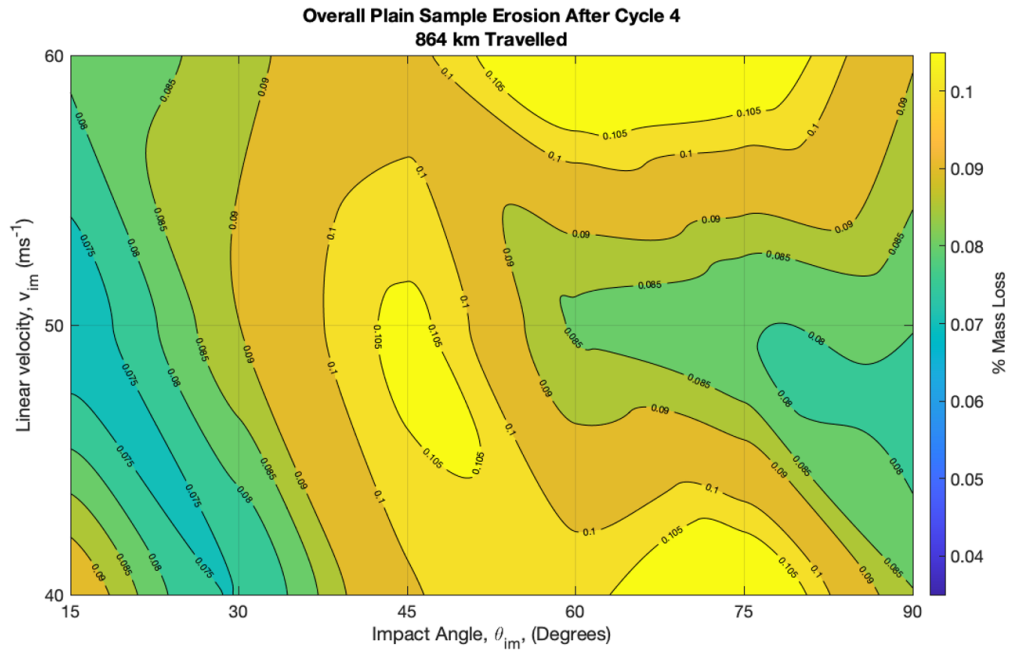
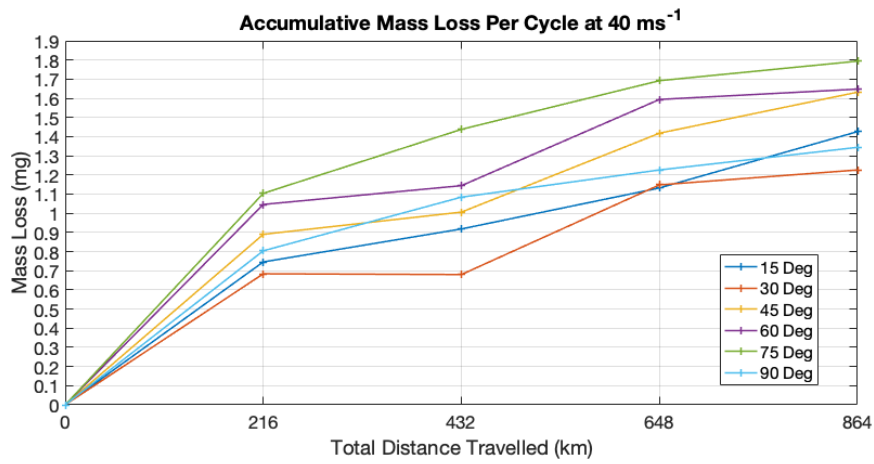
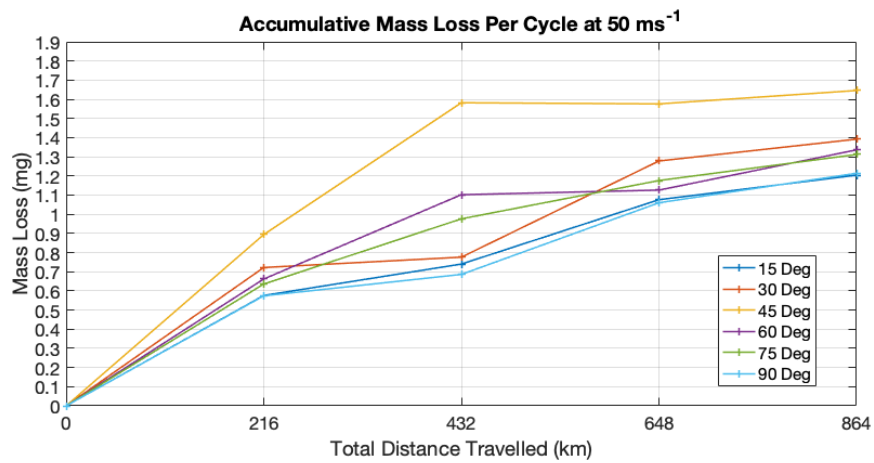


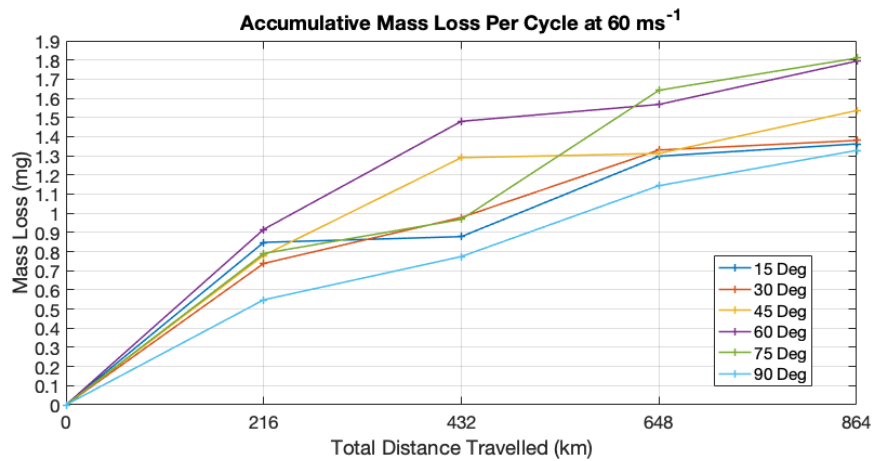
Figure 8.6: Wastage map post Cycle 4. The sample with the highest percentage mass loss after full testing occurred at an impact angle of $\theta_{im} = 60^\circ$, $v_{im} = 60 ms^{-1}$ with a loss of 0.116% (1.794 mg). The lowest percentage mass loss occurred at $\theta_{im} = 15^\circ$, $v_{im} = 50ms^{-1}$ with a loss of 0.07% (1.204 mg).



(a)



(b)



(c)

Figure 8.7: Accumulative mass loss for: a) $v_{im} = 40ms^{-1}$ b) $v_{im} = 50ms^{-1}$ c) $v_{im} = 60ms^{-1}$

large increase in erosion from the previous cycle and also some concentrated areas in which there was considerably more mass loss which include $v_{im} = 50ms^{-1}$ at $\theta_{im} = 45^\circ$ and $v_{im} = 60ms^{-1}$ at $\theta_{im} = 60^\circ$ these two samples show a large difference from the surrounding samples illustrated by the tightly packed erosion lines. The impact angles these samples were subjected to are therefore the most damaging within this experiment.

Figure 8.5 shows the wear map for the third cycle the samples were exposed to, which is now equivalent to 648km travelled. This wear-map still displays an increase in erosion for most samples; however the rate of mass loss has decelerated and the difference between cycle two to three is considerably less than the difference between cycle one to two. The general distribution between all the samples is more neutralised within this cycle as the range in mass loss between the least and most eroded sample is lower than it is in cycle two. This can be visualized on the wear-map as the spacing between the erosion lines is greater.

Figure 8.6 shows the wear map for the fourth and final cycle the samples were exposed to, totalling 864km. The trends this wear map displays are very similar to the third cycle as the mass loss of the samples continues to increase, however the range between the samples decreases. This is also illustrated as the erosion contours grow even further apart.

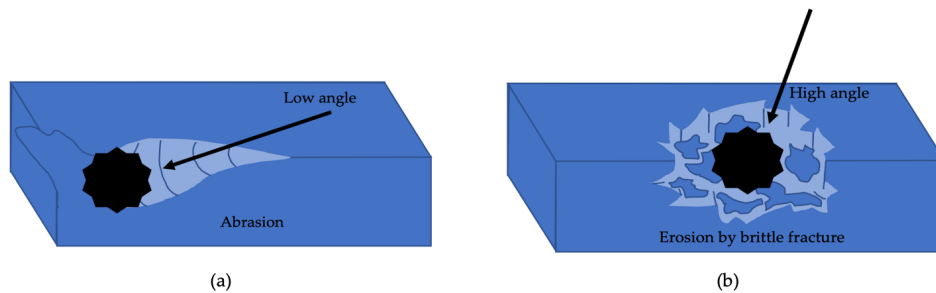


Figure 8.8: Wear mechanisms for particle impacts with a a) low angle of impact b) high angle of impact. Adapted from [90]

From the literature the two main forms of erosion the sample will encounter during testing are ductile abrasion and brittle fracture as seen in Figure 8.8. Although these figures are examples of particle impacts; similar damage features were observed for high velocity water impacts as seen in the recorded SEM images. At low angles of impact there is a higher probability (depending on conditions [192]) of a ductile response from the material, resulting in deformation and gouging. At higher angles of impact, the material will have a more brittle response, potentially resulting in a fracture, crack or delamination. These mechanisms are the initial stages of erosion, which create initiation sites which are more vulnerable to further erosion, due to the increased surface roughness. These sites are normally small pinholes in the material and are broken down quickly by lateral jetting [129], exploiting pinholes to form cracks and remove material from the sample.

Erosion mechanisms are determined by the material being subjected to these conditions, such as in this investigation where a composite material is eroded [193]. In the wind turbine industry, composites are used due to their combined properties of strength, from the glass fibers, and increased strain properties, from the epoxy resin matrix. Glass fibers are very susceptible to brittle fracture when subject to high velocity impact, likely to be broken and removed, especially at high angle impacts. The epoxy resin matrix protects the glass fibres from this damage, having high elasticity and resistance to high impact angle brittle fracture. It is, however, at risk from low angle of impact, ductile abrasion. Therefore, when the top surface of the composite is compromised, and pinholes emerge from the material, it is a possibility that the fibers are exposed and become unprotected from high velocity water droplet impacts. This trade-off is shown in Figure 8.9 and indicates why there was an initial spike in cycle two at $v_{im} = 60ms^{-1}$ at $\theta_{im} = 60^\circ$ and at $v_{im} = 50ms^{-1}$ at $\theta_{im} = 45^\circ$. At these conditions the water droplet compromises the elastic epoxy layer with ductile abrasion, further exploiting the hard glass fibres with brittle fracture and lateral jetting which optimizes mass removal.

After the 4 cycles were complete, a SEM analysis was carried out on the samples,

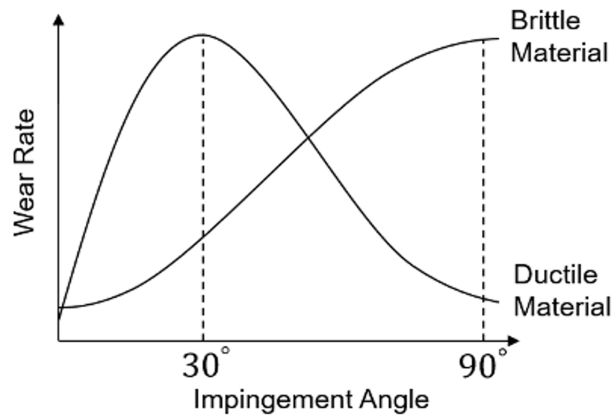


Figure 8.9: Ductile / Brittle wear rate according to impact angle – Adapted from [90]

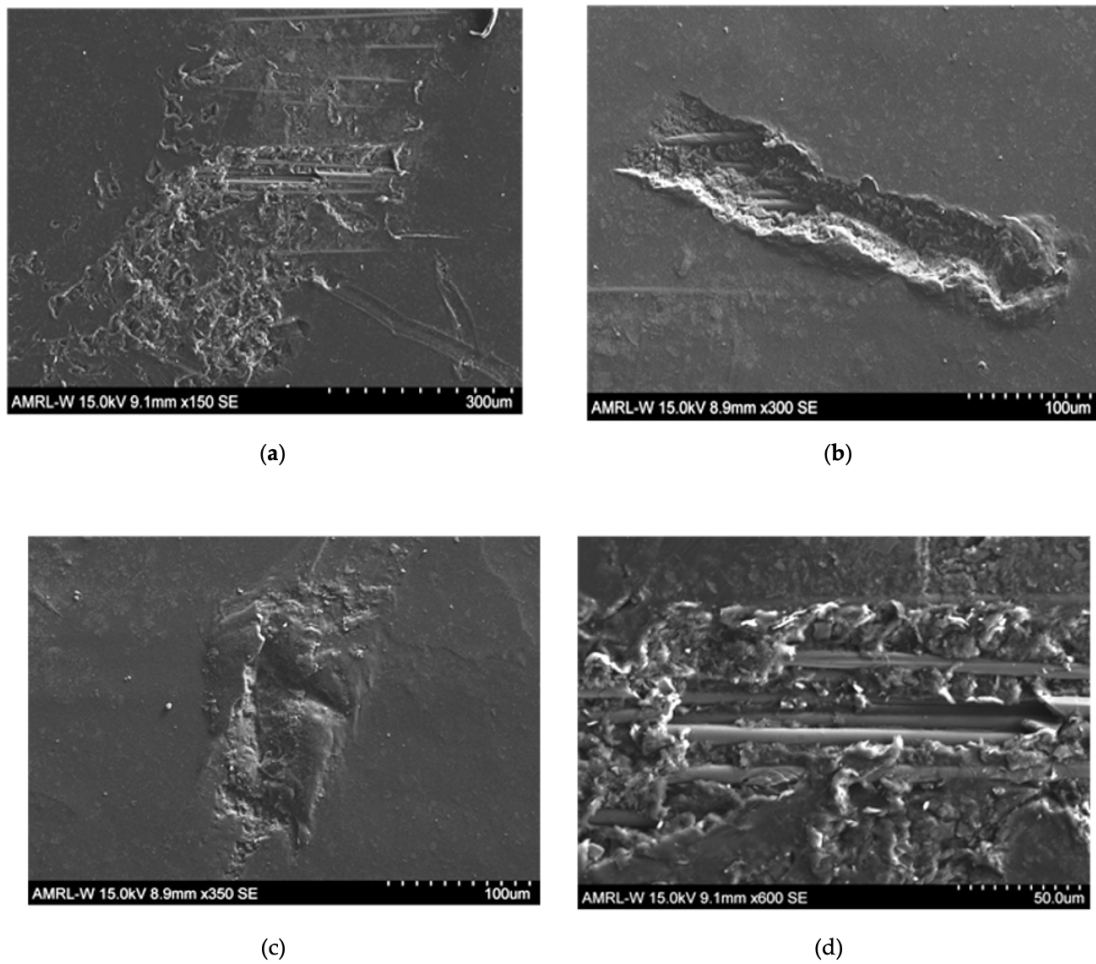


Figure 8.10: SEM images of erosion damage from droplet impact at: a) $\theta_{im} = 15^\circ$ x150 Mag b) $\theta_{im} = 60^\circ$ x300 Mag c) $\theta_{im} = 75^\circ$ x350 Mag d) $\theta_{im} = 15^\circ$ x600 Mag

seen in Figure 8.10. From these images the following can be observed; a) pinholes in the material and some exposed fibres, b) a classical example of ductile abrasion, c) a pinhole that would be unprotected from lateral jetting and the cavity being deepened and fractured, d) a view of exposed fibers, assumed to be uncovered after abrasion of the top epoxy layer.

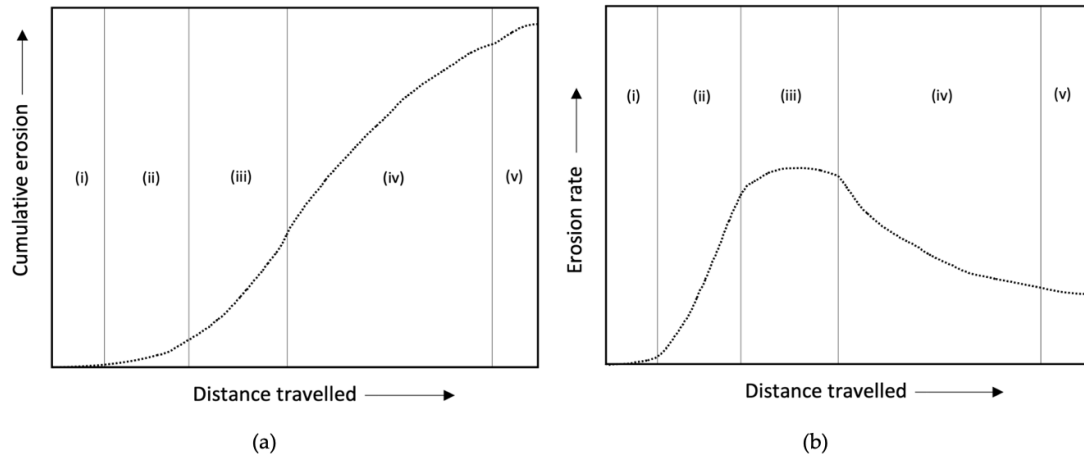


Figure 8.11: Characteristic erosion-versus-distance travelled curves. (a) Cumulative erosion versus exposure duration (time, or cumulative mass or volume of liquid impinging). (b) Corresponding instantaneous erosion rate versus exposure duration. Adapted from [194]

Mass loss data, that was used to create the wear maps, was also formatted to display the wear rate of the samples over the three impact velocities as observed in Figure 8.7. This was completed in order to visualise the rate of mass loss between each cycle and also to compare trends with each sample. From all three line-graphs; $v_{im} = 40ms^{-1}$, $v_{im} = 50ms^{-1}$, $v_{im} = 60ms^{-1}$ it is clear the general trend is most of the erosion occurred in cycles one and two. Until cycle two the wear rate is approximately linear, after which the mass loss starts to reduce. In the literature [71, 108, 195] the trend is shown in Figure 8.11 where the erosion of a material is set into five distinct sections: incubation stage, acceleration stage, maximum rate stage (sometimes called first steady-state stage), deceleration stage and terminal or final steady-state stage. From this investigation minimal incubation was evident as there was early mass loss

that continued linearly into cycle two, then cycle three and four are described by the final erosion region. It is proposed that the G10 epoxy glass samples which were used in this investigation had some initial surface roughness in order to initiate top layer erosion, shortening the incubation period.

8.1.8 Conclusions

- The wear-maps as a function of impact angle and impact velocity were created using the experimental results demonstrated insights into the trends of erosion throughout the four cycles samples were exposed to. The wear-maps also allowed to visualise the magnitude of variation between samples in the same cycle, as the contours which separated each range of mass loss worked similarly to isobar lines on a pressure map. When the contours are tightly packed together a large difference in mass loss is highlighted and vice versa.
- The samples which experienced the most erosion were subjected to impact angles ranging between $45^\circ \leq \theta_{im} \leq 60^\circ$. This was theorised to be due to the synergistic effects of ductile abrasion, brittle fracture and lateral jetting interacting in this impact angle range. The SEM images confirmed the existence of these wear mechanisms and how material was lost from the sample.
- The impact velocity changes the peak impact angle at which the erosion takes place.
- For the effect of exposure time, the raindrop erosion rate showed minimal incubation time as the first response from the material was a linear relationship which then reduced with longer exposure. The levels of erosion could be visualised over the three regimes for the conditions studied. The trend generally followed the same pattern as observed in the literature the exception being the incubation stage which was not observed during his testing.

8.2 Effect of Bending Stress on Rain Erosion in On-Shore and Off-Shore Conditions

The work in this section was peer reviewed and accepted for publication in the journal of Bio and Tribo-Corrosion titled "Some thoughts on mapping tribological issues of wind turbine blades due to effects of onshore and offshore raindrop erosion" K Pugh, G Rasool, MM Stack, Journal of Bio-and Tribo-Corrosion 4 (3), 1-8 (2018) and "Raindrop erosion of composite materials: some views on the effect of bending stress on erosion mechanisms" K Pugh, G Rasool, MM Stack, Journal of Bio-and Tribo-Corrosion 5 (2) (2019)"

8.2.1 Aims and Objectives

Within this investigation, two potential issues of increased erosion due to stress and sea water (which can have damaging effects on the performance [196]) are being investigated in order to try and understand whether their effects act independently or whether they have a synergistic relationship. This research is of importance now as it encompasses both current wind turbines, primarily land based, and the new offshore structures. It considers the current operating wind turbines and whether approximate life expectancy is accurate and investigates whether stress on the blade has a considerable effect on the leading edge erosion. It also addresses future blade development as these two factors of bending stress and leading-edge rain erosion are likely to be more of significance than the older smaller blades that are less optimised. This investigation will also consider the effect of both factors in off shore and onshore conditions in order to research the effects in both locations.

8.2.2 Experimental Apparatus

The experimental rig used for this investigation was an existing setup within the tribology department at The University of Strathclyde. This rig was previously described in section 8.1. Adjustments were made to this rig to allow a bending stress to be applied to the sample. This was achieved by redesigning the sample holder to pre-stress the sam-

ple in a static 3-point bend. The sample holder was then attached to the whirling arm rig to undergo rain erosion while the sample was under stress in the 3-point bend. The bending stress was calculated by measuring the deflection the sample was experiencing. Each sample was subjected to approximately 2mm of deflection and the bending stress was then determined depending on the sample's width, length and thickness. Due to the scale of this rig with a radius of only 0.3m the samples were required to be small.

Before each test was carried out the samples were cut to size at least 2 days prior. On the day of the experiment the samples were weighed using a 5-point scale. The parameter being tested on specific experiments were set accordingly and the water supply to the tank was engaged to allow time for the environment to reach equilibrium. The samples were then inserted, and the experiment began.

After the completion of each experiment the samples were left to dry. The samples were reweighed at least 24 hours after testing to ensure they had reached a stable water absorbance and their weights would be comparable.

8.2.3 Test Conditions

The variables tested within this investigation are as follows; $v_{im} = 40ms^{-1}$, $50ms^{-1}$, $60ms^{-1}$; $\theta_{im} = 15^\circ$, 30° , 45° , 60° , 75° , 90° ; liquid medium: fresh water to simulate rain and 3.5% salt solution to simulate salt water. The impact velocity changed slightly during this investigation as the sample holders were heavier and thus made the rig unable to achieve $v_{im} = 60ms^{-1}$ as it was unstable.

To ensure the experiment was reliable; the temperature was kept constant and measured using a thermometer inside the tub; the distance the samples covered was (108km). This was achieved by varying the time; the droplet size was kept constant by only using 23G needles; the flowrate of the pump was kept constant at 0.377ml/s by keeping the pump at the same setting; the material for the test samples was kept constant using G10 epoxy glass laminate.

The stressed samples were pre-loaded in the custom sample holder by means of a threaded central member. this member can be adjusted to alter the 3 point bending stress on the samples. The stress applied to the samples tested was calculated to be 210MPa.

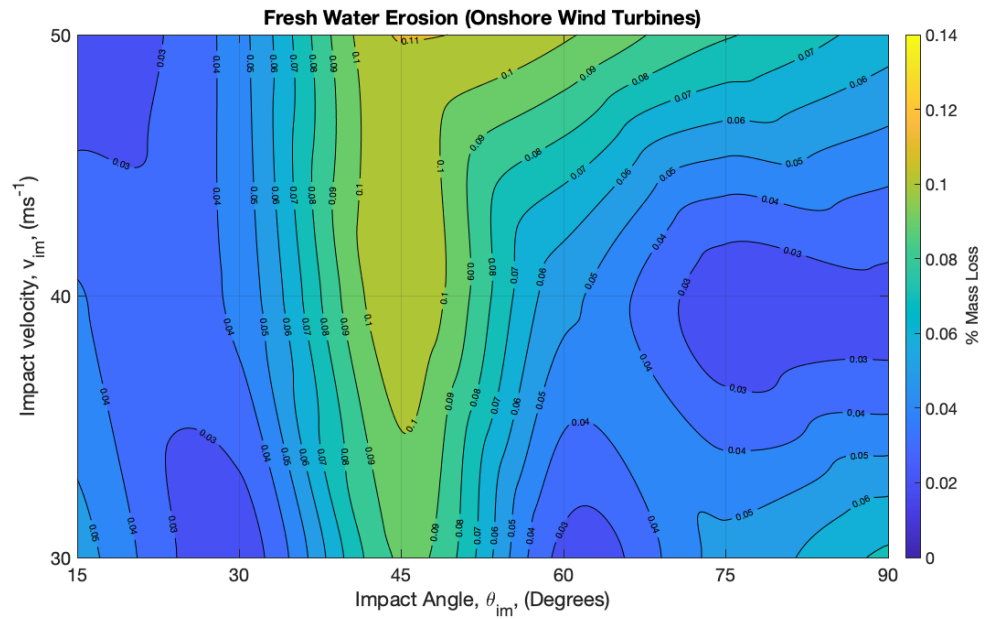
8.2.4 Post Processing

During the removal of the samples from the rig, the samples were given a wash in order to minimise the quantity of salt crystals on and within the sample. After all the samples were weighed post testing, their changes in mass were formatted within excel and MATLAB to create a wear map and a contour map which both allow easy comparison of different conditions and the amount of erosion at each variable.

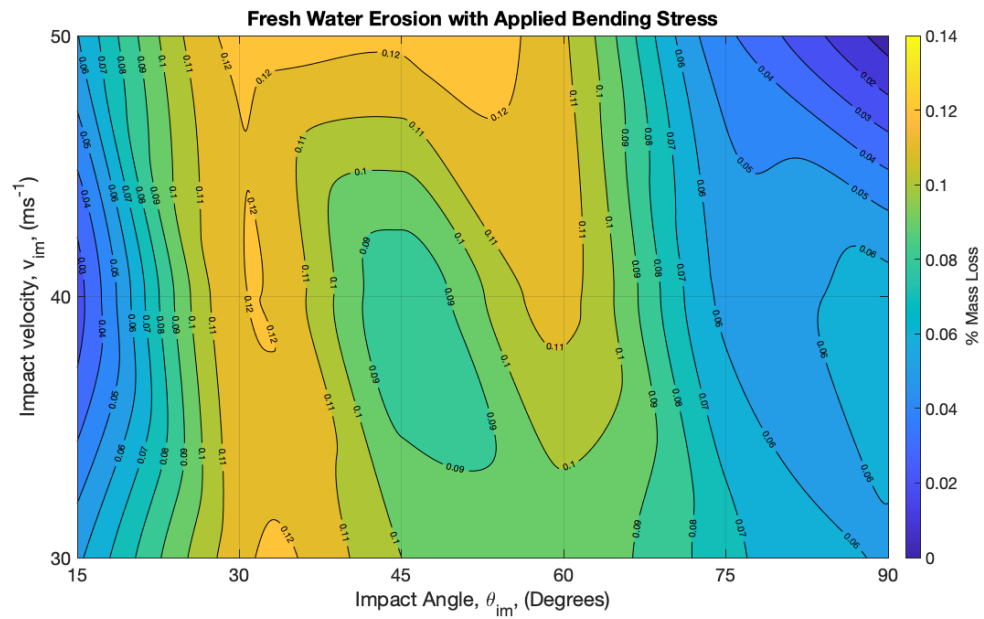
For visual inspection a reflected light microscope and SEM were used to observe surface damage on the samples. As discussed in section 6.2 there are pros and cons for the use of optical versus SEM.

8.2.5 Results

The results from this investigation are shown as follows in the form of wear maps, line graphs and micrographs.

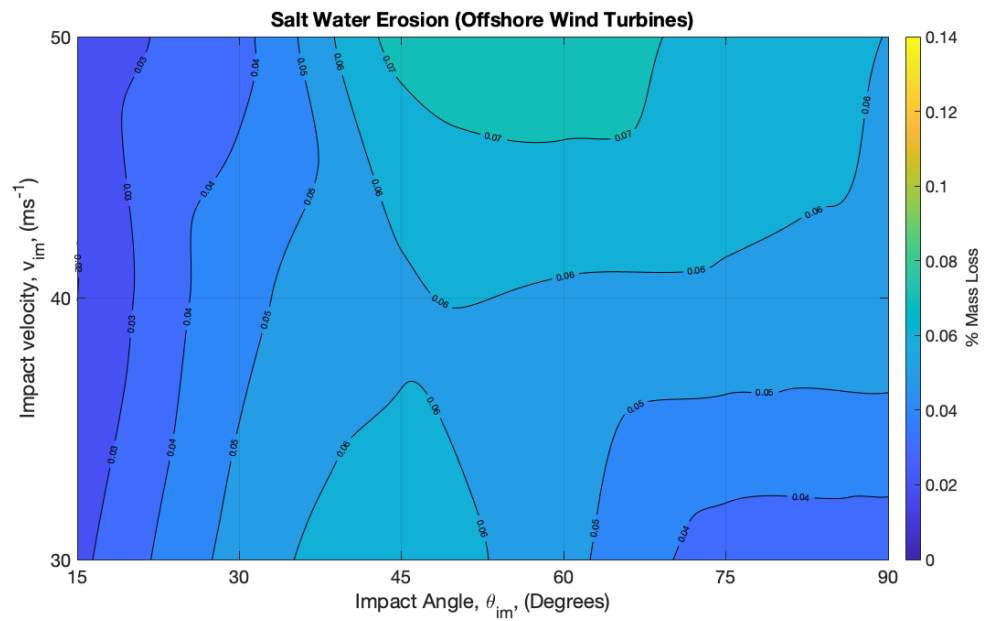


(a)

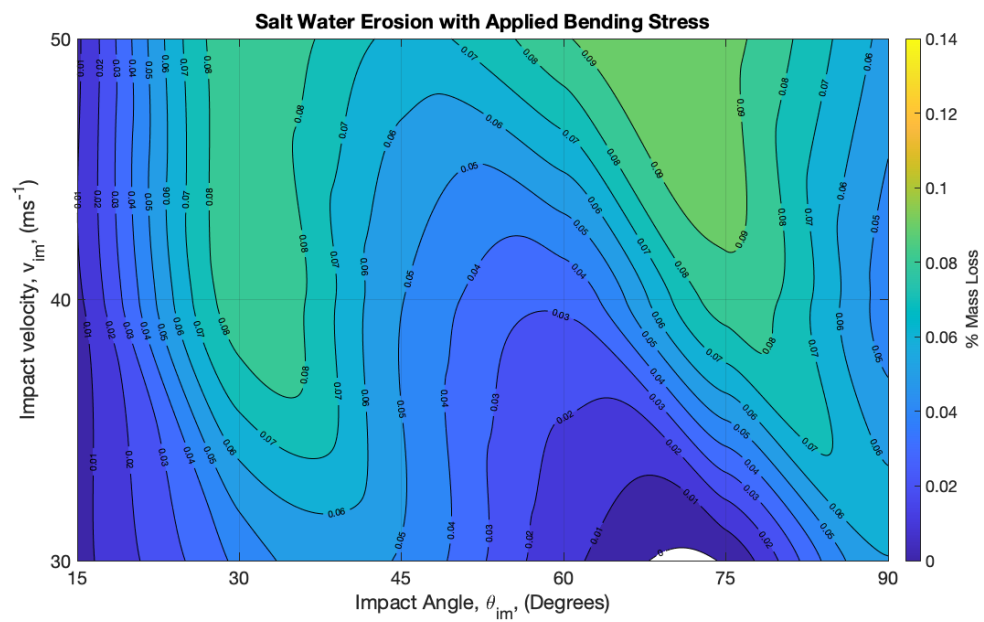


(b)

Figure 8.12: Percentage mass loss of fresh water erosion with (a) no applied bending stress (b) an applied bending stress



(a)



(b)

Figure 8.13: Percentage mass loss of salt water erosion with (a) no applied bending stress (b) an applied bending stress

8.2.6 Discussion of Unstressed Fresh Water Erosion

The first experiment that was conducted was fresh water with no applied stress. From Figure 3 the conditions that yielded the most erosion was at the maximum speed of $v_{im} = 50ms^{-1}$ and at droplet angle of $\theta_{im} = 45^\circ$ with a mass loss of 0.11%. From the wear map it is clear where the transition between negligible erosion to relatively high erosion occurs. This has been observed within the literature [56]. This is theorised to be the threshold incubation energy sufficiently significant enough to initiate erosion. This is characterised as the energy required to produce erosion on a sample, determined by the droplets mass and velocity. This behaviour was observed with the majority of all the experiments tested. This was also observed in the SEM images of the samples as the erosion was concentrated in the areas where the fibres were closest to the surface and hence the top layer of epoxy was the thinnest (Figure 8.14) .

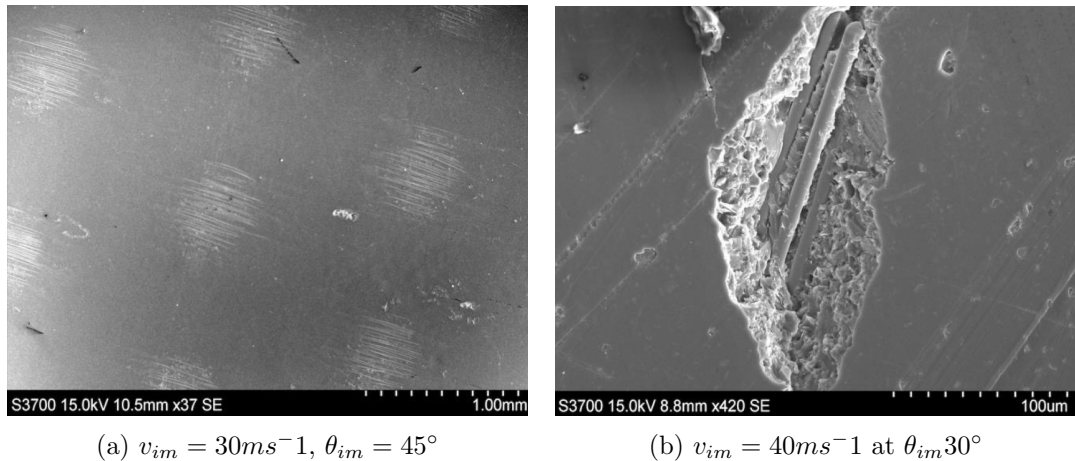


Figure 8.14: SEM images of fresh water erosion on an unstressed sample

In the first experiment (i.e. fresh water with no applied stress) the most erosive impact angle range was $45^\circ \leq \theta_{im} \leq 60^\circ$. This range of angles is interesting as classically ductile materials typically exhibit maximum erosion at relatively low angles of impact $20^\circ \leq \theta_{im} \leq 30^\circ$ whereas with classically brittle materials the erosion increases continually until $\theta_{im} = 90^\circ$ is reached [197]. This behaviour has been modelled using solid particle impacts; however, the same behaviour has been observed using liquid

impacts during these experiments.

The wear maps from this experiment, Figures 8.12a can also be visualised as a line graph shown in Figure 8.15. From this graph it can be concluded that the material is neither experiencing fully ductile or fully brittle properties as the impact angle with the most erosion is $\theta_{im} = 45^\circ$. This can be explained as G10 epoxy glass is a composite material involving a brittle glass fibre with a ductile matrix binding the fibres together. The surface features evident on the eroded samples are more in common with ductile gouging or ploughing type features rather than the fracturing or localised shattering that is evident in brittle materials [197]. As a result, the behaviour could be classed as quasi-ductile. These results agree well with the work of Ahamed et al [198] where tidal erosion was studied. It is interesting that although this work investigated erosion of G10 composite in slurries of sea water and sand (SiC), the impact angle exhibiting peak erosion is the same; thus, analogous behaviour was observed albeit in different conditions.

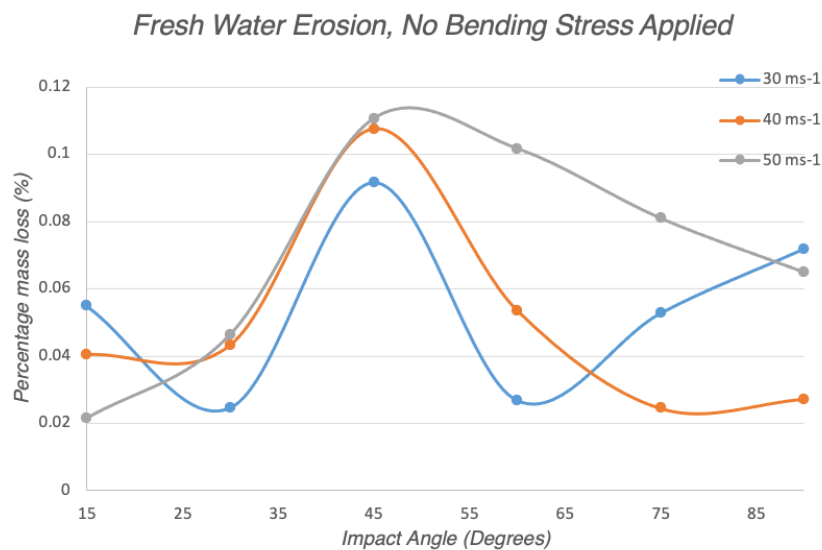


Figure 8.15: Mass loss of sample subject to fresh water erosion and no bending stress applied over various impact angles

8.2.7 Discussion of Unstressed Salt-Water Erosion

The second experiment that was conducted was with 3.5% salt water solution to simulate the effects of sea water on wind turbine blades under the same parameters to which the fresh water was tested. This was to determine if offshore wind turbines are eroding differently to those on shore. Figure 8.16 below depict the erosion occurring to an extent where the glass fibres on the surface are exposed.

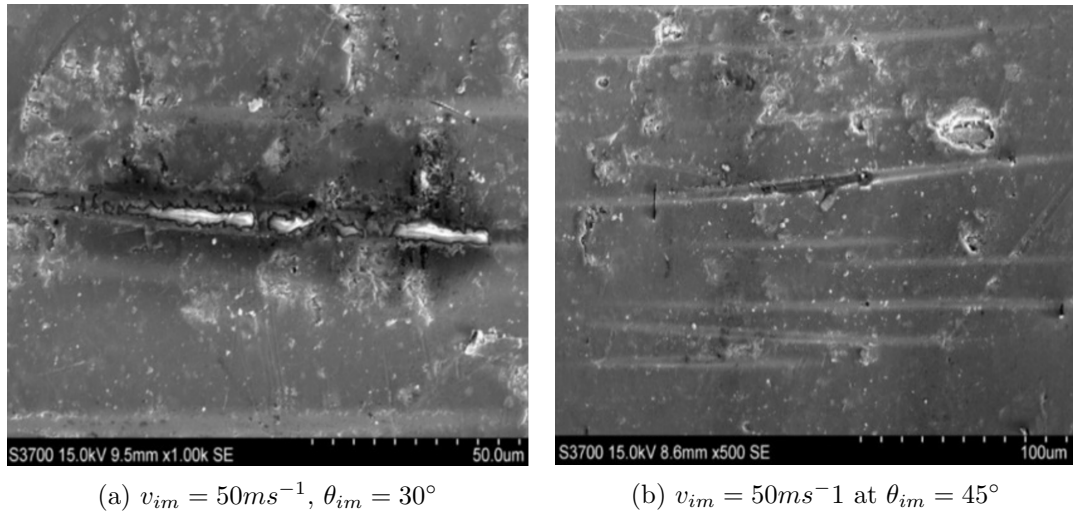


Figure 8.16: SEM images of salt water erosion on an unstressed sample subject to salt water erosion

The wearmap produced in Figure 8.12a was constructed with experimental data with neutral water and the wearmap in Figure 8.13a was constructed using 3.5% saline solution as sea spray. The results showed that neutral water had more mass loss from the wear maps, however the SEM examination results were contradictory as there was more damage present on the samples which were subject to salt water impacts. An EDX (Energy Dispersive X-ray) analysis was carried out on the samples to determine their composition and it was concluded that the samples which were being eroded by salt water, despite having a thorough rinse still retained small quantities of salt as there were significantly higher sodium and chlorine in the salt water samples compared to the neutral water samples and these crystals can be observed in the SEM micro-graph in Figure 8.17.

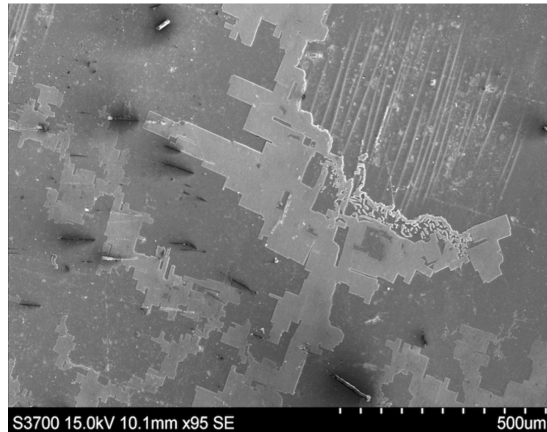


Figure 8.17: SEM image of salt crystals remaining on the surface after washing

The maximum mass loss during this experiment was experienced at $v_{im} = 50ms^{-1}$, $\theta_{im} = 60^\circ$ with a total loss of 0.077%; this can be observed in the wear map, Figure 8.13a. The line graph (Figure 8.18) that was produced from the wear maps of the salt water testing (Figure 8.13a) is shown below. These results show neither fully “ductile” nor “brittle” erosion behaviour [197] as described in the literature in a similar fashion to the result exposed in fresh water.

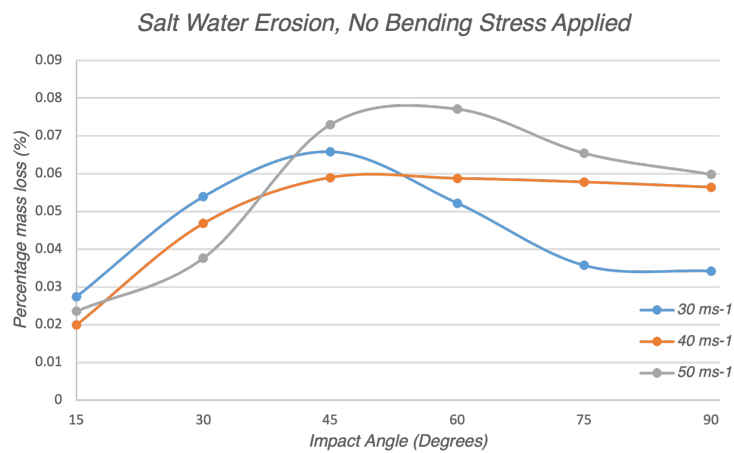


Figure 8.18: Mass loss of sample subject to salt water erosion and no bending stress applied over various impact angles

8.2.8 Discussion of Applied Bending Stress in Fresh Water and Salt Water Erosion

The next tests that were conducted were a repeat of the fresh water and salt water experiments but under a static 3-point bend. This was to replicate the stresses which large wind turbine blades experience while in operation.

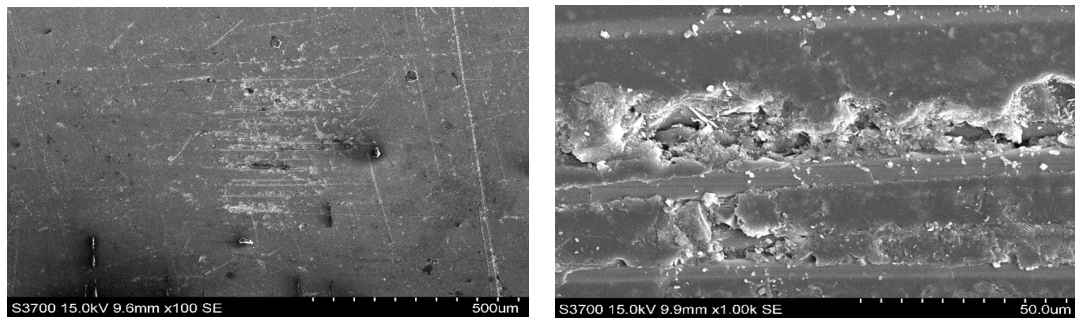
The maximum mass loss was $v_{im} = 50ms^{-1}$ at $\theta_{im} = 30^\circ$ and $\theta_{im} = 45^\circ$ with a 0.12% mass loss, this can be observed in the wear map in Figure 8.13a. This mass loss can be seen in the SEM images in Figure 8.19a and 8.19b as the top layer of epoxy is eroded to the point where the fibres closest to the surface are exposed. The erosion is accelerated in this region due to the surface being slightly rougher at this point and the ploughing mechanism of the water droplet seems to have more effect on the surface by removing material. This is also observed in the optical microscope images of the unstressed sample (Figure 8.20a and 8.20b) as the point at which the fibres are closest to the surface show a greater dark area. From the wear maps in Figures 8.12b and 8.12a an unusual pattern occurred over the different impact angles in that greater erosion was evident at a larger range of impact angles.

As can be observed from Figures 8.18 and 8.15 the fresh water erosion experiment produced a greater peak percent mass loss than salt water erosion with the peak percentage mass loss occurred at the same impact angle. Analysis of the samples showed two significant features; firstly the extent of erosion appeared significant in the salt water erosion samples, secondly significant salt crystals were still present on and with the material, even after washing. From this observation the direct correlation of mass loss and erosion degree for salt water specimens can be misleading due to the residual weight of the salt within the specimen. The SEM analysis indicated greater erosion for the salt water samples than the fresh water.

The manner in which erosion occurs on the material from liquid impacts changes depending on the impact angle, in the same fashion as a particle impact. At lower im-

at lower impact angles the mechanism is more abrasion dominant resulting in shearing of the top surface; this can result in significant mass loss to the material, as once the top layer of the matrix is compromised, the fibres which are more brittle are exposed. This is seen in an SEM image Figure 8.19b. It is postulated that the high surface stresses influence the resultant damage caused by the liquid impact on the material. As a result, the classical ductile to brittle crossover graph [197] for the stress test would be altered.

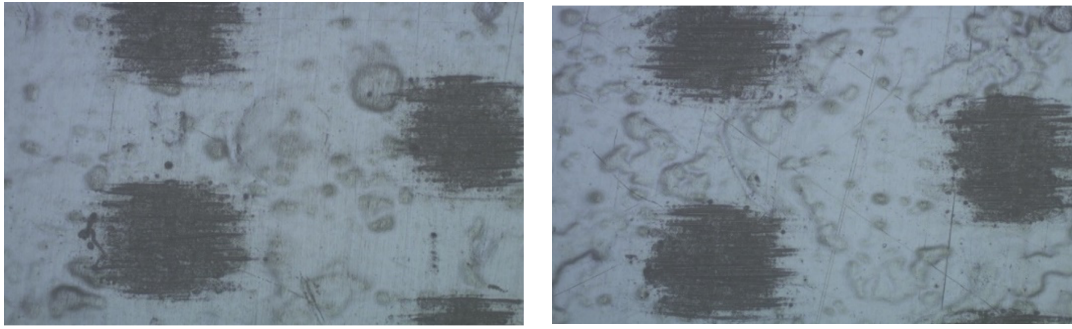
At higher impact angles, the water droplet induces a much larger force perpendicularly onto the sample resulting in sub surface cracks and brittle/ fatigue type wear, potentially leading to delamination [90]. These two erosive mechanisms synergise to produce a distinctive pattern of erosion found in Figures 8.12a, 8.13a, 8.15 and 8.18 which is consistent with the literature [197]. When the tensile side of the stressed sample is exposed to rain erosion, however, it varies from this pattern.



(a) Fresh water at $v_{im} 50ms^{-1}$, $\theta_{im} = 30^\circ$ (b) Salt water at $v_{im} = 50ms^{-1}$ at $\theta_{im} = 45^\circ$

Figure 8.19: SEM images of erosion on the GFRP samples subject to an applied bending stress

The stressed samples showed different surface features in the optical microscope images as a circular ridge formation; this was not present in the optical microscope images of the unstressed samples (shown in Figures 8.20a and 8.20b). It is postulated that this is the result of the stresses on the material. The feature can be observed in the Figure 8.21.



(a) Fresh water at $v_{im} = 50\text{m/s}$, $\theta_{im} = 30^\circ$ (b) Salt water at $v_{im} = 50\text{m/s}$ at $\theta_{im} = 45^\circ$

Figure 8.20: Optical microscope images of erosion on the GFRP samples subject to an applied bending stress

It is postulated these features are associated with deformations of the top surface due to the impact of a water droplets which can be termed SICD (Surface Impact Circular Deformation). In Figure 8.21a there appears to be an area of microcracking in the top surface to the right of the SICD; this was speculated to result from the impact of a droplet causing tensile stresses. This crack could explain the slightly higher magnitude mass loss in the stress tests compared to the unstressed tests as this crack is liable to increase the erosion rate resulting in the glass fibres being at an increased risk of erosion which would lead to considerably more mass loss.

SICDs were only found on the stressed samples; this was likely due to the sample being held under conditions closer to its fracture stress and the effect of any additional stress on the sample by a liquid impact has more chance to cause deformation of the top surface, resulting in a greater visible distribution to the surface. The shape of the SCIDs can be described from the shockwave that the droplet creates on the sample.

A comparison between an unstressed and stressed sample can be shown in the line graph in Figure 8.22, illustrating $v_{im} = 50\text{m/s}$ using fresh water as the erosive medium.

From this graph (Figure 8.22), the stressed sample experiences higher erosion over a larger range of impact angles and experiences erosion beyond threshold at lower angles

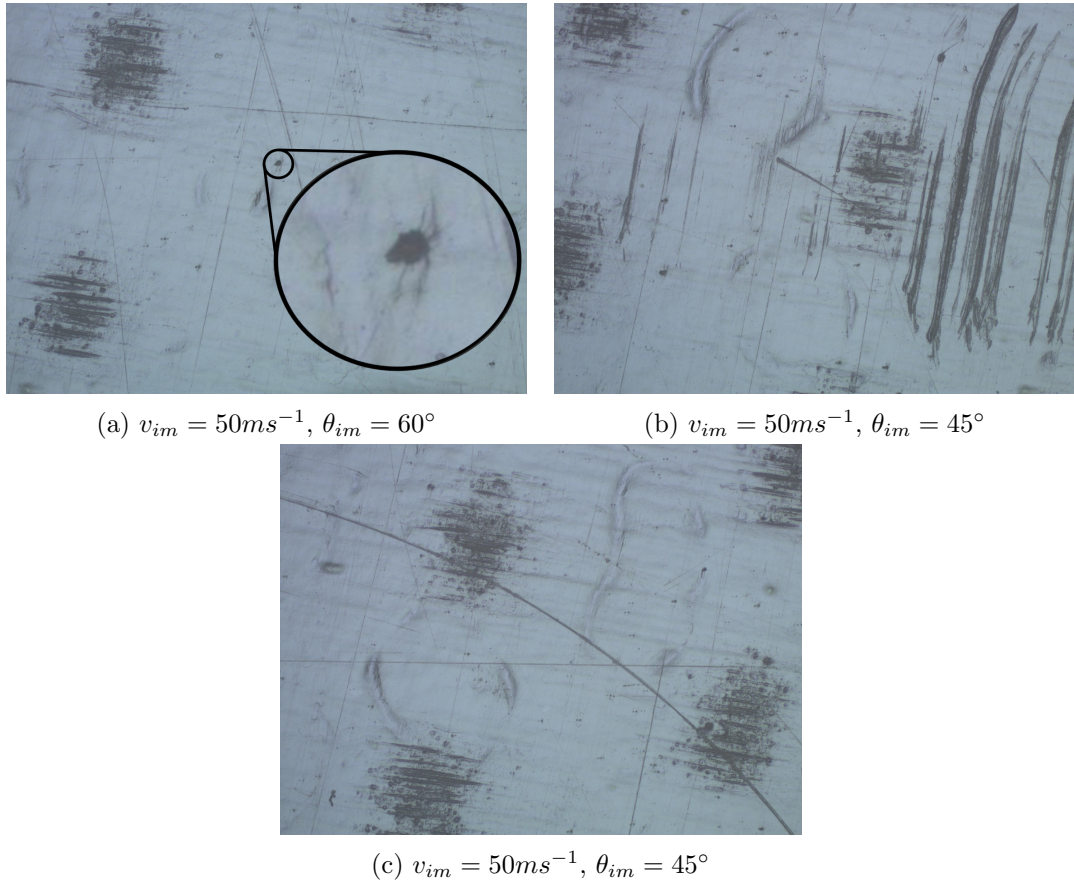


Figure 8.21: Optical microscope images of fresh water erosion on the GFRP samples subject to an applied bending stress

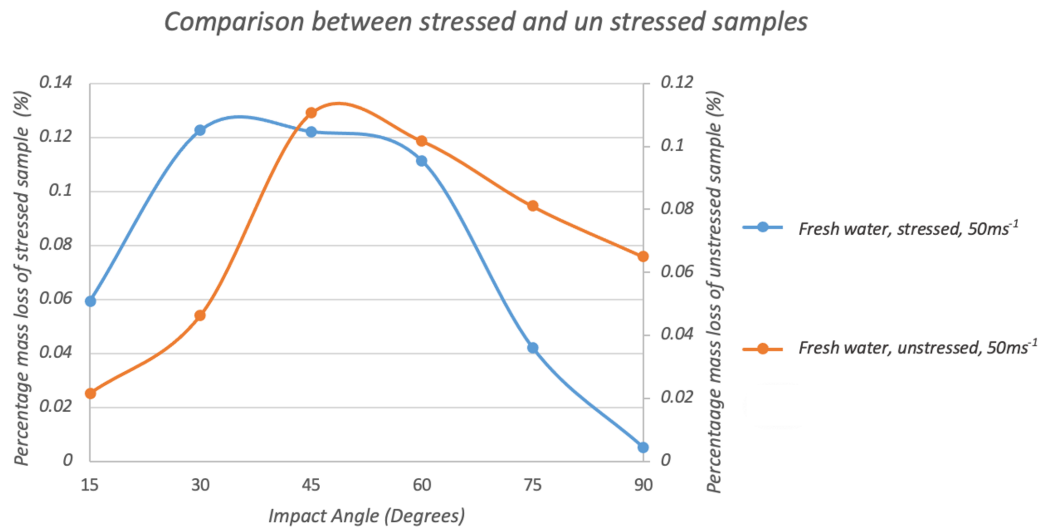


Figure 8.22: Comparison of mass loss between the stressed and unstressed GFRP sample

of impact. It can, therefore, be deemed that the stressed sample is more susceptible to erosion than the unstressed sample. It is postulated that the stressed sample is experiencing a larger crossover between abrasion and brittle/fatigue erosion which allows the top epoxy surface of the material to be breached and have fibre exposure. This behavioural change when the material is stressed is theorised to be due to the additional stress from the droplet impact causing deformation (as all stresses are additive). The graph suggests the sample is now behaving in a more “ductile” than “brittle” manner due to the slight shift to the left. This change could be due to the polymer (which is the more ductile portion of the material) governing the behaviour rather than the brittle glass fibres. Experimental evidence to support this would be the presence of SICDs on the surface, with these features indicative of ductile behaviour due to the applied stress.

During the salt water testing of the pre-stressed samples, the same pattern of a wider range of impact angles experiencing more considerable erosion was observed. In addition the salt water tests clearly illustrate that above 30ms^{-1} the salt water erosion becomes increasingly brittle. This suggests similar mechanisms were involved for both

exposure media.

The results were also collated into a mechanistic map, in a similar method to Rasool [199]. This is shown in Figure 8.23

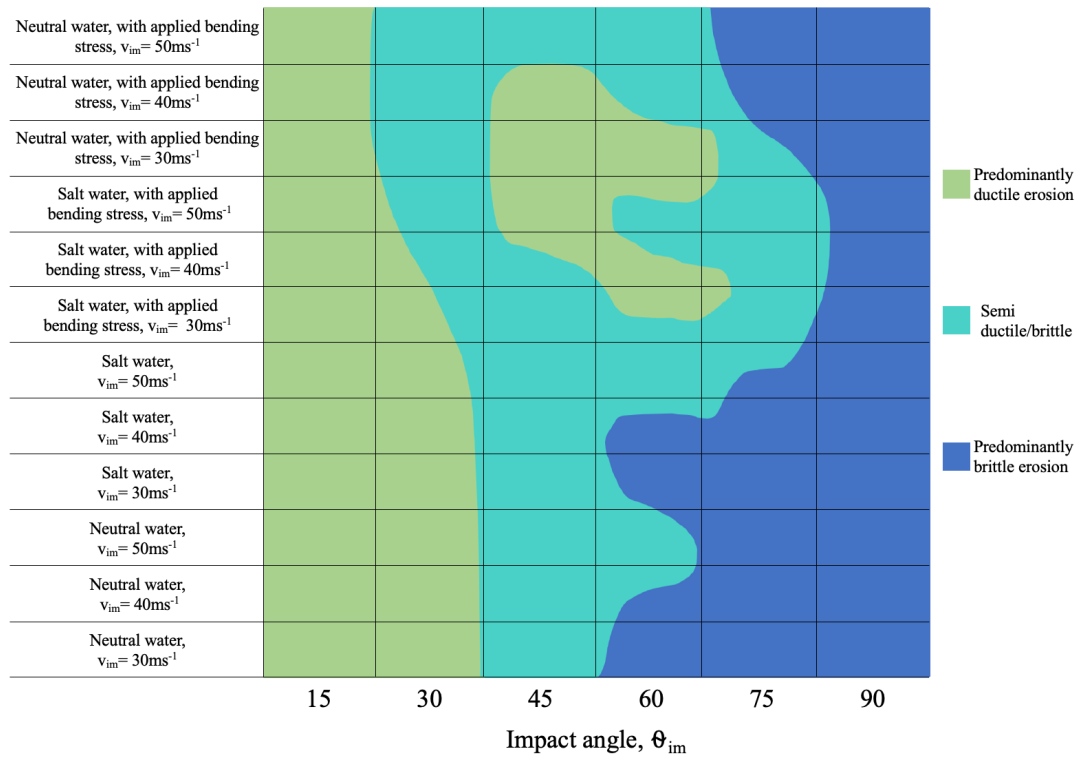


Figure 8.23: Erosion mechanistic map

8.2.9 Conclusions

1. Studies have indicated that there is a difference in material behaviour observed for rain erosion on a wind turbine blade when the material is unstressed compared to when the material has an applied load.
2. The difference in behaviour is theorised to be due to the synergy between the initial stress plus the stress from the droplet impact, causing deformation of the epoxy/polymer of the material when under stress.
3. Increases in the stress state of the material subject to testing has had two effects;

the first was higher erosion over a larger range of impact angles. This was due to a larger crossover between the abrasive mechanism and the brittle/ fatigue mechanism by the droplet. The second was a different surface interference on the material due to the droplet impact which resulted in the creation of morphological feature on the top surface, Surface Impact Circular Deformation, (SICDs).

4. It was concluded that for these studies, the erosive medium for liquid impact did not significantly affect the range of impact angles at which the highest erosion rates were observed.
5. Salt water erosion showed more significant damage to the surface of the samples and as a result it was deemed that sea water spray does increase the erosion rate on wind turbine blades for equal measures of exposure. In the field off-shore wind turbines are likely to experience increased droplet interactions due the spray from the waves in addition to the rainfall.

8.3 High Speed Rain Erosion in Large Scale Experiment

8.3.1 Aims and Objectives

The WARER utilised in these experiments was designed, manufactured and commissioned as part of this research to study the effects of rain erosion on materials at a significantly higher velocity than studied previously and with superior precision. It was designed to provide an extremely valuable tool for further investigation into the impact phenomenon associated with water droplets and the leading edge of large, multi-megawatt wind turbine blades. The flexibility and capabilities of this new and larger rig allowed the opportunity for a continuation of the study into the effect of bending stress on the wind turbine material under higher impact velocities as it was possible to expand the test criteria utilising this new facility and operate at impact velocities greater than $v_{im} = 60ms^{-1}$ ($v_{im} = 60ms^{-1}$ for stressed samples) and larger samples with variable stresses applied. The sample holders were specifically manufactured for

this investigation and the aims for the research were as follows:

- To investigate the effect different magnitudes of bending stress applied to the wind turbine blade material to quantify the effect this has on the erosion rate of the surface and to investigate what effect this has on the degradation mechanisms that will be active.
- To investigate the wear rate of these samples under bending stress at three levels of impact velocity and three angles of impact. Their mass loss will be measured intermittently in order to predict further erosion of the material. The highest velocity will simulate the speed achievable by the larger turbines and those under future development.

The first round of experiments investigated the effect of bending stress on wind turbine blade material subject to rain erosion was restricted to a fixed stress for all the experiments conducted. In this study three stresses are investigated as well as a control with no stress applied. It was expected that this study would provide valuable information on the relationship between the internal stresses of the material and the rate at which mass is lost from the material. This would therefore allow for more accurate erosion calculations to be made for the newer turbine blades which are being commissioned. These turbines are trending to significant larger sizes this will, not only increase the impact velocity at the tip but due to weight of the blade size it could also significantly increase the stresses experienced as blade design is optimised for these demanding designs. As shown in the literature [57] the impact droplet occurrence is a high stress event over a very short period of time. It is hypothesised that as stresses are additive the combination of the physical bending stresses of the blade in operation with the water droplet impact event will change resulting in greater mass loss and erosion.

8.3.2 Experimental Constants

As this investigation was primarily researching the effects of bending stress on erosion rate of wind turbine blade materials, where possible other variables were kept constant within the experimental rig and the values were selected to best represent the environmental conditions encountered at a wind farm located within Scotland. These constants include;

- Temperature
- Rain rate
- Number of impacts during experimentation
- Size of water droplets
- Sample material
- Humidity

Most of these parameters were set at a predetermined constant before the experiment to align with previous experimental campaigns and others including temperature and humidity were unable to be set but were closely monitored in order to detect and fluctuations.

As mentioned previously the droplet size was chosen to match the previous experiment and this was measured using the high-speed camera and the determined droplet diameter for this experiment is 2.40mm.

The rain rate was kept constant throughout at 50mm/h and this was calibrated thoroughly by testing the flow rate of the pumps and making sure the motor controller and pump combination was producing the same flowrate for all 4 pumps. The value of 50mm/h was also determined as this is on the higher end of realistic rainfall for Europe and with the temperatures and droplet size for the experiment it was emulating real world environmental conditions. This rainfall rate was previously used in the smaller

rig and gives the opportunity for results comparison.

For the temperature and humidity, these parameters were measured, however, they were not controlled. The test rig is located in an air-conditioned, large scale lab setting and is placed in a sub floor thick walled, blast proof pit. As a result, the environmental conditions are largely stable. The temperature and humidity were measured throughout the experiment. The general temperature remained constant throughout the experiment measured at $T = 18^{\circ}C$ and the humidity varied from between 36% and 62%. This variation relative humidity did not affect the experiment (proven by repeat samples) as there was a significant drying period post testing.

8.3.3 Experimental Variables

The variables for the experiments were the impact velocity, angle of impact and the stress applied to the sample (σ_{bend}). Three impact velocities were chosen; $v_{im} = 60, 70$ and $80ms^{-1}$, three angles were chosen; $\theta_{im} = 30, 60$ and 90° and four different stresses were chosen, these values were 0, 87.5, 175 and 350MPa. The impact velocities were selected to replicate the impact velocities of larger, multi-megawatt turbines that are being implemented into the grid more regularly and also to be coherent with previous experiments using this material. The angles chosen were based on the previous experimental data in sections 8.1 and 8.2.

The calculated stresses using computational methods in section 7 was 79.6MPa for a steady windspeed of $10ms^{-1}$ and a blade length of 117.3m. This has established the lower bound stress for testing. The decision to include greater stresses of 350MPa was in order to take cognisance of increase loads due to wind gusts and could represent future turbine blades which will be inevitably longer and with optimised design will likely experience higher stresses. 350MPa should be the upper limit as the flexural strength of the material is 448MPa, giving it a safety factor of 0.78 and it is unlikely that a component would be implemented onto a turbine blade with anything higher. Increments of stresses applied to the samples was chosen in doubling magnitude until

350MPa to allow for both linear and log patterns to be observable, therefore the final stresses which were chosen were 0Mpa 87.5Mpa, 175MPa and 350MPa.

8.3.4 Bending Stress Calculations

The previous experiment conducted on the effect of bending stress coupled with rain erosion was carried out with only one level of stress. For this experiment however, in order to try and discover the relationship between the magnitude of erosion with respect to the magnitude of bending stress present in the material. To accurately measure the correct deflection required to produce the target bending stress the following diagrams and equations were utilised shown in Figure 8.24.

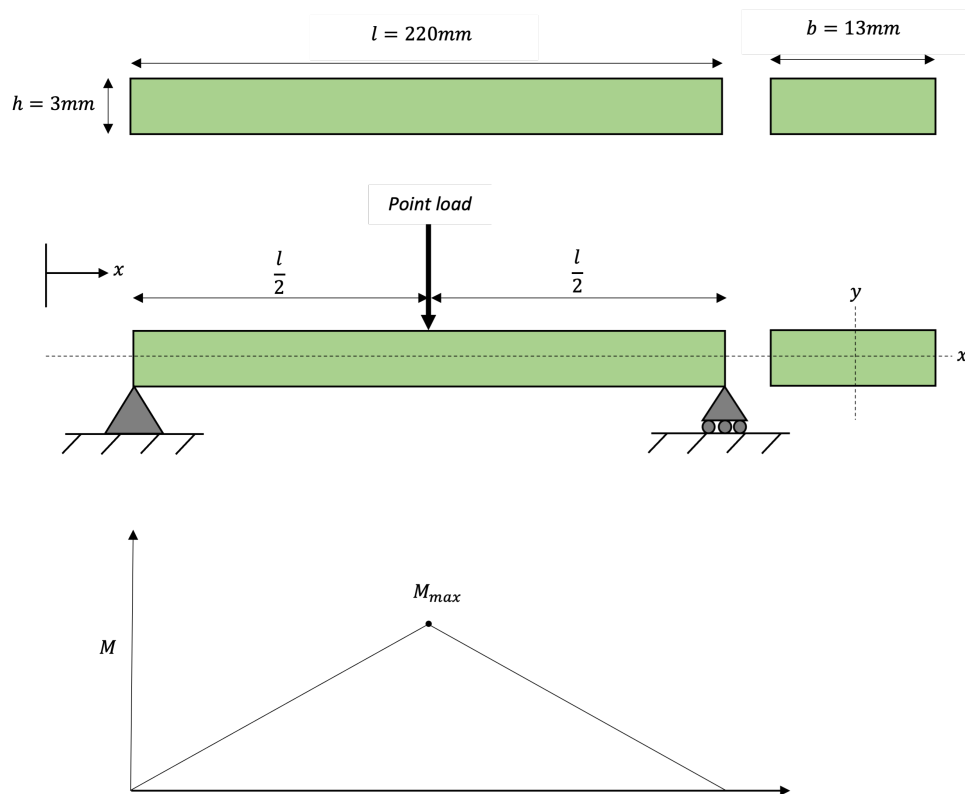


Figure 8.24: Diagram of GFRP sample under load displayed as a simply supported beam

$$y = \frac{h}{2} \quad (8.1)$$

$$\delta_{\max} = \frac{Fl^3}{48EI} \quad (8.2)$$

$$M = \frac{Fl}{4} \quad (8.3)$$

$$\sigma = \frac{My}{I_x x} \quad (8.4)$$

$$\sigma = \frac{12 E h \delta_{\max}}{2 l^2} \quad (8.5)$$

Figure 8.24 shows the way in which the bending stress is applied to the GFRP sample, which is notated in green in the diagram. The point load is applied in the middle of the sample by a threaded bolt to which the deflection of the material can be finely adjusted and the maximum bending stress is located at the midpoint along the length of the sample. In order to calculate the correct deflection needed to produce the required bending stress equations 8.1, 8.2, 8.3, 8.4 and 8.5. Where y is the distance to the axis, δ is the deflection, F is the force applied by the bolt during deflection, E is the youngs modulous of the GFRP sample, σ is the bending stress, M is the moment applied by the bolt acting on the supports and I is the second moment of area.

Equations 8.1, 8.2, 8.3, 8.4 are all standard equations from structure theory and when combined together they give the relationship seen in equation 8.5. This equation then allows for the calculation of the precise deflection needed to produce the required bending stresses. When the experiment was being setup digital calipers were used to accurately measure the correct deflection. A sample in its holder can be seen in Figure 8.25.

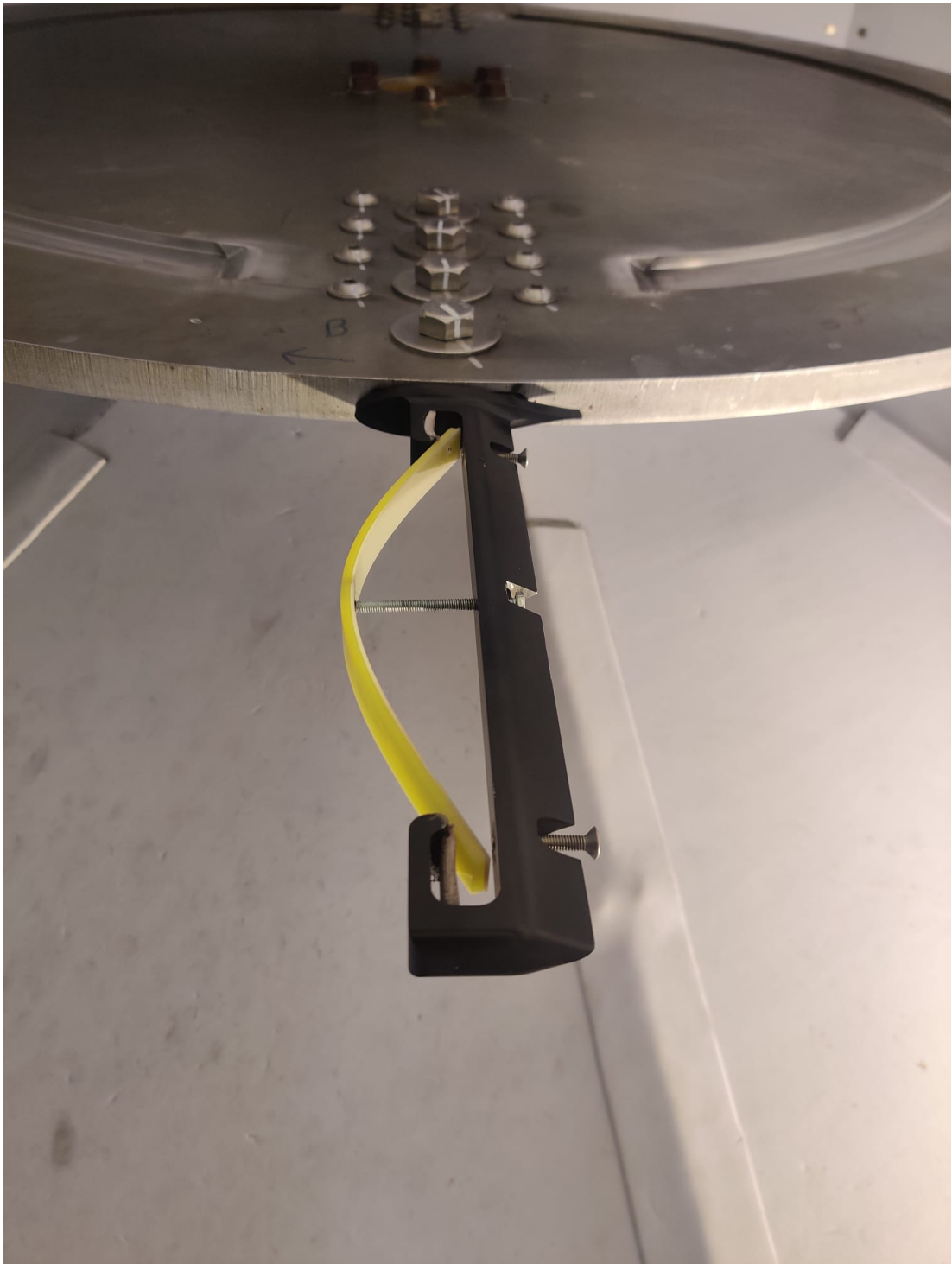


Figure 8.25: GFRP sample stressed to 350MPa in the holder within the WARER

It was planned to test 3 samples at 4 different stresses, 3 different velocities and 3 different angles giving a total of 108 samples. The reason for 3 samples under each test condition was to calculate an average to reduce experimental error. Each sample was inserted into the WAREER for a distance of 2,160km. As there were samples which would be travelling at slower velocities this resulted in the time of exposure varying. The distance travelled by the sample is more representative test as the number of impacts the sample will endure will be more constant. Springer [113] also used this approach in his model.

As the accumulation of erosion was of interest and how the GFRP material degrades the 2,160km was broken down into four stages, 0 – 216km, 216 – 432km, 432 – 1080km, 1080 – 2160km. The reason to stop the first experiment at 216km was to align with the previous experiment which increased in increments of 216km and this would allow for a comparison between the small rig and the new larger rig. The last distance of 2160km was taken as an arbitrary value for the $v_{im} = 60ms^{-1}$ experiment to last 10 hours.

Once the samples have been tested and dried in a neutral environment, they were weighed after each of the four stages of the experiment and logged. While completing the weighing of the samples a close visual inspection was performed on each of the samples in order to determine if there were any notable surface imperfections which were not present before the experiment. If there were any visible surface defects it was noted and they were analysed more closely under the optical microscope.

From Section 6.2 it was deemed the optimal method for analysis on rain erosion samples is by a profilometer. This method was implemented into this investigation shown in Figure 6.9 and provided in depth information on the sample surface. In order to document the progress of erosion the optical microscope was utilised which allowed for some detailed imagery of the surface topography allowing the analysis of the surface and the development of these surface defects.

In summary the input parameters are as shown in table 8.3

Test Parameters	WARER
Impact Velocity, v_{im} (ms^{-1})	60, 70, 80
Rainfall rate (mmh^{-1})	50
Droplet size (mm)	2.4
Impact angle, θ_{im} ($^{\circ}$)	30,60,90
Test intervals (km)	216, 432, 1080, 2160

Table 8.3: Summary of test parameters for high speed rain erosion testing

8.3.5 Experimental Procedure

The experimental procedure is summarised below:

- The GFRP samples were carefully placed into the their holder as shown in Figure 8.25.
- The sample was then secured into place and the middle bolt was turned until the specific deflection for the required bending stress was acquired.
- The water pumps were primed, this involved turning on all the peristaltic pumps until all air is removed from the system.
- All safety checks were completed in the underground bunker.
- The main isolator switch is engaged to turn on the power.
- The bunker is then evacuated and all gates are closed and all interlocks are activated.
- The motor drive is then programmed to spin up to the desired speed via the computer located on top of the bunker as shown in Figure 5.4.
- Once the disc is maintaining the desired rotational velocity, the pumps are then powered on to the desired flow rate to start the production of droplets. This is

the start point of the experiment and hence a timer is started for the required length of the experiment.

- While the rig is operational personnel must be present at control panel for safety reasons in order to observe the CCTV and the oscillation outputs from the accelerometers.
- Once the timer is complete the pumps are deactivated stopping the experiment. The motor drive is also stopped within the same moment and the spinning assembly slowly comes to a rest.
- Once the spinning assemble has come to a complete rest the bunker is granted accessibility by the interlocks.
- The power is then cut at the main isolator switch.
- The samples are then carefully removed.
- The samples are given 24 hours to dry in a controlled environment before being analysed and weighed.

8.3.6 Results and Discussion

The test matrix was not completed. After testing 102 samples, the new large scale WARER was instructed to be shut down by the health and safety department of the University. The HSE's concern was the failure of a colleagues sample holder during his commissioning phase. This failed sample holder was a different design to the one utilised in this test programme. This incident was completely contained within the 3mm of stainless steel shell of the test rig. In addition the test rig is located in a 620mm thick concrete bunker separating the rig from any personnel. This incident was classified as a near miss event and the test rig remains out of commission.

Although the test program was not completed the new WARER performed exemplary as it was very controllable, reliable and for this experiment completely safe.

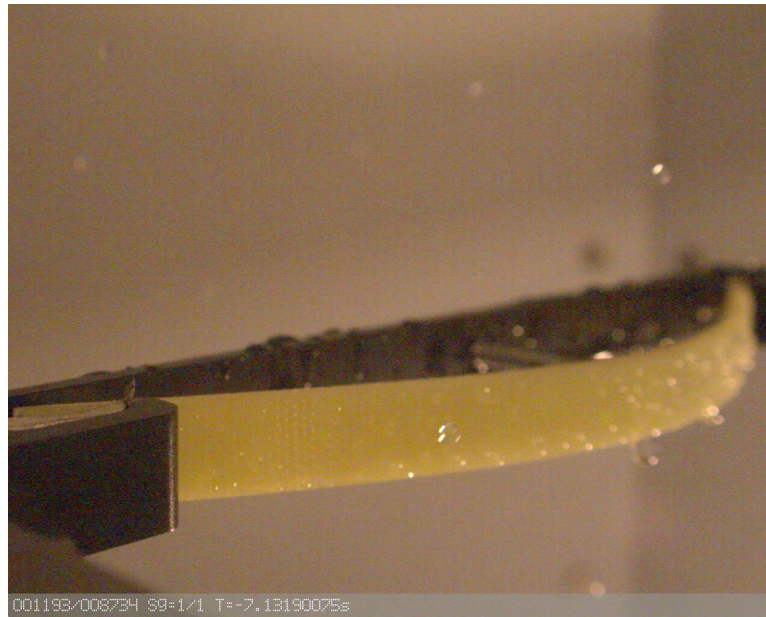


Figure 8.26: GFRP sample in the WAREER captured with the Cronos 1.4 high speed camera

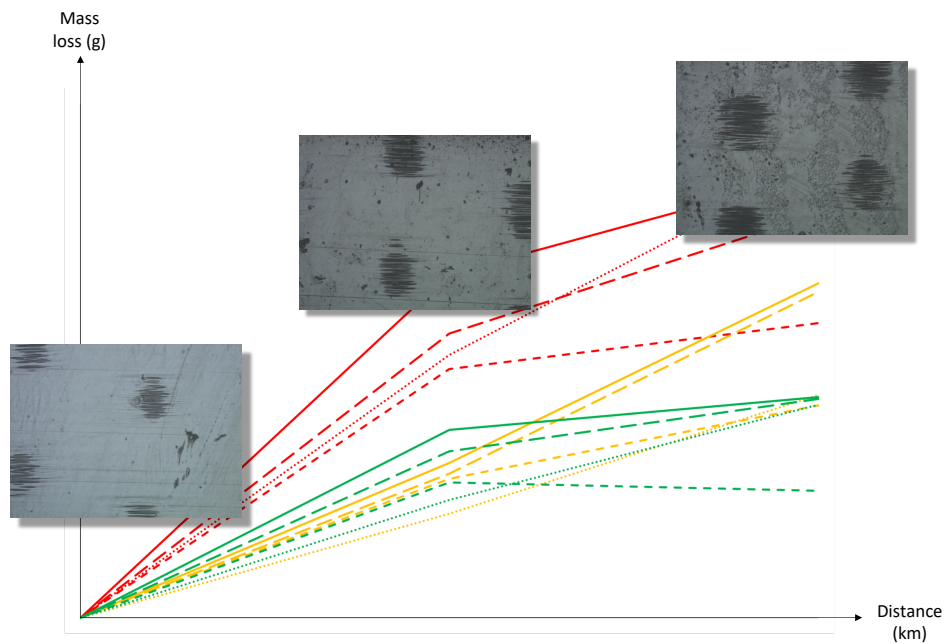


Figure 8.27: Results from the high speed WAREER illustrated as a line graph of mass loss over distance including all impact velocities with optical microscope images of a sample subject to $v_{im} = 80ms^{-1}$ and 350MPa at 0km, 216km and 432km

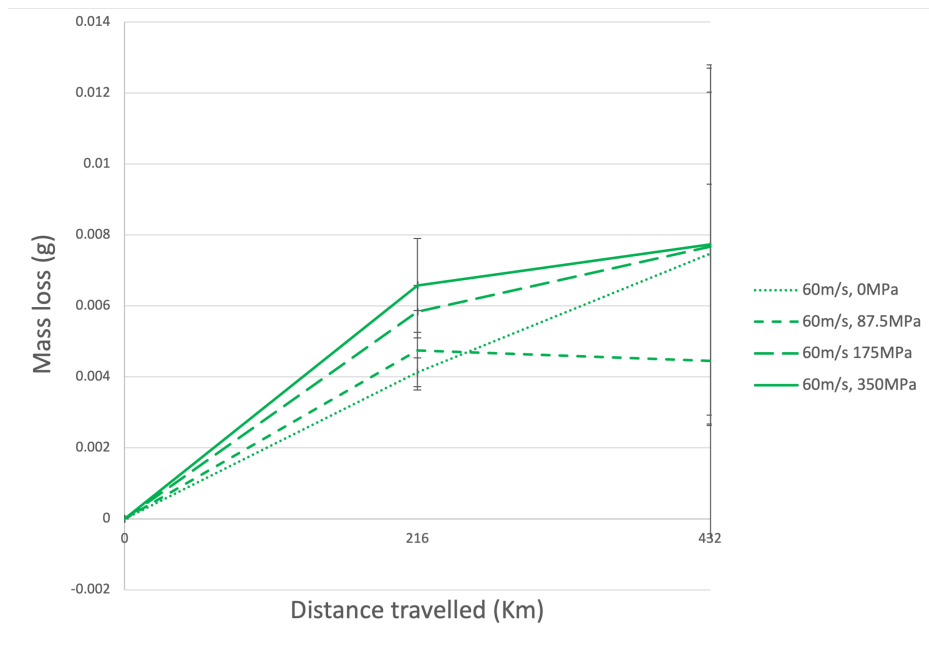


Figure 8.28: Results from the high speed WARER illustrated as a line graph of mass loss over distance travelled at $v_{im} = 60ms^{-1}$

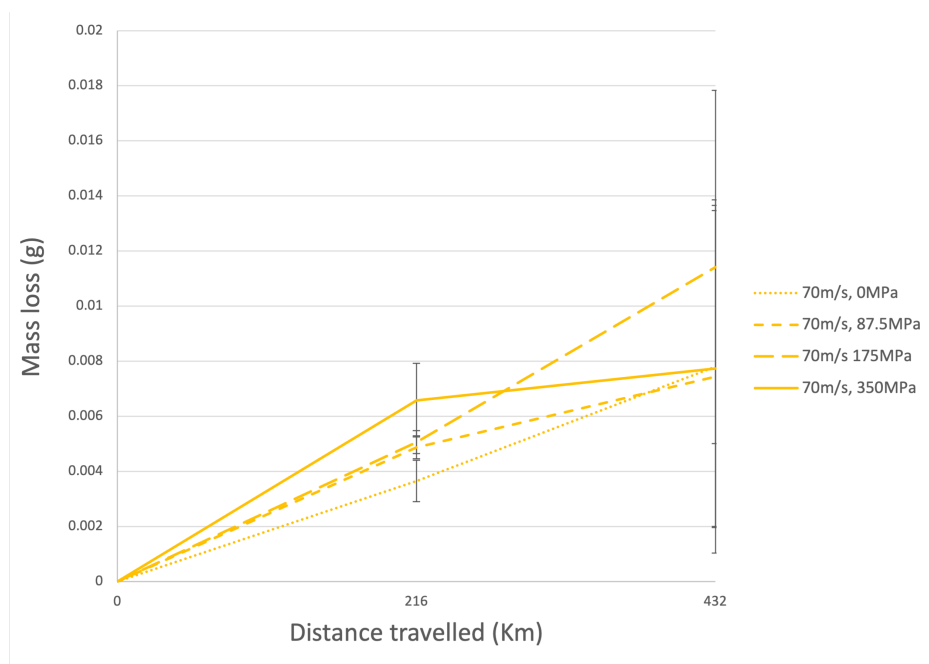


Figure 8.29: Results from the high speed WARER illustrated as a line graph of mass loss over distance travelled at $v_{im} = 70ms^{-1}$

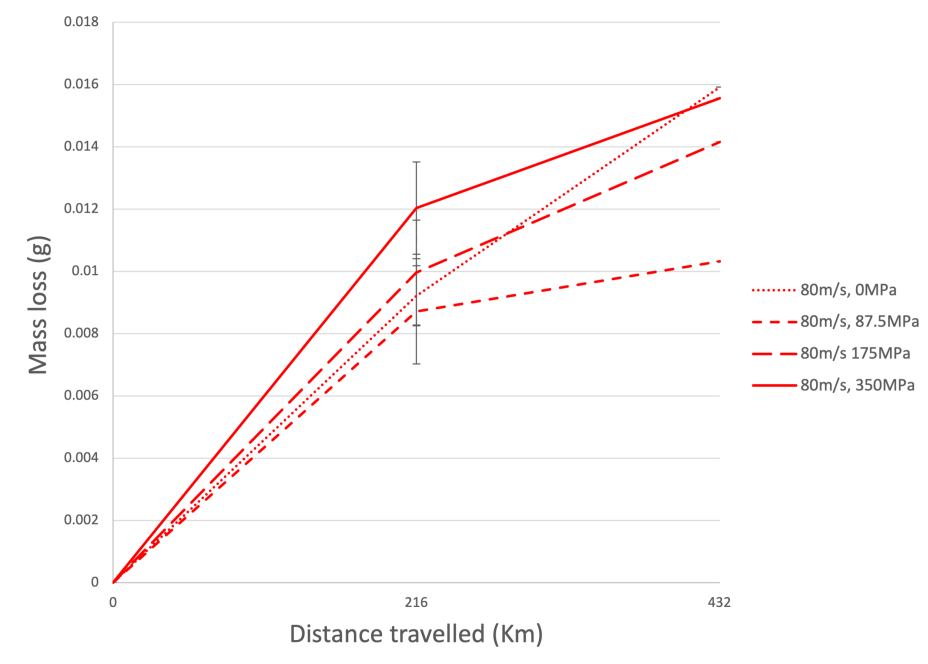


Figure 8.30: Results from the high speed WAREER illustrated as a line graph of mass loss over distance travelled at $v_{im} = 80ms^{-1}$

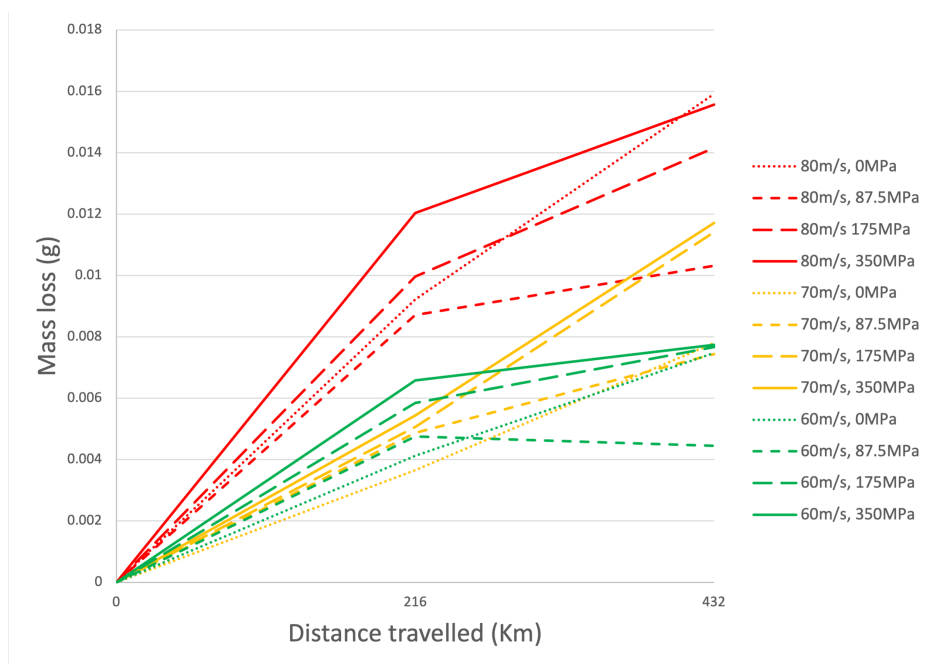


Figure 8.31: Results from the high speed WAREER illustrated as a line graph of mass loss over distance including all impact velocities

An extremely useful tool throughout this investigation for the clarification of dynamics is the high-speed camera, which is capable of 36,000fps (frames per second). While the samples were in the rig being eroded the high-speed camera was used to clarify that the droplets were in fact impacting the sample as expected. Figure 8.26 is a frame from this videography and clearly shows the impact of a droplet onto the rotating sample.

Figure 8.27 is the combination of the data produced at $v_{im} = 80ms^{-1}$ with overlaid micro-graphs showing the erosion at each stage. It can be observed that the progression of erosion is evident on the surface of the GFRP sample as the small pits become more common in the latter stages as the top layer of epoxy starts to thin and degrade by the impacting water droplets.

The experiments that were concluded were the first two stages of all four stresses, all three speeds and at 90° however not all repeat tests were concluded for these parameters. The data which was collected during testing is illustrated in Figures 8.26, 8.27, 8.28, 8.29 and 8.30 .

From the result it can be concluded that there was loss in mass from the first 216km worth of exposure with all impact velocities and bending stress combinations. The mass loss recorded at low distances showed little difference between $60ms^{-1}$ and $70ms^{-1}$, however at longer duration's a clearer differentiation exists with greater mass loss at higher velocity. The general trend in accumulation was similar to that observed in earlier experiments, but was not in accordance with that reported by Springer [113]. From Springer's book "erosion by liquid impact" [71] it is discussed the different stages of accumulation of erosion with respect to time, and he states that it follows three distinct stages. The first being the incubation zone where there is no notable weight loss of the sample for an initial period of time. The second stage denoted as steady weight loss rate comes immediately after the incubation period and is a period of time which the rate of weight loss is nearly constant and the weight loss varies almost linearly with

time. The last stage named the final erosion region is not discussed as intently as the trend becomes unpredictable and the relationship between weight loss and exposure time becomes more complex and unknown. These stages, however, were not observed in the data presented from this investigation as there was no apparent incubation time as there was significant almost immediate loss in mass. With this conformation with earlier results, it can be argued that there could be another explanation to the trend in accumulation of erosion.

Springer's [71] explanation of the incubation period is one in which there is little to no erosion that occurs within a given period of time starting at the first point of impact. From this work and previous investigations however, this phenomenon was not observed. From a mechanistic point of view, it is difficult to explain why there would be a period of time when there would be no loss of mass from the material when the droplet impact will be exerting forces, enough to eject material from the first impact. It is agreed that the effects of erosion are unlikely to have an effect of the energy production of a wind turbine until it becomes more considerable, and this could be thought of as an incubation period of wear for larger structures. This can be seen in the work done by Drew Eiensberg who collected data on the energy losses of wind turbines due to rain erosion and it can be seen there is a delay in any loss seen in Figure 8.32.

Other investigations [52, 92–94, 146] researching the effect of rain erosion have also reported differences within the trend in initial erosion which would normally be considered the incubation period, Figure 8.33 shows these investigations and how they differentiate from each other and the standard set by Springer [71].

From Springer [71] the next stage after the incubation period is an interval where the time of exposure is almost linearly proportional to the weight loss. This is rarely observed when testing materials erosion resistance. From the experimental results it is normally either an increasing erosion rate or decreasing erosion rate. The linearity of Springers model [71] allows for simpler calculations for erosion predictions. From a

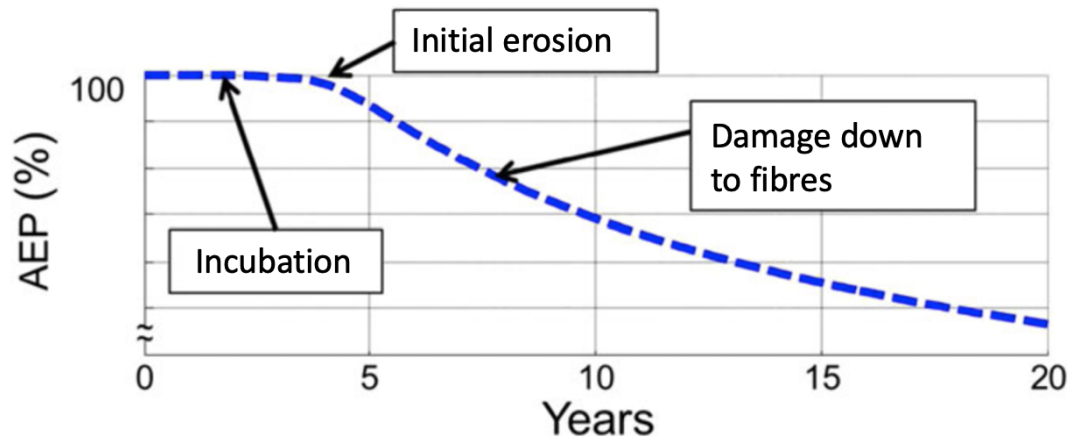


Figure 8.32: Annual energy production from a wind turbine as it declines over time due to rain erosion, adapted from [114]

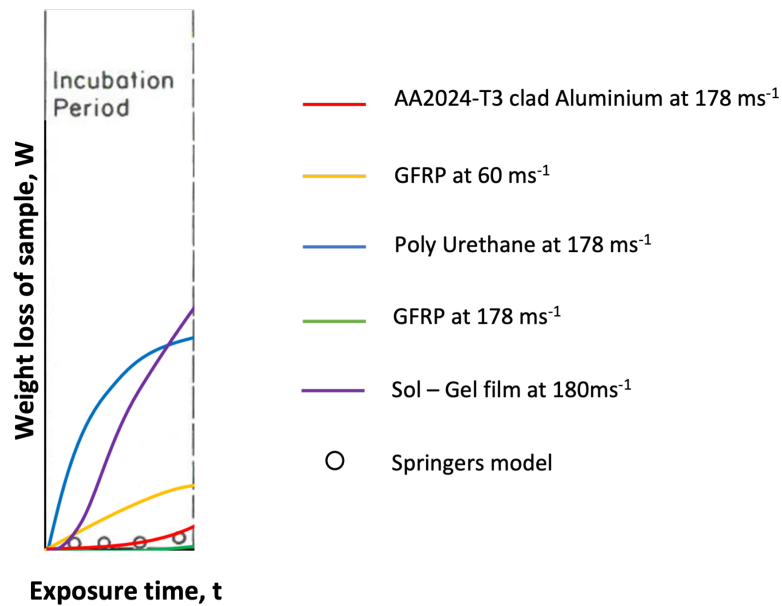


Figure 8.33: Weight loss of material over exposure time in the mid section set out by Springer [71] outlining the Incubation period [92–94, 146, 200]

mechanistic perspective it is difficult to understand why the mass loss would be linear as the erosion on the sample modifies the surface for the subsequent erosion thus it is not steady state. Reviewing experimental results in the literature revealed a variety of relationships [52, 93, 94] as shown in Figure 8.33. The aluminium clad testing by [146] did show a very similar response to the model set out by Springer [71] however the other four tests were significantly different. In the study conducted by Siddons [93] which is represented in the yellow line in Figures 8.28, 8.29 and 8.30 he also found that there was no incubation period present and damage inflicted by liquid impingement resulted in immediate damage to the GFRP sample. In the section where a linear relationship according to Springer [71] should occur, in Siddon's [93] results the rate of erosion decreases before increasing again.

From the surface topography analysis, it can be observed that before the sample is tested there are microscopic pits with sharp edges in the top layer of epoxy as shown in Figure 8.27. From the literature these surface geometries are vulnerable to liquid impingement erosion. This could be a reason for the lack of incubation period in rain erosion testing as these features on an untested sample are almost immediately eroded at the microscopic level and the pits are opened up giving an initially fast mass loss with the surrounding edges being rounded off and less susceptible for erosion. Once all the harsh edges and microscopic pits have suffered some erosion and the edges are now rounded it enters a state which is more erosion resistant and the erosion rate will tend to decrease which be seen in most of the investigation shown in Figure 8.33 as the weight loss of the sample tends to progress at a lower rate after the initial rapid loss. Erosion will continue to occur in most scenarios just at a slower rate as shown in Figure 8.34 where the majority of the data has a less steep gradient suggesting a slower erosion rate.

After some time the erosion of the surface of GFRP will start to increase again as the top layer of epoxy wears thin and the glass fibres are exposed. Once the glass fibres are susceptible to erosion the erosion rate can increase dramatically due to the brittle nature of the glass fibres, it can also be slightly unpredictable as there is possibility of

larger pieces of mass being removed from the sample.

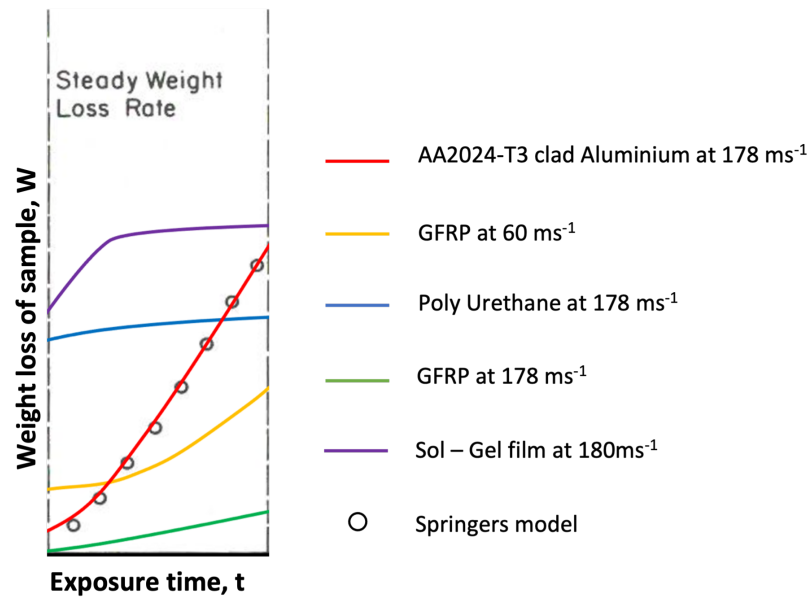


Figure 8.34: Weight loss of material over exposure time in the mid section set out by Springer [71] outlining the steady weight loss rate stage of rain erosion. [92–94,146,200]

The unpredictability of the relationship between the exposure time and the weight-loss of the sample depicts the final stage or erosion set out by Springer [71]. It is not discussed in much detail as the material loses its usefulness and in the case of wind turbines this would be a category 5 damage which would involve serious repairs and the possibility of a replacement turbine blade. The final stage is shown in Figure 8.35 and not too much information can be drawn from this section, however it is worth noting the variability in the different investigations. The complete weight loss over exposure time graph, showing all three stages is shown in Figure 8.36

From Figures 8.28, 8.29, 8.30 it is the general trend that the higher bending stress applied to the sample results in a greater the mass loss. This aligns with the initial hypothesis that the bending stress and the impact stress of the droplet connecting with the sample are additive creating a greater impact force on the material and hence making it more vulnerable to erosion.

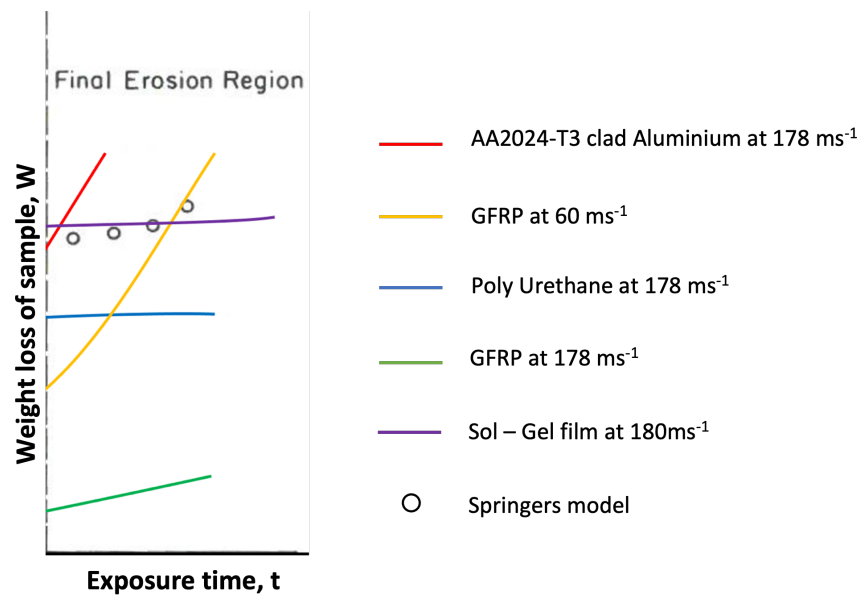


Figure 8.35: Weight loss of material over exposure time in the mid section set out by Springer [71] outlining the steady weight loss rate stage of rain erosion. [92–94,146,200]

As it was deemed the optimal method of analysis for rain erosion testing from Section 6.2 a profilometry study was completed on one of the samples subject to $v_{im} = 80ms^{-1}$ and $\sigma_{bend} = 150MPa$ bending stress. The level of detail obtained from this analysis surpasses the previously gained data as it equates what the surface roughness quantities are, along with a high resolution image of the sample outlining the high and low points. This information will allow for direct comparison between samples and allow the determination a change in surface roughness in order to confirm or deny hypothesis. At this time the University of Strathclyde does not have this equipment so in order to obtain these images seen in Figure 8.37 the samples were required to be sent away for analysis, making it difficult to assess the damage of all the samples.

8.3.7 Conclusions

From the results of this investigation, this research finds that there is no apparent incubation period for liquid impact erosion as proposed principally by Springer [71] and utilised by others throughout the literature. This work has shown that there was almost

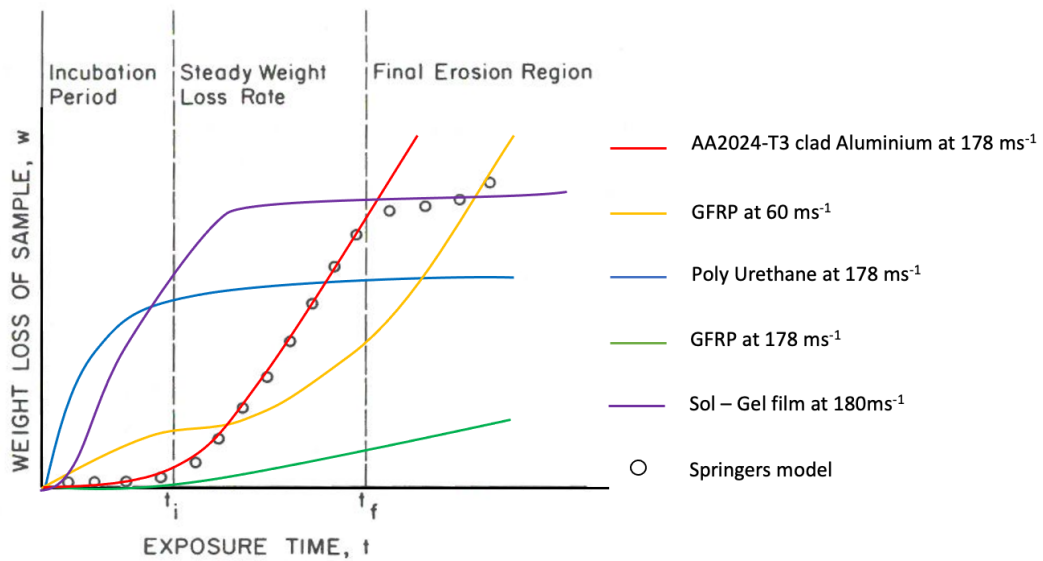
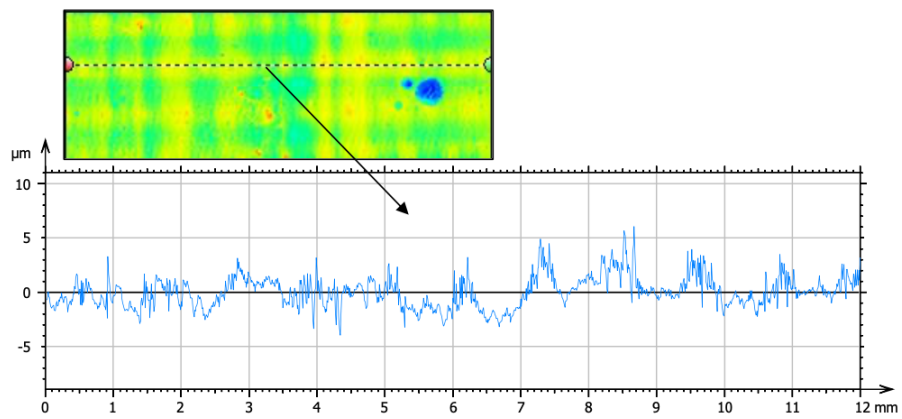
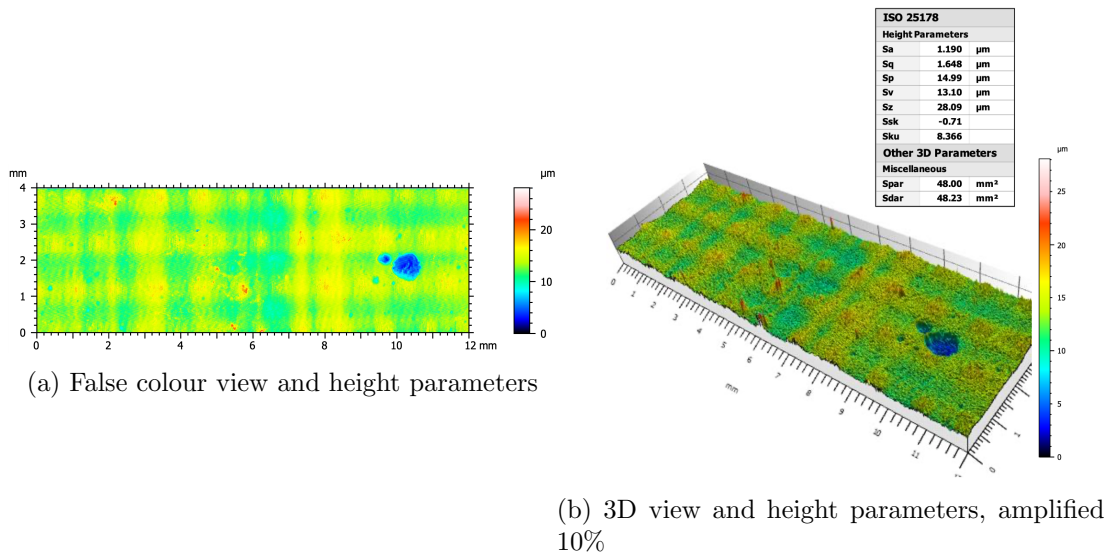


Figure 8.36: Weight loss of material over exposure time showing the three previous regions combined. [71, 92–94, 146, 200]

immediate mass loss in the samples when subject to liquid impingement. A review of experimental results on GFRP and other materials has revealed that there is a diverse range of curve shapes when correlating weight loss to exposure time. It is conceivable that the Springer hypothesis [71] only applies on low speed impacts which would not breach the threshold stress for immediate erosion and deformation of the surface.

A hypothesis for the trend in mass loss can be broken down to three stages which differ from Springer [71]. Initially when the sample is impacted from water droplets any imperfections on the surface are quickly targeted and eroded, hence, giving an initial spike in erosion rate. These surface features are promptly smoothed and therefore more erosion resistant thus slowing the erosion rate. As the top surface of epoxy begins to thin the glass fibre weave starts to be exposed and is much more susceptible to erosion and mass loss and the erosion rate of the sample then begins to increase once again. The results agree with the tertiary stage of erosion where the material has lost its usefulness and becomes erratic in its mass loss. Increasing stress generally increases the rate and magnitude of erosion, however all four different stresses follow the same



ISO 4287		
Amplitude parameters - Primary profile		
Pq	1.429 μm	Root-mean-square (RMS) Deviation of the raw profile.
Pp	6.044 μm	Maximum peak height of the raw profile.
Pv	3.956 μm	Maximum valley depth of the raw profile.
Pz	10.00 μm	Maximum height of the raw profile.
Pc	5.759 μm	ISO 4287 amendment 2 Mean height of the raw profile elements.
Pt	10.00 μm	Total height of raw profile.
Pa	1.120 μm	Arithmetic Mean Deviation of the raw profile.
Amplitude parameters - Roughness profile		
Rq	0.4053 μm	Gaussian filter, 0.08 mm Root-mean-square (RMS) deviation of the roughness profile.
Rp	0.6491 μm	Gaussian filter, 0.08 mm Maximum peak height of the roughness profile.
Rv	0.6385 μm	Gaussian filter, 0.08 mm Maximum valley depth of the roughness profile.
Rz	1.288 μm	Gaussian filter, 0.08 mm Maximum Height of roughness profile.
Rc	3.212 μm	Gaussian filter, 0.08 mm, ISO 4287 amendment 2 Mean height of the roughness profile elements.
Rt	5.120 μm	Gaussian filter, 0.08 mm Total height of roughness profile.
Ra	0.3259 μm	Gaussian filter, 0.08 mm Arithmetic mean deviation of the roughness profile.

(c) Profile extraction and height parameters

Figure 8.37: CLSM scan of a GFRP sample subject to $v_{im} = 80\text{ms}^{-1}$ impact velocity and $\sigma_{bend} = 150\text{MPa}$

Chapter 8. Experimental Work

pattern of damage accumulation.

Chapter 9

Construction of a Predictive Model

In order to optimise the maintenance on wind turbine blades to achieve the objective of reduced downtime and carry out works when deemed necessary, having an accurate predictive model would be extremely useful. There are two main methods of developing predictive models; experience based or experimental results based. Experience based models can be useful, but, their usability tends to be limited for older applications. For newer wind turbines the experience has not yet been earned, thus, extrapolation from a smaller, older applications can be unreliable.

In order to create an experimental result based predictive model a data base must be collected encompassing a variety of variables. It also requires a meteorological study to correlate the input variables including rainfall rate, sea water spray and hailstone collision possibility to the erosion rates concluded in experimental testing using these variables. Once this link has been established and other factors are entered, including the design and length of turbine blade then an accurate output of the given erosion of the turbine blade can be calculated. As the data is finite the values between the data points must be determined as well as appropriate projection evaluated in order to create a useful prediction model. Historically, studies have attempted this method with

aerospace application in mind and using a single impact and the correlating stresses as the basis for the model. Although this creates a working tool, there is room for optimisation and within this research it builds upon the existing models and hopefully improves the prediction accuracy.

9.1 History of Rain Erosion Prediction Models

The characterisation and evaluation can be represented in a mathematical model using the input parameters from the experimental investigations including impact velocity, droplet size, internal bending stress (blade length) etc and the output would be the response from the material, usually as a mass or volume loss value. The definition and measurement of the target response can vary with different types of material, however, in this application it can be assumed to be predominantly GFRP. This section of the predictive model mainly incorporates the stresses of the droplet impact and the consequent surface defects.

Rain erosion prediction models had notable recognition between the 1960's and 1980's, during this period many numerical and analytical models were developed in particular Blower's analytical model [62], Hwang [201], Lesser and Field [202] Rosenblatt [63, 203] and Adler [68]. A thorough review was completed by Lesser and Field [202] which encapsulates the analytical and numerical models on the impact pressures and distributions experienced in the water droplet erosion event at an intermediate speed range (below supersonic but above falling velocity). It was concluded that the major features of such an impact are high edge pressures, lateral jetting and cavitation which are all covered in section 3.3.4. It was also concluded that the various impact-test devices rarely correlated well which reflects the conclusions from Section 8.1 which displayed differences in mass loss to the corresponding micrographs. This can also point to the discrepancies' between various experimental investigations which show a lack of incubation period during initial erosion.

9.2 Development of Rain Erosion Predictive Models

Since the 1980s there have been developments on the prediction models of rain erosion and notable work has been completed by Castorrini et al [204] where they have a modern take on a historic problem. Some key advancements from the earlier work carried out on this topic include the targeted application of wind turbines and also a mass/volume loss focus over an extended period of time rather than a single impact stress focus.

Castorrini et al [204] utilised machine learning in order to predict the erosion on wind turbine blades for a given impact velocity and rain fall rate. The machine learning algorithm utilises a database of experimental data to output impact patterns and dynamics. One notable method used within this investigation is the substitution of incubation period with incubation energy. For their model some of it was based on the Springer [71] model, however, the incubation period was difficult to generate due to problems with variability hence the incubation energy was created. This parameter is different from the incubation period as it is not a count for the number of impacts before erosion can occur but it is a threshold energy which when surpassed will instigate mass loss within the target material. From the equation given by Castorrini et al [204] for the incubation energy it is dependent on the mass of the droplet and its velocity impacting onto the target material. Therefore in real life conditions where the tangential velocity of the tip of a turbine blade is roughly constant and the rain in the surrounding area can be defined (i.e the impact velocity and droplet mass can be estimated to a certain level of accuracy) and the resulting incubation energy surpasses the threshold value to initiate mass loss then the turbine in question would not experience an incubation period and immediately experience erosion. This is also true when simulating erosion within an experimental environment as both the impact velocity and droplet mass is controlled and when that combination exceeds the threshold energy, the target material will be eroding as soon as it is impacted.

Chapter 9. Construction of a Predictive Model

This phenomenon was experienced during the testing of this investigation as there was immediate mass loss from the target sample after the first round of exposure time to droplet impacts. The additional variable which was included within the experimental work of this research was the bending stress within the target material, which simulates the turbine blades and the stresses which will occur due to their size and the effects of gravity and wind.

A summary of the testing work performed and the variables included within the research are listed below:

Investigations:

- Onshore fresh water Wind Turbine erosion
 - With varying impact angles and velocities
- Sea spray for Offshore Wind Turbine erosion
 - With varying impact angles and velocities
- Accumulation of erosion and the progression of mass loss
 - With varying impact angles and velocities
- The Effect of bending stress
 - With varying impact velocity and accumulation mass loss inspection

Constants throughout the investigations:

- Droplet diameter
- Temperature
- Humidity
- Distance travelled between inspection

Chapter 9. Construction of a Predictive Model

- Rainfall rate
- material

Variables investigated and their application to Wind Turbines:

- Impact Angle - Area of leading edge affected
- Impact Velocity - Rotational velocity of the turbine blades and the radius from the root
- Bending Stress - Design and size of the blade
- Water Salinity - Location, Onshore or Offshore
- Exposure Time - Lifetime in operation

These parameters are essential for creating a database of erosion for various combinations of variables. In order to determine a useful predictive model, the wind turbine location is very important as this will determine the environmental parameters, namely wind speed, water salinity and the exposure duration to erosive media for example rain. In all previous models which have been reviewed the rain occurrence has not featured. The number of days of rainfall is very important for onshore wind life prediction as when there is no rainfall the degradation rate is very low. In order to have a practical model a study was completed to correlate the distribution of rainfall across the United Kingdom and Ireland and the mass loss of turbine blades.

9.3 Geographical Data

The work in this section was peer reviewed and accepted for publication in the journal of lubricants titled "Rain erosion maps for wind turbines based on geographical locations: A case study in Ireland and Britain" K Pugh, MM Stack, Journal of Bio-and Tribo-Corrosion 7 (1), 1-7 (2021)

Erosion rates of wind turbine blades are not constant, they depend on many external factors including meteorological differences relating to global weather patterns. In order to track the degradation of the turbine blades it is important to analyse the distribution and change in weather conditions across the country. This case study addresses rainfall in Western Europe using the UK and Ireland data to create a relationship between the erosion rate of wind turbine blades and rainfall for both countries. The two variables were then combined with other data including hailstorm events and locations of wind turbine farms to create a detailed map of erosion with relation to wind turbine blades.

Typically wind turbine farms are constructed in barren locations due to land availability, wind speeds as identified on meteorological maps and away from local beauty spots; however, this results in turbines being subjected to harsh conditions and in some locations heavy rainfall. Within this case study, data from the Met Office [205] and experimental data will be combined in order to map the UK and Ireland in terms of erosion on wind turbine blades. This is being carried out to display the relationship between the locations of wind turbine farms and their environment. This will, in turn, also aid in visualizing the wind farms that are at higher risk from erosion degradation and will require more maintenance to mitigate failures and increasing power output by keeping the blades smooth and promoting greater aerodynamic efficiency.

It should be noted that the turbine blades will inevitably experience differing rainfall rates throughout the year, which will, in turn, result in varying erosion rates. To

map this phenomenon, the months of highest and lowest rainfall were chosen which were January and May respectively. Showing two varying months throughout the year will hopefully provide more insight than a yearly average and allow for contrast to be seen throughout the year.

The rain data was accumulated from the met office UK and from Irish Data [206]. This data included a 20-year average of the rainfall in the wettest month of the year: January and the driest month of the year: May [207]. This was selected to demonstrate the two extremes throughout the year and to visualise that even in the dry months there is still considerable erosion occurring at the leading edge of a turbine blade. These data sets were averaged and formatted into a geographical map shown in Figure 9.1. The rainfall mostly averages between 50-500mm of rain with some few areas showing more extreme rain. It is clear that the month of May experiences considerably less rain as it shows highs of 300mm whereas this rate is fairly common in January. The areas of intensity are very similar in both months with the west coast of Scotland showing a higher rainfall and also the west coast of Ireland, predominantly the south west coast of Ireland displaying very heavy rainfall. These are historically harsher climates due to the prominent westerly wind from the Atlantic [208]. This leads to further erosion as the largest windfarms are located in these areas due to the increased power output from the consistent wind [209]. This is a very common trade-off when building a windfarm as the conditions that yield the most power generation are also the conditions which deteriorate the turbine blades most rapidly and thus the life of the turbine will be reduced [210].

An experimental methodology was employed for this part of the research, utilising the previously used smaller WARER within the Tribology Laboratory. The methodology was the same as before where samples of GFRP would be inserted into the WARER for set exposures in order to initiate erosion due to the water impacts. For this research the exposure periods were directly related to the magnitude of rainfall for the months of January and May.

One of the assumptions that was made in order to relate the two data sets was that the wind turbines were always turning when it was raining. Although this might result in an overestimation in erosion, it is deemed a worst-case scenario that has a possibility of occurring. The percentage mass loss is also just related to the samples which were tested, which was G10 epoxy glass with no coating, this would represent the very tip of the leading edge of a wind turbine blade.

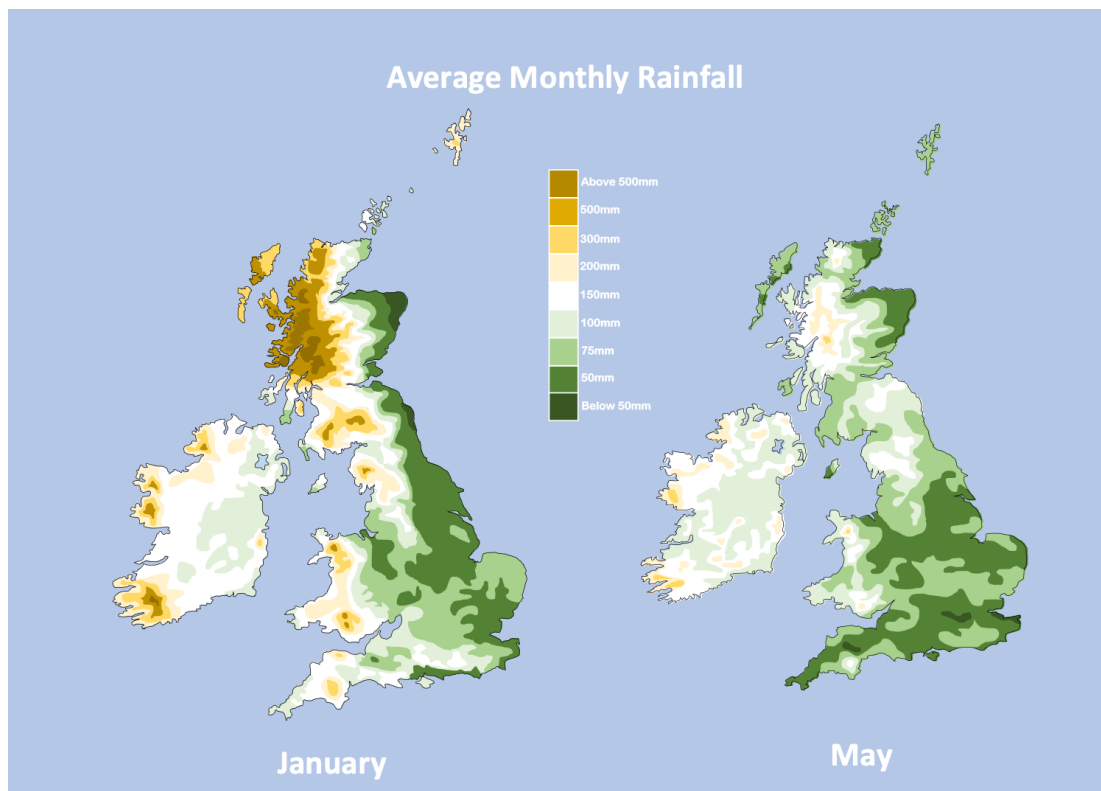


Figure 9.1: The average rainfall in the months of January and May

Part of the experimental process was also to understand sea water effects which help describe the erosion behaviour of offshore wind turbines. This was completed by running a saltwater solution through the experimental rig to simulate offshore conditions. Previous work on this topic by the current research group, showed similar results which concluded that the saltwater proved more erosive when subject to high velocity

impacts from the leading edge of the turbine blade and would create larger and more destructive cracks and loss of material from the sample [211]. The added effect of the more consistent wind from offshore conditions with the sea water climate is conducive to an erosive atmosphere and hence a shorter life span of turbine blades. Offshore wind farms have many other problematic characteristics including the corrosive nature of sea water which will attack any metallic parts and the anchoring of the structure to the seabed, however, the remote locations and the large blade size allows very significant energy capture [212]. Even though offshore wind turbines encounter major drawbacks such as increased levels erosion and corrosion, the advantage of having the open space to build larger, more efficient wind turbines with more consistent wind makes them economically more viable [213].

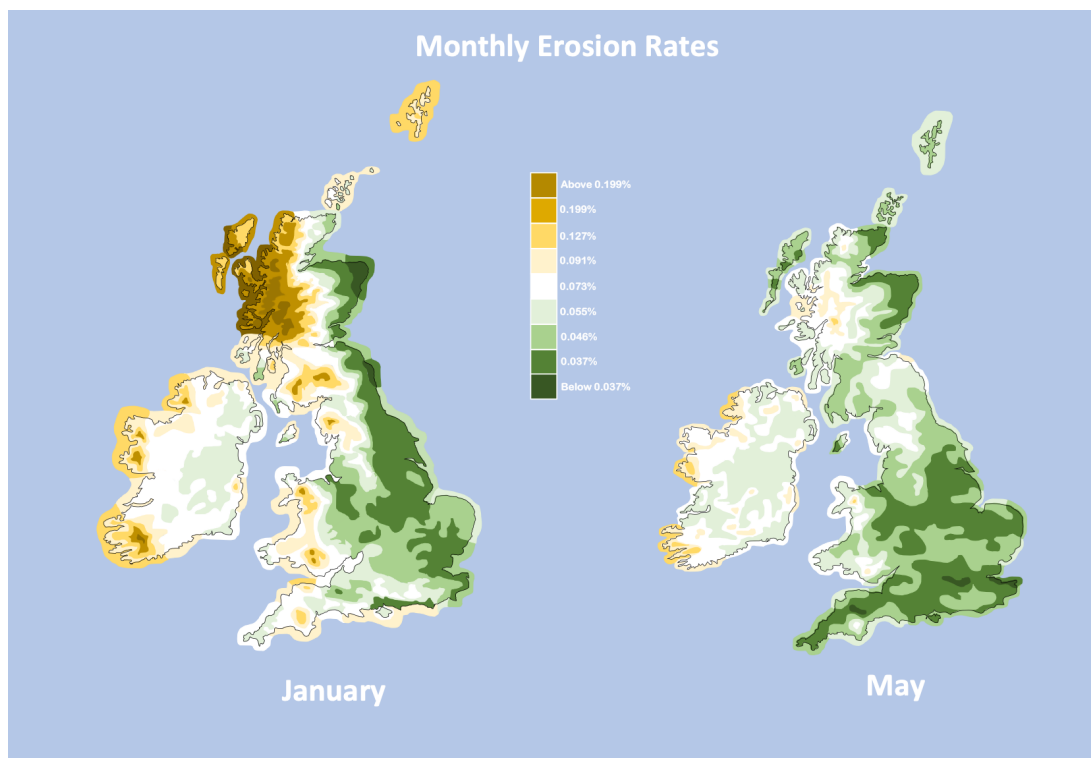


Figure 9.2: The monthly erosion rates in January and May

Once the rainfall maps were created the link between rainfall rate and erosion rate could be made. This was carried out by taking the results from the experiments and

processing them to take account of the regional rainfall. This was accomplished by running the experimental rig at time intervals to relate to the rainfall rate. The induced rainfall rate within the rig was 50mmh^{-1} ; hence the testing was stopped intermittently every hour and weighed in order to determine the mass loss which would represent the damage by erosion. The results were converted into percent mass loss with a maximum of 0.199% which relates to 500mm of rainfall and a minimum of 0.037% which relates to 50mm of rainfall. Although mass loss is not the most precise measurement for erosion [214] it does allow for comparisons to be made which is advantageous in this situation.

The measurement of mass loss can related to the efficiency of the turbine, which is also why this measurement was used to map erosion across the UK and Ireland. When material is lost from the wind turbine blades it will affect the aerodynamic profile of the blades, with more mass loss the greater the effect it will generally have. The disturbed airflow over the blade will impede the performance of the turbine as a whole, as now with a damaged blade, it will require a higher airflow or blade angle in order to produce the same output [215]. This has been proven experimentally within the literature which considered the drag coefficients of compromised blades [216] and also the microscopy of material subject to rain droplets at high velocities [217].

With the rainfall data only available for on land, it made it more difficult to map the erosion rates offshore. The data was interpolated to compensate for this; however, most offshore wind turbines are beyond the map data as presently constructed. The rainfall rate was assumed to be similar to the rainfall rate at the shore to the same resolution as the rest of the map, however, from experimental testing, the saltwater experiments displayed more erosion from examinations performed and this was accounted for in the algorithm. This was incorporated into the maps and can be seen in Figure 9.2 where the erosion rate increase as it navigates offshore.

Construction of these maps, thus allows for further comparison to be made including

Chapter 9. Construction of a Predictive Model

locations of major wind farms and also areas of high hail rates which is displayed in Figure 9.3. Even though the rainfall rate maps cover all precipitation, it is important to locate areas of high hail impact as these tribological actions can be detrimental to its structural integrity. The probability of hail striking wind turbine blades is lower and identifying the specific damage caused by hail would be difficult due to the cumulative effect of erosion. Quantifying the damage would be difficult to ascertain and it could possibly be masked as the outcome of heavy rainfall erosion, the impacts of hail have been proven experimentally to cause substantial damage.

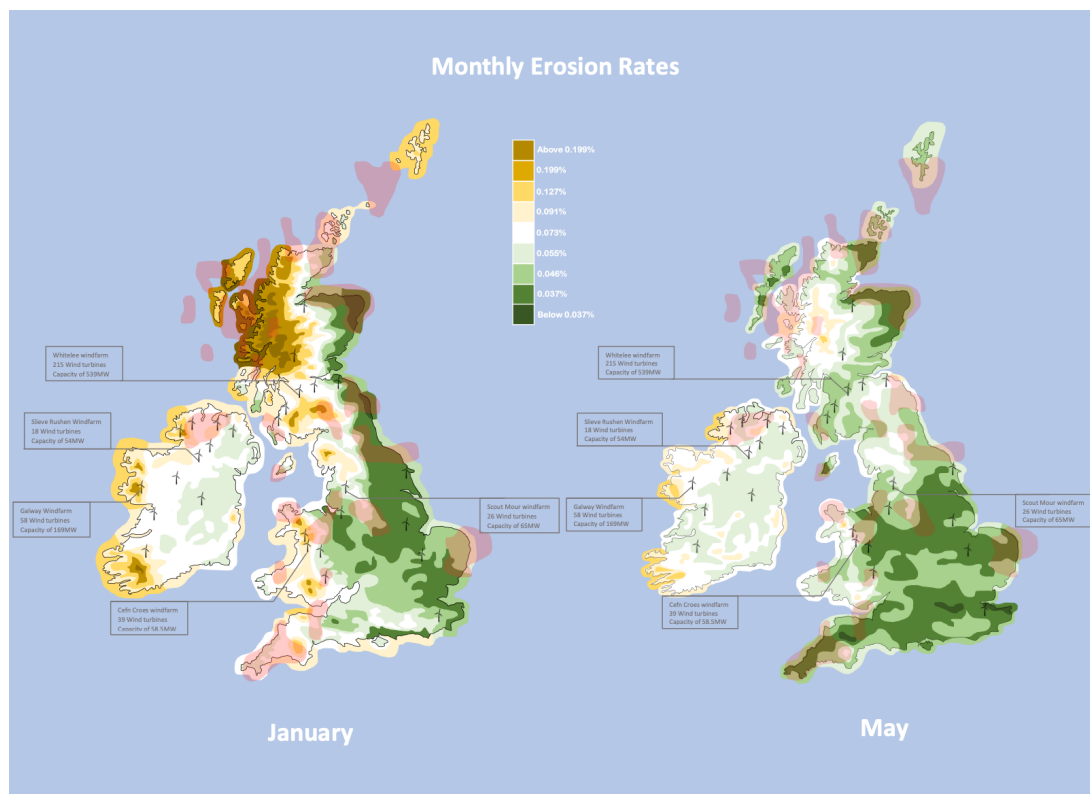


Figure 9.3: The monthly erosion rates in January and May with overlays of major wind turbine farms and areas of frequent hail [218].

In a study looking into ballistic ice impacts, it was shown that the impact would delaminate and crack the composite material [219]. This would not only create a weak point in the blade structure itself but also create an initiation site for rain erosion to occur and for crack propagation into the structure of the blade. The areas of frequent hail are shown in Figure 9.3 as the red overlay, and from the maps it is clear that the

west coast is more adversely affected by hail. Unfortunately, there was limited data on hail in The Republic of Ireland; therefore, assumptions on this issue for this area of the map need to be treated with caution.

Also superimposed onto the map in Figure 9.3 is the locations of some large wind farms and the largest in Scotland, England, Ireland, Wales, Northern Ireland and The Republic of Ireland have been labelled. This not only allows for a comparison between the size of the various windfarms in each region but also how adversely affected each one is by the climate and the subsequent erosion. Most of the windfarms are in severe weather locations but, as discussed previously, this is a trade off between greater access to consistent wind to the lifetime of the blades.

There are some additional modifications which will help optimise these maps when they are recreated with future results. The main extension would be the use of additional data to help aid the validity of the results and as mentioned previously if enough data is available then a dynamic map could be potentially created.

There are many additions which could be made to the erosion data and the weather data which could provide further insight into geographical differences including the droplet size, pH value and intensity which would aid the erosion data. These data sets however are difficult to pinpoint as they are mostly stochastic.

The most important evolution for these maps would be the inclusion of offshore rain data to include the large offshore wind farms that could not be included within this study due to the lack of resources involving the climate. With more area, becoming available off the coast of Scotland and Ireland the inclusion of this data would be greatly beneficial.

In conclusion, the data from the rainfall within the UK and Republic of Ireland were formatted together to produce a cross border map showing the average rainfall across

Chapter 9. Construction of a Predictive Model

the two countries in both January and May averaged over the last 20 years. These maps were then converted to an erosion map and displaying the degradation of the turbine blades from rain droplet impacts by using experimental data that was linked to the quantity of rainfall. This was coupled by saltwater erosion to simulate offshore wind turbines which are subject to being eroded by sea water (salt spray corrosion enhanced erosion) in the atmosphere. These two maps were then superimposed to display areas of frequent hail and the locations of each country's largest wind turbine farm. This was carried out in an attempt to visualise the erosion patterns across both Ireland and the UK.

From both maps it is clear that even in the months with little rain, the turbine blades can be degrading over time due to erosion. The general trend consists of greater potential erosion present in the west coast of both the UK and The Republic of Ireland with the highest potential erosion areas being the north west of Scotland where the land tends to be at a higher elevation and also the south west of Ireland where there is no protection from the prevailing wind over the Atlantic.

The locations of frequent hailstorms across the UK and the republic of Ireland could be considered stochastic, however the locations of some major wind farms overlap with frequent hail; this can be seen predominantly in Northern Ireland. This overlap could potentially reduce the lifetime of the turbine blades at an increased rate due to more powerful impacts from hailstones.

The concept of creating these maps was to provide this data for the development of a predictive model that has wind turbine location as a variable, this could be later improved by the maps incorporating up to date real time data. This is particularly important due to weather changes over periods of time on the annual cycle.

9.4 Data Projection Method

The need for a prediction model and accompanying descriptive equations is necessary as the experimental data only provides finite information. In order to bridge the gap between the data points gathered through experimentation a projection method is required. A projection method allows for future predictions to be calculated with respect to the earlier data generated. Such prediction models could be extremely useful for wind turbine owners and operators as the mass loss from the leading edge of the blades create a less aerodynamic profile and hence a decline in output power from the turbine. Models allow for the prediction of erosion and allow for maintenance and repairs to be carried out at the optimal time with minimal inspection required. The timing of completing repairs is important when operating a wind turbine as there will be a finite period where the erosion which occurs on the leading edge will not significantly impact the output energy as seen in Figure 8.32. During this time there may be visible damage to the blade but action is not required as it will only have a minor effect on the output energy. The optimal time to maintain the blades is just before the turbine starts to significantly lose efficiency, this will keep the turbine producing power at its rated value with minimal downtime to perform targeted appropriate repairs.

Predictive models have been created in the past including the Springer [71] model [113]. There are normally different stages to the erosion curve and from the research conducted in this study it was concluded that there are three stages however they differ from the stages described by Springer [113] and they are as follows:

- **Primary:** Before a single droplet even impacts the material the surface will contain micro imperfections including pits and gouges, these defects are vulnerable to erosion and hence when subject to environmental conditions the material can lose mass at an initially fast rate on the micro-scale. The mode of erosion is mainly lateral jetting which targets the surface imperfections and some deformation on the epoxy top layer from the high impact stresses of the water droplet.

- **Secondary:** Once the imperfections of the material which are vulnerable to erosion have all been targeted the material becomes more erosion resistant. This is due to the smoothing of all the sharp edges creating a smoother surface which is more difficult to erode. The material still continues to erode as the pits and gauges are opened up further. This results in the initial erosion rate of water droplet impacts to be decrease.
- **Tertiary:** While the erosion continues in the material from continuous water impacts the top layer of epoxy thins and has potential to expose the underlying fibres. The glass fibres in GFRP are much more brittle in order to give the material beneficial stiffness properties however the fibres themselves are very susceptible to erosion and are vulnerable to brittle fracture and ultimately ejection from the material. This mechanism increases the erosion rate and it begins to increase dramatically.

This trend of an initial rapid rate followed by decreasing rate then an increasing rate is similar to the trends experienced in creep (strain versus time) damage data. Interestingly this new approach of decreasing then increasing rate of creep damage has largely replaced the more traditional description of a steady state secondary creep regime. This change in philosophy is similar to that being proposed in this research to replace the steady state erosion regime described by Springer [71]. For this newer description of the creep damage behavior a constitutive relationship based on theta projection method is available and has been created by Wilkshire and Evans [220]. These projections were used to establish a quantitative relationship between the exposure time and the mass loss from the material. A modified formula by Song et al [221] was used. The theta values derived for the three speeds of 60, 70 and $80ms^{-1}$ are given in Table 9.1. Due to the interrupted test schedule the duration's are relatively short and therefore the projections should be revisited when more test data becomes available.

These projections were then used within Excel based calculations along with integrated experimental data and geographical rainfall rates to produce a predictive model

	$v_{im} = 60ms^{-1}$ (Red)	$v_{im} = 70ms^{-1}$ (Orange)	$v_{im} = 80ms^{-1}$ (Green)
θ_1	0.0981	0.0082	0.0061
θ_2	2.014	1.831	1.595
θ_3	0.0113	0.0094	0.00793
θ_4	5E-2	5E-2	5E-2

Table 9.1: Theta values for each of the prediction curves.

to estimate the erosion of varying sizes and designs of wind turbine blades at specific postcode locations. In order to make this model user friendly and able to be applied easily in the field it was further developed into an iOS app.

This prediction model has a number of limitations inherent in relative early stage laboratory based work. These limitations are as follows:

- Impact velocity range, $30ms^{-1} < v_{im} < 80ms^{-1}$
- Geographical location limited to the UK and Ireland
- Off-shore locations to with 10km of the shore
- Blade material is GFRP without additional coatings
- Droplet size of 2.25mm
- Temperature $20^{\circ}C$
- Test program not completed
- Accuracy of longer term prediction with shorter term data
- Lack of comparison between eroded blades and samples due to industrial sensitivity

9.5 Prediction Model and Application

As mentioned in the previous section 9.4 the projection method and predictive model is necessary to interpolate between the experimental data points and to estimate the erosion in the near future to provide information to allow the optimal timing of maintenance and repairs. The objective for the model which has been developed as part of this research was to be able to predict the life expectancy of various blades of different design and geographical location, this was achieved by combining the following:

- **Whether the turbine in question was Onshore or Offshore:** This was deemed important due to the higher erosion rates which occur to off-shore wind turbines as they are not only larger but they are subject to sea water spray and from Section 8.2 it was concluded that the salinity of the water plays a role in the intensity of erosion and was therefore taken into account for the prediction model.
- **The manufacturer and design of the blade:** This is important as different styles of blade from various manufacturers can have varying internal stresses within the material which, as shown in Section 8.3 a higher stress applied to the material results in a higher erosion rate.
- **The length of the blade:** When referring to multi-megawatt turbines this parameter is normally related to the tip speed of the turbine blade, however, there are some exceptions depending on the design and manufacturer. As shown in Sections 8.1, 8.3, 8.2 the effect of impact velocity of a water droplet impacting onto turbine blade material is directly related to the mass loss of the material.
- **How long the turbine has been in operation:** From Sections 8.1 and 8.3 the effect of accumulation of erosion was investigated and the patterns or erosion were distinguished.
- **Location of wind turbine site:** Depending on where the turbine is situated can have a drastic effect on the erosion rate of the blades due to the varying

distribution of rain across a country. As shown in section 9.3 the erosion rate over the areas of the UK and Ireland can vary depending on factors such as rainfall, sea water spray and chance of hail damage.

All these factors were taken into consideration and influence the algorithm which predicts the erosion within the model and displayed within an app. The app was developed utilising "Open as App" which is a web based app builder which runs from excel data. This allowed the predictions to be generated utilising the test data and for the results to be displayed in a user friendly interface that is portable. Figure 9.4 is a demonstration of the app in operation as it showcases four different Wind farms; Bein Ghlas wind farm, Meikle Carewe wind farm, Walney wind farm and Upper Holton wind farm. These wind farms possess varying characteristics including onshore and off shore, massive state of the art turbines and older mid range turbines. This is designed to show the wide range of capabilities from the app. The details of the inputs are given in Table 9.2. Note the output power, diameter and tip speed were obtained from the manufacturers data sheets for each wind turbine.

Wind Farm	Manufacturer of Wind Turbine	Output Power of one Turbine	Diameter	Tip Speed	Estimated Bending Stress σ_{bend}
Beinn Ghlas	Siemens Bonus	0.6 MW	44m	$62ms^{-1}$	81 MPa
Meikle Carewe	Siemens Gamsea	0.85 MW	52m	$84 ms^{-1}$	93 MPa
Walney	Vestas	8.25 MW	164m	$104ms^{-1}$	324 MPa
Upper Holton	Senvion	2.05 MW	82m	$73ms^{-1}$	204 MPa

Table 9.2: Input parameters for the demonstration of the predictive model app

The App is currently a proof of concept and in order to determine whether the blades pass or fail it requires an input criteria. The app is set up to determine what level of erosion is present on the turbine blades in the categories of: Light, Moderate,

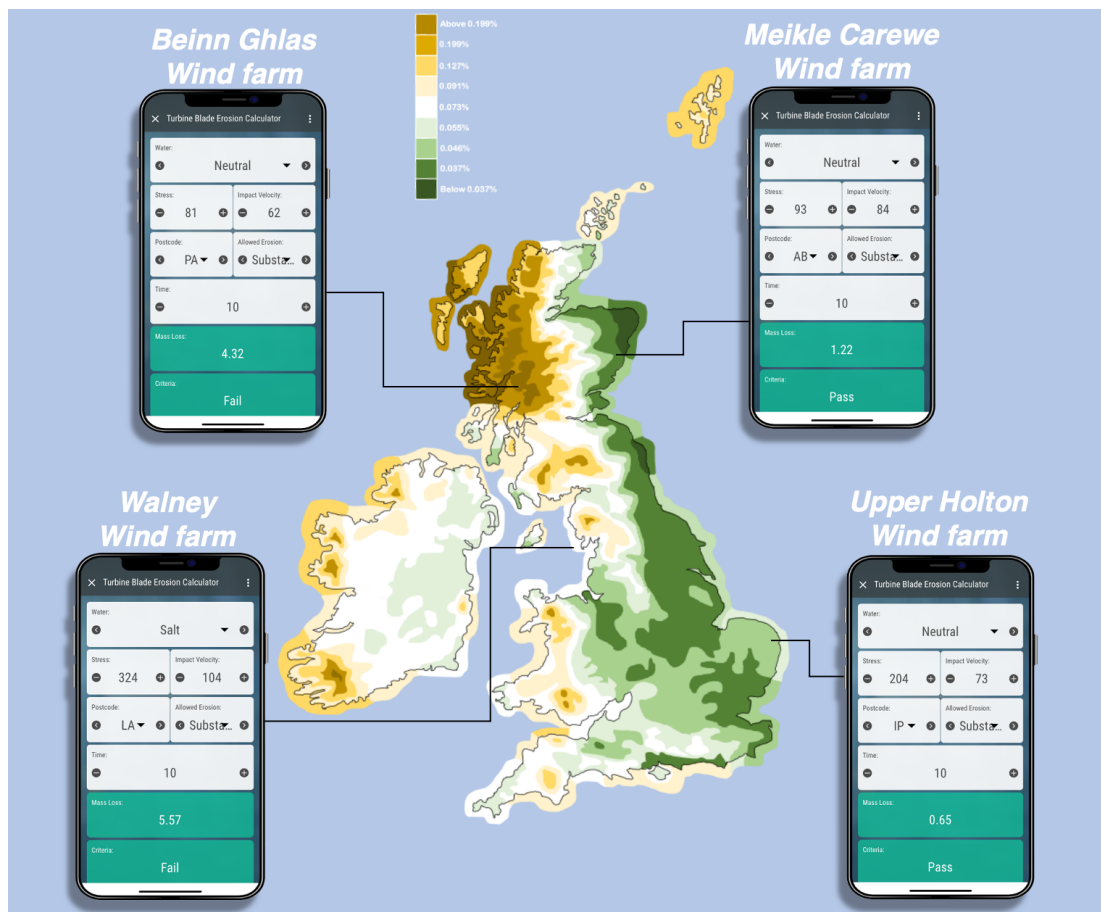


Figure 9.4: A map of the UK and Ireland showing four wind turbine farms and the result from the inputs of the projection app for a projected 10 year life

Substantial, Major and Fatal. As the app is still in its development stages the criteria was estimated for each of the stages as 10%, 20%, 30%, 70% and 100% respectfully. These are percentages of lifetime based upon the theta prediction of the mass loss. 100% is the estimated mass loss at the leading edge that would result in the blade requiring replacement and 0% being a fresh blade with no impacts of water droplets.

In Figure 9.4 the failure criteria was set to substantial erosion, equivalent to a 30% of the mass loss that would require blade replacement due to leading edge erosion. This level of life depletion was chosen as it is envisaged that significant energy production will be lost due to the erosion of the leading edge. Within the app the acceptable life depletion percentage is customizable, allowing each wind turbine owner to determine their acceptance criteria Although the wind farms are all of different vintages it was not known whether any blade repairs or replacements had been conducted, as a result, the time period on each was set at 10 years. In the app interface a failure will appear when the erosion surpasses this criteria which occurred for both the Walney wind farm and the Beinn Ghlas wind farm. However depending on the individual wind farm owner or operator they can adjust the level of allowed erosion. Table 9.3 displays the wind farms and whether they would pass or fail at each allowed erosion criteria.

Wind Farm	Light	Moderate	Substantial	Major	Fatal
Beinn Ghlas	Fail	Fail	Fail	Pass	Pass
Meikle Carewe	Fail	Fail	Pass	Pass	Pass
Walney	Fail	Fail	Fail	Fail	Pass
Upper Holton	Pass	Pass	Pass	Pass	Pass

Table 9.3: Demonstration of whether the blades at each of the wind farms selected pass or fail on the given criteria within the app for a 10 year life

Attempts to correlate this predicted data with actual field data was not possible.

Chapter 9. Construction of a Predictive Model

Enquiries regarding blade life to wind farms and the manufacturers did not engender any specific data. From the literature it is widely regarded that turbine blades have a variable life with some blades requiring repair in as short a span as 2-3 years. In general, however, it is widely regarded that blades will have an operational life of around 15 years [222].

Chapter 10

Overall Discussion

There is significant environmental and political will to pivot our energy sources from fossil fuels such as coal, oil and gas which are the primary sources of green house gas emissions to renewable energy sources. Worldwide, and particularly in Scotland, wind energy is a major contributor to this more sustainable greener future.

In order to maximise the energy generated from the investment, wind turbines have significantly increased in size with individual blades now in excess of 110m and there has been a shift from onshore locations to offshore wind farms. These developments have exacerbated the problem of blade erosion due to consequential higher velocities and more onerous environmental operating regimes. The increase in erosion had the effect of decreasing blade performance and thus turbine efficiency.

There has been previous research in this field of blade erosion studies, however, there are gaps in the available data, significantly the effect that stress on the blades has on the erosion rate. As a result, this research modelled the environmental effects on a larger blades utilising CFD and calculated baseline stresses with FEA to guide the parameters used for testing.

The tests were initially performed using modified sample holders on the existing WARER test facility. This generated valuable information; however, the facility was

limited, primarily on velocity. As discussed previously wind turbine blades have increased in size and a consequence of this is that the tip speeds have increased for the same rpm. As a result, this research designed, contributed to the manufacture and commissioned a new larger WAREER that offers greater flexibility, control, speed and safety over the existing facility.

Correctly analysing the test specimens is a critical aspect to evaluate the rain erosion resistance of the material. The available techniques were evaluated as part of this research. It was evident that the surface analysis techniques were continuing to evolve and it was apparent that utilising multiple analytical tools can work in harmony to accurately define the surface parameters and monitor the changes when subjected to erosion. The combined techniques selected for this research work were to assess the magnitude of the erosion using mass loss, the identification of the location and extent utilising profilometry and to identify the relevant features using SEM and optical microscopy.

Utilising these techniques, tests on G10 GFRP at various, angles, test mediums (rain and salt water), stresses and durations were analysed. This revealed the angles more prevalent to attack, the impact energy and thus thresholds for erosion, the problems of interpreting sea water results (due to residual salt crystals) and the effect that stress has on the peak erosion angles. These results are depicted in wear maps and line graphs and are discussed in detail throughout this thesis.

The examination of the post test samples also revealed valuable information on the morphology of the erosion. This work has shown that the initial surface can contain manufacturing defects that can quickly propagate by erosion these defects are generally small pinholes. In addition, this work has also identified halo features on the stressed samples that are assumed to be associated with deformations of the top surface due to the impact of a water droplets. These have been termed SICD (Surface Impact Circular Deformation). With regard to the material loss both ductile abrasion and brittle

fracture have been observed with a higher probability (depending on conditions [15]) of a ductile response from the material, resulting in deformation and gouging. At higher angles of impact, the material will have a more brittle response, potentially resulting in a fracture, crack, or delamination.

Although significant test work was conducted during this research the tests utilising the new larger scale WAREER were not completed. This was a result of the University safety department withdrawing the permit for operation following the failure of the sample holder utilised in a separate research programme. Personal safety was the top priority in designing and locating the test rig and even though the failed fragments were contained within the primary barrier and the rig is located in a concrete bunker this was classified as a near miss. No further testing was permitted and at the time of writing this is still the case.

Despite this unexpected cessation, this research had generated valuable data that in some areas such as susceptible angles of attack build upon the current knowledge whereas other data for example the effect of stress introduces a new parameter that can influence the erosion rate. The results demonstrated that the applied bending stress increases the erosion rate. This aligned with the initial hypothesis that the bending stress and the impact stress of the droplet connecting with the sample are additive creating a greater impact force on the material and hence making it more vulnerable to erosion. The stressed samples also exhibited higher erosion over a larger range of impact angles. It is postulated that the stressed sample is experiencing a larger crossover between abrasion and brittle/fatigue erosion which allows the top epoxy surface of the material to be breached and have fibre exposure. This behavioural change when stressed is theorised to be due to the additional stress from the droplet impact causing deformation. Evidence to support this includes the observation of the presence of SICD's on the surface of the stressed sample. In addition, the data generated from this work challenges the currently perceived understanding with regard to the developmental stages of erosion. This is particularly true in respect to the three stages of erosion described

by Springer [71]. Here it is described as firstly the incubation zone where there is no notable weight loss of the sample for an initial period of time, the second stage denoted as steady weight loss rate follows the incubation period where the rate of weight loss is nearly constant and thus the weight loss varies almost linearly with time. The last stage named the final erosion region is where the trend becomes unpredictable. This work proposes an alternative theory for the accumulation of damage. This research data indicates that there is an almost immediate loss in mass caused by the impacts from rain, causing mass loss from pre-existing defects such as pinholes in the material. Importantly it is proposed that there is no steady state erosion period; alternatively, it is submitted that this initial high rate of erosion gradually decreases before increasing again at longer durations. From a mechanistic perspective post erosion of the initial defects the irregularities would round off decreasing the erosion rate until the erosion has penetrated through the outer layer of epoxy and exposed the glass fibres. Due to the brittle nature of these fibres, the erosion rate would then start to increase.

This alternative theory for the stages of erosion damage is critically important when modelling the damage evolution in order to use this to predict remaining useful life. For this purpose, utilising the incubation period followed by steady state would offer a relatively straight forward uncomplicated approach, despite this, as it was not the pattern of erosion progress observed in this research it was not employed. A theta projection method was the method utilised following a review of the literature. It is noteworthy that the theta projection was largely developed for creep life predictions to express a similar pivot in understanding from steady state secondary rate to a decreasing followed by increasing rate.

One of the objectives of this research was to maximise the benefit of the information generated to help optimise turbine blade maintenance and thus maintain the efficiency of blade whilst minimising downtime. To this end, to generate the high velocity impacts being experienced in the new large multi megawatt wind turbines a large scale WARER was designed, built within the University, and commissioned as part of this

research. To achieve the objective of accurate maintenance predictions requires not only the data generated utilising stressed samples in the high speed WAREER but also detailed knowledge of the environmental conditions that the wind turbines are exposed to. Consequently a map of rain and hail was collated for the United Kingdom and Republic of Ireland. Crucial for utilising this information is the relationship between this information and the test data. To accomplish this, correlations were determined for rain rates and testing. The final outcome was a predictive model with the inputs of service life, blade size (to correlate with stress), location and utilising the theta projection and environmental correlations a prediction of the maintenance is generated. To make it user friendly in the field this was subsequently adapted to an IOS application available to use on mobile devices.



Figure 10.1: Severe leading edge erosion of a turbine blade. Source [52]

This prediction model is important for the correct timing of maintenance. LEE reduces the output power of wind turbines as the disturbance in flow over the aerofoil reduces the lift produced by the blade ultimately affecting the efficiency of the power plant up to 16% over a decade [223]. The LEE as shown in Figure 10.1 [52] is an extreme case which has not been adhered to within an appropriate time. On the contrary it would be ineffective to inspect a turbine that would not have been under the conditions to eroded to the point where it affected the output power as it would require downtime of the turbine. Therefore lies an ideal time to perform inspections and maintenance.

In conclusion, the wind industry has been making significant advancements in terms of turbine efficiency and generating capacity, powered by significantly larger and optimised blades. The research to understand the modes and rate of blade degradation has been trailing due to the durations required to conduct appropriate tests and analyse the data. This research has endeavoured to bridge some of this gap by constructing a new high speed test facility, introducing the effect of stress in erosion rate and creating a predictive model utilising the generated test data and actual environmental conditions for the specific locations of the wind turbine the overall objective of this work was to increase the current knowledge and create a useful tool that can aid the industry today.

Chapter 11

Conclusions

The need for this research has become more evident even from the time between starting and finishing this interval of the research as the financial and economical state of the world, including renewable energy has changed. The need for wind energy and for it to be reliable has become a must when securing the energy needs for everyone. The ways in which the the wind energy industry has answered this question is by deploying larger off-shore wind turbines to meet demand. This research has tackled the problem with the difficulties faced from the damaging effects of harsh environmental conditions has to the leading edge of the blade and thus reducing its efficiency.

The way in which this problem was tackled was first to understand the physics of the event of a water droplet impacting a material and the relating stresses, then to further this knowledge by understanding the design of a wind turbine blade and the loads it encounters while in operation. To measure these erosion effects in a laboratory setting a specific methodology was devised and a custom testing facility was designed, manufactured and commissioned to carry out the individual tests to replicate environmental conditions faced for wind turbine blades in operation. These tests concluded that the erosion rate was determined by numerous factors including; the impact velocity, the impact angle, the stress applied to the material and the duration of exposure.

When increasing the impact velocity, simulating a longer blade, the erosion rate of

the material increased due to the increased forces acting on the material and higher velocity of lateral jetting. This was concurrent throughout all of the tests conducted.

In the experiments involving the adjustment of the impact angle between the GFRP sample and the water droplet it was concluded that the lower impact angles resulted in a more ductile mechanistic response which was confirmed by micro-graph images of gouging. Whereas in the higher impact angle tests the GFRP sample had a much more brittle response with pits and removal of material observed from the micro-graphs. The highest erosion rate was visible from the intermediate impact angles which showed an ductile-brittle response.

Investigating the stress within the material founded some interesting results. These tests were to simulate larger off-shore wind turbines where the extremely large blades are under internal stresses as well as high impact velocities. The results showed a greater increase in erosion rate and also new surface interference (SICDs) on the material due to the synergistic effect of the internal stress and the impact stresses from the droplet.

The investigation which aimed to explore the effects of salt water erosion to simulate the effects of sea water spray proved to be difficult to analyse. When examining the samples it was evident that salt water crystals had formed on the surface and within cracks and gouges which had detrimental effects on the mass loss results. It was clear, however, there was increased erosion on samples which had been tested with salt-water compared to rainwater from the micro-graphs but it was unable to quantify the difference.

The experimental tests which included an investigation into the cumulative effects of erosion by measuring the mass loss after set exposure times concluded in results which differed from the historical literature on rain erosion. The main difference which was observed was there was no incubation period as proposed by Springer [71]. There

Chapter 11. Conclusions

was almost immediate mass loss within the material and it was hypothesised that there is an incubation energy between the reaction between the droplet and the material which when surpassed the material starts to erode.

In the effort to combine the knowledge gained from this research into a useful tool a predictive model was developed. This model predicted the erosion of a turbine blade given its specific geometry, size and location. It operated by utilising the theta prediction model which was developed when trying to improve the secondary stages of creep. It was found that the theta prediction fitted the erosion curve competently and thus worked effectively.

Overall this study has made efforts to advance the research in order to make wind energy more predictable and hence reliable.

Chapter 12

Recommended Future Work

There some aspects of this work which can be improved and which required more time than this project was allocated. If this research were to be continued, the areas in which would be of personal importance would be the improvement of gathering experimental data and the evolution of the predictive model.

The research conducted within this study broke new grounds within the University as one of the largest and most powerful experimental rigs of its type was designed, manufactured and commissioned in house. The capabilities of this rig, however, were not fully utilised within this research and there are many ways in which it can be utilised to generate more data in fully understanding the erosion rate of wind turbine blades. For this research specifically the natural progression would be initially to complete the intended experiments and then continue by completing much longer tests to the point where the material fails. The rig was also designed with salt water in mind as all of the materials used in construction are corrosion resistant, however no salt water tests were conducted, these tests would also aid the data gathering.

Some alternative NDT methods should be used in future work which were unable to be employed during this research. The main technique which would have resulted in useful information is the intermittent use of a profilometer during testing to observe the progression of erosion, however for this technique to be conducted the equipment would

Chapter 12. Recommended Future Work

need to be present within the University to allow the continuation of the samples to be tested after analysis. Other forms of analysis which would be interesting for future work would be the inclusion of ultrasound, radiology and microwave imaging to observe any effect under the surface of the material from an internal stress applied during rain erosion impacts.

In order to improve upon the work completed on the predictive model within this research, a comparison to actual data recorded from a wind turbine in operation is required. This was attempted, however, wind turbine operators are sensitive with sharing information which shows damage to their machinery. The inclusion of this data would allow a more accurate model to be constructed as the leading edge of the blade from a turbine which has been in operation for a known period of time under known weather conditions including the amount of rainfall could be directly compared to experimental samples and then a relationship from the experimental run time to life in field can be determined.



Figure 12.1: Nickel Cobalt coating on an aeroplane propeller to protect it against LEE. Source [224]

Chapter 12. Recommended Future Work

Some further avenues which the research could follow could include testing the resistant coatings applied to turbine blades when they have been eroded. This will also aid the predictive model as it will allow a larger range of lifetime exposure. Other coatings which could be tested experimentally are the new developments applied to wind turbines and also potential replacements which have been used in other industries including nickel cobalt coating as shown in Figure 12.1 which are commonly used in aeroplane propellers and oil refineries.

Bibliography

- [1] BBC Scottish Government. Energy statistics for scotland q4 2020 figures. <https://www.bbc.co.uk/news/uk-scotland-56530424>, Mar 2021. Accessed: 2021-09-30.
- [2] Ivan Komusanac, Guy Brindley, and Daniel Fraile. Wind energy in europe in 2018—trends and statistics. *Wind Europe: Brussels, Belgium*, 2019.
- [3] American Clean Power Acp. A majority renewables future. <https://cleanpower.org/resources/a-majority-renewables-future/>, Dec 2020. Accessed: 2022-06-01.
- [4] Ryan Wiser, Mark Bolinger, Ben Hoen, Dev Millstein, Joseph Rand, Galen Barbose, Naïm Darghouth, Will Gorman, Seongeun Jeong, and Ben Paulos. Land-based wind market report: 2022 edition. Technical report, Lawrence Berkeley National Lab.(LBNL), Berkeley, CA (United States), 2022.
- [5] Saad Sayeef, Simon Heslop, David Cornforth, Tim Moore, Steven Percy, John Ward, Adam Berry, and Daniel Rowe. Solar intermittency: Australia’s clean energy challenge. characterising the effect of high penetration solar intermittency on australian electricity networks. *Global cc institute*, 2012.
- [6] BP. Statistics review of world energy, 69th edition. <https://www.bp.com/content/dam/bp/business-sites/en/global/corporate/pdfs/energy-economics/statistical-review/bp-stats-review-2020-full-report.pdf>, 2020. Accessed: 2021-02-07.
- [7] Adnan Durakovik. Bp and enbw set sights on scottish offshore wind. <https://www.offshorewind.biz/2021/05/11/bp-and-enbw-set-sights-on-scottish-offshore-wind/#:~:text=BP%20and%20EnBW%20Secure%20Prime%20Wind%20Real%20Estate%20offshore%20UK&text=BP%20aims%20to%20have%20developed,point%20of%20Final%20Investment%20Decision.>, May 2021. Accessed: 2021-04-19.
- [8] Sigrid Kusch-Brandt. Urban renewable energy on the upswing: A spotlight on renewable energy in cities in ren21’s “renewables 2019 global status report”, 2019.
- [9] K Padmanathan, N Kamalakannan, Padmanaban Sanjeevikumar, Frede Blaabjerg, Jens Bo Holm-Nielsen, G Uma, R Arul, R Rajesh, A Srinivasan, and J Baskaran. Conceptual frame-

Bibliography

- work of antecedents to trends on permanent magnet synchronous generators for wind energy conversion systems. *Energies*, 12(13):2616, 2019.
- [10] Mark Hugh Keegan. *Wind turbine blade leading edge erosion, an investigation of rain droplet and hailstone impact induced damage mechanisms*. PhD thesis, The University of Strathclyde, Glasgow,UK, 2014.
- [11] Mohammed G Khalfallah and Aboelyazied M Koliub. Effect of dust on the performance of wind turbines. *Desalination*, 209(1-3):209–220, 2007.
- [12] Trevor J. Price. Blyth, james (1839–1906), electrical engineer and university teacher. <https://www.oxforddnb.com/view/10.1093/ref:odnb/9780198614128.001.0001/odnb-9780198614128-e-100957>, September 2017. Accessed: 2021-03-02.
- [13] Tony Burton, Nick Jenkins, David Sharpe, and Ervin Bossanyi. *Wind energy handbook*. John Wiley & Sons, 2011.
- [14] Christina Olivecrona. Wind energy in denmark. *Green Budget Reform1995*, pages 55–67, 2014.
- [15] Ross Vennell. Exceeding the betz limit with tidal turbines. *Renewable Energy*, 55:277–285, 2013.
- [16] MA Yurdusev, RAŞİT Ata, and NS Çetin. Assessment of optimum tip speed ratio in wind turbines using artificial neural networks. *Energy*, 31(12):2153–2161, 2006.
- [17] Peter J Schubel and Richard J Crossley. Wind turbine blade design. *Energies*, 5(9):3425–3449, 2012.
- [18] R Dominy, P Lunt, A Bickerdyke, and J Dominy. Self-starting capability of a darrieus turbine. *Proceedings of the Institution of Mechanical Engineers, Part A: Journal of Power and Energy*, 221(1):111–120, 2007.
- [19] IDFC Private Equity. Green light for unique nova offshore wind turbine. *renewable energy focus*, page 17, 2009.
- [20] Erich Hau and Horst von Renouard. Electrical power from the wind—the first attempts. *Wind Turbines: Fundamentals, Technologies, Application, Economics*, pages 23–65, 2006.
- [21] RT Griffiths. The effect of aerofoil characteristics on windmill performance. *The Aeronautical Journal*, 81(799):322–326, 1977.
- [22] Theodore Theodorsen and United States. National Advisory Committee for Aeronautics. *Theory of wing sections of arbitrary shape*. US Government Printing Office, 1932.
- [23] Eric Pla, Lukas Pfarr, Eirik Torhaug, Christoffer Meek, Lukas Sebastian, Lehle Thomas, and Svensson Moen. Design and modeling of a small wind turbine. Technical report, Norwegian University of Science and Technology, 11 2015.
- [24] R. Wolfson. Environment and climate, 2nd ed. new york: Norton. `\protect\unhbox\voidb@x\protect\penalty\M\http://www.wind-power-program.com/popups/powercurve.htm`, Mar 2012. Accessed: 2022-12-27.

Bibliography

- [25] Povl Brøndsted, Hans Lilholt, and Aage Lystrup. Composite materials for wind power turbine blades. *Annu. Rev. Mater. Res.*, 35:505–538, 2005.
- [26] R Gasch and J Twele. Wind power plants. fundamentals, design, construction and operation. solarpraxis, 2002.
- [27] Dayton A Griffin and Michael D Zuteck. Scaling of composite wind turbine blades for rotors of 80 to 120 meter diameter. *J. Sol. Energy Eng.*, 123(4):310–318, 2001.
- [28] Mahmood M Shokrieh and Roham Rafiee. Simulation of fatigue failure in a full composite wind turbine blade. *Composite structures*, 74(3):332–342, 2006.
- [29] Guide to composites - gurit. <https://www.gurit.com/-/media/Gurit/Datasheets/guide-to-composites.pdf>, Jul 2015. Accessed: 2019-11-29.
- [30] Bharat Bhushan and Pak Lim Ko. Introduction to tribology. *Appl. Mech. Rev.*, 56(1):B6–B7, 2003.
- [31] FJ Heymann. Liquid impingement erosion, asm handbook, vol. 18, asm international, materials park, 1992.
- [32] E Honegger. Tests on erosion caused by jets. *Brown Boveri Rev*, 14(4):95–104, 1927.
- [33] E Honegger. Corrosion and erosion of steam turbine blading. *Brown Boveri Rev*, 12:263–278, 1924.
- [34] H S Kirols, D Kevorkov, A Uihlein, and M Medraj. Water droplet erosion of stainless steel steam turbine blades. *Materials Research Express*, 4(8):086510, aug 2017.
- [35] VA Ryzhenkov, AI Lebedeva, and AI F Mednikov. Erosion wear of the blades of wet-steam turbine stages: Present state of the problem and methods for solving it. *Thermal engineering*, 58(9):713–718, 2011.
- [36] N Yasugahira, K Namura, R Kaneko, and T Satoh. Erosion resistance of titanium alloys for steam turbine blades as measured by water droplet impingement. In *Titanium Steam Turbine Blading*, pages 383–402. Elsevier, 1990.
- [37] Cyrus B Meher-Homji, Thomas R Mee, et al. Gas turbine power augmentation by fogging of inlet air. In *Proceedings of the 28th Turbomachinery Symposium*. Texas A&M University. Turbomachinery Laboratories, 1999.
- [38] Jobaidur Rahman Khan. *Fog cooling, wet compression and droplet dynamics in gas turbine compressors*. PhD thesis, University of New Orleans, 2009.
- [39] AK Gujba, L Hackel, D Kevorkov, and M Medraj. Water droplet erosion behaviour of ti-6al-4v and mechanisms of material damage at the early and advanced stages. *Wear*, 358:109–122, 2016.
- [40] GF Schmitt. Coatings for erosion resistance. *Mechanical properties, performance, and failure modes of coatings*, pages 148–164, 1984.

Bibliography

- [41] S Karstadt, J Werner, S Münz, and R Aymanns. Effect of water droplets caused by low pressure egr on spinning compressor wheels. In *Proceedings of the 19th Supercharging Conference Dresden, Aachen, Germany*, pages 17–18, 2014.
- [42] Omid Gohardani. Impact of erosion testing aspects on current and future flight conditions. *Progress in Aerospace Sciences*, 47(4):280–303, 2011.
- [43] S Van der Zwaag and JE Field. Rain erosion damage in brittle materials. *Engineering Fracture Mechanics*, 17(4):367–379, 1983.
- [44] AA Fyall. Practical aspects of rain erosion of aircraft and missiles. *Philosophical Transactions for the Royal Society of London. Series A, Mathematical and Physical Sciences*, pages 161–167, 1966.
- [45] Omid Gohardani. Impact of erosion testing aspects on current and future flight conditions. *Progress in Aerospace Sciences*, 47(4):280–303, 2011.
- [46] N Fujisawa, S Takano, K Fujisawa, and T Yamagata. Experiments on liquid droplet impingement erosion on a rough surface. *Wear*, 398:158–164, 2018.
- [47] Kei Fujisawa, Takayuki Yamagata, and Nobuyuki Fujisawa. Liquid droplet impingement erosion on groove roughness. *Nuclear Engineering and Design*, 330:368–376, 2018.
- [48] Nobuyuki Fujisawa, Takayuki Yamagata, and Keitaro Wada. Attenuation of wall-thinning rate in deep erosion by liquid droplet impingement. *Annals of Nuclear Energy*, 88:151–157, 2016.
- [49] UK Health and Safety Executive. Public report of the fire and explosion at the conocophillips humber refinery, 2001.
- [50] Mohamed Elhadi Ibrahim and Mamoun Medraj. Water droplet erosion of wind turbine blades: Mechanics, testing, modeling and future perspectives. *Materials*, 13(1):157, 2019.
- [51] Ross Gunn and Gilbert D Kinzer. The terminal velocity of fall for water droplets in stagnant air. *Journal of Atmospheric Sciences*, 6(4):243–248, 1949.
- [52] L. Bartolomé and J. Teuwen. Prospective challenges in the experimentation of the rain erosion on the leading edge of wind turbine blades. *Wind Energy*, 22(1):140–151, 2019.
- [53] Aytaç Kubilay, Dominique Derome, Bert Blocken, and Jan Carmeliet. Cfd simulation and validation of wind-driven rain on a building facade with an eulerian multiphase model. *Building and environment*, 61:69–81, 2013.
- [54] William F Adler. Rain impact retrospective and vision for the future. *Wear*, 233-235:25–38, 1999.
- [55] Daniel C Harris. *Materials for infrared windows and domes: properties and performance*, volume 158. SPIE press, 1999.

Bibliography

- [56] B Amirzadeh, A Louhghalam, M Raessi, and M Tootkaboni. A computational framework for the analysis of rain-induced erosion in wind turbine blades, part i: Stochastic rain texture model and drop impact simulations. *Journal of Wind Engineering and Industrial Aerodynamics*, 163:33–43, 2017.
- [57] John Edwin Field, Martin B Lesser, and JP Dear. Studies of two-dimensional liquid-wedge impact and their relevance to liquid-drop impact problems. *Proceedings of the Royal Society of London. A. Mathematical and Physical Sciences*, 401(1821):225–249, 1985.
- [58] Stanley Smith Cook. Erosion by water-hammer. *Proceedings of the Royal Society of London. Series A, Containing Papers of a Mathematical and Physical Character*, 119(783):481–488, 1928.
- [59] JP Dear and JE Field. High-speed photography of surface geometry effects in liquid/solid impact. *Journal of Applied Physics*, 63(4):1015–1021, 1988.
- [60] F. J. Heymann. On the Shock Wave Velocity and Impact Pressure in High-Speed Liquid-Solid Impact. *Journal of Basic Engineering*, 90(3):400–402, 09 1968.
- [61] FJ Heymann. High-speed impact between a liquid drop and a solid surface. *Journal of Applied Physics*, 40(13):5113–5122, 1969.
- [62] RM Blowers. On the response of an elastic solid to droplet impact. *IMA Journal of Applied Mathematics*, 5(2):167–193, 1969.
- [63] M Rosenblatt, YM Ito, and GE Eggum. Analysis of brittle target fracture from a subsonic water drop impact. *Erosion: Prevention and Useful Applications; Adler, WF, Ed.; American Society for Testing and Materials: Philadelphia, PA*, page 227–254, 1979.
- [64] J.E Field. Elsi conference: invited lecture: Liquid impact: theory, experiment, applications. *Wear*, 233-235:1–12, 1999.
- [65] William F. Adler. Waterdrop impact modeling. *Wear*, 186-187:341–351, 1995. 8th International Conference on Erosion by Liquid and Solid Impact.
- [66] FJ Heymann. Erosion by liquids. *Mach. Des*, 10:118–124, 1970.
- [67] DC Jenkins and JD Booker. The impingement of water drops on a surface moving at high speed. In *Symp. Aerodynamic Capture of Particles*, pages 97–103, 1960.
- [68] WF Adler. The mechanics of liquid impact. *Academic Press, Treatise on Materials Science and Technology*, 16:127–183, 1979.
- [69] Akbar Hojjati Najafabadi, Reza Shoja Razavi, Reza Mozaffarinia, and Hamed Rahimi. A new approach of improving rain erosion resistance of nanocomposite sol-gel coatings by optimization process factors. *Metallurgical and Materials Transactions A*, 45(5):2522–2531, 2014.
- [70] Olive G Engel et al. Waterdrop collisions with solid surfaces. *Journal of research of the national bureau of standards*, 54(5):281–298, 1955.

Bibliography

- [71] G. S. Springer, C. I. Yang, and P. S. Larsen. Analysis of rain erosion of coated materials. *Journal of Composite Materials*, 8(3):229–252, 1974.
- [72] GE Cossali, G Brunello, A Coghe, and M Marengo. Impact of a single drop on a liquid film: experimental analysis and comparison with empirical models. In *Italian congress of thermo-fluid dynamics UIT, Ferrara*, volume 30, pages 1–12, 1999.
- [73] Rui Li, Hisashi Ninokata, and Michitsugu Mori. A numerical study of impact force caused by liquid droplet impingement onto a rigid wall. *Progress in Nuclear Energy*, 53(7):881–885, 2011.
- [74] L. Huang, J. Folkes, P. Kinnell, and P.H. Shipway. Mechanisms of damage initiation in a titanium alloy subjected to water droplet impact during ultra-high pressure plain waterjet erosion. *Journal of Materials Processing Technology*, 212(9):1906–1915, 2012.
- [75] B. Luiset, F. Sanchette, A. Billard, and D. Schuster. Mechanisms of stainless steels erosion by water droplets. *Wear*, 303(1):459–464, 2013.
- [76] Olive G Engel. Erosion damage to solids caused by high-speed. *Journal of Research of the National Bureau of Standards*, 61(1):47, 1958.
- [77] A Thiruvengadam, SL Rudy, and M Gunasekaran. Experimental and analytical investigations on liquid impact erosion. *ASTM Special Technical Publication*, pages 249–287, 1970.
- [78] GS Springer and CB Baxi. A model for rain erosion of homogeneous. *Erosion, Wear, and Interfaces with Corrosion*, 567:106, 1974.
- [79] A Thiruvengadam, SL Rudy, and M Gunasekaran. Experimental and analytical investigations on liquid impact erosion. *ASTM Special Technical Publication*, pages 249–287, 1970.
- [80] MS Mahdipoor, HS Kirols, D Kevorkov, P Jedrzejowski, and M Medraj. Influence of impact speed on water droplet erosion of tial compared with ti6al4v. *Scientific reports*, 5(1):1–17, 2015.
- [81] Y.I. Oka and H. Miyata. Erosion behaviour of ceramic bulk and coating materials caused by water droplet impingement. *Wear*, 267(11):1804–1810, 2009. ICAP 2008.
- [82] CF Kennedy and JE Field. Damage threshold velocities for liquid impact. *Journal of materials science*, 35(21):5331–5339, 2000.
- [83] Drew Eisenberg, Steffen Laustsen, and Jason Stege. Wind turbine blade coating leading edge rain erosion model: Development and validation. *Wind Energy*, 21(10):942–951, 2018.
- [84] H.M. Slot, E.R.M. Gelinck, C. Rentrop, and E. van der Heide. Leading edge erosion of coated wind turbine blades: Review of coating life models. *Renewable Energy*, 80:837–848, 2015.
- [85] B. Amirzadeh, A. Louhghalam, M. Raessi, and M. Tootkaboni. A computational framework for the analysis of rain-induced erosion in wind turbine blades, part ii: Drop impact-induced stresses and blade coating fatigue life. *Journal of Wind Engineering and Industrial Aerodynamics*, 163:44–54, 2017.

Bibliography

- [86] WF Adler. The mechanics of liquid impact. *Academic Press, Treatise on Materials Science and Technology*, 16:127–183, 1979.
- [87] WF Adler and RF Vyhna. Rain erosion of ti-6al-4v. In *Proceedings of the 4th International Conference on Rain Erosion and Associated Phenomena, Meersburg, Germany*, pages 8–10, 1974.
- [88] A.K. Gujba, L. Hackel, D. Kevorkov, and M. Medraj. Water droplet erosion behaviour of ti-6al-4v and mechanisms of material damage at the early and advanced stages. *Wear*, 358-359:109–122, 2016.
- [89] A Thiruvengadam, SL Rudy, and M Gunasekaran. Experimental and analytical investigations on liquid impact erosion. *ASTM Special Technical Publication*, pages 249–287, 1970.
- [90] Gwidon W. Stachowiak and Andrew W. Batchelor. 11 - abrasive, erosive and cavitation wear. In Gwidon W. Stachowiak and Andrew W. Batchelor, editors, *Engineering Tribology (Third Edition)*, pages 501–551. Butterworth-Heinemann, Burlington, third edition edition, 2006.
- [91] Xiao Chen, Wei Zhao, Xiao Lu Zhao, and Jian Zhong Xu. Preliminary failure investigation of a 52.3 m glass/epoxy composite wind turbine blade. *Engineering Failure Analysis*, 44:345–350, 2014.
- [92] E. F. Tobin, T. M. Young, and D. Raps. Evaluation and correlation of inter-laboratory results from a rain erosion test campaign. In *Proceedings of 28th International Congress of the Aeronautical Sciences*, 2012.
- [93] C. Siddons, C. Macleod, L. Yang, and M. M. Stack. An experimental approach to analysing rain droplet impingement on wind turbine blade materials. *EWEA 2015 Annual Event*, 2015.
- [94] KY Chiu, FT Cheng, and Hau Chung Man. Evolution of surface roughness of some metallic materials in cavitation erosion. *Ultrasonics*, 43(9):713–716, 2005.
- [95] Frederick G Hammitt, James F Lafferty, Robert Cheesewright, Martin T Pitek, Dale J Kempainen, and Terry M Mitchel. Laboratory scale devices for rain erosion simulation. Technical report, The University of Michigan, College of Engineering, Department of Nuclear Engineering, 1967.
- [96] Colin R Seward, Charles S James Pickles, and John E Field. Single-and multiple-impact jet apparatus and results. In *Window and Dome Technologies and Materials II*, volume 1326, pages 280–290. SPIE, 1990.
- [97] EF Tobin, TM Young, D Raps, and O Rohr. Comparison of liquid impingement results from whirling arm and water-jet rain erosion test facilities. *Wear*, 271(9-10):2625–2631, 2011.
- [98] FP Bowden and JH Brunton. Damage to solids by liquid impact at supersonic speeds. *Nature*, 181(4613):873–875, 1958.

Bibliography

- [99] Frank Philip Bowden and JH Brunton. The deformation of solids by liquid impact at supersonic speeds. *Proceedings of the Royal Society of London. Series A. Mathematical and Physical Sciences*, 263(1315):433–450, 1961.
- [100] William F Adler. Rain impact retrospective and vision for the future. *Wear*, 233:25–38, 1999.
- [101] Agrim Sareen, Chinmay A Sapre, and Michael S Selig. Effects of leading edge erosion on wind turbine blade performance. *Wind Energy*, 17(10):1531–1542, 2014.
- [102] TJ Methven and B Fairhead. A correlation between rain erosion of perspex specimens in flight and on a ground rig. *Ministry of Aviation, Aeronautical research council*, 1960.
- [103] GF Schmitt and CJ Hurley. Development and calibration of a mach 1.2 rain erosion test apparatus. Technical report, AFML-TR-70-240, Air Force Materials Laboratory, Wright-Patterson Air Force . . . , 1970.
- [104] Carolyn Westmark and G Wm Lawless. A discussion of rain erosion testing at the united states air force rain erosion test facility. *Wear*, 186:384–387, 1995.
- [105] AA Deom, A Luc, S Amara, and DL Balageas. Towards more realistic erosion simulation tests for high velocity em and ir windows. *Wear*, 233:13–24, 1999.
- [106] JH Brunton. A discussion on deformation of solids by the impact of liquids, and its relation to rain damage in aircraft and missiles, to blade erosion in steam turbines, and to cavitation erosion-high speed liquid impact. *Philosophical Transactions of the Royal Society of London. Series A, Mathematical and Physical Sciences*, 260(1110):79–85, 1966.
- [107] TM Young, B Humphreys, and JP Fielding. Investigation of hybrid laminar flow control (hlfc) surfaces. *Aircraft design*, 4(2-3):127–146, 2001.
- [108] E. F. Tobin, T. M. Young, D. Raps, and O. Rohr. Comparison of liquid impingement results from whirling arm and water-jet rain erosion test facilities. *Wear*, 271(9-10):2625–2631, 2011.
- [109] ASTM. Standard Test Method for Liquid Impingement Erosion Using Rotating Apparatus. Standard, ASTM, December 2021.
- [110] H. Busch, G. Hoff, G. Langbein, G. Taylor, D. C. Jenkins, M. A. Taunton, A. A. Fyall, R. F. Jones, and T. W. Harper. Rain erosion properties of materials. *Philosophical Transactions for the Royal Society of London. Series A, Mathematical and Physical Sciences*, pages 168–181, 1966.
- [111] DNVGL. DNVGL-CP-0424: Coatings for protection of FRP structures with heavy rain erosion loads. *Class Programme*, 2016.
- [112] A DESIGNERS’HANDBOOK SERIES. Design guidelines for the selection and use of stainless steels. *A designers handbook series no. 9014*, 1976.
- [113] G. S. Springer. *Erosion by Liquid Impact*. A Halsted Press book. Scripta Publishing Company, 1976.

Bibliography

- [114] D. Eisenberg, S. Laustsen, and J. Stege. Wind turbine blade coating leading edge rain erosion model: Development and validation. *Wind Energy*, 21(10):942–951, 2018.
- [115] H. M. Slot, E. R. M. Gelinck, C. Rentrop, and E. Van Der Heide. Leading edge erosion of coated wind turbine blades: Review of coating life models. *Renewable Energy*, 80:837–848, 2015.
- [116] H. M. Slot, R. M. IJzerman, M. le Feber, K. Nord-Varhaug, and E. van der Heide. Rain erosion resistance of injection moulded and compression moulded polybutylene terephthalate pbt. *Wear*, 414:234–242, 2018.
- [117] E. Cortés, F. Sánchez, A. O’Carroll, B. Madramany, M. Hardiman, and T. Young. On the material characterisation of wind turbine blade coatings: the effect of interphase coating–laminate adhesion on rain erosion performance. *Materials*, 10(10):1146, 2017.
- [118] M. K. Lee, W. W. Kim, C. K. Rhee, and W. J. Lee. Liquid impact erosion mechanism and theoretical impact stress analysis in tin-coated steam turbine blade materials. *Metallurgical and Materials Transactions A*, 30(4):961–968, 1999.
- [119] M. H. Keegan, D. H. Nash, and M. M. Stack. On erosion issues associated with the leading edge of wind turbine blades. *Journal of Physics D: Applied Physics*, 46(38):383001, 2013.
- [120] M. Sankarasubramanian, M. Torabizadeh, Z. A. Putnam, J. C. Moosbrugger, M. Y. Huang, and S. Krishnan. Enhanced elastomer toughness and fracture properties imparted by chemically reactive flat nanoparticles. *Polymer Testing*, page 105932, 2019.
- [121] B. N. J. Persson and E. A. Brener. Crack propagation in viscoelastic solids. *Physical Review E*, 71(3):036123, 2005.
- [122] A. Tcharkhtchi, S. Farzaneh, S. Abdallah-Elhirszi, B. Esmaeillou, F. Nony, and A. Baron. Thermal aging effect on mechanical properties of polyurethane. *International Journal of Polymer Analysis and Characterization*, 19(7):571–584, 2014.
- [123] ISO. Pd iso/ts 19392-1:2018 paints and varnishes — coating systems for wind-turbine rotor blades. part 1: Minimum requirements and weathering. *ISO Standards*, 2018.
- [124] E. A. Valaker, S. Armada, and S. Wilson. Droplet erosion protection coatings for offshore wind turbine blades. *Energy Procedia*, 80:263–275, 2015.
- [125] S. Zhang, K. Dam-Johansen, S. Nørkjær, P. L. Bernad, and S. Kiil. Erosion of wind turbine blade coatings – design and analysis of jet-based laboratory equipment for performance evaluation. *Progress in Organic Coatings*, 78:103 – 115, 2015.
- [126] S. Zhang, K. Dam-Johansen, P. L. Bernad, and S. Kiil. Rain erosion of wind turbine blade coatings using discrete water jets: Effects of water cushioning, substrate geometry, impact distance, and coating properties. *Wear*, 328:140–148, 2015.

Bibliography

- [127] A. O'Carroll, M. Hardiman, E. F. Tobin, and T. M. Young. Correlation of the rain erosion performance of polymers to mechanical and surface properties measured using nanoindentation. *Wear*, 412:38–48, 2018.
- [128] Á. Pomázi and A. Toldy. Multifunctional gelcoats for fiber reinforced composites. *Coatings*, 9(3):173, 2019.
- [129] F. J. Heymann. Erosion by liquids. *Machine Design*, 10:118–124, 1970.
- [130] M. C. Shaw and G. J. DeSalvo. The role of elasticity in hardness testing. *Metallography, Microstructure, and Analysis*, 1(6):310–317, 2012.
- [131] M. Grundwürmer, O. Nuyken, M. Meyer, J. Wehr, and N. Schupp. Sol-gel derived erosion protection coatings against damage caused by liquid impact. *Wear*, 263(1-6):318–329, 2007.
- [132] O. Gohardani. Impact of erosion testing aspects on current and future flight conditions. *Progress in Aerospace Sciences*, 47(4):280–303, 2011.
- [133] A. G. Evans, M. E. Gulden, G. E. Eggum, and M. Rosenblatt. Impact damage in brittle materials in the plastic response regime. Technical report, ROCKWELL INTERNATIONAL THOUSAND OAKS CALIF SCIENCE CENTER, 1976.
- [134] K. Pugh, G. Rasool, and M. M. Stack. Some thoughts on mapping tribological issues of wind turbine blades due to effects of onshore and offshore raindrop erosion. *Journal of Bio-and Tribo-Corrosion*, 4(3):50, 2018.
- [135] E. F. Tobin, O. Rohr, D. Raps, W. Willemse, P. Norman, and T. M. Young. Surface topography parameters as a correlation factor for liquid droplet erosion test facilities. *Wear*, 328:318–328, 2015.
- [136] A. Sareen, C. A. Sapre, and M. S. Selig. Effects of leading edge erosion on wind turbine blade performance. *Wind Energy*, 17(10):1531–1542, 2014.
- [137] S. Zhang, S. Kiil, K. Dam-Johansen, and P. L. Bernad Jr. *Accelerated rain erosion of wind turbine blade coatings*. Danmarks Tekniske Universitet (DTU), 2014.
- [138] K. Pugh, G. Rasool, and M. M. Stack. Raindrop erosion of composite materials: some views on the effect of bending stress on erosion mechanisms. *Journal of Bio-and Tribo-Corrosion*, 5(2):45, 2019.
- [139] J. L. Thomason, J. Carruthers, J. Kelly, and G. Johnson. Fibre cross-section determination and variability in sisal and flax and its effects on fibre performance characterisation. *Composites Science and Technology*, 71(7):1008–1015, 2011.
- [140] University of Strathclyde. Scanning electron microscopes — university of strathclyde. <https://www.strath.ac.uk/research/advancedmaterialsresearchlaboratory/rangeofanalyses/compositionalanalysis/scanningelectronmicroscopes/>, 2019. Accessed: 2021-09-30.

Bibliography

- [141] J. Foldyna, J. Klich, P. Hlavavcek, M. Zelevnak, and J. Svcuvcka. Erosion of metals by pulsating water jet. *Tehnicki vjesnik*, 19(2):381–386, 2012.
- [142] P. Lammel, L. D. Rafailovic, M. Kolb, K. Pohl, A. H. Whitehead, G. Grundmeier, and B. Gollas. Analysis of rain erosion resistance of electroplated nickel–tungsten alloy coatings. *Surface and Coatings Technology*, 206(8-9):2545–2551, 2012.
- [143] A. Davis, Y. H. Yeong, A. Steele, E. Loth, and I. S. Bayer. Nanocomposite coating superhydrophobicity recovery after prolonged high-impact simulated rain. *Rsc Advances*, 4(88):47222–47226, 2014.
- [144] F. P. Bowden and J. H. Brunton. The deformation of solids by liquid impact at supersonic speeds. *Proceedings of the Royal Society of London. Series A. Mathematical and Physical Sciences*, 263(1315):433–450, 1961.
- [145] C.J.R. Sheppard and A. Choudhury. Image formation in the scanning microscope. *Optica Acta: International Journal of Optics*, 24(10):1051–1073, 1977.
- [146] E. F. Tobin and T. M. Young. Analysis of incubation period versus surface topographical parameters in liquid droplet erosion tests. *Materials Performance and Characterization*, 6(2):144–164, 2017.
- [147] A. Selmi. Void effect on carbon fiber epoxy composites. In *Second International Conference on Emerging Trends in Engineering and Technology (ICETET), London, May*, pages 30–31, 2014.
- [148] L. Di Landro, A. Montalto, P. Bettini, S. Guerra, F. Montagnoli, and M. Rigamonti. Detection of voids in carbon/epoxy laminates and their influence on mechanical properties. *Polymers and Polymer Composites*, 25(5):371–380, 2017.
- [149] K. B. Katnam, A. J. Comer, D. Roy, L. F. M. Da Silva, and T. M. Young. Composite repair in wind turbine blades: an overview. *The Journal of Adhesion*, 91(1-2):113–139, 2015.
- [150] M. H. Keegan, D. Nash, and M. Stack. Modelling rain drop impact on offshore wind turbine blades. *ASME Turbo Expo 2012*, pages Article–GT, 2012.
- [151] J. Chen and S. J. Bull. Approaches to investigate delamination and interfacial toughness in coated systems: an overview. *Journal of Physics D: Applied Physics*, 44(3):034001, 2010.
- [152] Collaboration for NDT Education. Wavelength & defect detection. *NDT Resource Center*, 2001.
- [153] J. F. Vandenrijt, F. Languy, C. Thizy, and M. Georges. Laser ultrasound flexible system for non-contact inspection of medium size and complex shaped composite structures made of carbon fiber reinforced polymer. In *Multidisciplinary Digital Publishing Institute Proceedings*, volume 2, page 455, 2018.
- [154] O. Focke, M. Kalms, C. V. Kopylow, and W. Jueptner. Ndt of free formed cfrp composites with laser ultrasonic. In *12th Asia Pacific Conference on NDT*, 2006.

Bibliography

- [155] R. Halmshaw. Non-destructive testing. second edition. *Edward Arnold, Mill Rd, Dunton Green, Sevenoaks, Kent TN 13 2 YA, UK, 1991. 323*, 1991.
- [156] RA Pethrick. Non-destructive evaluation (nde) of composites: dielectric techniques for testing partially or non-conducting composite materials. In *Non-Destructive Evaluation (NDE) of Polymer Matrix Composites*, pages 116–135. Elsevier, 2013.
- [157] B. Ehrhart, B. Valeske, and C. Bockenheimer. Non-destructive evaluation (nde) of aerospace composites: methods for testing adhesively bonded composites. In *Non-destructive evaluation (NDE) of polymer matrix composites*, pages 220–237. Elsevier, 2013.
- [158] B Stakenborghs. Evisivescan microwave scanning ndt. *NPL Project VITCEA*, 2015.
- [159] M Gower, M Lodeiro, A Aktas, and R Shaw. Validated inspection techniques for composites in energy applications. *NPL Project VITCEA*, 2015.
- [160] NPL. Microwave ndt for composites explained. *NPL E-Training Course*, 2019.
- [161] ASTM International. ASTM G73-10(2017) Standard Test Method for Liquid Impingement Erosion Using Rotating Apparatus. *ASTM International*, 2017.
- [162] L. Boermans and H. Selen. On the design of some airfoils for sailplane application. *Technical Soaring*, 7(1):13–35, 1981.
- [163] R. S. Ehrmann. *Effect of Surface Roughness on Wind Turbine Performance*. PhD thesis, Texas A&M University, 2014.
- [164] E. Sagol, M. Reggio, and A. Ilinca. Issues concerning roughness on wind turbine blades. *Renewable and Sustainable Energy Reviews*, 23:514–525, 2013.
- [165] I. F. Zidane, K. M. Saqr, G. Swadener, X. Ma, and M. F. Shehadeh. On the role of surface roughness in the aerodynamic performance and energy conversion of horizontal wind turbine blades: a review. *International journal of energy research*, 40(15):2054–2077, 2016.
- [166] G. Pechlivanoglou, S. Fuehr, C. N. Nayeri, and C. O. Paschereit. The effect of distributed roughness on the power performance of wind turbines. In *ASME Turbo Expo 2010: Power for Land, Sea, and Air*, pages 845–855. American Society of Mechanical Engineers, 2010.
- [167] Peter J Schubel and Richard J Crossley. Wind turbine blade design. *Energies*, 5(9):3425–3449, 2012.
- [168] Galih Bangsa. Comparison of blade element method and cfd simulations of a 10 mw wind turbine. *Fluids*, 3(4):73, 2018.
- [169] Xinzi Tang, Ruitao Peng, and Xiongwei Liu. Design and finite element analysis of mixed aerofoil wind turbine blades. *Sandia National Laboratories*, 2011.
- [170] Xinzi Tang. *Aerodynamic design and analysis of small horizontal axis wind turbine blades*. PhD thesis, University of Central Lancashire, 2012.

Bibliography

- [171] Mingwei Ge, Le Fang, and De Tian. Influence of reynolds number on multi-objective aerodynamic design of a wind turbine blade. *PloS one*, 10(11):e0141848, 2015.
- [172] Franck Bertagnolio, Niels Sørensen, Jeppe Johansen, and Peter Fuglsang. Wind turbine airfoil catalogue. *U.S. Department of Energy Office of Scientific and Technical Information*, 2001.
- [173] Siemens Gamesa Renewable Energy. Offshore wind turbine: Sg 14-222 dd. <https://www.siemensgamesa.com/en-int/products-and-services/offshore/wind-turbine-sg-14-222-dd.>, May 2021.
- [174] Matthew Huaiquan Zhang. *Wind resource assessment and micro-siting: science and engineering*. John Wiley & Sons, 2015.
- [175] Egbert Torenbeek. *Advanced aircraft design: conceptual design, analysis and optimization of subsonic civil airplanes*. John Wiley & Sons, 2013.
- [176] Siemens Gamesa Renewable Energy. Sg 14-222 dd. <https://www.siemensgamesa.com/en-int/products-and-services/offshore/wind-turbine-sg-14-222-dd.>, 2021. Accessed: 2022-07-03.
- [177] Kyoungboo Yang. Geometry design optimization of a wind turbine blade considering effects on aerodynamic performance by linearization. *Energies*, 13(9):2320, 2020.
- [178] Hoyland Jorg. *Challenges for large wind turbine blades*. PhD thesis, Norwegian University of Science and Technology, 2010.
- [179] D Todd Griffith. The snl100-01 blade: carbon design studies for the sandia 100-meter blade. *Sandia National Laboratories Technical Report, SAND2013-1178*, 2013.
- [180] D Todd Griffith, Thomas D Ashwill, et al. The sandia 100-meter all-glass baseline wind turbine blade: Snl100-00. *Informe Técnico, Sandia National Laboratories*, 2011.
- [181] Matthew Huaiquan Zhang. *Wind resource assessment and micro-siting: science and engineering*. John Wiley & Sons, 2015.
- [182] Olimpo Anaya-Lara, Nick Jenkins, Janaka B Ekanayake, Phill Cartwright, and Michael Hughes. *Wind energy generation: modelling and control*. John Wiley & Sons, 2011.
- [183] Lin Wang, Robin Quant, and Athanasios Kolios. Fluid structure interaction modelling of horizontal-axis wind turbine blades based on cfd and fea. *Journal of Wind Engineering and Industrial Aerodynamics*, 158:11–25, 2016.
- [184] Henk Kaarle Versteeg and Weeratunge Malalasekera. *An introduction to computational fluid dynamics: the finite volume method*. Pearson education, 2007.
- [185] J Laursen, P Enevoldsen, and S Hjort. 3d cfd quantification of the performance of a multi-megawatt wind turbine. In *Journal of Physics: Conference Series*, volume 75, page 012007. IOP Publishing, 2007.

Bibliography

- [186] Galih Bangga. Comparison of blade element method and cfd simulations of a 10 mw wind turbine. *Fluids*, 3(4):73, 2018.
- [187] Luca Lavaroni, Simon J Watson, Malcolm J Cook, and Mark R Dubal. A comparison of actuator disc and bem models in cfd simulations for the prediction of offshore wake losses. In *Journal of physics: conference series*, volume 524, page 012148. IOP Publishing, 2014.
- [188] Abtin Namiranian. *3D simulation of a 5MW wind turbine*. Department of mechanical engineering, Blekinge Institute of Technology, Karlskrona, Sweden, 2011.
- [189] Weifei Hu, Insik Han, Sang-Chul Park, and Dong-Hoon Choi. Multi-objective structural optimization of a hawt composite blade based on ultimate limit state analysis. *Journal of mechanical science and technology*, 26:129–135, 2012.
- [190] Leon Mishnaevsky Jr, Kim Branner, Helga Nørgaard Petersen, Justine Beauson, Malcolm McGugan, and Bent F Sørensen. Materials for wind turbine blades: An overview. *Materials*, 10(11):1285, 2017.
- [191] K Pugh, JW Nash, G Reaburn, and MM Stack. On analytical tools for assessing the raindrop erosion of wind turbine blades. *Renewable and Sustainable Energy Reviews*, 137:110611, 2021.
- [192] BD Jana and MM Stack. A note on threshold velocity criteria for modelling the solid particle erosion of wc/co mmcs. *Wear*, 270(7-8):439–445, 2011.
- [193] J. Chen, J. Wang, and A. Ni. A review on rain erosion protection of wind turbine blades. *Journal of Coatings Technology and Research*, 16(1):15–24, 2019.
- [194] George E Totten. *Liquid Impingement Erosion*, volume 18. ASM Handbook, 2017.
- [195] TH Hoksbergen, I Baran, and R Akkerman. Rain droplet erosion behavior of a thermoplastic based leading edge protection system for wind turbine blades. In *IOP Conference Series: Materials Science and Engineering*, volume 942, page 012023. IOP Publishing, 2020.
- [196] Cinzio Arrighetti, Giovanni Maria De Pratti, and Raffaele Ruscitti. Performance decay analysis of new rotor blade profiles for wind turbines operating in offshore environments. *Wind Engineering*, 27(5):371–379, 2003.
- [197] IM Hutchings. *Tribology: friction and wear of engineering materials*, london: Edward arnold, 1992. *Google Scholar*, 1984.
- [198] Rafee Abdulmajeed Rafee Ahamed, Cameron M Johnstone, and Margaret M Stack. Impact angle effects on erosion maps of gfrp: applications to tidal turbines. *Journal of Bio-and Tribo-Corrosion*, 2(2):1–11, 2016.
- [199] Ghulam Rasool, Shayan Sharifi, Cameron Johnstone, and Margaret M Stack. Mapping synergy of erosion mechanisms of tidal turbine composite materials in sea water conditions. *Journal of Bio-and Tribo-Corrosion*, 2(2):1–15, 2016.

Bibliography

- [200] Samuel Groucott, Kieran Pugh, Iasonas Zekos, and Margaret M Stack. A study of raindrop impacts on a wind turbine material: Velocity and impact angle effects on erosion maps at various exposure times. *Lubricants*, 9(6):60, 2021.
- [201] Yen C Huang, FG Hammitt, and WJ Yang. Hydrodynamic phenomena during high-speed collision between liquid droplet and rigid plane. *Journal of Fluids Engineering*, 1973.
- [202] MB Lesser and JE Field. The impact of compressible liquids. *Annual review of fluid mechanics*, 15:97–122, 1983.
- [203] M Rosenblatt, GE Eggum, LA DeAngelo, and KN Kreyenhagen. Numerical investigation of water drop erosion mechanisms in infrared-transparent materials. Technical report, CALIFORNIA RESEARCH AND TECHNOLOGY INC WOODLAND HILLS, 1976.
- [204] Alessio Castorrini, Paolo Venturini, Alessandro Corsini, and Franco Rispoli. Machine learnt prediction method for rain erosion damage on wind turbine blades. *Wind Energy*, 24(8):917–934, 2021.
- [205] Met Office. Uk actual and anomaly maps. <https://www.metoffice.gov.uk/research/climate/maps-and-data/uk-actual-and-anomaly-maps>, 2022. Accessed: 2022-04-03.
- [206] Séamus Walsh. 01-new long-term rainfall averages for ireland. In *National Hydrology Seminar*, 2012.
- [207] Monthly rainfall in uk. <https://www.statista.com/statistics/584914/monthly-rainfall-in-uk/>, 2022. Accessed: 2022-04-03.
- [208] PD Jones, CG Kilsby, Colin Harpham, Vassilis Glenis, and Aidan Burton. Uk climate projections science report: Projections of future daily climate for the uk from the weather generator. *UK Climate Projections science report*, 2009.
- [209] Adela Bâra, Anda Velicanu, Ion Lungu, and Iuliana Botha. Natural factors that can affect wind parks and possible implementation solutions in a geographic information system. In *International Conference on Development, Energy, Environment, Economics, Puerto de la Cruz, Tenerife*, pages 50–54. Citeseer, 2010.
- [210] Mahmood M Shokrieh and Roham Rafiee. Simulation of fatigue failure in a full composite wind turbine blade. *Composite structures*, 74(3):332–342, 2006.
- [211] Kieran Pugh, Ghulam Rasool, and Margaret M Stack. Some thoughts on mapping tribological issues of wind turbine blades due to effects of onshore and offshore raindrop erosion. *Journal of Bio-and Tribo-Corrosion*, 4(3):1–8, 2018.
- [212] Zheng Li, Menghua Zhao, and Zhe Chen. Efficiency evaluation for offshore wind farms. In *2006 international conference on power system technology*, pages 1–6. IEEE, 2006.
- [213] Peter Tavner. *Offshore wind turbines: reliability, availability and maintenance*, volume 13. IET, 2012.

Bibliography

- [214] K Pugh, JWK Nash, MM Stack, and G Reaburn. Review of analytical techniques for assessing rain drop erosion resistance of materials. In *14th Conference on Sustainable Development of Energy, Water and Environment Systems*, 2019.
- [215] Robert Schaefer Ehrmann. *Effect of surface roughness on wind turbine performance*. PhD thesis, Texas A&M University, 2014.
- [216] Agrim Sareen, Chinmay A Sapre, and Michael S Selig. Effects of leading edge erosion on wind turbine blade performance. *Wind Energy*, 17(10):1531–1542, 2014.
- [217] Kieran Pugh, Ghulam Rasool, and Margaret M Stack. Raindrop erosion of composite materials: some views on the effect of bending stress on erosion mechanisms. *Journal of Bio-and Tribo-Corrosion*, 5(2):1–12, 2019.
- [218] Hamish Macdonald, David Infield, David H Nash, and Margaret M Stack. Mapping hail meteorological observations for prediction of erosion in wind turbines. *Wind Energy*, 19(4):777–784, 2016.
- [219] Mark Hugh Keegan, David Nash, and Margaret Stack. *Wind Turbine Blade Leading Edge Erosion: An investigation of rain droplet and hailstone impact induced damage mechanisms*. PhD thesis, University of Strathclyde, 2014.
- [220] Russell W Evans and Brian Wilshire. Creep of metals and alloys. *US Department of Energy*, 1985.
- [221] Ming Song, Tong Xu, Qijiang Wang, Weilian Wang, Yedong Zhou, Min Gong, and Chao Sun. A modified theta projection model for the creep behaviour of creep-resistant steel. *International Journal of Pressure Vessels and Piping*, 165:224–228, 2018.
- [222] Leon Mishnaevsky Jr and Kenneth Thomsen. Costs of repair of wind turbine blades: Influence of technology aspects. *Wind Energy*, 23(12):2247–2255, 2020.
- [223] Iain Staffell and Richard Green. How does wind farm performance decline with age? *Renewable energy*, 66:775–786, 2014.
- [224] Weather Guard. Leading edge erosion: Why we keep failing to solve it. <https://weatherguardwind.com/leading-edge-erosion/>, 2022. Accessed: 2022-07-07.

List of Figures

1.1	2019 New onshore and offshore wind installation in Europe [2]	2
1.2	Total US investment wind and solar - cumulative capital investment, 2020-2030 [3]	3
1.3	Growth in size of wind turbines since 1980 and future prospects [9]	4
1.4	Maximum tip velocity and rotor diameter for various wind turbine suppliers [10]	4
2.1	Wind turbine constructed by James Blyth at his Marykrik home circa 1887 [12]	7
2.2	Construction of the Smith-Putnam Wind Turbine [13]	8
2.3	Smith-Putnam Wind Turbine on Grandpa's Knob, [13]	9
2.4	Modern and historical rotor designs, linking to Table2.1. Source [17]	11
2.5	Variation of the λ - C_p curve depending on the pitch angle of the blades (β)	15
2.6	Aerodynamic forces acting on a turbine blade. Source [17]	16
2.7	C_p and C_t plot against λ . [23]	16
2.8	Typical wind turbine power with wind velocity. [24]	17
2.9	Wind turbine blade displayed as a cantilever beam under a uniformly distributed load from an aerodynamic lift force [17]	18
2.10	Flapwise bending along the axis xx [17]	19
2.11	Wind turbine blade modelled as a cantilever beam under gravitational load [17]	21
2.12	(a)Specific stiffness and strength of various material groups (b)Specific stiffness and strength of various material groups, highlighting CFRP and GFRP [10]	23
2.13	Stress strain curve of composite material and its components [10]	24
2.14	Tensile and Compressive stress strain line graphs for various fibres used within composites [29]	27
3.1	Blades in a low pressure stage in a steam turbine [36]	30
3.2	Compressor of a gas turbine [39]	31
3.3	A commercial aircraft showing the density of wear from WDE by black dots [45]	32
3.4	Fire and explosion at the ConocoPhillips Humber refinery in 2001 showing(a)The failed elbow causing the explosion(b) Fire and secondary fireball [49]	32

List of Figures

3.5	Steam pipes of a nuclear power plant experiencing WDE [50]	33
3.6	Terminal velocity of water droplets of various diameters [51]	34
3.7	The probabilistic density of raindrop size due to the rain fall rate [53]	36
3.8	The fragmentation of an oversized droplet [32]	37
3.9	Impact at $150ms^{-1}$ between a water droplet and a metal disc. Source [59]	40
3.10	Schematic view of a shock wave propagation occurring during the impact between a material and a falling droplet illustrating the three stress waves propagating the material. Source [45]	41
3.11	Schematic of the beginning of lateral jetting formation [50]	43
3.12	Ratio of lateral jetting to impact velocity, redrawn by [50]	43
3.13	Time dependency of lateral jetting immediately after droplet impact on a surface [70]	44
3.14	Possible mechanisms of erosion including a) A low impact angle producing abrasion b) a high impact angle at a relatively low impact velocity inducing surface fatigue c) a high impact angle from a relatively high impact velocity producing brittle fracture or multiple deformation d) at extreme high impact velocities which result in surface melting e)macroscopic erosion with secondary effects f) crystal lattice degradation from impacts by atoms. [90]	50
3.15	Impingement angle of a particle causing erosion of a surface [90]	51
3.16	Graphs depicting the trend in wear rate over impingement angle of a (a)Brittle material (b)Ductile material [90]	52
3.17	Impingement angles onto the leading edge of a wind turbine blade	53
4.1	Regions of a wind turbine blade. Source [91]	54
4.2	Classification of erosion test facility, adapted from [50]	56
4.3	Jet erosion testing facility [96]	57
4.4	(a)The principle of how the PJET test rig operates. (b)A laboratory photograph of PJET	58
4.5	Ballistic/ rocket sled facility showing (a) An Overview of the rocket sled at Holloman Air Base in New Mexico. (b) The polymeric bead arrays supported on fine threads in a styrofoam frame placed on the test track for impact with specimens mounted in wedged-shaped holders on the front end of the rocket sled. The specimen arrangement is seen in the background. [100]	59
4.6	Schematic of the University of Illinois at Urbana-Champaign low-turbulence subsonic wind tunnel. [101]	60
4.7	WARER facilities (a)University of limerick [108] (b)R&D Commercial rig (c) WARER utilised by Busch et al in dornier system gmbh friedrichshafen, germany [110]	62
5.1	ANSYS computational analysis to calculate the turbulence within the WARER running at 1000rpm	65

List of Figures

5.2	Structural analysis computed with Solwidworks to determine natural frequencies of the motor stand.	66
5.3	Motor stand frame under the main octagon of the WARER.	67
5.4	Schematic of the WARER at the University of Strathclyde.	68
5.5	WARER at the University of Strathclyde (Picture taken January 2022).	69
5.6	WARER with the lid removed (Picture taken January 2022).	69
5.7	Sample holder mounted in position within the WARER.(Picture taken February 2022)	72
5.8	Analysis set up for the sample holder using the in built Solidworks software	73
5.9	Stress map of the main spinning disc and the sample holder	74
5.10	Setup for measuring the droplet diameter	76
5.11	Falling droplet captured in high speed in order to evaluate its diameter	77
5.12	Control Panel for WARER (Picture taken February 2022)	79
5.13	Video feed from the CCTV cameras set up to monitor the WARER.(Picture taken February 2022)	80
6.1	Hardness Vs. Rain Erosion Resistance of polymers. Figure from O’Carrol et al. [127].	88
6.2	Damage Threshold Velocity (DVT) Vs. droplet diameter using 6.4 from [133] for epoxy coatings with different fracture toughnesses. Figure adapted from [119]. Rayleigh wave velocity, $c_R = 942ms^{-1}$, Density of water, $\rho_w = 1000kg/m^3$, Speed of sound in water, $c_w = 1490 ms^{-1}$	90
6.3	Comparrison between SEM imaging and Optical imaging [139]	92
6.4	SEM at the University of Strathclyde within the Advanced Materials Research Laboratory [140]	93
6.5	SEM image of pinholes on GFRP [93]	94
6.6	SEM image of glass fibre [138]	94
6.7	Stylus profilometer [138]	95
6.8	Optical profilometer [93]	95
6.9	CLSM scan of sample subject to salt water erosion [139]	96
6.10	Displayed here is a graph showing defect size vs. approximate frequency required to detect it. Materials data was sourced from Slot et al. [115]. Wave speed was calculated using the equation provided by Springer [113]. Frequency was calculated using the standard wave equation $c = \lambda f$, where c is the speed of sound, f is the frequency and λ is the wavelength.	99
6.11	Line graph displaying weight loss against time [113]	102
6.12	Wear-map showing mass loss with respect to impact velocity and angle [138].	103

List of Figures

7.1	Typical wind loading on a wind turbine blade root to tip for a rotating scenario ignoring gravitational effects calculated using a CFD approach comparing different mesh refinement density in the (a) Axial and (b) Tangential directions [168]	108
7.2	Turbine blade split up into elements dr , and details of the aerofoil basic characteristics at each element along the blade length R visually allowing the high angle of attack at which wind turbine blades are set to be observed.	109
7.3	Lift coefficient against angle of attack for the Du93-W-210 aerofoil as obtained through computational and experimental data [172]	111
7.4	Aerofoil shapes for different thickness to chord ratios (as indicated by percentage values in the aerofoil name) used along the designed blade length	112
7.5	Optimal and linearised final blade twist angles for the blade geometry generated along the blade radius	113
7.6	Optimal and linearised final blade chord length for the blade geometry generated along the radius	114
7.7	Final blade aerodynamic shell geometry as modelled in CAD showing the aerofoil shape at the different elements along its length	114
7.8	Final blade material distribution and thickness as set for the FEA analysis	115
7.9	Final blade geometry computer model used for FEA analysis	116
7.10	Wind loading - $10ms^{-1}$ wind speed loading at an operational pitch with a rotational velocity of $0.7rad/s$ about the z-axis	117
7.11	Fluid geometry for CFD analysis	118
7.12	Final CFD ANSYS Fluent mesh as used for the simulation of the aerodynamic loading on the blade	119
7.13	Final mesh for the generated blade	121
7.14	Analysis Settings as implemented in ANSYS for the CFD loading results showing the rotational velocity, gravitational loading and surface aerodynamic pressure loading	121
7.15	CFD loading for axial force loading. Single blade results showing cumulative axial force from root to tip.	122
7.16	CFD loading for Tangential force loading.	122
7.17	CFD Total Deflection results for operational pitch at $10ms^{-1}$ wind loading. Maximum deflection of $1.1014m$ at a blade radius of $117.3m$.	123
7.18	CFD Equivalent von Mises stress results for operational pitch at $10ms^{-1}$ wind loading. Maximum equivalent stress of $79.573MPa$ at a blade radius of $0m$ on the inner surface geometry) and minimum equivalent stress of $77484Pa$ at a radius of $117.3m$.	124

List of Figures

7.19	CFD Maximum Principal Stress results for operational pitch at $10ms^{-1}$ wind loading. Maximum principal stress of 63.092MPa (tension) at a blade radius of approximately 105m and minimum principal stress of -0.84047MPa at a blade radius of approximately 117.3m.	124
8.1	Test sample impact angle simulated to that of a point on a wind turbine leading edge . . .	129
8.2	Whirling arm erosion rig in the tribology lab within The University of Strathclyde . . .	130
8.3	Wastage map post Cycle 1. Highest percentage mass loss occurred at $\theta_{im} = 75^\circ$, $v_{im} = 40ms^{-1}$ with a loss of 0.070% (1.104 mg). The lowest percentage mass loss occurred at $\theta_{im} = 90^\circ$, $v_{im} = 60ms^{-1}$ with a loss of 0.037% (0.548 mg)	135
8.4	Wastage map post Cycle 2. the highest percentage mass loss occurred at $\theta_{im} = 45^\circ$, $v_{im} = 50ms^{-1}$ with a loss of 0.102% (1.58 mg). The lowest percentage mass loss occurred at $\theta_{im} = 30^\circ$, $v_{im} = 40ms^{-1}$ with a loss of 0.042% (0.68 mg)	135
8.5	Wastage map post Cycle 3. The highest percentage mass loss occurred at $\theta_{im} = 75^\circ$, $v_{im} = 40ms^{-1}$ with a loss of 0.107% (1.692 mg). The lowest percentage mass loss occurred at $\theta_{im} = 90^\circ$, $v_{im} = 50ms^{-1}$ with a loss of 0.070% (1.06 mg)	136
8.6	Wastage map post Cycle 4. The sample with the highest percentage mass loss after full testing occurred at an impact angle of $\theta_{im} = 60^\circ$, $v_{im} = 60ms^{-1}$ with a loss of 0.116% (1.794 mg). The lowest percentage mass loss occurred at $\theta_{im} = 15^\circ$, $v_{im} = 50ms^{-1}$ with a loss of 0.07% (1.204 mg).	136
8.7	Accumulative mass loss for: a) $v_{im} = 40ms^{-1}$ b) $v_{im} = 50ms^{-1}$ c) $v_{im} = 60ms^{-1}$	137
8.8	Wear mechanisms for particle impacts with a a) low angle of impact b) high angle of impact. Adapted from [90]	138
8.9	Ductile / Brittle wear rate according to impact angle – Adapted from [90]	140
8.10	SEM images of erosion damage from droplet impact at: a) $\theta_{im} = 15^\circ$ x150 Mag b) $\theta_{im} = 60^\circ$ x300 Mag c) $\theta_{im} = 75^\circ$ x350 Mag d) $\theta_{im} = 15^\circ$ x600 Mag	140
8.11	Characteristic erosion-versus-distance travelled curves. (a) Cumulative erosion versus exposure duration (time, or cumulative mass or volume of liquid impinged). (b) Corresponding instantaneous erosion rate versus exposure duration. Adapted from [194]	141
8.12	Percentage mass loss of fresh water erosion with (a) no applied bending stress (b) an applied bending stress	146
8.13	Percentage mass loss of salt water erosion with (a) no applied bending stress (b) an applied bending stress	147
8.14	SEM images of fresh water erosion on an unstressed sample	148
8.15	Mass loss of sample subject to fresh water erosion and no bending stress applied over various impact angles	149
8.16	SEM images of salt water erosion on an unstressed sample subject to salt water erosion	150

List of Figures

8.17 SEM image of salt crystals remaining on the surface after washing	151
8.18 Mass loss of sample subject to salt water erosion and no bending stress applied over various impact angles	151
8.19 SEM images of erosion on the GFRP samples subject to an applied bending stress	153
8.20 Optical microscope images of erosion on the GFRP samples subject to an applied bending stress	154
8.21 Optical microscope images of fresh water erosion on the GFRP samples subject to an applied bending stress	155
8.22 Comparison of mass loss between the stressed and unstressed GFRP sample	156
8.23 Erosion mechanistic map	157
8.24 Diagram of GFRP sample under load displayed as a simply supported beam	162
8.25 GFRP sample stressed to 350MPa in the holder within the WARER	164
8.26 GFRP sample in the WARER captured with the Cronos 1.4 high speed camera	168
8.27 Results from the high speed WARER illustrated as a line graph of mass loss over distance including all impact velocities with optical microscope images of a sample subject to $v_{im} = 80ms^{-1}$ and 350MPa at 0km, 216km and 432km	168
8.28 Results from the high speed WARER illustrated as a line graph of mass loss over distance travelled at $v_{im} = 60ms^{-1}$	169
8.29 Results from the high speed WARER illustrated as a line graph of mass loss over distance travelled at $v_{im} = 70ms^{-1}$	169
8.30 Results from the high speed WARER illustrated as a line graph of mass loss over distance travelled at $v_{im} = 80ms^{-1}$	170
8.31 Results from the high speed WARER illustrated as a line graph of mass loss over distance including all impact velocities	170
8.32 Annual energy production from a wind turbine as it declines over time due to rain erosion, adapted from [114]	173
8.33 Weight loss of material over exposure time in the mid section set out by Springer [71] outlining the Incubation period [92–94, 146, 200]	173
8.34 Weight loss of material over exposure time in the mid section set out by Springer [71] outlining the steady weight loss rate stage of rain erosion. [92–94, 146, 200]	175
8.35 Weight loss of material over exposure time in the mid section set out by Springer [71] outlining the steady weight loss rate stage of rain erosion. [92–94, 146, 200]	176
8.36 Weight loss of material over exposure time showing the three previous regions combined. [71, 92–94, 146, 200]	177
8.37 CLSM scan of a GFRP sample subject to $v_{im} = 80ms^{-1}$ impact velocity and $\sigma_{bend} = 150MPa$	178

List of Figures

9.1	The average rainfall in the months of January and May	187
9.2	The monthly erosion rates in January and May	188
9.3	The monthly erosion rates in January and May with overlays of major wind turbine farms and areas of frequent hail [218].	190
9.4	A map of the UK and Ireland showing four wind turbine farms and the result from the inputs of the projection app for a projected 10 year life	198
10.1	Severe leading edge erosion of a turbine blade. Source [52]	205
12.1	Nickel Cobalt coating on an aeroplane propeller to protect it against LEE. Source [224]	211

List of Tables

2.1	Modern and historical rotor designs, table adapted from [17]. Peak efficiency is dependant on design, values displayed are maximum values [20]	12
2.2	A typical modern day 2MW wind turbine adapted from [17]	13
2.3	Material properties for fibres used in composites [29]	26
3.1	Summary of the erosion conditions in some applications [50]	33
5.1	Corrosion rates of materials used on WAREER. 1mpy = 0.025mm/year 5mpy = 0.127mm/year (The maximum allowable stainless steel metal temperature is 50° to mitigate the potential for Cl-SCC)	71
5.2	Sample holder stresses when operating at 1000rpm	73
5.3	Safety factors of Sample holder operating at 1000rpm	73
5.4	Peak stress found within analysis of spinning main disc with sample holders in position	74
5.5	Safety factor of disc spinning at 1000rpm	74
5.6	results from measuring various gauges of needles	76
6.1	Outlining the preferred testing methods to obtain parameters that are relevant to rain erosion	85
6.2	Thin sandwich structures of Teflon and rubber have been imaged, alternating in material to mimic delamination. The layers of Teflon were estimated using microwave imaging techniques respectively. Adapted from [156].	101
7.1	Material properties for G10 epoxy glass used for computational analysis	116
7.2	Maximum Stress in compression and tensile.	125
8.1	Experimental duration	132
8.2	material properties of G10 epoxy glass used in this experiment	134
8.3	Summary of test parameters for high speed rain erosion testing	166

List of Tables

9.1	Theta values for each of the prediction curves	195
9.2	Input parameters for the demonstration of the predictive model app	197
9.3	Demonstration of whether the blades at each of the wind farms selected pass or fail on the given criteria within the app for a 10 year life	199